Department of Exploration Geophysics

Intrinsic and scattering attenuation from borehole seismic and well log data

Abdulaziz Farraj Alasbali

This thesis is presented for the Degree of
Doctor of Philosophy
of
Curtin University

March 2016

Declaration

To the best my knowledge and brief, this thesis contains no material previously published by any other person expect where due acknowledgement has been made. This thesis contains no material has been accepted for the award of any degree or diploma in any university.

Signature: 

Date: 9.3.2016

To my parents, my wife and my respected brothers and sisters.

Abstract

Over the past few decades, seismic amplitude analyses have become widely used in geophysical prospecting, especially for reservoir characterisation and monitoring. Hence, understanding the different factors affecting seismic amplitudes is important for the success of geophysical prospecting.

Attenuation of seismic energy and the resulting changes in the shape of the transient waveforms are a fundamental feature associated with the propagation of seismic waves in real materials. Reflection amplitudes are affected by attenuation in the overburden. Such variations can be erroneously taken for anomalies caused by variations in the reservoir properties, which require reflection amplitudes to be corrected for attenuation effects before being used for reservoir characterisation. It is therefore important to understand attenuation and its spatial variations.

Vertical seismic profiling (VSP) is a seismic acquisition technique in which the measurement of the seismic signal generated at the surface is recorded by a number of seismic sensors located in a well. It has been used to study seismic attenuation since the 1950s. VSP provides the most reliable data for attenuation studies for several reasons, including its ability to record both the downgoing and the upgoing wavefield and its high signal-to-noise ratio.

In this study, I develop a robust workflow for the estimation of apparent attenuation from the VSP data and the contribution of scattering from log data to evaluate the relative contribution of different mechanisms. To achieve these objectives, a large dataset was used, including VSP data, supporting wireline logging data (i.e., sonic logging data) and surface seismic data from several regions. The data were tested using a number of algorithms that estimated seismic attenuation (Q). Numerical modelling was also used to test Q estimation algorithms and quantify the relative contribution of the scattering component.

Thirty-seven wells from the North West Shelf in Western Australia (NWSWA) were selected to study the distribution of seismic attenuation and its mechanisms. Several wells from the Middle East (ME) region were also included to expand the study to a variety of geological settings.

In relation to the North West Shelf wells, the values of estimated seismic attenuation (i.e., Q values) were observed to be 16 and above. Younger sediments did not exhibit any significant attenuation. The upper limit of Q values was impossible to estimate as the reliability of Q estimates decreases with the increased value of Q and is limited by the sensitivity and the spatial resolution of the method. It was not possible to estimate $Q > 500$ robustly from the field VSP data. Attenuation was characterised as having three distinct levels: a Q of 200 and above reflected low attenuation, a Q between 65 and 200 reflected moderate attenuation and a Q of 65 and below reflected high attenuation. As detailed in Chapter 4, the estimation of Q was reliable for the high quality data (e.g., data from the Guardian 1 and Kentish Knock 1 wells). Significantly, approximately 60% of the Q values in this study ranged from 65 to 200; however, only 25% of the estimated values reflected high attenuation. Conversely, in the Middle East dataset the extent of the apparent attenuation was 46 and below and the high attenuation of this area had a significant effect on the quality of the seismic images.

The results of this research provide a clearer understanding of the spatial distribution and mechanisms of seismic attenuation behaviour across a variety of regions, including the NWSWA and the Middle East. Further, the results provide valuable information that will assist future researches in seismic attenuation.

Acknowledgements

First of all I would like to thank my Father, Farraj Alasbali and Mother, Jamilah Alasbali, who have support me through whole my life and my study. Special thanks goes to my wife, Reem, for her love and support throughout my study and for my kids, Khaled, Fahad, Alwaleed, Haya and Haifa, for their patience and understanding. I am grateful to acknowledge King Abdulaziz City for Science and Technology (KACST) for granting my PhD and providing the financial support during my study. Thanks are given to the Ministry of Petroleum and Mineral Resources of the Kingdom of Saudi Arabia and King Abdulaziz City for Science and Technology (KACST) for their cooperation and provision of the data.

I would like to thank sincerely my supervisor Dr Roman Pevzner, for his help, guidance, valuable advice and outstanding supervision. Throughout my PhD, his suggestions and motivation have always been of great value. I am also grateful to my co-supervisor Dr. Konstantin Tertyshnikov for his good advice and support during my PhD. Also, I am thankful to the head of Department of Exploration Geophysics, Professor Boris Gurevich, for his valuable comments.

I want to thank the faculty and all staff and my colleagues in the Department of Exploration Geophysics. Also I am very thankful to my brothers and sisters, for their supports and encouragements. I am also grateful to other Friends: Mohammed Khoshnavaz, Mohammed Alhosni, Muhammad Hossain, Felix Menu, Majed Almalki, Eva Caspari, Faisal Alonaizi, Mamdoh Alajmi, Khaled Alyousef, for their strong motivation and a serene working environment.

I wish to express my gratitude to Mr Robert Verstandig for technical support in my thesis and to the secretarial, Deirdre Hollingsworth, Judith Tournay, Jennifer McPherson, Rhiannon Howe and Zuzanna Kuklinski. I'm grateful to the many scientists who shared their time and knowledge with me.

The financial support by the sponsors of the Curtin Reservoir Geophysics Consortium (CRGC) is acknowledged. Gratitude is extended to H. Schmidt (Massachusetts institute of Technology for releasing OASES software. And also I

would like to thank Schlumberger for providing Petrel software through Curtin University.

Table of Contents

List of figures

List of tables

Chapter 1. Introduction

This chapter provides an introduction to the study and an overview of seismic attenuation and its importance. It also sets out the objectives, the proposed research method and the structure of the thesis.

1.1 Importance of seismic attenuation

Over the past few decades, seismic amplitude analyses have become widely used in geophysical prospecting especially for reservoir characterisation and monitoring. These methods include various poststack attribute analysis, amplitude-versus-offset (AVO), acoustic and elastic inversions (Prskalo, 2004). Hence, an understanding of the different factors affecting seismic amplitudes is important for the success of geophysical prospecting.

Attenuation of seismic energy and the resulting changes in the shape of the transient waveforms is a fundamental feature associated with the propagation of seismic waves in real materials. Seismic amplitudes are often affected by the attenuation in the overburden. Such variations can be erroneously taken for anomalies caused by variations in the reservoir properties, which require reflection amplitudes to be corrected for attenuation effects before being used for reservoir characterisation. It is therefore important to understand attenuation and its spatial variations.

Several factors can affect the amplitude decay of seismic waves (Hatton et al., 1986), including geometrical spreading (or divergence) of the wavefront, interface transmission losses, multiple reflection, scattering and absorption. These phenomena are controlled by properties of rock formations such as mineral composition, lithology, permeability and, porosity, fluid properties such as compressibility, viscosity and saturation and the spatial distributions of these properties. Hence, the study of seismic attenuation and its spatial distribution can potentially provide valuable information about these rock and fluid properties. Rapoport and Ryjkov (1994) observed a strong correlation between attenuation and oil pools using VSP data in Russia and Asia. Similarly, Mitchell et al. (1996) used seismic data from Texas to connect the presence of gas with high values of attenuation. Martín et al. (1998) found a strong correlation between attenuation and the presence of oil when using 3D seismic data from Eastern

Venezuela. An investigation into layer-*Q*'s can assist in correlating attenuation and lithology (Tonn, 1991). Sun and Goldberg (2000) also discussed the correlation between attenuation and lithology. The connection can be used to identify the lithology of an area and assist in finding potential hydrocarbon reservoir sites.

1.2 Estimation of seismic attenuation from borehole seismic data

Vertical seismic profiling (VSP) is a seismic method in which the seismic sources are deployed at or near the surface and the seismic signal is recorded using receivers set in a borehole. There are four types of VSP: standard, deviated well, offset and walk-away (Oristaglio (1985).

VSP has been used to study seismic attenuation since the 1950s. Ricker (1953) and Levin and Lynn (1958) reported that the width of the wavelet increase as the wave propagates down the hole. Gal′perin (1974) proposed the systematic use of VSP for attenuation studies. VSP is considered the most suitable for attenuation studies for the following main reasons:

- Unlike surface seismic surveys, which analyse the propagation of reflected and refracted waves, VSP records contain also a direct downgoing wave. This provides a substantial advantage because the amplitudes are not affected by reflection or refraction coefficients, but only by factors such as geometrical spreading and attenuation.
- VSP has a capability to sample the downgoing wavefield at various known depths (Matsushima, 2006); hence, it provides an opportunity to estimate local or interval attenuation at each depth interval.
- VSP is a suitable tool for attenuation estimates because VSP data are usually characterised by a high signal-to-noise ratio (S/N) and wide amplitude spectra compared with surface seismic measurements. A high S/N is the result of the fact that, in VSP, geophones are located in boreholes, which have a very quiet environment and where the level of ambient noise is very low. Further, the amplitude and bandwidth of

downgoing direct waves are larger than in reflected waves as direct waves are not affected by reflection coefficients and only propagate one way (from surface to geophone). Additionally, in zero-offset and offset VSP, the measurements are conducted with a constant source position and are therefore unaffected by laterally changing near-surface properties or source coupling.

Extensive studies have been undertaken using a variety of methods, such as velocity dispersion (Sun et al., 2009), amplitude decay (McDonal et al., 1958), changing amplitude spectra (Hauge, 1981; Quan and Harris, 1997; Blias, 2011), analytical signal (Engelhard, 1996), pulse deformation in the time domain (Gladwin and Stacey, 1974) and spectral ratio (Tonn, 1991; Blias, 2011). The most common approach used to study attenuation is the spectral ratio method (Ganley and Kanasewich, 1980). However, although it is a useful technique, it has some limitations.

Blias (2011) proposed a modification to overcome low vertical resolution and low accuracy. Gladwin and Stacey (1974) used the pulse rise-time method to study the *Q* structure of the earth. Amundsen and Mittet (1994) used various techniques of *Q*-factor estimation from VSP data, including pulse-broadening, amplitude decay method and spectral-ratio. Tonn (1991) examined ten different techniques for *Q* estimation and found that only the highest-quality VSP data has important information in the fields of VSPs sedimentary basins, which is investigated by the computed attenuation. Many methods for the study of attenuation have been proposed; however, there is still a lack of understanding of the limitations and uncertainties associated with various techniques.

Most studies of seismic attenuation from VSP focus on one or a small number of wells. However, to use attenuation for amplitude corrections or reservoir characterisation, it is essential to understand how attenuation varies spatially. Hence, I propose a more systematic study using a substantial number of wells from two regions namely, the NWSWA and the Middle East, to analyse attenuation on a regional scale. This will provide an understanding of the correlation between estimations of *Q* values vertically and laterally for the lithology of a variety of wells in order to develop a robust technique that can be applied in a variety of regions in future investigations.

1.3 Main causes of attenuation

Attenuation can be defined as a process of energy loss caused by the propagation of seismic waves in a medium. These changes affect the amplitude and shape of waves (Pujol, 2003). Previous studies have shown that estimated attenuation (commonly known as apparent attenuation) is an amalgamation of absorption and scattering attenuation (O'Doherty and Anstey, 1971; Schoenberger and Levin, 1974; 1978; Menke, 1983).

Absorption refers to energy loss resulting from anelastic processes or internal friction during wave propagation. When the wave passes through the earth, the energy converts to heat. The attenuation of propagating waves due to absorption is consistent with a linear theory of wave propagation in which dispersion is a necessary consequence of absorption (Futterman, 1962).

The second cause is scattering attenuation. Scattering occurs due to the heterogeneity of the medium. Small scale heterogeneities can scatter a portion of the wave's coherent energy in all directions. In a layered medium, the wave loses energy as it is reflected at each interface. Thus in scattering, coherent energy is converted into scattered wave energy.

Absorption is believed to be controlled by rock and fluid properties, while scattering is mainly controlled by heterogeneity. Thus, for the analysis of surface seismic data it is necessary to understand the comparative importance of the two attenuation mechanisms and to quantify them for measuring attenuation. Thus, it is important to separate intrinsic absorption and scattering to understand the nature of the observed attenuation.

One way to separate absorption and scattering is to estimate scattering attenuation from well log data. Indeed, if sonic and density logs are available in a well along with VSP data, the log data can be used to construct a detailed 1D elastic earth model. The reflectivity method can then be used to compute synthetic VSP seismograms. Attenuation can be estimated from the synthetic VSP seismograms using the same method as that applied to the field data. As the model used to compute synthetic VSP seismograms is ideally elastic (no absorption), the attenuation estimated

from synthetic VSP seismograms will be scattering attenuation. Absorption can then be estimated by subtracting the scattering attenuation estimated from synthetic seismograms from apparent (total) attenuation obtained from field seismograms.

1.4 Thesis objectives

The main objectives of this thesis were to construct a robust and consistent methodology to estimate the vertical and lateral distribution of seismic attenuation from borehole seismic data and to evaluate the relative contribution of anelastic absorption and scattering. To achieve these objectives, a large dataset was evaluated that comprised of VSP and log data. Additional objectives of this research included:

- quantifying uncertainties of Q estimation from VSP data
- investigating the spatial resolution of the estimates
- identifying the conditions required for different attenuation mechanisms to dominate
- exploring the relationships between seismic attenuation and other properties of the geological units across several areas.

1.5 Research

This research was conducted in several stages using the zero-offset VSP data of several wells in the NWSWA and Middle East regions obtained from the Department of Mining and Petroleum of Western Australia (DMPWA) and the Ministry of Petroleum and Mineral Resources of the Kingdom of Saudi Arabia respectively. A workflow was then designed to prepare the data to estimate Q. Additionally, any lateral and vertical variations of Q were analysed in detail within the boreholes.

First, a literature review was undertaken of methods of apparent Q estimation using VSP data and mechanisms of seismic attenuation. The review examined the most common publications to gain an understanding of the issue. A preliminary literature

screening showed that, to date, the majority of research in the field of seismic attenuation estimation using VSP data has only examined one or a few boreholes. Notably, Müller et al. (2012) conducted studies on seismic attenuation estimation for five boreholes from rig-source VSPs. Using log data, they noted that a larger-scale research effort based on a greater number of boreholes would improve the reliability of the apparent *Q* estimates and provide an understanding of the mechanisms of attenuation.

Second, a large dataset was collected, which comprised of high-quality zero-offset (VSP) data supported by wireline logging data from several regions. Log data was averaged in a regular blocks of given thickness, all blocks were of the same thickness in one model. It was anticipated that both reflectivity and finite difference methods for synthetic data would be used. The research sought to understand the relative contribution of absorption and scattering *Q* factors for various geological settings and to develop the characterisation of transmission loss, scattering attenuation and anelastic absorption by using different datasets that contain varying lithologies, such as sedimentary and hard-rock environments.

The bulk of the research concentrated on zero-offset VSP data analysis scattering attenuation; however, vertical attenuation anisotropy was also investigated using walk-away VSP data (both field and synthetic) in the Middle East region.

The centroid frequency shift (CFS) method was used to perform the *Q* estimation. To obtain a reliable *Q* estimation, the method was applied at intervals of the borehole exhibiting a near-linear amplitude decay over depth. Finally, to obtain a better understanding of how attenuation occurs in the boreholes, the wells from NWSWA provided by the DMPWA were divided into several areas to build well sections in order to find the relationship between the *Q* value and the lithology of the study area.

1.6 Thesis structure

This thesis is divided into six distinct chapters, which are outlined below.

Chapter 1 provides an introduction to the study and an overview of seismic attenuation and its importance. It also sets out the objectives of the thesis, the research method and the structure of the thesis.

Chapter 2 provides an overview of the main factors of seismic amplitude and reviews apparent, scattering and intrinsic attenuation and a review of seismic attenuation. It sets out a definition of the value of Q estimations and introduces the principles underlying a variety of methods used to measure seismic attenuation.

Chapter 3 discusses the workflow and method used to estimate apparent attenuation and its scattering components through 1D wave modelling.

Chapter 4 presents the findings and outcomes of the research undertaken in the North Carnarvon Basin wells. It also presents information relating to the geological settings, data availability and VSP data acquisition parameters.

Chapter 5 presents the findings of the research undertaken in the Middle East, including geological settings, VSP and well log data availability. The estimation of apparent attenuation and the contribution of scattering are also verified. Further, the chapter outlines the estimated vertical transverse isotropy (VTI) anisotropy parameters and principal observations.

Chapter 6 summarises the research outcomes and presents the conclusions drawn from the research in relation to the research objectives.

Appendix A contains the field and synthetic data results for the North Carnarvon Basin wells.

Appendix B contains copyright releases, permission to use information used from the published papers referred to in this thesis, and permissions granted for the use of a number of figures.

Chapter 2. Seismic Attenuation

This chapter provides an overview of the main factors of seismic amplitude and reviews seismic attenuation theory. Further, it defines apparent, scattering attenuation and intrinsic attenuation and sets out a definition of the attenuation (Q) estimations. It also introduces the principles underlying a variety of methods used to estimate seismic attenuation.

2.1 Factors affecting seismic amplitude

In the field of VSP data analysis, it is important to take into account all factors affecting seismic amplitudes. This section presents a general overview of these factors.

Hatton, et al. (1986) noted that causes of seismic attenuation include geometrical spreading (or divergence) of the wavefront, transmission losses, absorption and scattering attenuation. These factors significantly affect seismic amplitudes. Further, O'Doherty and Anstey (1971) stated that several factors can affect reflection amplitudes: multiple reflection, interface transmission losses, absorption, interface reflection coefficient and spherical divergence. Sheriff (1975) asserted that the major factors affecting seismic amplitude are energy portioning, absorption and attenuation, geometrical spreading, scattering in the near surface, source and receiver array response, and interference due to fine layering. Figure 2.1 identifies these factors.

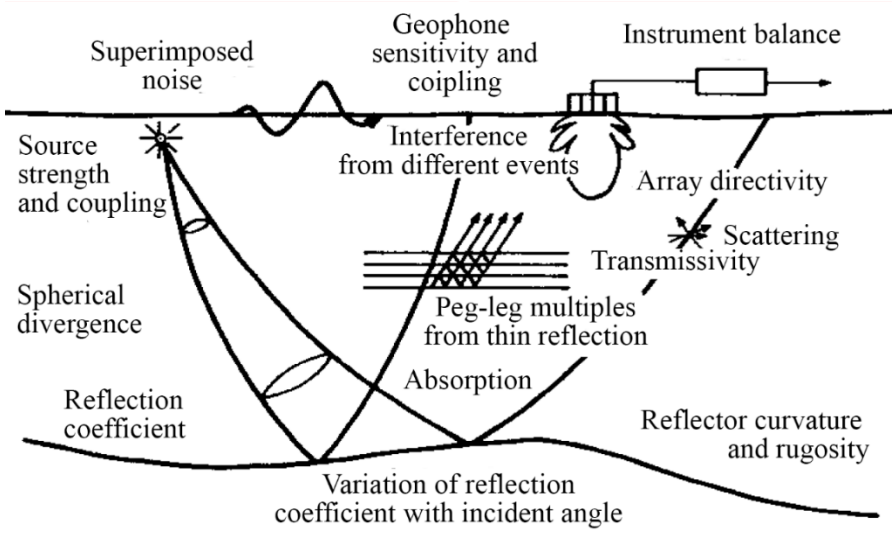

Figure 2-1. The diagram reflects the factors affecting seismic amplitude (Sheriff, 1975).

Under the linear system theory, the amplitude spectrum of a wave recorded by a receiver *SR*(*f*) can be expressed as a function of the spectrum at the seismic source and a combination of factors (both dependent on frequency and not) affecting the amplitude:

$$SR(f) = \mathrm{G}(f) \cdot D \cdot H(f) \cdot S_0(f) \qquad (2\text{-}1)$$

where f is linear frequency; $G(f)$ includes instrument response, source and receiver coupling, radiation pattern, and frequency-independent transmission losses; D is characterizes wavefront divergence; $S_0(f)$ is the amplitude spectrum of the emitted wave; and $H(f)$ describes the effect of attenuation (Quan and Harris, 1997).

2.1.1 Divergence of the wavefront

Geometrical spreading, which is often referred to as spherical divergence, is an important factor controlling seismic amplitudes (Wang and McCowan, 1989). Amplitude decay due to divergence only results from geometrical effects. It is a result of the initial energy E input distributed by a source over a sphere as $E/4\pi r^2$. As the radius r of the sphere increases, the energy density decreases; since amplitude is proportional to the square root of energy, the amplitude of spherical wave is decreasing proportional to 1/radius**.** For instance, in a homogeneous acoustic medium, spherical wavefronts emanate from a source, and the pressure amplitude of the wave is the inverse of the wavefront radius (Newman, 1973). Conversely, in a real earth model, variations of velocity with depth must be taken into account, as wavefronts will be affected by refraction effects. Newman (1973) provided derivations for the layered earth model for an arbitrary source-receiver offset. In addition, the divergence correction for normal incidence for a layered media is given by:

$$d(t) = \frac{tV_{RMS}^2}{V_1} \qquad (2\text{-}2)$$

where t is the two-way reflection time, V_{RMS} is the root-mean-square (RMS) velocity usually used in normal moveout (NMO) correction and V_1 is the velocity in the first layer. However, when the offset distance increases, the solution of the quadratic equation will not produce a good approximation. It should be noted that primary and

multiple reflections cannot be compensated at the same time because of the difference in RMS velocities. According to Newman (1973), in primary reflections, attenuation due to divergence will be larger than in multiple reflections propagating at the same time.

For horizontal layering and traces recorded at the short offsets, a proportional compensating factor $t\ V^2$ is required, where V is the time-weighted RMS velocity commonly used in NMO calculations. Therefore, divergence factors are proportional to the distance from a virtual image of the source at depth, as opposed to actual distance travelled by the

2.1.2 Transmission losses

The effect commonly referred to as Transmission loss (TL) is the displacement of energy occurring as the seismic wave travels through an interface such as the earth. This results in the energy of the transmitted wave being lessened with energy being conserved by creation of a reflected wave. In relation to energy conservation, energy reflected through an interface cannot be transmitted. Therefore, transmission loss is relative to the size of the reflection coefficient (Sheriff, 1973). Moreover, loss of energy can occur if the amplitude of a transmitted wave is either larger or smaller than the amplitude of the incident wave (Sheriff, 1973).

Hatton et al. (1986) noted that the transmission of energy is reduced by partial reflection at interfaces according to the impedance contrast. Thick layers of constant character that provided gradual velocity increase with depth had fewer effects on energy transmission losses, whereas the impedance contrast in cyclic sequences caused a major loss. However, when substantial thin layering occurs, transmission loss may be over-estimated due to a complex interference pattern between the primary and interbed multiples (O'Doherty and Anstey (1971), see section 2.1.3

2.1.3 Attenuation

The reduction of frequency content and the amplitude in the signals that travel through the earth are considered responsible for seismic attenuation (Portsmouth et al., 1993). As a result of attenuation, the amplitude of the seismic wave decreases and the low-frequency portion of the wave range becomes dominant when seismic signals are evaluated at varying distances from the source (Goloshubin and Bayuk, 2010).

The seismic attenuation effect on the amplitude spectrum of a direct wave is measured by a receiver positioned at a given depth. As defined by Ward and Toksöz (1971), the following function *H(f)*:

$$H(f) = exp\left(-f \int_{ray} \alpha_0 dl\right), \tag{2-3}$$

where *f* is linear frequency and α_0 is the attenuation coefficient, which is related to the quality factor *Q* (representing quality, the absorption factor). As defined by Quan and Harris (1997), the expression is:

$$\alpha_0 = \frac{\pi}{Qv}, \tag{2-4}$$

where *v* is the velocity of the wave. Shearer (1999) borrowed a proportionality constant known as *Q* from electrical engineering defined as:

$$\frac{1}{\mathrm{Q}(\omega)} = -\frac{\Delta \mathrm{E}}{2\pi \mathrm{E}} \tag{2-5}$$

where *Q* is the quality factor, E is the peak strain energy and ΔE is the energy loss per cycle. After *Q* cycles, the amplitude decreases from the original value by around 4 %. In this thesis, *Q* and *v* are assumed to be independent of frequency unless otherwise specified.

The connection between *Q* (as the quality factor) and the strength of the seismic attenuation is an inverse relation. That is, a low *Q* value is more attenuating than a

high *Q* value. A valid approximation is possible when considering Q >> 1. Therefore, this estimation is more appropriate for seismic application.

Alternatively, Q can be expressed as a function of travel time. This is more appropriate when considering a seismic application because the wave is propagating forward:

$$A(t) = A_0 e^{\frac{-wt}{2Q}} \tag{2-6}$$

Equation (2-2) shows that if *Q* is independent of frequency (constant *Q*) or varies slowly with frequency, then higher-frequency components attenuate faster than lower-frequency components. High-frequency waves go through more oscillations for any given time than low-frequency waves. Therefore, the pulse widens at successive distances as the wave travels away from the source, and attenuation removes the high-frequency component of the pulse as the wave propagates.

Numerous studies have indicated that attenuation can be estimated from the field seismic data (O'Doherty and Anstey, 1971; Schoenberger and Levin, 1978; Menke, 1983). This is known as apparent attenuation and is typically assumed to have two contributors: intrinsic attenuation (wave energy decay due to inelastic absorption) and scattering (wave energy decay due to loss of coherence). O'Doherty and Anstey (1971) show that the apparent attenuation is related to the scattering and intrinsic attenuation by the following equation:

$$\frac{1}{Q_{apparent}} = \frac{1}{Q_{scattering}} + \frac{1}{Q_{intrinsic}} \tag{2-7}$$

Intrinsic attenuation or absorption is a process by which the energy of the propagating wave is progressively reduced due to of the conversion of a portion of its total energy into heat. Absorption occurs because the medium in which the wave propagates is not ideally elastic. Such media are called anelastic; that is, when such a medium is subjected to some external stress, and then the stress is removed, the medium is not returned to its original state because some portion of the elastic energy is lost in the process. Many mechanisms cause anelastic absorption. For fluid-saturated

rocks, the most important mechanism is viscous dissipation caused by the wave-induced flow of the pore fluids relative to the solid matrix (Pride et al., 2003; Müller et al., 2010). Another important mechanism of absorption is viscoelasticity. Viscoelastic behaviour is typical for heavy oils; hence, this mechanism is important for rocks saturated with heavy oils; such as oil sands (Batzle et al., 2006; Makarynska et al., 2010).

As mentioned above, the other primary cause of attenuation is scattering. Scattering is a process by which the energy of the coherent propagating wave is progressively reduced owing to its portion transferinto elastic waves scattered by inhomogeneities so that the total elastic energy of all waves is conserved. Thus, scattering can occur in a purely elastic medium, but the medium must be inhomogeneous. For instance, if a medium contains inclusions such as cavities, vugs or cracks, the propagating wave will be scattered (diffracted) by these inhomogeneities in all directions, and the energy of the direct wave will be reduced. Scattering can also be caused by fine layering, as the passing waves undergo multiple reflections at each interface. Scattering by fine layering is similar in nature to transmission loss (discussed in Section 2.1.2), but it is frequency-dependent due to a complex pattern of constructive and destructive interference between the passing waves and multiple reflections, which results in an increase in low frequencies and attenuation of high frequencies (O'Doherty and Anstey, 1971; Schoenberger and Levin, 1974; Shapiro and Hubral, 1996). Scattering due to fine layering is controlled by the variations of elastic properties and density within a stratigraphic sequence and is therefore also known as stratigraphic filtering. For scattering attenuation to be the main cause of attenuation, the variation of elastic properties between layers must be quite strong.

2.2 Estimation of apparent attenuation from VSP data

A variety of methods may be used to provide a *Q* estimation, including amplitude decay, spectral ratio, spectral amplitude matching, pulse deformation, centroid frequency shift (CFS), time-domain match-filter, velocity dispersion-oriented and waveform inversion-oriented. Each method has limitations and strengths; however, the CFS was chosen for this study because of its reliability in *Q* estimations. The method was modified to allow for the decrease of spectrum widths in the frequency domain with the distance of wave propagation..

The most common approach used to study attenuation is the spectral ratio method (Ganley and Kanasewich, 1980). This technique has been proven to be useful; however, it has some limitations. Blias (2011) proposed a modification to overcome low vertical resolution and low accuracy. Engelhard (1996) proposed the analytical signal method, and Markus (1974) the spatial-ratio method, while Quan and Harris (1997) used the CFS method.Gladwin and Stacey (1974) used the pulse rise-time method to study the *Q* structure of the earth. Amundsen and Mittet (1994) employed various techniques of *Q*-factor estimation using VSP data, including pulse-broadening, amplitude decay and spectral ratio. Tonn (1991) examined 10 different techniques for *Q* estimation, by using the computed attenuation, and found that the highest-quality VSP data had important information in two field of VSP sediments.

and Tonn (1991) cited the match-technique method, while Jannsen et al. (1985), Tonn (1991) and (Blias, 2011) preferred the spectrum-modelling method. Using VSP data, Tonn (1991) undertook an extensive comparison of the methods for *Q* estimation and concluded that the spectral ratio method is the best method for a noise-free scenario. Patton (1988) and Tonn (1991) noted that the estimation provided by the spectral ratio method may deteriorate drastically with increasing noise; therefore, a reliable estimation is questionable, and it is more useful to obtain an estimate from the surface reflecting data. Sheriff and Geldart (1995) determined that the tuning effect of local thin-beds should be addressed properly for the estimation from reflection data.

Müller, R. Pevzner, M. Lebedev, M. Urosevic and R. Galvin (2012) reached similar conclusions; however, they found that the CFS and spectral amplitude matching methods were considerably more stable in evaluating and estimating the

apparent *Q* compared with the spectral ratio method. They also pointed out that the main problems with apparent *Q* estimates are source instability, poor spatial resolution, interference, requirements for the recording hardware and potential effects related to the presence of seismic anisotropy.

The following sections provide a brief overview of the common suite of *Q* estimation techniques.

2.2.1 Amplitude decay method

The amplitude decay method used to measure *Q* (Tonn, 1991). *Q* is expressed in terms of the ratio of two amplitude spectra at corresponding receivers, located at R1 and R2, and the amplitudes are measured at the same frequency for both receivers. If it is assumed that the source signature remains unchanged and the radiation pattern disturbs receivers uniformly, then the ratio of amplitude spectra of a downgoing seismic wave can be expressed as:

$$\text{In}\ \frac{S_{R1}(f)}{S_{R2}(f)} = \pi f . \frac{\Delta l}{v} . \frac{1}{Q} . + M = \pi f . \Delta t . \frac{1}{Q} + M \qquad (2\text{-}8)$$

The *Q* estimate can be calculated by rearranging the above equation:

Where Δl = distance between the receivers

Δt = difference in arrival times

M = constant responsible for wavefront divergence and transmission losses;

$$\frac{1}{Q} = \frac{v}{\pi f \Delta l}\left(\text{In}\ \frac{S_{R1}(f)}{S_{R2}(f)} - M\right) = \frac{1}{\pi f \Delta t}\left(\text{In}\ \frac{S_{R1}(f)}{S_{R2}(f)} - M\right) \qquad (2\text{-}9)$$

After the application of corrections, the logarithm of the amplitude decay at a given frequency is plotted as a function of depth. The time of the first arrival and the gradient of the slope give the attenuation estimate (McDonal, Angona, Mills, Sengbush, Van Nostrand and White, 1958; Pujol and Smithson, 1991; Tonn, 1991; Pujol et al., 1998). Quan and Harris (1997) doubted the reliability of this method because amplitude distortion is caused by many factors, including the coupling of the source and the receiver, scattering, and reflection effects.

2.2.2 Spectral ratio method

Equation 2-9 says that the logarithm of the spectral ratio of two direct waves is a linear function of frequency. Q can thus be calculated by fitting a straight line to the log of that ratio. The spectral ratio is one of the most frequently used methods (Schoenberger and Levin, 1974; Ganley and Kanasewich, 1980; Hauge, 1981; Shaw et al., 2008) because it is not constrained by receiver coupling settings, geometrical spreading and transmission losses.

According to Hauge (1981), *Q* mechanisms contribution to attenuation include spherical divergence and the dependence of pulse amplitude on impedance. Picotti and Carcione (2006) pointed out that the frequency-independent scaling factor as part of the intercept term of the linear regression is the main advantage of the spectral ratio method. As this would not affect the *Q* estimation, it does not require knowledge of frequency-independent factors such as geometrical spreading and transmission losses, and it is less dependent on receiver coupling conditions.

Dasgupta and Clark (1998) applied the classical spectral ratio method to designatured and NMO stretch-corrected common midpoint CMP gather on trace-by-trace basis to obtain the apparent *Q* versus offset (QVO). Cheng and Margrave (2008) developed a more complex spectral ratio method that uses both the phase spectra of signals and the amplitude spectra. The classic spectra ratio method produces difficulties and may take considerable time to automatically select an appropriate frequency band for the *Q* estimation when spectral ratios are not linearly distributed evenly.

Cheng and Margrave (2011) determined a complex spectral ratio method that employs both phase spectra of signals and the amplitude spectra, where *Q* is estimated by solving an inverse problem to minimise the misfit between the modelled and measured complex spectral ratios as an addition to the classic spectral ratio method. Patton (1988) and Tonn (1991) concluded that the spectral ratio method may deteriorate dramatically due to increasing noise.

2.2.3 Spectral amplitude matching technique

Blias (2011) indicated that low accuracy and weak vertical resolution are the pitfalls of the spectral ratio method and proposed a modification by reducing the misfit between the spectrum recorded at the second receiver and its prediction made through the spectrum recorded at the first receiver:

$$W\ (Q,K) = \left\| S_{R2}(f) - K\ \cdot\ S_{R1}\ (f) \exp -\pi f\ \cdot\ \Delta t.\frac{1}{Q}\ \right\|_{L2} \rightarrow\ min \quad (2\text{-}10)$$

where K covers all frequency-independent factors. Employing the fact that $\partial W(Q,K) - \partial K = 0$ at the minimum transforms this objective function into a function of only one variable.

2.2.4 Pulse deformation methods

The evaluation of changes in the shape of the wavelet during its propagation through the attenuating media forms the basis for a group of methods that includes pulse broadening (Ricker, 1953), pulse rise-time (Gladwin and Stacey, 1974) and the pulse power method (Stainsby and Worthington, 1985). Gladwin and Stacey's (1974) study resulted in finding an empirical dependence of pulse rise time τ on the time of propagation of the pulse *t* (as explained in the following equation

$$\tau = \tau_0 + C \int_0^1 Q^{-1} dt \quad (2\text{-}11)$$

where $\boldsymbol{\tau}_o$ is the rise-time of the source, C is constant, $\boldsymbol{\tau}$ is the arrival time of the maximum slope and *Q* is the quality factor. A value of C = 0.53 ± 0.04 is obtained in hard rocks using ultrasonic measurements (Gladwin and Stacey, 1974).

2.2.5 Centroid frequency shift method

The changes in centroid frequency and its variance can be used to measure the *Q* factor. Quan and Harris (1997) stated centroid frequency and variance respectively as:

$$f_R = \frac{\int_0^\infty f \cdot S_R(f)\, df}{\int_0^\infty S_R(f)\, df} \tag{2-12}$$

and

$$\sigma_R^2 = \frac{\int_0^\infty (f - f_R)^2 \cdot S_R(f)\, df}{\int_0^\infty S_R(f)\, df} \tag{2-13}$$

A shift in the centroid frequency between receivers, along the ray path for an amplitude spectrum defined in terms of Gaussian function, is:

$$\frac{(f_{R1} - f_{R2})}{\sigma_R^2} = \int_{ray} \frac{\pi}{Qv}\, dl \tag{2-14}$$

The above equation requires a scaling factor for non-Gaussian spectra. Picotti and Carcione (2006) indicated that the Centroid Frequency Shift (CFS) method is based on the fact that higher frequencies decay faster than lower ones when passing through any medium. As a result, the centroid frequency of the signal spectrum is downshifted when moving from the source to the receiver. They stated that this method is more reliable than the spectral ratio method when the signal used is broadband and attenuation is high enough to generate evident high-frequency losses. Matsushima (2007) also employed this method for zero-offset VSP data.

2.2.6 Time-domain match-filter method

For *Q* estimation, Cheng and Margrave (2012) suggested a time-domain match-filter method, which was shown to be robust to noise while being suitable for application to surface reflection data. Jannsen, Voss and Theilen (1985), supported by Tonn (1991) and Blias (2011), purported that this method is a complex wavelet-modelling method that uses wavelet estimation—a time-domain counterpart to

spectrum modelling. Cheng and Margrave (2012) projected a time-domain match-filter method for *Q* estimation, that was robust to noise and could be applied to surface reflection data. Spectrum modelling, without dividing the spectra, is a modified approach to a spectral ratio method. Both the match-filtering method and the match-technique method (Raikes and White, 1984; Tonn, 1991) propose matching at different stages of the *Q* estimation procedure.

2.2.7 Velocity dispersion oriented technique

Frequency-independent *Q* was evaluated by analysing phase velocities on uncorrelated VSP data (Sun, Milkereit and Schmitt, 2009). After comparing a number of methods for measuring velocity dispersion, the authors suggested that moving-window cross-correlation was the best method. They advocated a 6 % velocity variation over a frequency range from 8 Hz to 180 Hz, but the evaluated *Q* values were extremely low.

2.2.8 Waveform inversion oriented techniques

Several studies have utilised viscoelastic waveform inversion algorithms for attenuation estimations (Dietrich and Bouchon, 1985; Amundsen and Mittet, 1994; Toverud and Ursin, 2005; Yang et al., 2009). If knowledge of fine-scale velocity fields can be obtained, this approach has good potential for the estimation of intrinsic attenuation devoid of scattering constituents.

2.3 Estimation of scattering attenuation from well logs

During the passage of a wave through an array of thin layers in the subsurface, the original coherent seismic pulse undergoes distortion and amplitude loss due to multipath reflections, transmission and the resulting destructive/ constructive interference. This occurs despite the overall wavefield energy being conserved. Aki and Chouet (1975) suggested that the resulting seismic wavefield recordings are a superposition of a seismic primary waves—that is, the distorted initial pulse plus coda waves. Additionally, the layer stack acts on the seismic wavefield as a filter. This is also known as stratigraphic filtering. If sonic and density log data are available in a vertical well in a horizontally layered medium, the scattering attenuation can be estimated from the well log data. As the total (or apparent) attenuation can be obtained from VSP seismograms (see Section 2.2), the intrinsic attenuation (absorption) can be estimated by subtracting the scattering attenuation from the apparent attenuation (see Equation 2-15).

2.3.1 Estimation of scattering attenuation from the generalised O'Doherty–Anstey theory

Based on the power spectrum of the reflection-coefficient series, O'Doherty and Anstey (1971) derived a frequency-domain stratigraphic filter that can be used as an equation for Q for scattering attenuation:

$$Q^{-1} \approx \omega \acute{\mathrm{M}}(2\omega) \tag{2-16}$$

where $\acute{\mathrm{M}}(\omega)$ is the power spectrum of the logarithmic impedance fluctuations. The impedance fluctuations can be obtained from P-wave sonic and density logs. The power spectrum can be obtained by computing the autocorrelation function of the logarithmic impedance fluctuations and taking the Fourier transform of the autocorrelation function. This approach has been analysed in a number of theoretical wave propagation models in layered media. Burridge et al. (1988) and Asch et al. (1991) investigations of multiple scattering elastic and scalar wave problems

improved the correlation knowledge between the result and the theory of wave localisation—known as O'Doherty–Anstey (ODA)

Shapiro and Hubral (1996) derived a stochastic generalisation of the ODA findings and provided a dynamic equivalent medium description for the propagation of elastic waves. Despite being based on a number of assumptions, the ODA theory precisely describes the scattering in the frequency domain both in the low-frequency limit (Backus averaging) and the high-frequency limit (Ray theory hypothesis). Generally, the ODA theory is simple and has been applied successfully to remove the effect of overburden losses in order to enhance the precision of AVO studies in certain sedimentary basins (Shapiro and Hubral, 1999).

2.3.2 Estimation of scattering attenuation from full-wave modelling

Another way of estimating scattering attenuation is to compute the synthetic VSP seismogram from the sonic and density log (assuming that all layers are elastic) and then estimate attenuation from the synthetic seismogram in the same way as apparent attenuation is estimated from a field seismogram. As the synthetic seismogram is computed for elastic media, the attenuation estimated from the synthetic seismograms is scattering attenuation.

The simulation for seismic wave propagation in 1D layered media is built in terms of an integral transform in which the wavefield in the frequency domain is expressed as an integral over time-harmonic plane waves (Aki and Richards, 1980). The matrix propagator method (Thomson, 1950; Haskell, 1953; Fuchs and Müller, 1971) is used to calculate the reflection and transmission coefficients for plane waves in an array of layers. This approach enables a recursive computation of plane wave 4*4 transmission matrices from 4*4 matrices for individual layers.

The use of 4*4 matrices is economical in relation to memory usage; however, it faces numerical instability when, for one layer, the propagation angle for some waves is greater than the critical angle for P-waves, but smaller than that for P-SV waves. At such angles, P-waves become transient in this layer, making one element of the layer matrix exponentially larger, while others are undefined. a number of methods have

been proposed to overcome this instability (Dunkin, 1965; Thrower, 1965; Kennett, 1974; Molotkov, 1984; Kennett, 2009), some of which are extremely complex (Fryer and Frazer, 1987). However, the most well-known methods are the invariant embedding method (Kennett, 1974; 2009) and the global matrix method (GBM) (Schmidt and Tango, 1986).

The GBM is employed in the OASES software available from the Massachusetts Institute of Technology (MIT). The GBM generates a global 4n*4n matrix of the layer system so that very large and very small exponential values cancel each other out, resulting in numerical stability. In comparison with similar software packages, OASES can handle thousands of layers and can compute anisotropic elastic layers with vertical symmetry axis (VTI layers), fluid layers and frequency-dependent attenuation. The flexibility of locating receivers anywhere in the isotropic solid and fluid media favours modelling for zero-offset, walk-away VSP and surface seismic data (Schmidt, 2004).

Another advantage of OASES is its capability to generate seismograms for the vertical and horizontal components of particle velocity/pressure, which allows it to model two-component geophone and hydrophone data. Point source, line source and plane wave calculations can also be conducted with this software. OSIRIS commercial software employs an identical approach. It has been noted that for a large number of layers, GBM-generated seismograms may involve some false features (Mi and Margrave, 1998). These are expected in modelling generally, as the inferences that are made depend on the choice of computational parameters. These can be fixed through appropriate practice.

Chapter 3. Estimation of Seismic Attenuation from Zero-offset VSP and Log Data

This chapter discusses a workflow and method for estimating apparent attenuation from VSP data and its scattering component through 1D wavefield modelling.

3.1 The workflow

The workflow consisted of the following steps:

- Zero-offset field VSP data were used to estimate the apparent attenuation under the modified CFS method.
- The scattering component of the attenuation for the same formations was derived using an approach similar to that applied to synthetic VSP seismograms and computed using a 1D elastic velocity model derived from log data.

Further, details of each step are provided below. However, this section first discusses, the practical aspects of the CFS method (Pevzner et al., 2012) and the modifications required to ensure that the method would be applicable to data analysis are within significant media attenuation. As discussed in Chapter 2, the CFS method is used to estimate seismic attenuation based on frequency shift data (Quan and Harris, 1997). This method was selected because it provides a strong estimate and is considered to be an appropriate tool for apparent Q estimation. Hu (2011) demonstrated that this approach is independent of geometrical spreading effects and reflection/transmission loss; thus, it is believed to be more robust than other methods.

A detailed examination of the CFS method revealed that it produces underestimated Q^{-1} values for highly attenuated layers and/or large spatial distances between receivers. Figure 3.1 outlines the relative error in Q^{-1} estimations obtained using the CFS method (V_P = 2,000 m/s) as computed for a plausible range of Q^{-1} and receiver separations (ΔZ). As shown the method can produce unacceptable results (i.e., for ΔZ = 500 m and Q^{-1} = 0.05 the error will reach ~50%).

As a centroid frequency of the propagative wave decreases linearly with travel distance and the ratio of amplitude spectra will define the attenuation coefficient. Hence, Equation 2-7 is considered to reliably evaluate the CFS method. This method is sufficient to implement the estimate of the apparent attenuation. Müller, R. Pevzner, M. Lebedev, M. Urosevic and R. Galvin (2012) studied the stability of the CFS method with other approaches in relation to errors in amplitude spectra estimates.

This comparison demonstrated the advantages of the CFS technique over other methods. This methodology enables a qualitative analysis of the attenuation to be carried out through a visual inspection of the CFS curves; layers with a constant attenuation coefficient will have a constant slope. It was shown that the spectral ratio technique was much less stable in the presence of even random white noise, while both the CFS method and the spectral matching technique were substantially more robust (Pevzner, Galvin, Gurevich and Müller, 2012).

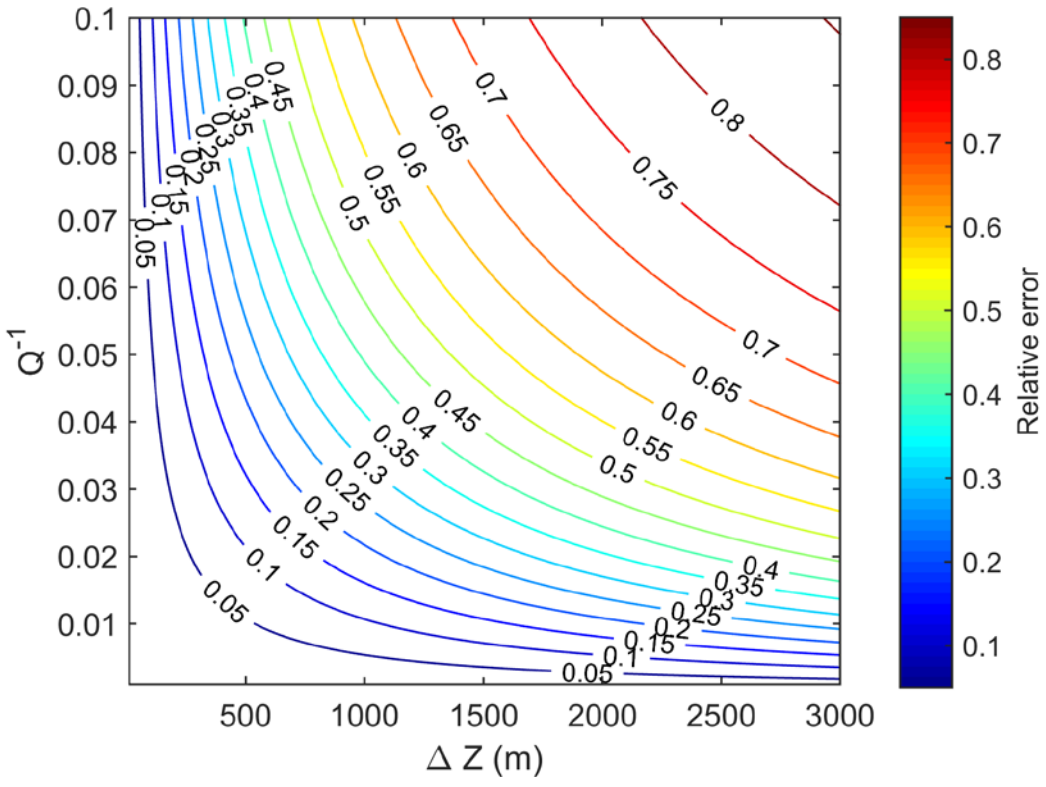

Figure 3-1. Relative error in Q^{-1} estimations obtained using the CFS method (VP = 2,000 m/s).

This behaviour occurred, because Equation 2-14 (Quan and Harris, 1997) failed to properly take into account changes in the shape of the amplitude spectra (expressed as frequency variations) with the distance of propagation. To overcome this issue, the approach was modified so that the variance of the amplitude spectrum at the source (or top receiver, as used by Matsushima (2007)) was not used in the denominator; rather, the average variance for the source-receiver (or receiver-receiver) pair was used. Thus;

$$2\,\frac{(f_{R1}-f_{R2})}{\sigma_{R1}^2+\sigma_{R2}^2}\approx\int_{ray}\frac{\pi}{Qv}\,dl \qquad (3\text{-}1)$$

where f_{R1} is the centroid frequency on upper receiver, f_{R2} is the centroid frequency on the bottom of the receiver and $\sigma^2_{1,2}$ is the variance of the amplitude spectra in relation to centroid frequency. Equation 3-1 reflects that an additional scaling factor applies for non- Gaussian spectra. Matsushima (2007) applied this approach to ZVSP data. This formula is valid for the amplitude spectra described by the Gaussian function. By using this modified formula to estimate the relative error as identified previously, the results become more accurate (see Figure 3.2. Relative error in Q^{-1} estimations *obtained* using the CFS method (VP = 2,000 m/s). Further, the majority of the practically meaningful pairs of ΔZ m and Q^{-1} enabled a recovery of Q^{-1} with less than 5% error.

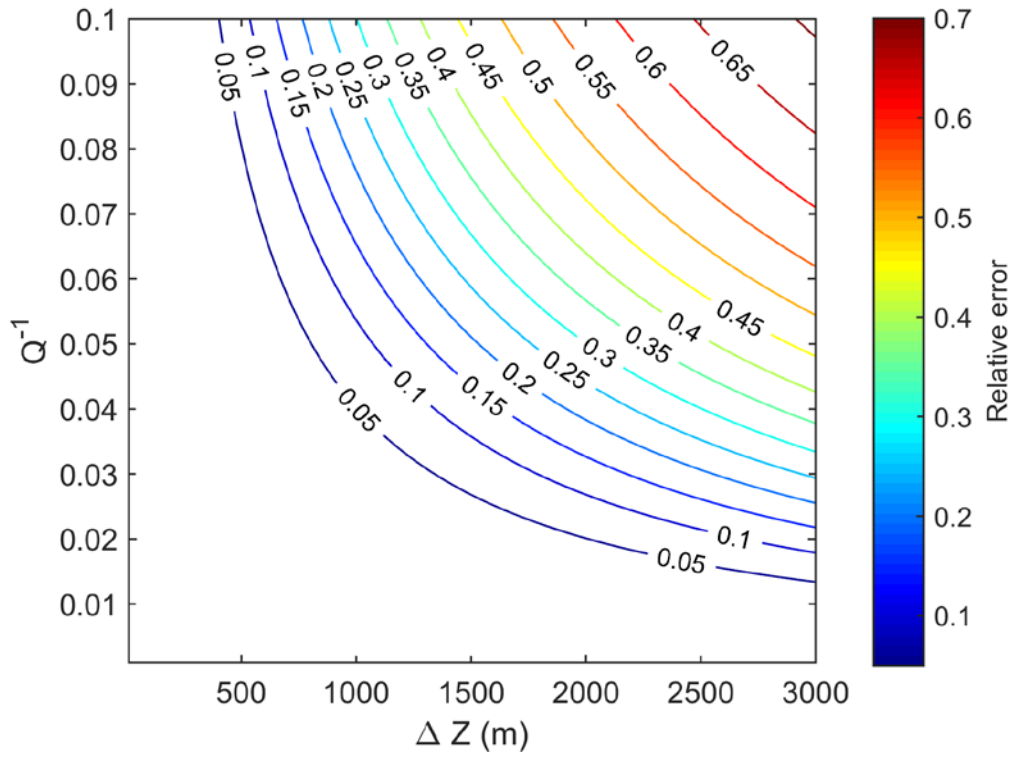

Figure 3-2. Relative error in Q^{-1} estimations obtained using the CFS method (VP = 2,000 m/s).

3.2 Data analysis workflow

This section describes, the workflow that can be used to estimate apparent attenuation parameters along the boreholes of zero-offset VSP data. The main workflow consisted of the following stages:

- data conditioning
- computation of attributes related to attenuation, such as centroid frequency and amplitude decay curve,and
- estimations of *Q* for the thick-layered model.

Figure 3.3 shows the data from well PER 01, which was drilled in 2008 by Woodside Petroleum, in the North Carnarvon Basin, Western Australia. The vertical component of 3C VSP data was only used in this study to estimate the attenuation parameters. However, 3C data were loaded and the orientation of the horizontal components was performed using the polarisation of a direct P-wave to evaluate the structure of the wavefield closest to the first arrivals.

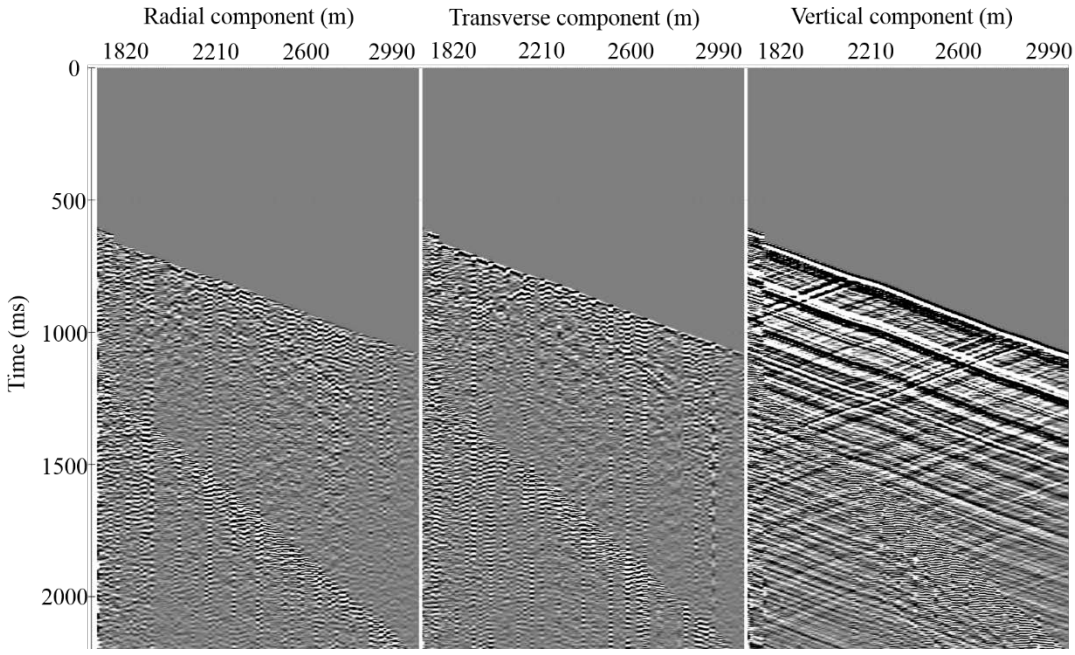

Figure 3-3. PER 01 3C VSP un-oriented data radial (left panel) transverse (middle panel), and vertical (right panel) components.

A polarisation analysis of the direct wave was conducted to orient the horizontal components in radial and transverse directions. A comparison was made between the estimated dip angle of polarisation of the direct P-wave, the angle between the vertical axis, the direction from the source to receiver to QC orientation and the vector fidelity of the tool (see Figure 3.4).

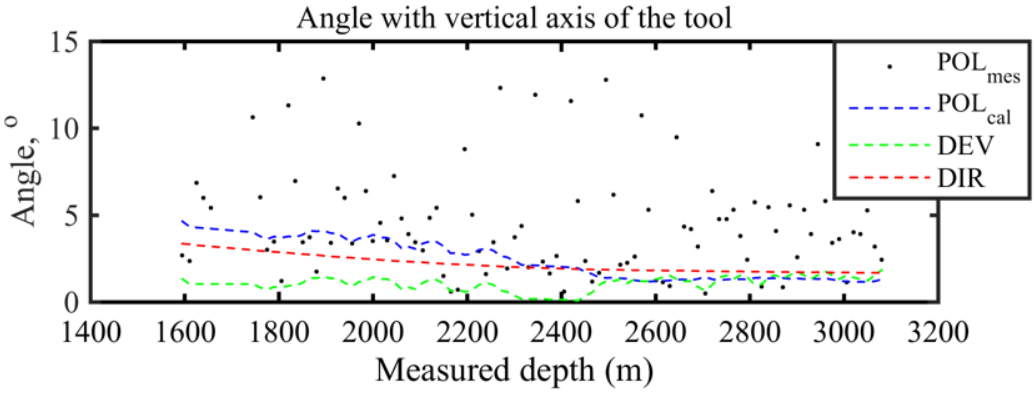

Figure 3-4. PER 01 results of the orientation (black dots) measured polarisation of the P-wave in relation to the vertical axis of the VSP tool; calculated polarisation of the P-wave in relation to the vertical axis of the VSP tool (blue dash line); well inclination (green dash line); angle between a vertical direction and the direction of the P-wave propagation (red dash line).

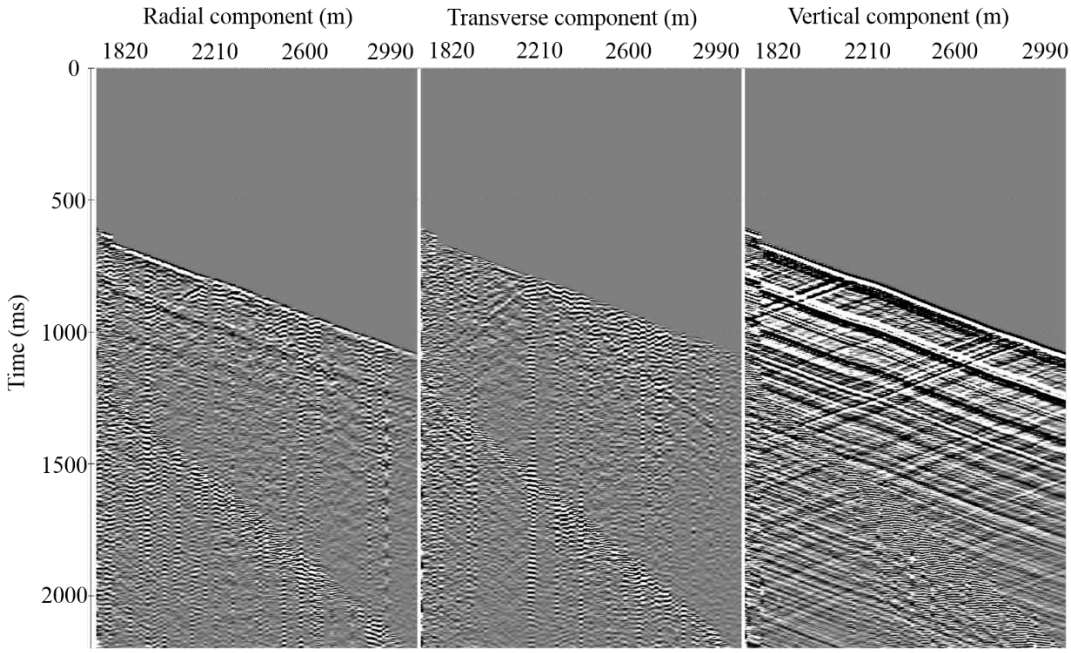

Figure 3-5. PER 01 3C VSP oriented data radial (left panel) transverse (middle panel), and vertical (right panel) components.

Figure 3.5 shows the results of the orientation and reflects the horizontal components that contained significant amounts of shear waves generated by the source and PS converted waves.

3.3 Data conditioning

Before the attenuation parameters could be estimated, the zero-offset VSP data was conditioned to:

- correct the amplitudes for the geometrical spreading of a wavefront; and
- separate the downgoing energy for the analysis.

It is to avoid contamination of the estimated amplitude spectrum, the upcoming energy had to be suppressed from the analysis interval. Several techniques can be used to perform wavefield separation, including F-K filter, 2D median filter in time domains and wave-by-wave optimisation.

A static correction to flatten the arrival of the direct wave was also applied (Canales, 1984). Thus, frequency–space (FX) deconvolution (Canales, 1984) was used to address the upcoming waves and remove unpredictable noise from the seismogram.

The actual parameters of the FX deconvolution applied to PER 01 data were a minimum frequency of 0 Hz, a maximum frequency of 180 Hz, a length of filter of seven samples and a pre-whitening of 50%. For other wells, the parameters were allowed to vary.

The residuals were calculated to ensure that FX deconvolution was applied correctly to the data (e.g., most of the upgoing waves were suppressed, but no significant damage was caused to the shape of the downgoing waves). The residuals were obtained by subtracting the data obtained before FX deconvolution from the data obtained after FX deconvolution (see; the results of this subtraction presented in Figure 3.6). The data after FX deconvolution were used to estimate the amplitude decay using the maximum absolute amplitude of the first extremum.

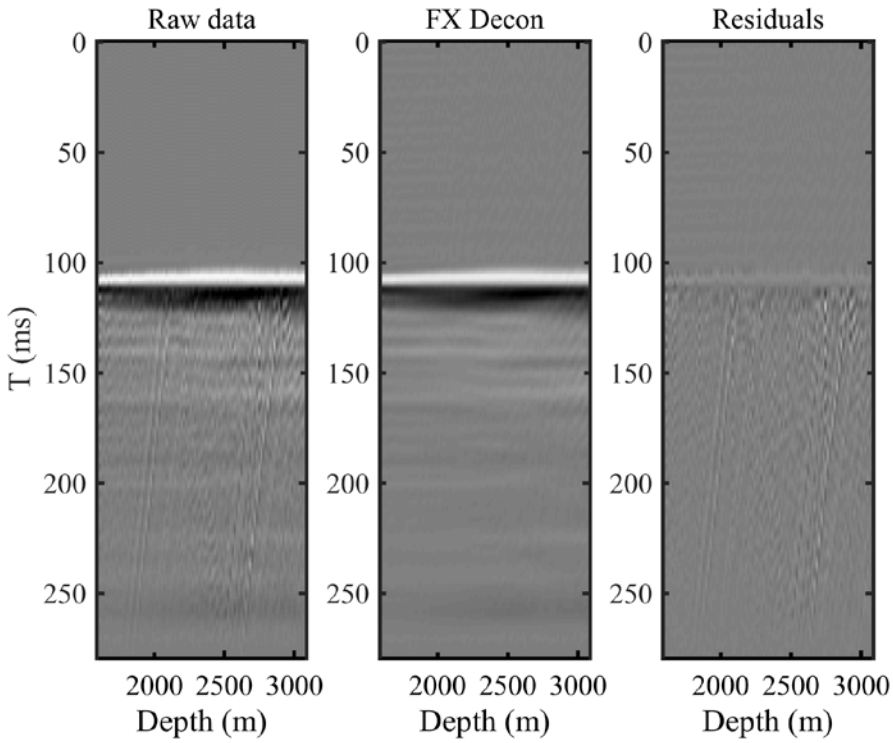

Figure 3-6. PER 01 attenuation of upgoing wave using FX deconvolution: original data (left), result of FX deconvolution (middle) and the difference (right).

In the next stage, the time-domain traces were transformed to amplitude spectra using a Fast Fourier Transform (FFT). Various researchers have used different time windows of between 50-100 ms (Shaw, Worthington, White, Andersen and Petersen, 2008) and 1,000 ms (Blias, 2011). Following the test, a time window of approximately 300-400 ms was selected, as it had a good spectral resolution, but did not include the portion of the record with poor S/N ratios. To further reduce the influence of interference from upgoing waves, the spectra along the depth axis was smoothed using a running average (i.e., window size three traces x one sample) (see Figure 3.7).

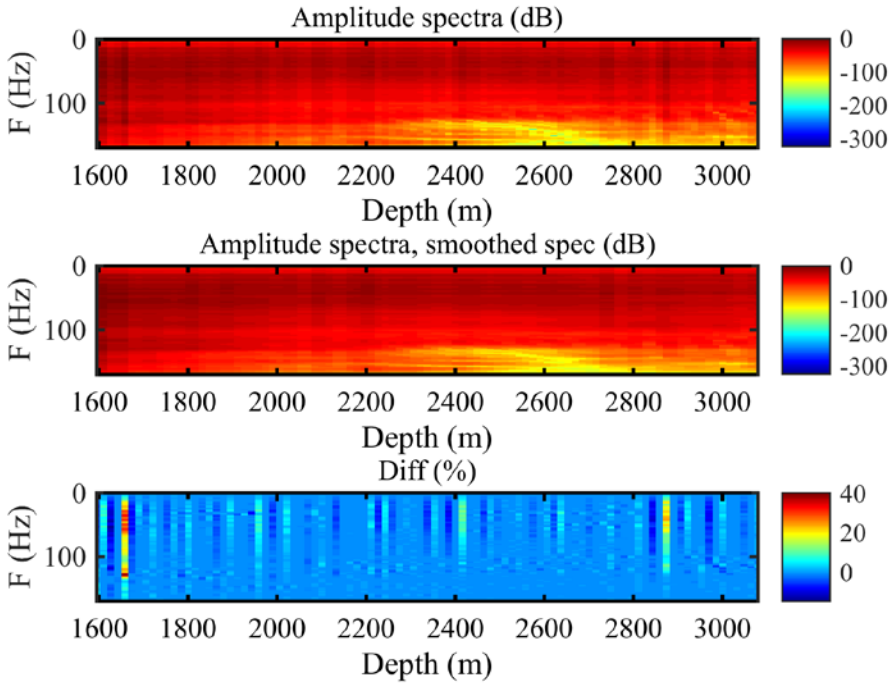

Figure 3-7. PER 01 amplitude spectra estimation; actual spectra after FX deconvolution (top); smoothed amplitude spectra using the three trace window filter (middle); and the relative difference between the spectra and the smoothing result (bottom).

At this stage, velocity information was required to apply a divergence correction (Newman, 1973). The first break picks were used to determine this correction and evaluate interval and RMS velocity.

3.3.1 Estimation of amplitude and centroid frequency decay

Figure 3.8 shows the amplitude decay that occurred at different frequencies. The centroid frequency and the square root of its variance were computed and results are presented in Figure 3.9. The term ‘square root of the variance’ was used to refer to ‘deviation’ as it has the same units as frequency. To obtain approximate Q estimates, amplitude and centroid frequency decay curves were used. (Pujol and Smithson, 1991; Pujol, Luschen and Hu, 1998).

The layers with substantial attenuation, were qualitatively distinguished using energy decay curves at different frequencies (see Figure 3.8). Such layers are distinguished by a steeper dip of the curves at higher frequencies. To quality control QC the estimates, centroid frequency decay and centroid frequency variance curves were used to obtain interval *Q* values and an amplitude decay curve. Equations 2-2 and 2-3 were used to compute amplitude decay in relation to the Q estimates. Thus, the relationship between amplitude decay calculated from the computed Q and directly from the seismogram was a superb sign of the Q estimates.

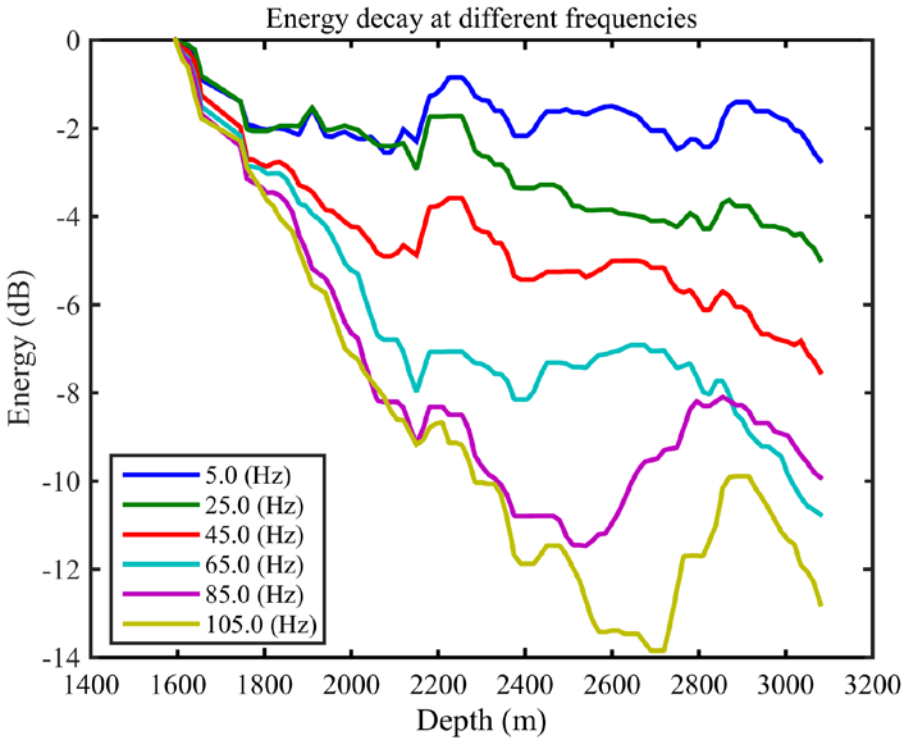

Figure 3-8. PER 01 results of amplitude decay at different frequencies.

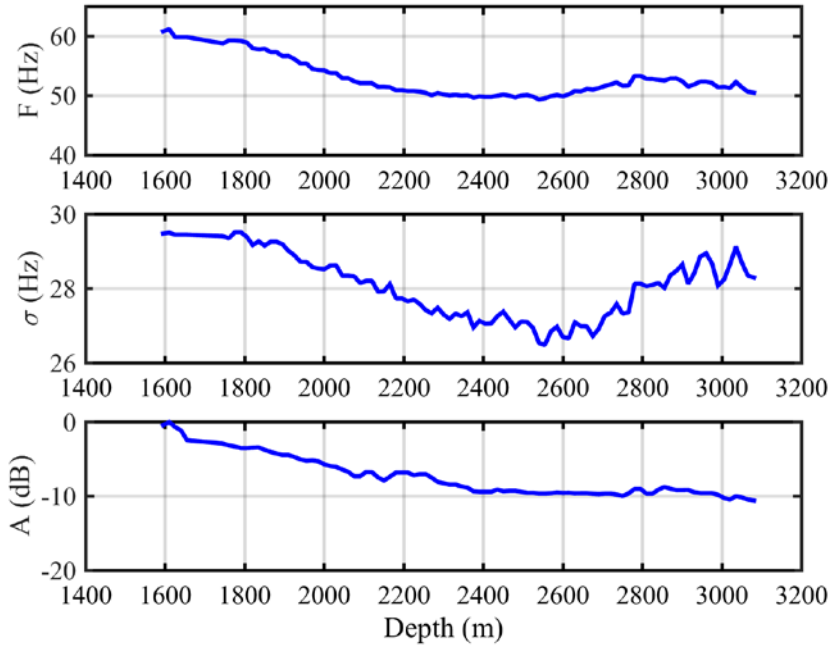

Figure 3-9. PER 01 results of ZVSP data analysis, (corrected for wavefront divergence); Centroid frequency (top); deviation of the spectra (middle); and amplitude of the main peak in the wavelet (bottom).

3.3.2 Estimation of Q^{-1} for the thick-layered model

Using Equation 2-14, the modified CFS approach was used to obtain the layer Q^{-1} model. The results of this inversion are shown in Figure 3.10 and Figure 3.11. As shown the thick-layer Q^{-1} values have been realistically reconstructed.

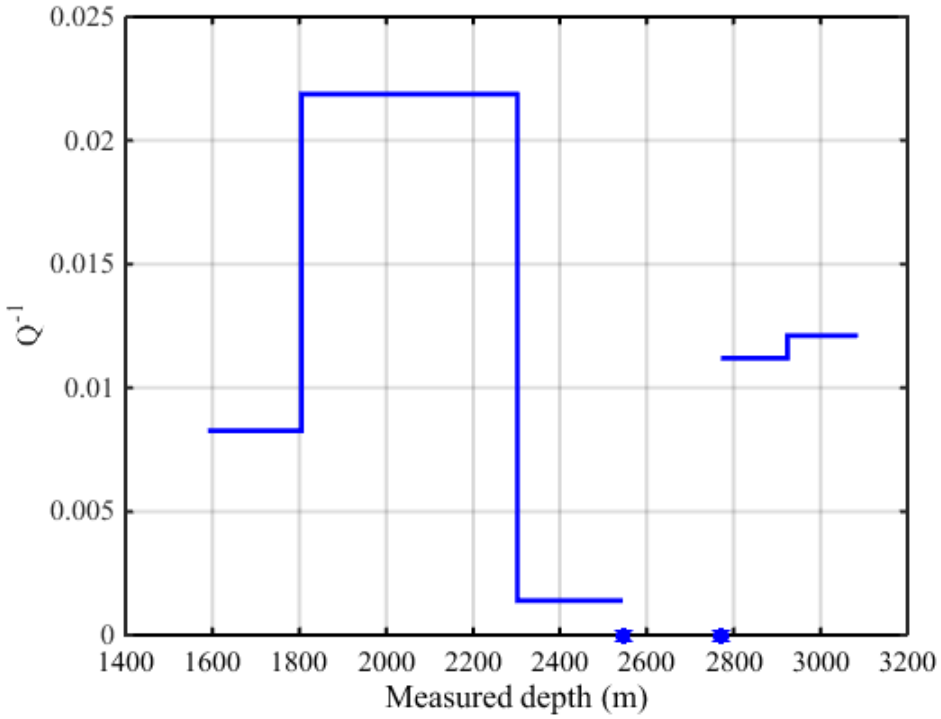

Figure 3-10. PER 01 results of the thick layered Q^{-1} estimation.

Figure 3.11 shows the results of the compensation of the amplitude decay curve for attenuation using centroid frequency at each depth and estimated Q values. Compensations were made for both the divergence of the wavefront and attenuation; thus, the blue curve contains amplitude decay due to frequency-independent transmission losses.

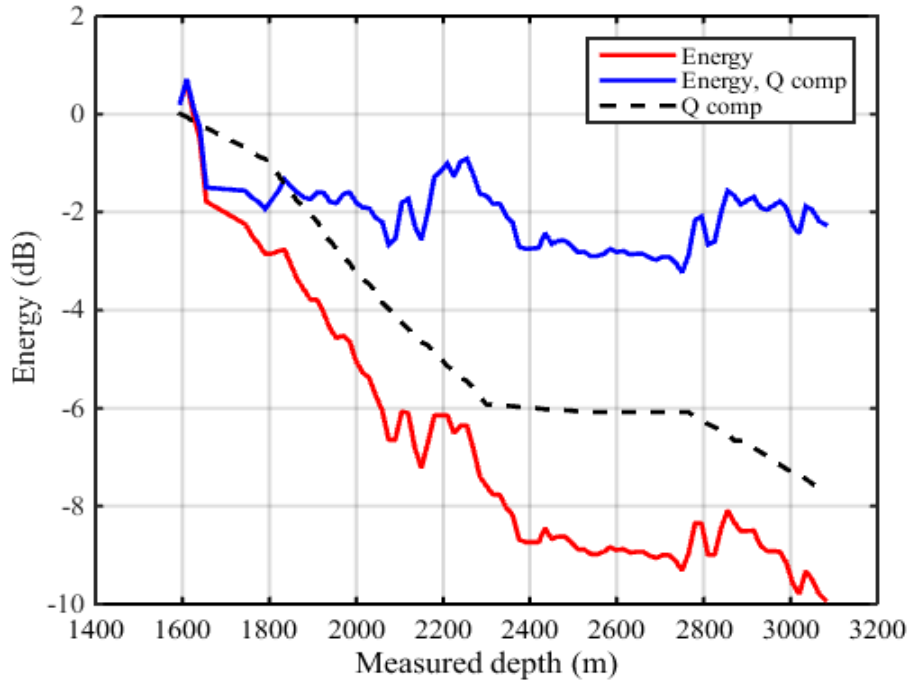

Figure 3-11. PER 01 results of energy decay curve from direct waves (when divergence variation is applied) (red); attenuation component of the energy decay (black); and results of the energy decay compensation (blue).

3.4 Estimation of scattering attenuation from synthetic VSP data

Spreading into a stack of thin layers, a plane wave pulse becomes reflected and transmitted multiple times. Partially destructive and constructive interferences from these reflected and transmitted waves resemble a process of continuous wavefield energy reshuffling from an initially coherent pulse into scattered waves arriving with different time delays. The overall wavefield energy is conserved; however, the initially coherent pulse becomes distorted and reduced in amplitude. As a result, the seismic wavefield recordings are a superposition of a seismic primary wave (i.e., distorted initial pulse) plus coda waves (Aki and Chouet, 1975). Thus, it follows that the layer stack acts as a filter on the seismic wavefield, which known as stratigraphic filtering.

The effect of stratigraphic filtering is recognised as a source of seismic primary amplitude decay in exploration seismology. O'Doherty and Anstey (1971) quantified a frequency-domain stratigraphic filter function dependent upon the power spectrum of the reflection-coefficient series. It is essential that an accurate numerical simulation of seismic data be undertaken to quantify the relative effects of geometrical spreading, inelastic absorption, scattering attenuation, transmission loss and elastic anisotropy. Modelling of the wave propagation in a 1D earth is adequate and suitable for an analysis of VSP data in sedimentary environments, as scattering and transmission losses mainly occur due to the transmission and reflection effects caused by layering (Shapiro and Hubral, 1999).

High-resolution sonic/density well log data (in which the standard vertical resolution is half a foot, or 15.24 cm in oil wells enables the simulation of all these effects, including scattering due to fine layering. An integral transform approach, such as wavefield (in the frequency domain) written as an integral over time-harmonic plane waves is the most accurate approach to modelling seismic waves in 1D layered media (Aki and Richards, 1980).

Log data from several wells were used to estimate the contribution of the scattering attenuation. The workflow of the scattering attenuation estimation (Pevzner et al., 2014) comprised the following steps:

- building an elastic model using log data.
- upscale the model to a regular grid (0.5–1.5 m) using Backus (1962) averaging.
- computing synthetic VSP seismograms using the reflectivity method (OASES software).
- estimating scattering attenuation using the modified centroid frequency method.

Obtained attenuation values represent the scattering component due to the synthetic seismograms computed using an elastic model for all layers. In this study, this workflow was applied to several wells with a good log and VSP data coverage. An example of an estimation of the scattering Q (based on data from the PER 01 well) is provided in this chapter.

3.4.1 Computing synthetic seismograms

An initial model was produced to estimate scattering attenuation using synthetic VSP data. To compute synthetic seismograms for the scattering attenuation estimation, OASES software from the Massachusetts Institute of Technology (MIT) was used. The Global Matrix Method (GBM) was implemented in the software to overcome the instabilities of the integral transform approach. Müller, R. Pevzner, M. Lebedev, M. Urosevic and R. Galvin (2012) conducted comprehensive assessment of the modelling parameters.

Model files created from raw log data frequently have tens of thousands of layers and therefore require Backus averaging (Backus, 1962), which permits upscaling to any desired number of layers or layer thicknesses. In this study, once the initial layer properties were extracted and the Backus-averaged to the desired level, a detailed OASES input file was created. This file contained the layers properties, source/receiver geometry, source type/frequency, frequency sampling and wavenumber integration sampling parameters. OASES then computed the reflectivity

of the model and produced a .trf file containing the transfer function (reflectivity) of the layered medium in a frequency domain.

The reflectivity was then convolved with a user-chosen source wavelet and written to a binary file. Following this, the synthetic seismogram was viewed by importing this binary into a seismic processing software package such as RadExPro. For the PER 01 well, data were available from 2,020- 3,079 m. Figure 3.12 shows an elastic model. Above 2,020 m, Vp was taken from the VSP data and Vs were reconstructed as missing data using the Castagna's mudrock line equation (Castagna et al., 1985). The Gardner equation (Gardner et al., 1974) was used to recover missing density values, and Castagna's mudrock line equation (Castagna, Batzle and Eastwood, 1985) was then applied to estimate shear wave velocity values. Backus averaging (Backus, 1962) was used to upscale the model to a 0.5 m regular grid.

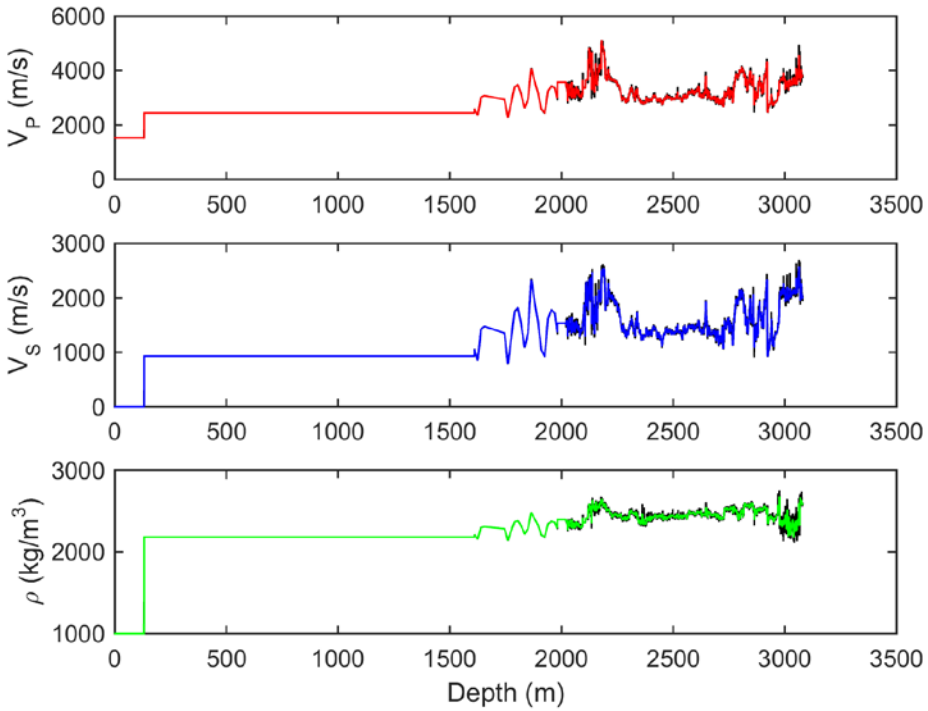

Figure 3-12. PER 01 elastic model. The black curve is log data and the coloured curves show the results of Backus averaging

Synthetic seismograms were computed by employing MIT's OASES global matrix algorithm (Schmidt and Jensen, 1985). To produce synthetic seismograms 80 Hz Ricker wavelet was used; receivers were placed at the same interval as the field data was acquired. Figure 3.13 shows the synthetic data that were generated by the zero-offset VSP vertical component.

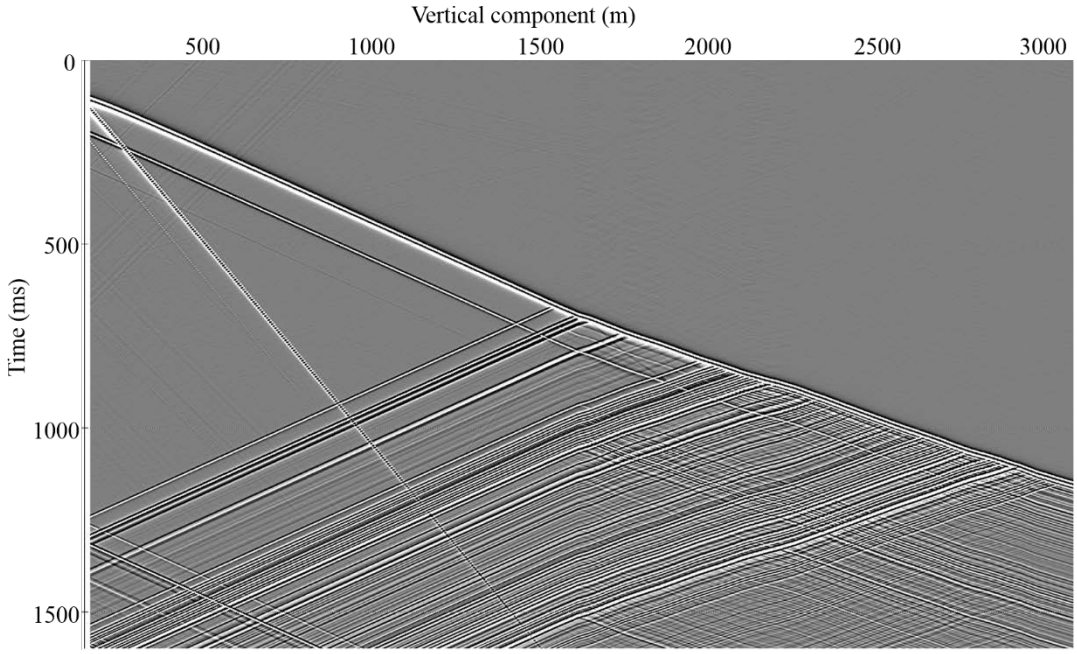

Figure 3-13. PER 01 Synthetic Zero-offset VSP seismogram vertical component.

3.4.2 Estimation of scattering attenuation

The modified centroid frequency method was used to estimate the scattering component of the attenuation. The same workflow as described in the previous section was applied. FX deconvolution was applied to the flattened data to suppress the upgoing energy (see Figure 3.14). Traces (i.e., time-domain) were transformed into amplitude spectra using the same parameters as those used for the field seismograms. Figure 3.15 shows the amplitude spectrum and the smoothed amplitude spectrum of the synthetic seismogram of the vertical component. It should be noted that no significant attenuation was observable on the spectra.

An analysis of the amplitude decay at different frequencies, the centroid frequency and the square root of its variance (see Figure 3.16 and Figure 3.17) showed that there was a ~ 0.63 Hz drop in centroid frequency at the depth of ~ 1,600 m. To assess the contribution of the scattering part to the apparent attenuation, Q estimates from synthetic data were compared to Q values from VSP records. Table 3-1 outlines the different values of Q estimates from the synthetic data against the estimates obtained from the real VSP records. This comparison is also shown in Figure 3.18 and Figure 3.19. Thus, it can be concluded that in the PER 01 well, the scattering attenuation was not a significant contributor of seismic attenuation.

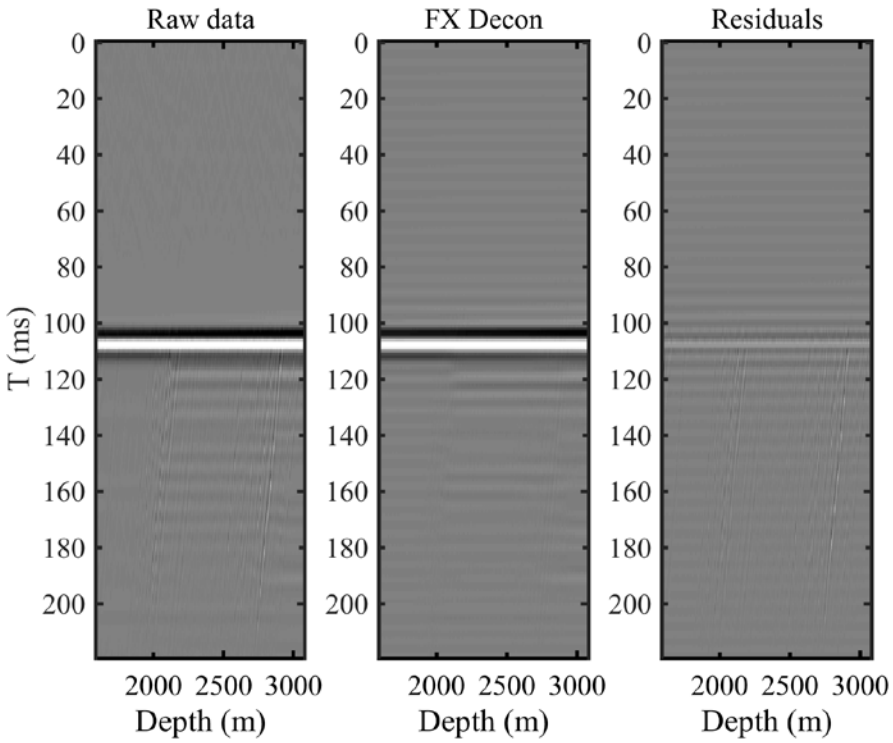

Figure 3-14. PER 01 synthetic data attenuation of upgoing waves using FX deconvolution: original data (left); result of FX deconvolution (middle); and the difference (right).

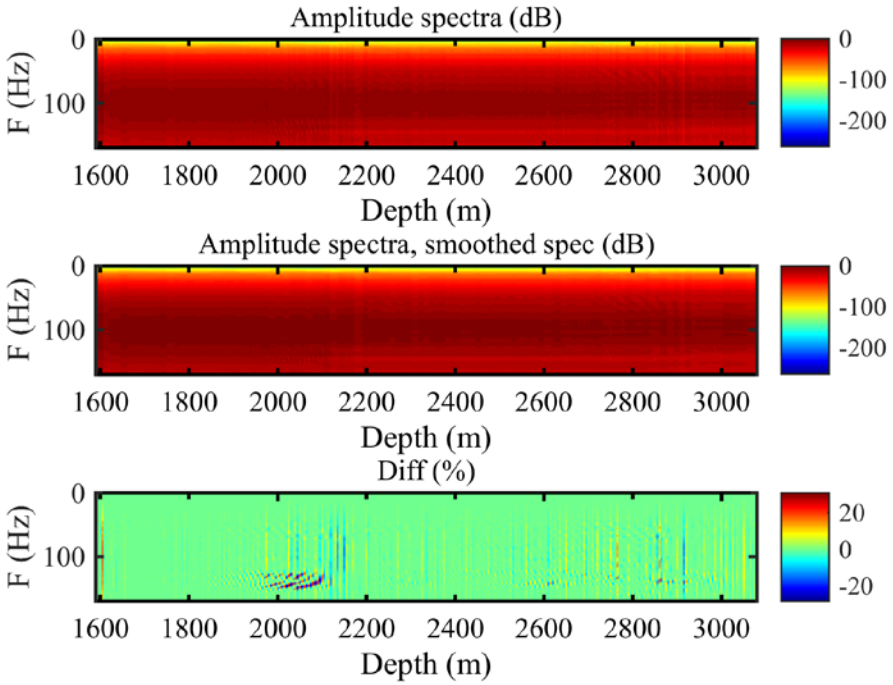

Figure 3-15. PER 01 synthetic data amplitude spectra estimation. Actual spectra after FX deconvolution (top); smoothed amplitude spectra by using three trace window filter (middle); and the relative difference between the spectra and the smoothing result (bottom).

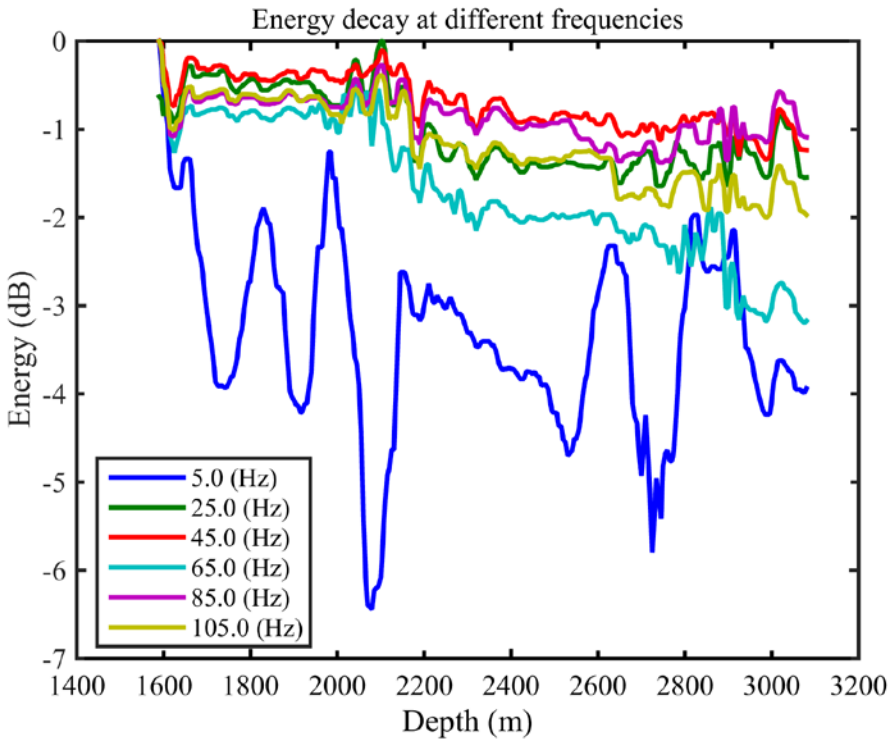

Figure 3-16. PER 01 synthetic data results from amplitude decay at different frequencies.

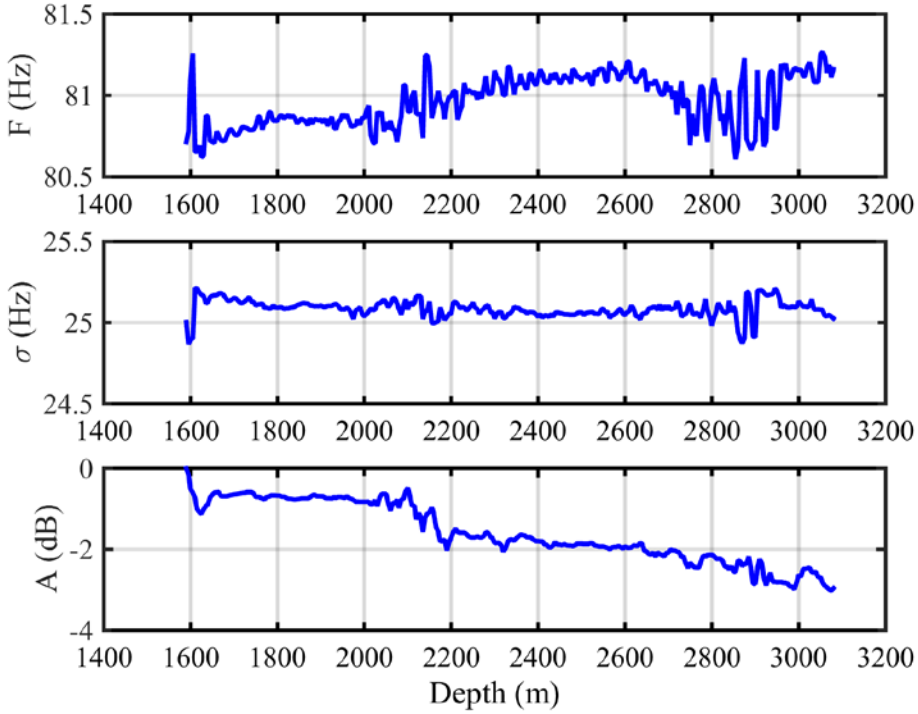

Figure 3-17. PER 01 synthetic data results of ZVSP data analysis (corrected for the divergence of the wavefront): centroid frequency (top); deviation of the spectra (middle); and amplitude of the main peak in the wavelet (bottom).

Table 3-1. Q^{-1} value for field and synthetic data.

Interval MD(m)	field		synthetic	
	Q^{-1}	Q	Q^{-1}	Q
1,595-1,805	0.00826	121	NaN	NaN
1,805-2,302	0.02188	46	NaN	NaN
2,302-2,545	0.00139	719	NaN	NaN
2,545-2,771	NaN	NaN	0.00213	470
2,771-2,924	0.01119	89	0.00190	526
2,924-3,080	0.01211	83	NaN	NaN

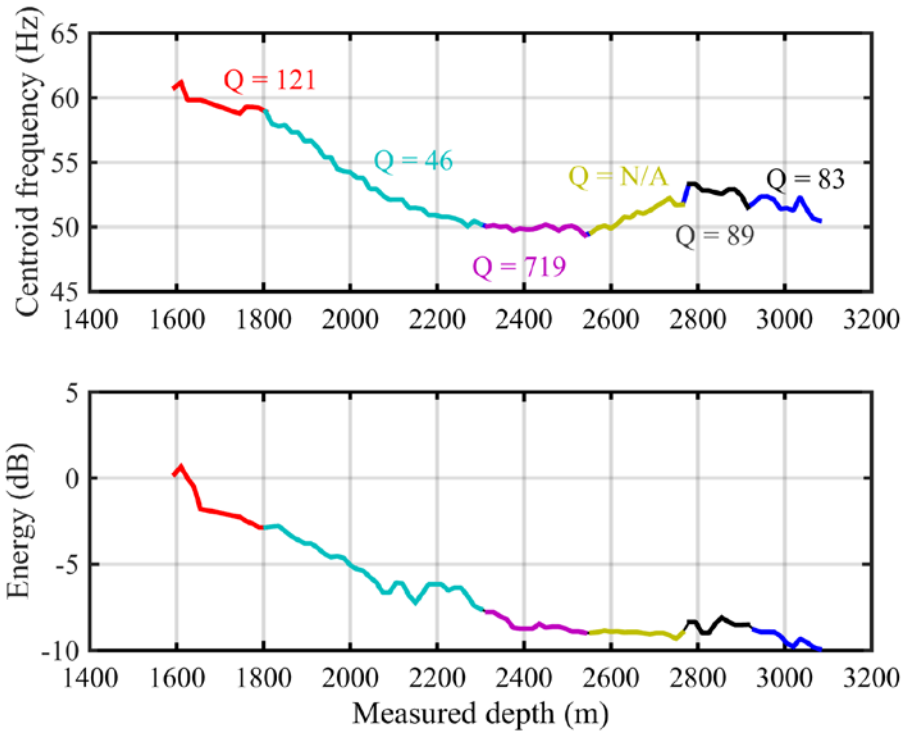

Figure 3-18. PER 01 field data results of centroid frequency (top) and energy (bottom) decay curves. Estimated attenuation values were divided into six interval boundaries as shown on the centroid frequency panel.

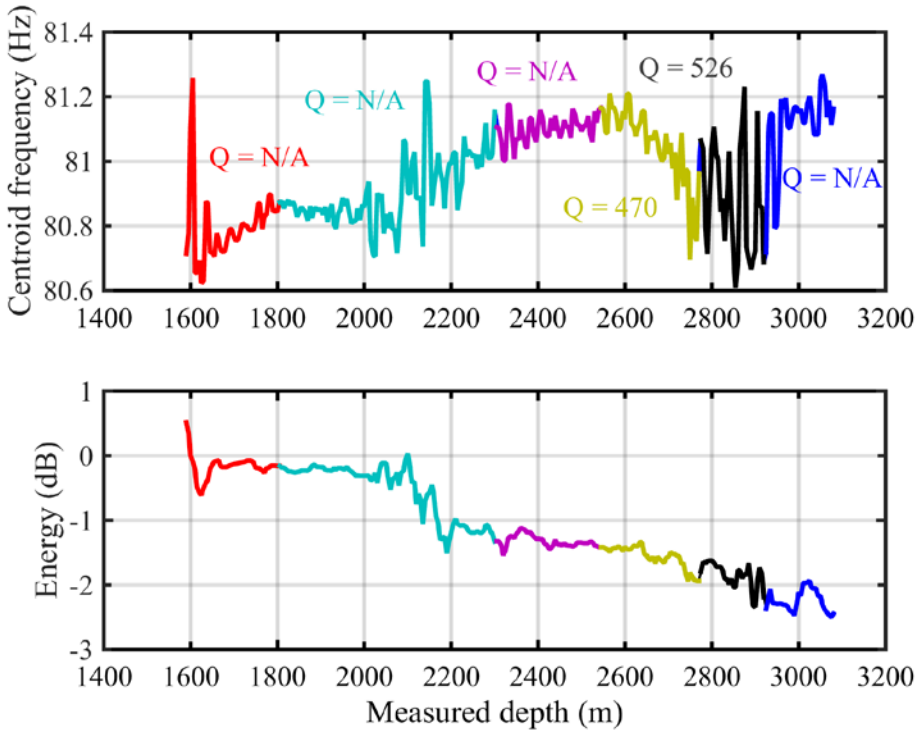

Figure 3-19. PER 01 synthetic data results of centroid frequency (top) and energy (bottom) decay curves. Estimated attenuation values were divided into six interval boundaries.

This study analysed 37 wells. Apparent attenuation was estimated for all wells; however, 11 wells were excluded for a number of reasons, including insufficient top formation and unreliable estimates due to well construction, interference and/or source stability. From the analysis, scattering attenuation was found between $Q = 470$ and $Q = 526$, reflecting low attenuation in PER 01, in Area 5.

In Area 3, the Q values were observed for two wells; that is, Wheatstone 2 and Wheatstone 3. Wheatstone 2 found that all intervals had low attenuation except Interval 3, which reflected moderate attenuation with the value of $Q = 140$. In Wheatstone 3, the scattering attenuation was low in all intervals. Three wells were only used for the scattering estimation and, of these, Wheatstone 2 reflected normal scattering attenuation, with Q 140 in Interval 3, compared to other intervals, which showed low attenuation. Conversely, Wheatstone 3 showed no significant attenuation across all intervals. A further explanation of these results is provided in the following chapters.

3.5 Complications in attenuation estimations

A variety of data complications affected the accuracy of the attenuation estimation. The estimation of attenuation from the VSP records required a careful assessment of the field data before any analysis could be undertaken. A number of factors can affect data including well construction, source instability and often unavoidable interference with different components of the wavefield. These factors are considered below.

3.5.1 Source instability

The seismic source related issues could complicate a VSP survey for a variety of reasons, including lack of repeatability. A reliable assessment of lithological changes and event correlations should be attained from a source with constant characteristics.

Additionally, small errors in the traveltimes of any of the above factors may result in large velocity errors. A monitoring geophone and appropriate signal processing could be used to improve source stability. Wingo (1981) and Zeitvogel (1982) used of the spectral ratio method for attenuation estimation to correct the ratios (at two depths) of source variations resulted in improved results.

The source conditions can change from case to case; for example, an ocean swell could result in a ship-mounted gun moving while shooting along a deviated wall. This occurred in the data for Tidepole 2. The red arrows in Figure 3.20 identify the distortions caused by the instability of the source signature on the seismogram and amplitude spectra (e.g., the seismic signal disturbances prevented accurate estimation attenuation).

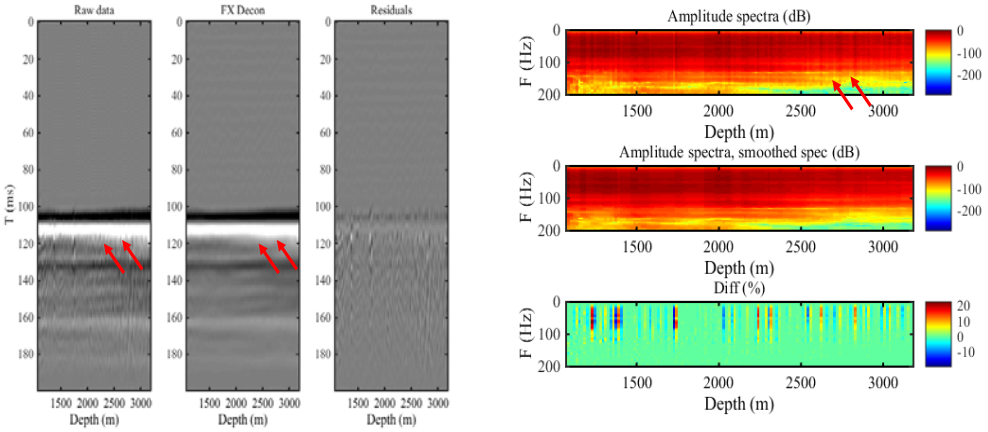

Figure 3-20. Tidepole 2 effects of unstable source conditions on the data (left panel) and on the amplitude spectra of traces (right panel). The red arrows point show the disturbances in the data and distortions in the amplitude spectra.

3.5.2 Changes in well construction

Borehole condition is an important factor affecting attenuation estimates, including well types, (e.g., vertical or deviated and, open or cased holes). A number of wells were examined and changes in well construction, were found along wellbores, including changes in the number of casings and transitions from cased sections to open holes. It should be noted that casing reverberation caused by poor-quality cementation can occur during changes to well construction.

Figure 3.21 shows the Briseis 1 well and provides an example of VSP data (vertical component). In Figure 3.22, the red square (indicating above the noise level) and the blue square (indicating below the noise level) are used to compare the amplitude and frequency spectra changes related to the casing noise. Significant frequency content changes, above and below the interval, were also present and caused reverberations that were often unexplained; however, these changes may have occurred as result of changes in coupling rather than abnormal attenuation.

The analysis of the Briseis 1 well in relation to seismic signal reflects the frequency spectra estimate of an upgoing event above and below the noise intervals. During the analysis, a 2D spatial median filter was used and first break static

corrections were applied to supress downgoing waves. The amplitude spectra of one of the upgoing waves in the areas above and below the casing noise were estimated.

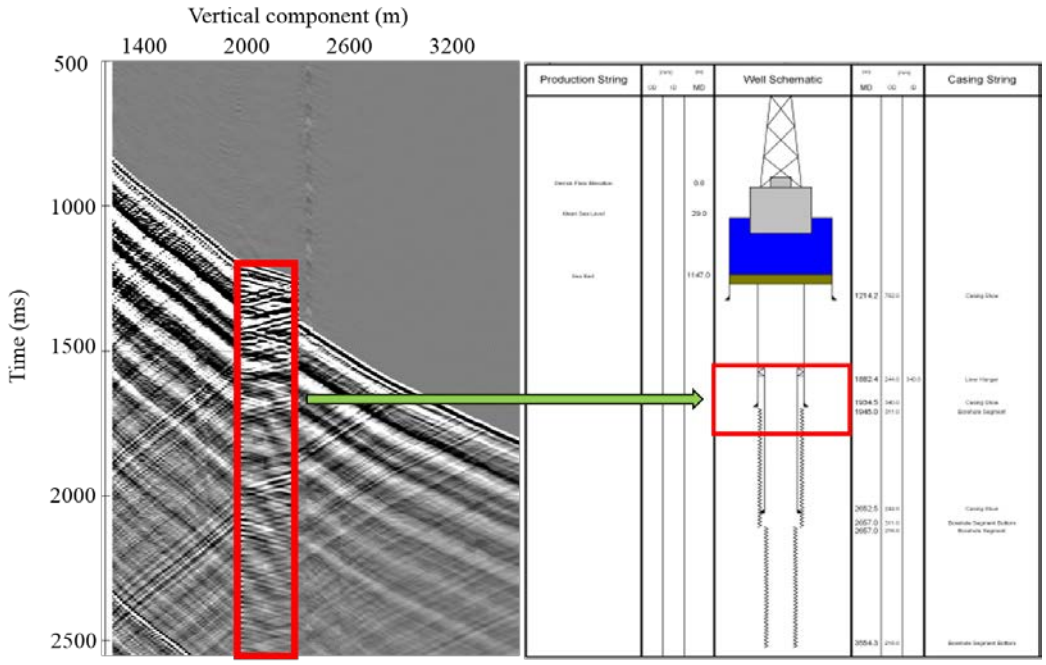

Figure 3-21. Briseis 1. Left panel: raw VSP data - vertical component (the red square shows the area contaminated by casing noise). Right panel: well sketch (red square shows the area around a casing shoe where noise is presented on the VSP data).

By comparing the two spectra in Figure 3.22, it is apparent that the interval has a higher frequency above the noisy zone than below the noisy zone. The much higher frequencies of the seismic signal would therefore result from construction and or casing coupling issues. Therefore, for the two data intervals (above and below the noisy zone), estimation of apparent attenuation had to be performed separately. Where wells were shown to have this issue, the analysis of attenuation was carried out autonomously to ensure the integrity of the data interval, as shown by the Briseis 1.

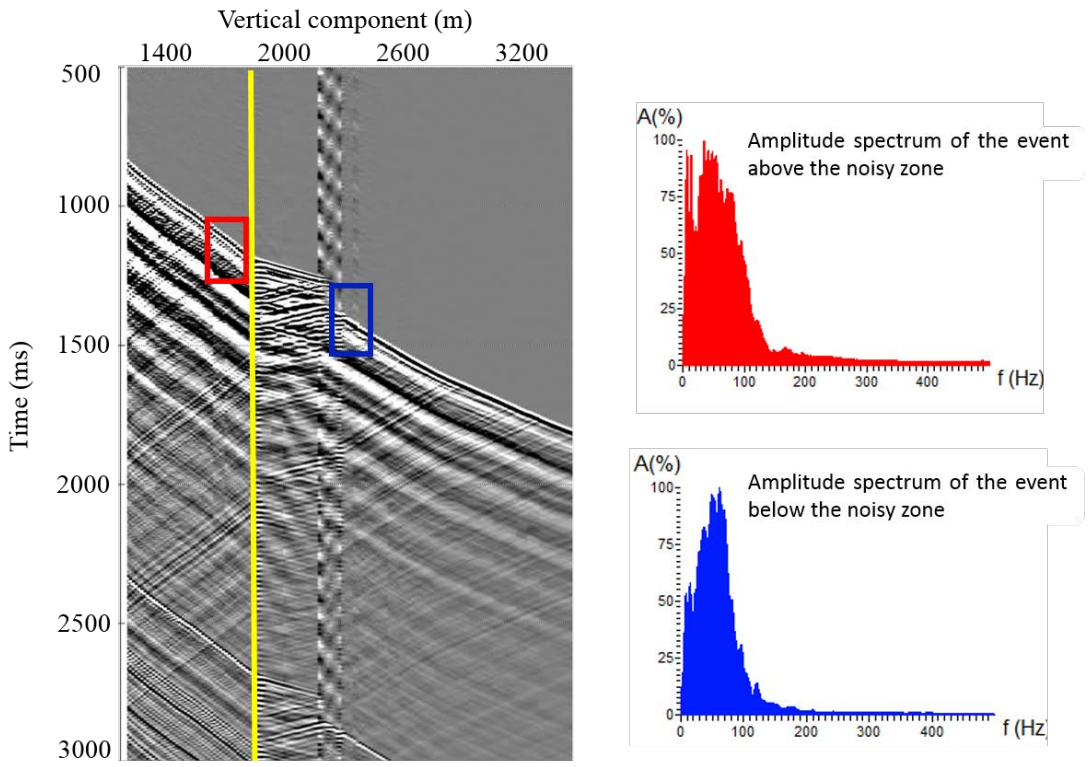

Figure 3-22. Briseis 1. Left panel: VSP seismogram of raw data (500–2,500 ms). The data on the left side of the yellow line occurred above the noise interval and the data on the right side of the yellow line occurred below the noise interval. The blue and red squares represent the areas of amplitude spectra estimation for one of the upcoming waves. Right panel: the amplitude spectra correspond to the areas on the left panel. Top: spectrum of the event above the casing noise zone is on the top and spectrum of the event below casing noise zone is on the bottom Interference with the events having similar traveltime curves to the direct wave.

3.5.3 Interference with energy from geological objects

Pevzner et al (2013) analysed several wells from the North West Shelf were analysed. and showed that attenuation estimates were likely to be significantly affected by interference of the direct wave with reflections from sub-vertical features (e.g., faults) and by minor variations in the depth of the VSP source; for example, interference between a downgoing direct wave and an event exhibited by a notch in amplitude spectrum in Maitland 2 made spectral analysis difficult and created uncertainty in estimated Q values (see Figure 3.23). Further, at a certain depth interval, the centroid frequency and amplitude decay expected from transmission loss did not occur. It is noted that the amplitude spectra are becoming wider.

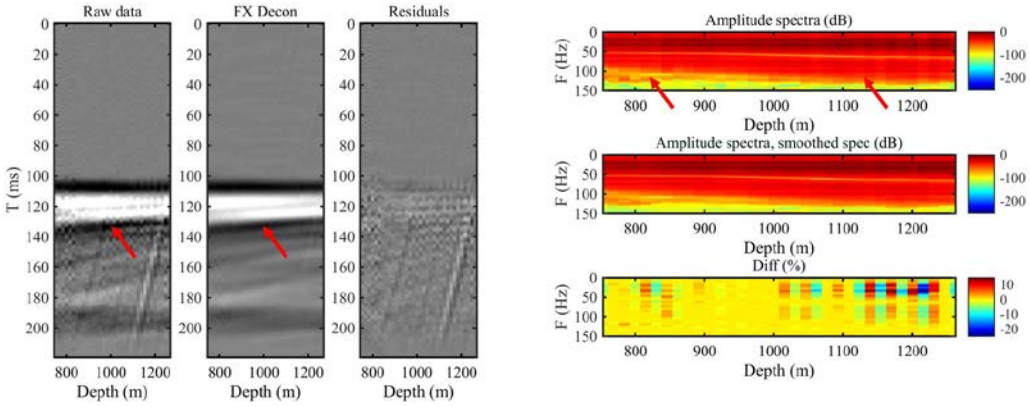

Figure 3-23. Maitland 2. Left panel: upgoing wavefield suppression using FX deconvolution (red arrow indicates interference with an event with similar apparent velocity). Right panel: amplitude spectra (red arrow indicates a notch in the amplitude spectrum due to interference).

Chapter 4. Distribution and Causes of Seismic Attenuation in Australia North West Shelf

This chapter demonstrates the findings and outcomes of the research undertaken in the North Carnarvon Basin wells. Information in relation to the geological setting, data availability and the VSP data acquisition parameters are presented.

4.1 Study area (geological setting)

The study area comprised the North Carnarvon, offshore Canning and Browse Basins located on the NWS of Australia (see Figure 4.1).

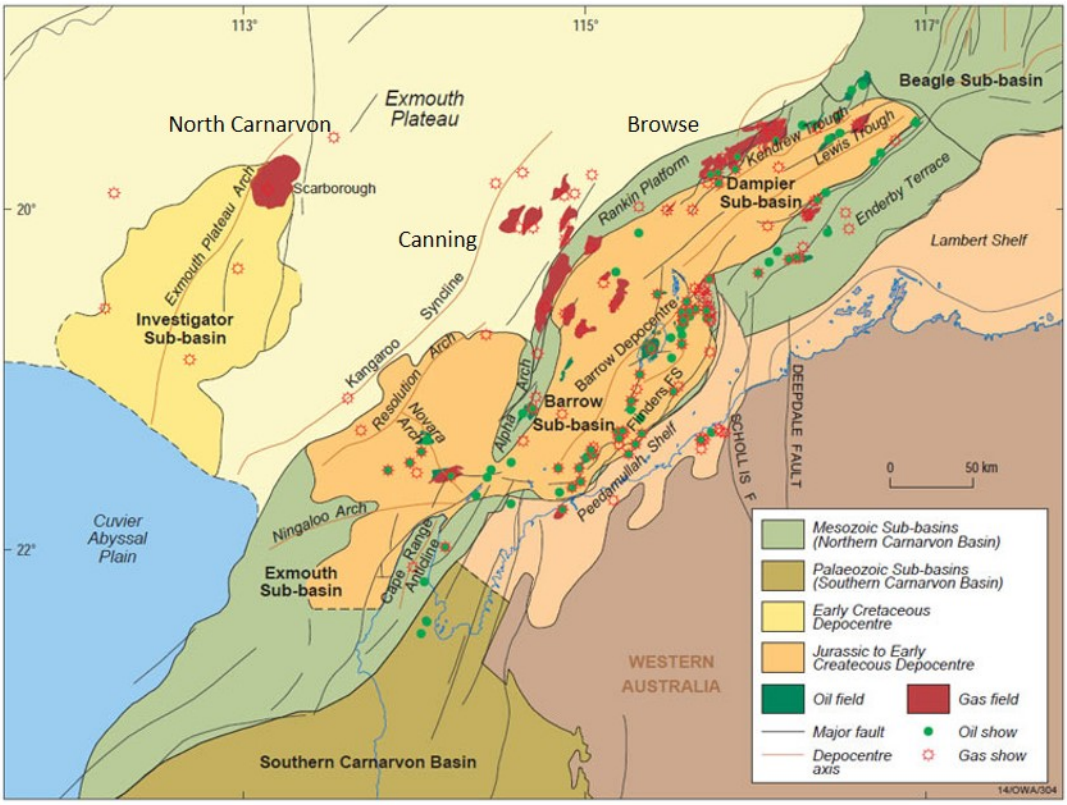

Figure 4-1. The Northern Carnarvon Basin. The green and red circles indicate the gas and oil shows, respectively. The red regions indicate the location of gas fields (Hocking, 1988).

The NWS is a rift margin with pre-rift Permo-Triassic intracratonic sediments, overlain by Jurassic to Cainozoic syn-rift and post-rift sediments deposited due to rifting and seafloor spreading (Longley et al., 2002). The basins within the NWS are the Northern Carnarvon, offshore Canning, Browse and Bonaparte Basins (collectively referred to as the 'Westralian Superbasin' (WASB) (Yeates et al., 1987)) and the Timor-Banda, an orogenic belt that formed in response to a collision (Neogene) between the distal edge of the WASB with the Banda Arc and the arc systems (Metcalfe, 1995; Keep et al., 2002)

As a result of the break up of Gondwana, the WASB is filled with thick Late Palaeozoic to Cainozoic sedimentary succession. The Northern Carnarvon Basin includes the Exmouth Plateau and three sub-basins (Exmouth, Barrow and Dampier). The sediments were formed from a pre-rift in the Late Palaeozoic period and during a tectonically active period in the Jurassic period, to a passive margin carbonate shelf in the Cenozoic period (Western Australia Department of Resources, 2008).

The NWS is generally defined by the Proterozoic Australian craton. The Palaeozoic (Devonian-Permian) section corresponds to the Gondwana break up when continental fragments drifted northward until, ultimately, the Eurasian craton coalesced (Metcalfe, 1995). These sequences (Longley, Buessenschuett, Clydsdale, Cubitt, Davis, Johnson, Marshall, Murray, Somerville and Spry, 2002) formed syn-rift and sag cycles filled with marine, deltaic and glacial deposits. The study area was difficult to map (except in a few localised areas) using seismic data due to the presence of thick overlying Mesozoic deposits (e.g., the shelfal regions of the Canning and the Northern Carnarvon Basins) (Bentley, 1988; Delfos and DEDMAN, 1988; Mory, 1988; Bradshaw et al., 1994; Kennard and Colwell, 1996).

The Northern Carnarvon Basin is one of a number of extensional basins that make up the NWS and is situated off the north coast of Western Australia. This basin is approximately 535,000 km^2 and is one of Australia's most explored and prospective areas of hydrocarbons (Hocking, 1988). A large natural gas project in the Greater Gorgon Area, known as the Gorgon project, is currently being developed in addition to the longstanding NWS Venture. This section presents the log data from exploration and appraisal wells in close proximity to the gas fields of the Greater Gorgon Area.

Two major en-echelon rift depocentres (comprising over 10,000 m thick Triassic sediment to more recent sediments) are the Barrow and Dampier Sub-basins (Tingate et al., 2001). The Exmouth Plateau is a subsided continental platform of primarily Triassic sedimentary succession that exceeds 15,000 m in thickness (Hocking, 1988). The major Triassic Mangroo formation consists of thick sandstone, claystone and minor coal members. These large sandstone units act as a reservoir rock for large gas accumulations on the Rankin Platform. The main gas sources for the Barrow and Dampier Sub-basins and the Exmouth Plateau are believed to be claystone and coal measures while numerous hydrocarbon accumulations are present in the Jurassic to Lower Cretaceous (Hocking, 1988).

In the Late Carboniferous period, another important rifting event occurred that gave rise to the WASB (Group, 1994) via the deposit of thick (predominantly) Permian and Mesozoic sediments (Bradshaw et al., 1988). In the Late Carboniferous to Early Permian periods, syn-rift succession comprised glacio-fluvial sediments transitioned upwards upwards into a thick sag section consisting of marine Permian shelfal, shallow water carbonates and sands overlain by a thick succession of shelfal Triassic shale. The Late Triassic to Late Jurassic periods corresponded to the drifting of the Lhasa block, followed by the movement of the West Burma and Woyla blocks (Metcalfe, 2013).

The Late Triassic section was deposited after an extensive phase, called the ‘Fitzroy Movement’, of considerable tectonism, erosion and uplift (Forman et al., 1981) along the edges of the craton which resulted in thick sediment influx (eroded from the uplifted onshore Canning Basin) in the Northern Carnarvon Basin (Nicoll and Foster, 1994). The Barrow Sub-basin is one of several Jurassic-Cretaceous depocentres in the Northern Carnarvon Basin. Sand-rich sediments of submarine-fan and fluvio-deltaic origins of the Lower Cretaceous (Berriasian) Barrow Group were deposited during the initiation of the continental break up of Australia and Greater India. An uplift of the hinterland resulted in deltaic progrades being deposited locally in the Browse area. With the separation of Greater India in the Valanginian, NWS underwent post-rift sag.

In the south, the remnants of the Barrow delta were reworked by transgression to form a small-localised delta in the offshore Broome area. During the Campanian,

an uplift of the hinterland caused an inversion in the Exmouth Plateau (Bradshaw, Yeates, Beynon, Brakel, Langford, Totterdell and Yeung, 1988; Tindale et al., 1998) and resulted in the transpressional growth of pre-existing rift related structures within the Barrow and Dampier Sub-basins. From the middle Late Cretaceous period, calcareous sedimentation began and continued through most of the Cenozoic period (Barber, 1988; Hocking, 1988; McClure et al., 1988). In the Neogene period, the NWS underwent a change in the regional stress field that reactivated the older transgressional structures in the North Carnarvon and Browse Basin.

The area examined in this study has been Western Australia's premier hydrocarbon province for the last 40 years and currently constitutes the majority of the state's total hydrocarbon production, accounting for more than one third of Australia's oil and gas production. The Northern Carnarvon Basin encompasses giant gas accumulations such as Io/Jansz, Gorgon and Scarborough (Western Australia Department of Resources, 2008) and produces more than half of Australia's total hydrocarbon production.

4.2 Data available for the study

This study sought to examine the spatial/regional variation of seismic attenuation using VSP data. Thus, data had to be acquired from a significant number of wells in one region.

This study was based on public domain (zero-offset) VSP and log data obtained from the DMPWA. In assembling the dataset, more than 400 wells were screened. The following criteria were applied to the wells:

- The presence of high-quality VSP and wireline log/logging while drilling data (following initial screenings, this study focused on wells drilled and logged after 2006);
- Boreholes must be vertical or close to vertical for the most significant VSP Interval.

The final dataset comprised data from 33 wells from the Carnarvon Basin and four wells from the Browse Basin. If interpretive well completion reports were available, stratigraphy was taken from these reports. The naming of the formations was standardized across the different operators.

4.3 VSP data acquisition parameters

VSP data used in this study were conducted between 2006 and 2010 (see Table 4.1). Typically, the data were acquired using 3C geophones or accelerometers as seismic sensors. In all of the wells, 3C tools were not oriented. A receiver step along a well was usually 15.24 m (i.e., 50 ft). Airguns or sleeve guns were used as seismic sources for all of the wells at ~5 m depth.

Table 4-1. Acquisition parameters of VSP data formations from the North West Shelf of Australia available for this study.

	Well name	Basin	Year	RT	Offset	Water depth	VSP data availability	TD	Source type	VSP tool
1	Adams 1	Carnarvon	2008	22.4	50.5 m	183.4	1,215–3,090	3,280	3 clustered airgun	GAC-D 3-axis orthogonal
2	Barberry 1	Carnarvon	2010	38.5	42 m	17.9	525–2,370	2,382	3 clustered airgun	GAC-D 3-axis orthogonal
3	Bath 1	Carnarvon	2010	38.4	42 m	15.4	523–1,400	1,420	3 clustered airgun	GAC-D 3-axis orthogonal
4	Belicoso 1	Carnarvon	2007	29	49.4 m	1,446	2,180–2,465	2,573	3 clustered airgun	GAC-D 3-axis orthogonal
5	Bleaberry, West 1	Carnarvon	2007	26.4	29.5 m	257.9	1,235–1,565	1,499	3 sleeve airgun	ASR-multi-component
6	Briseis 1	Carnarvon	2008	29	49 m	1,118	1,227–3,540	3,554	3 clustered airgun	GAC-D 3-axis orthogonal
7	Brulimar 1	Carnarvon	2008	21.1	50.5 m	171	2,028–3,243	3,259	3 clustered airgun	G-Guns/Rig Air/1800 psi
8	Brunello 1	Carnarvon	2007	25	54.63 m	150.8	1,845–3,354	3,274	Sleeve guns	ASR 2 shuttles 30 m spacing
9	Coniston 2	Carnarvon	2009	25	57 m	403.4	533–1,367	1,420	3 clustered airgun	GAC-D 3-axis orthogonal
10	Coniston 3	Carnarvon	2009	25	53 m	398.1	845.2–1,329	1,339	3 clustered airgun	GAC-D 3-axis orthogonal
11	Coniston 5	Carnarvon	2009	25	53 m	386	532–1,340	1,390	3 clustered airgun	GAC-D 3-axis orthogonal
12	Coniston 7	Carnarvon	2009	25	53 m	409.7	523–1,346	1,390	3 clustered airgun	VSIT-C (4 shuttles)

	Well name	Basin	Year	RT	Offset	Water depth	VSP data availability	TD	Source type	VSP tool
13	Dixon 2	Carnarvon	2006	26.4	46 m	84.7	2,405–2,720	3,739	3 clustered airgun	VSIT-C (4 shuttles)
14	Fletcher 1	Carnarvon	2007	20.5	52 m	152.3	1,720–2,964	2,970	3 clustered airgun	VSIT-C (4 shuttles)
15	Grange 1	Carnarvon	2008	22.2	64 m	177.1	1,420–3,885	3,890	3 clustered airgun	VSIT-C (4 shuttles)
16	Guardian 1	Carnarvon	2009	22.3	58 m	1,228	1,915–3,118	3,315	3 clustered airgun	VSIT-C (4 shuttles)
17	Halyard 1	Carnarvon	2008	25	54.63 m	111.5	1,520–2,840	3,315	Sleeve gun	ASR 2 shuttles 30 m spacing
18	Iago 2	Carnarvon	2008	25	52 m	119.6	529.8–3,620	3,625	3 clustered airgun	VSIT-C (4 shuttles)
19	Iago 3	Carnarvon	2008	25	53 m	151.2	724.5–3,409	3,410	3 clustered airgun	VSIT-C (4 shuttles)
20	Kentish Knock 1	Carnarvon	2009	22.3	58 m	1,228	1,309–2,504	2,525	Airgun (3 x 250 cu. inch G-gun)	VSIT-C (4 shuttles)
21	Lambert 8	Carnarvon	2008	25	63.6 m	135.9	1,295–4,020	4,042	Sleeve gun	ASR
22	Maitland 2	Carnarvon	2007	36.7	63.66 m	58.1	753.2–1,263	1,300	3-C SM4-3500-UB-10HZ Geophone	ASR 2 shuttles 15 m spacing
23	Martell 1	Carnarvon	2009	22.3	41 m	1,289	1,909–3,255	3,300	3 clustered airgun	VSIT-C (4 shuttles)
24	PER 01	Carnarvon	2006	23.3	97.3 m	131.1	1,595–3,080	3,227	1 x 450 C cu. inch G-gun	ASR
25	Pluto 3	Carnarvon	2006	22.4	50 m	584.6	1,489–3,453	3,530	3 clustered airgun	VSIT-C (4 shuttles)
26	Pluto 5	Carnarvon	2006	29	54 m	1,062	2,010–3,159	3,240	1 x 150 cu. inch G-gun	VSI (4 shuttles)
27	Rosella 2	Carnarvon	2009	38.2	47 m	104.3	879.3–3,203	3,325	3 clustered airgun	VSIT-C (4 shuttles)
28	Salsa 1	Carnarvon	2007	34	63.6 m	83.7	1,130–3,515	3,535	Sleeve gun	ASR
29	Tidepole 2	Carnarvon	2009	25	29.2 m	113	1,070–3,185	3,718	3 x 150 cu.in. G-gun array	G-Gun Array

	Well name	Basin	Year	RT	Offset	Water depth	VSP data availability	TD	Source type	VSP tool
30	Torosa 2	Browse	2007	22.9	43 m	465.7	2,762–4,727	4,811	3 x 250 cu. inch G-gun	VST-C (4 shuttles)
31	Torosa 3	Browse	2006	28.9	54 m	481	3,110–4,651	4,667	3 x 250 cu. inch G-gun	VST-C (4 shuttles)
32	Torosa 5	Browse	2008	24.1	46 m	404.8	2,837–4,633	4,470	4 x 250 cu. inch G-gun	VSI
33	Torosa 6	Browse	2008	35	92 m	44	3,130–4,746	4,754	2 x 250 clustered airgun	VSI
34	Wheatstone 2	Carnarvon	2007	26.3	46 m	212.9	1,039–3,589	3,231	3 clustered airgun	VSIT-C (4 shuttles)
35	Wheatstone 3	Carnarvon	2008	25	69.5 m	186.6	522.9–3,463	3,012	3 clustered airgun	VSIT-C (4 shuttles)
36	Xena 1	Carnarvon	2006	27.4	55 m	178	2,023–3,416	3,490	3 clustered airgun	VSIT-C (4 shuttles)
37	Xena 2	Carnarvon	2008	25	47 m	193.3	2,113–3,481	3,572	3 clustered airgun	VSI-C 4 levels

4.4 Spatial distribution of apparent attenuation

Thirty-seven wells from the NWSWA were analysed in this study. The locations of these wells are depicted in Figure 4.2 .

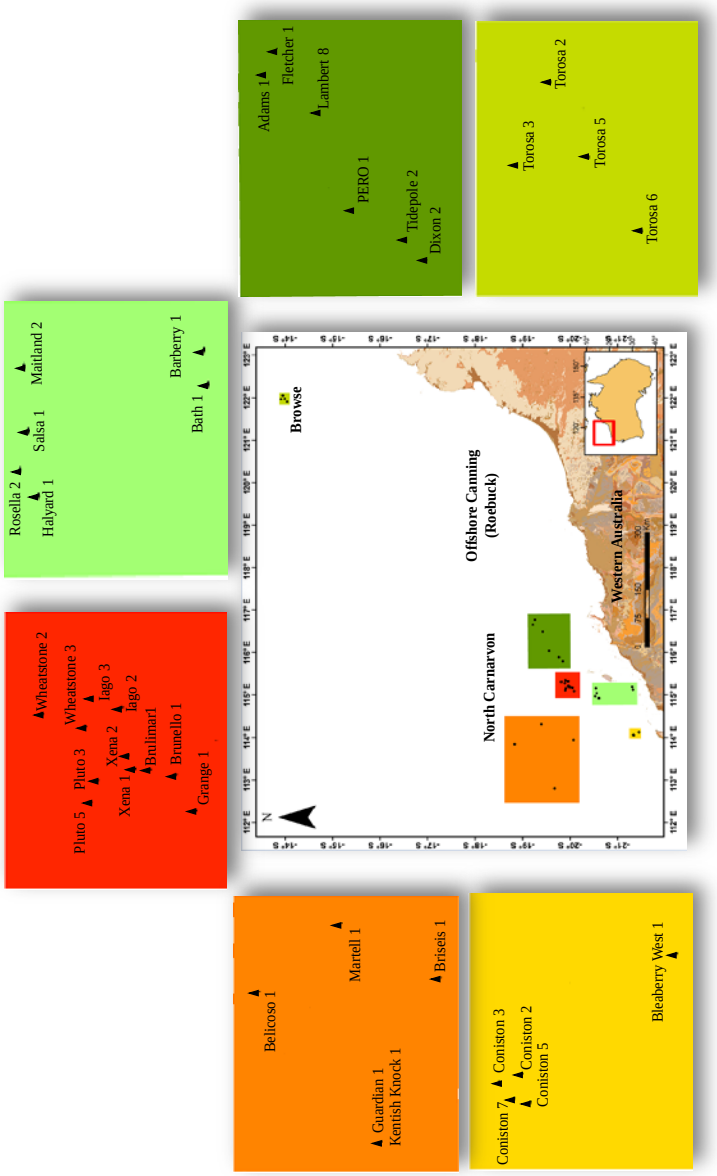

Figure 4-2. North West Shelf wells divided into six areas for cease of analysis.

To estimate apparent attenuation, the same workflow was applied to each well in the dataset. Appendix A assembles the results for all of the wells examined.

To estimate the contribution of scattering, a finely layered elastic model was built and an analysis of the synthetic VSP seismograms was used (see Chapter 3 for more details on the workflow). Appendix A presents the wells used used to estimate apparent attenuation as well as the results of scattering attenuation (PER 01, Wheatstone 2 and Wheatstone 3.

Table Table 4-2 defines eight wells from the North Carnarvon Basin and three wells from the Browse Basin that were excluded from the analysis for a number of reasons, including significant deviation, source instability, well construction, interference and a walk-above acquisition configuration.

Table 4-2. List of wells excluded from the analysis.

Areas	**Wells**	**Reasons**
Area 1	Bleaberry West 1	Strong, inconsistent behaviour of amplitude decay and centroid frequency decay curves.
Area 2	Belicoso 1	Inconsistent behaviour of amplitude decay and centroid frequency decay curves. Only ~300 m MD of the well is covered by VSP data.
	Briseis 1	The construction of the well at specific intervals resulted in the data being contaminated by casing noise. The quality of the data was acceptable; however, the defined intervals were affected because geological Top Formation was not available.
Area 3	Xena 1	Interference was observed between the downgoing P-wave and an event with similar apparent velocity.
	Xena 2	The well is deviated and the behaviour of the centroid frequency and energy curves were not aligned resulting in unreliable estimations.
Area 4	Maitland 2	Clearly the amplitude of the downgoing wavefield decreases with depth. However, I observed an increase in the frequency with depth thus the estimated Q values can be calculated but it is difficult to explain without the support of detailed geological information which is not available for this well. Thus, I excluded this interval from this well.

	Rosella 2	The behaviour of amplitude decay and centroid frequency decay curves are aligned, and the quality data were suitable for analysis; however, this well was excluded from the analysis, as the geological Top Formation was not available to define the intervals.
Area 5	Tidepole 2	Inconsistent behaviour of amplitude decay and centroid frequency decay curves from ~1,000 to 1,500 m and they were not aligned. Moreover, geological Top Formation are not available for the well to help in defining the intervals for *Q* estimation.
Area 6	Torosa 2,3,5 and 6	These wells had a different top formation compared to the North Carnarvon Basin wells. Additionally, the considerable distance of these wells from other well areas prevented correlations between the values of *Q* estimation of North Carnarvon Basin wells and the Browse Basin wells. Further, poor data quality led to unreliable estimations.

Given the large region covered by the study, it was divided into six separate areas. In Figure 4-2 the region marked with as areas with different colours represents (E-W) and is equal to approximately 400 km^2 while from (N-S) is equal to approximately 300 km^2 (i.e., the total area is approximately 120,000 km^2). Figure 4.3 shows five areas of the study region in the North Carnarvon Basin.

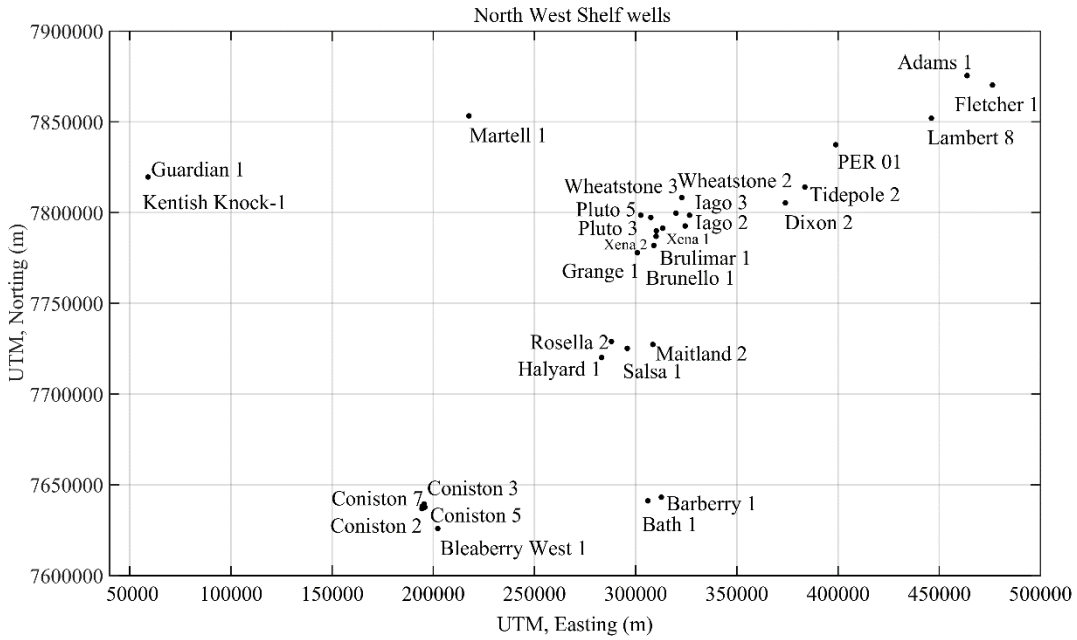

Figure 4-3. Relative location of the wells (included in the study) within the North Carnarvon Basin, Australia.

Apparent attenuation was estimated using a thick-layered model for each well. The centroid frequency decay curve was divided into four stratigraphic intervals based on the formation tops provided to assess the variations of the apparent attenuation in relation to the geological age of every well. Table 4-3 outlines the four stratigraphic intervals and the applicable ages of the sediments.

In order to highly estimate Q values and get proper comparative results among the wells, four intervals were selected based on the VSP availability following a review of the formation tops within a designated region. In relation to Interval 1, attenuation was not observed above the Trealla Formation. On the contrary, Interval 2 had important top formations; however, Muderong Shale was chosen because it is the principal formation for all wells within the NWS. Interval 3 had a variety of top formation information; however, Mungaroo Formation was chosen because no significant attenuation was observed across all the wells in this defined area. Interval 4 was selected because there was no demonstrated attenuation in the well area.

Table 4-3. The four stratigraphic intervals with applicable period age.

Interval	Stratigraphy Formation	Dominant lithology	Period	Age (Million Years)
1	From the top of the VSP curve to the Trealla Formation	Tertiary marls, Carbonates, low energy shallow marine	Neogene	(23.03–2.58)
2	From Trealla Formation to Muderong Shale	Carbonates, commonly fossiliferous, quartzose in places	Neogene Palaeogene Cretaceous	(23.03–2.58) (23.03-66) (145-66)
3	From Muderong Shale to the Mungaroo Formation	Siltstone and soft pyritic mudstone	Cretaceous Jurassic	(145±4-66) (201.3± 0.6-145±4)
4	From Mungaroo Formation to the end of the VSP curve	Mainly siliciclastic, marine siltstones and claystones	Triassic	(250-200)

To obtain an estimate of the apparent *Q* values for the chosen intervals, the modified CFS method was applied (see Figure 4.4 to Figure 4.10). In relation to the values of *Q*, in the following tables:

- The values of a low *Q* (i.e., above 200) are highlighted in blue in the tables;
- The values of a moderate *Q*: (i.e., between 65 and 200) are highlighted in green;
- The values of a high *Q* (i.e., below 65) are highlighted in red; and
- Unreliable estimates are highlighted in yellow.

The first layer estimates were computed from the top of the centroid frequency curve to the top formation boundary of the Trealla Formation, the second stratigraphic intervals were computed from the formation boundary of the Trealla Formation to the Muderong Shale, the third stratigraphic intervals were computed from the Muderong

Shale to the Mungaroo Formation and the fourth stratigraphic intervals were computed from the Mungaroo Formation to the end of the centroid frequency curve (see Table 4-3).

The results obtained in this study are of high accuracy. To find an explanation for this increased accuracy, the study region was divided into six areas and *Q* was measured across four intervals per well. A review of the results for each area is presented in Sections 4.4.1 to 4.4.6. Similarly, Figure 4.4 to Figure 4.6 shows the centroid frequency and amplitude decay curves for the wells from all areas within the North Carnarvon Basin as well as the reference logs (gamma ray), formation tops and the estimated apparent attenuation values. Table 4-4 to Table 4-9 show the estimates of the apparent attenuation for the thick-layered models performed at these wells.

4.4.1 Apparent attenuation from VSP data for Area 1

Area 1 comprised the Coniston 2, 3, 5 and 7 and the Bleaberry West 1 wells. Figure 4.4 shows the centroid frequency and amplitude decay curves for the wells from this area as well as the reference logs (gamma ray), formation tops and the estimated apparent attenuation values. Table 4-4 sets out the estimates of the apparent attenuation for the thick-layered models calculated at these wells. For all Coniston wells, a very good match between the centroid frequency decay and amplitude decay curves was observed, indicating the relatively high reliability of the *Q* estimates.

The Coniston wells exhibited similar behaviour across their frequency decay curves. For Interval 1, VSP data existed for Coniston wells 2, 3, 5 and 7; none of these wells showed significant attenuation and the minimum observed *Q* value was 296. Interval 2 had moderate attenuation in this area with *Q* values varying from 80 to 260. Estimates from Bleaberry West 1 were not reliable. For Interval 3, sediments in the Coniston 3 and Bleaberry West 1 wells exhibited moderate attenuation with *Q* values varying from 94 to 108; however, the other wells showed low attenuation. Sediments that corresponded to Interval 4 were not exposed by these wells.

Figure 4.4 shows all the wells analysed in this area. Coniston 5 and Coniston 7 had a similar centroid frequency profile with a VSP of approximately 550 m from the Trealla Formation to the Muderong Shale. There was high attenuation from the Trealla Formation to the Muderong Shale with approximate decreases of 10 Hz (72 to 62) and 7 Hz (74 to 67) for Coniston 5 and Coniston 7, respectively. A noticeable amplitude decay was observed with energy decreasing by approximately 3 dB for Coniston 5 and Coniston 7; however, Coniston 7 showed an increase after the Muderong Shale. Coniston 2 and Coniston 3 were similar in behaviour to Coniston 5 and Coniston 7 from the Trealla Formation to the Muderong Shale with attenuation decreasing by approximately 9 Hz (66 to 57) and 5 Hz (74 to 69) and an amplitude decay of approximately 4 dB and 3 dB, respectively.

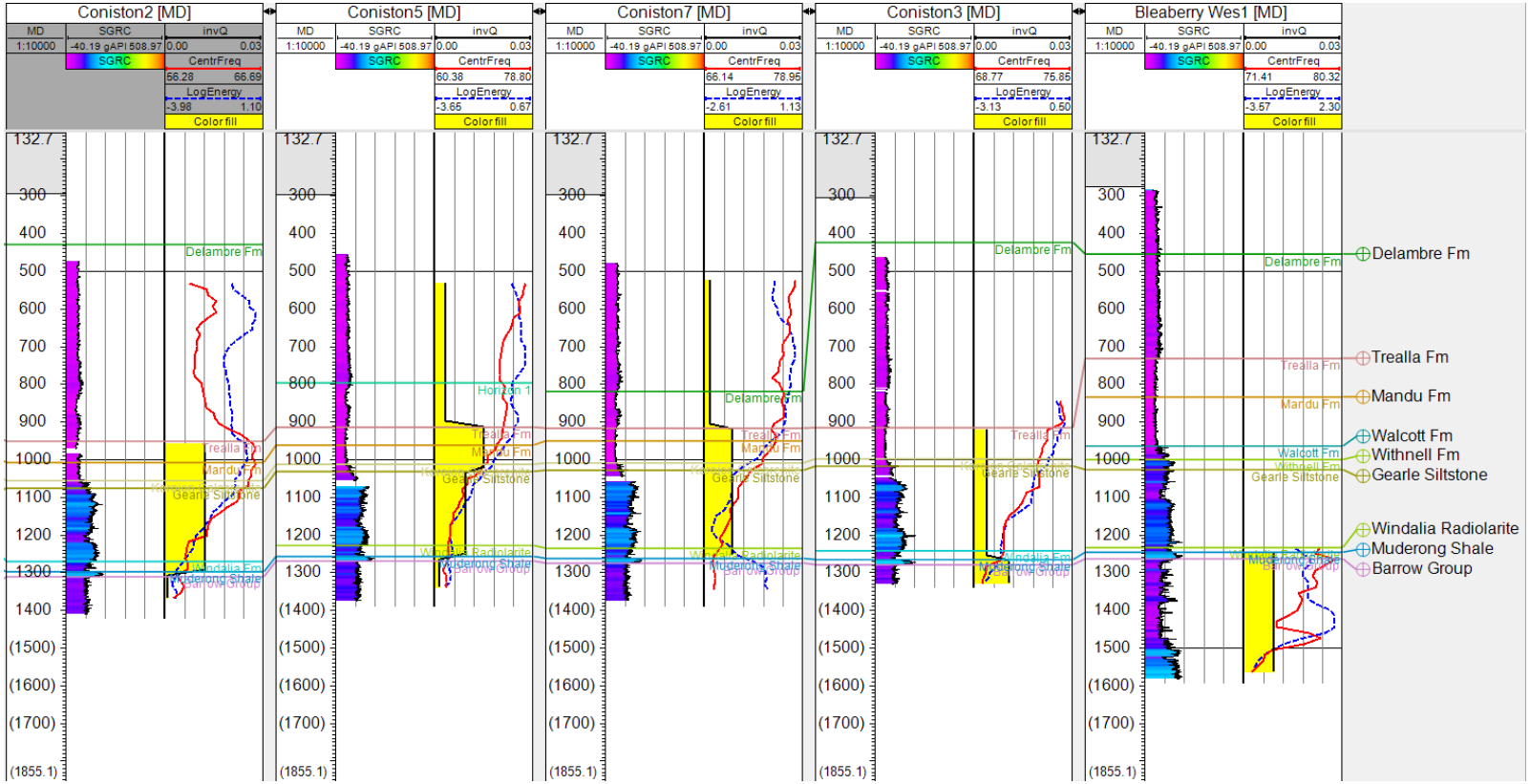

Figure 4-4. Well sections for Coniston wells (i.e., wells 2, 5, 7, 3) and the Bleaberry West 1 well. The first tract represents the gamma ray, the second tract represents the centroid frequency (the red curve) and log energy (the blue curve) and Q^{-1} (the yellow shape).

Table 4-4. The value of Q and Q^{-1} for the wells located in Area 1 at specific intervals.

Area	Well Name	VSP Data Availability (m MD)	Interval 1: Top of VSP Interval—Trealla Fm		Interval 2: Trealla Fm—Muderong Shale		Interval 3: Muderong Shale—Mungaroo Fm		Interval 4: Mungaroo Formation—End of VSP Interval	
			Q	Q^{-1}	Q	Q^{-1}	Q	Q^{-1}	Q	Q^{-1}
1	Coniston 2	533–1,367	NaN	NaN	82	0.01224	1301	0.00077		
	Coniston 3	845.2–1,329	NaN	NaN	260	0.00385	94	0.01065		
	Coniston 5	532–1,340	296	0.00337	78	0.01276	716	0.0014		
	Coniston 7	523–1,346	568	0.00176	116	0.00865	NaN	NaN		
	Bleaberry West 1	1,235–1,565			NaN	NaN	108	0.00922		

4.4.2 Apparent attenuation from VSP data for Area 2

This section details the results for the Belicoso 1, Briseis 1, Guardian 1, Martell 1 and Kentish Knock 1 wells. Kentish Knock 1 was previously the subject of research conducted by Pimentel (2011). Table 4-5 illustrates the available VSP data for these wells extending to the Mungaroo Formation. The centroid frequency decay and amplitude decay curves indicated a relatively high reliability of the *Q* estimates. Guardian 1 and Kentish Knock 1 exhibited comparable behaviour across their frequency decay curves; thus, suggesting that they are an evident match.

The *Q* values for Interval 1 are not displayed due to a lack of data. In relation to Interval 2, Martell 1 showed moderate attenuation with a *Q* value of 148; however, the estimate of Kentish Knock 1 was deemed unreliable. For Interval 3, Guardian 1 and Kentish Knock 1 had a significant high attenuation with *Q* values between 24 and 47. For Interval 4, Guardian 1 and Kentish Knock 1 showed a high attenuation with *Q* values of 35 to 56, but Martell 1 showed moderate attenuation with a *Q* value of 97.

Figure 4.5 displays the results of wells analysed in this area. Kentish Knock 1 had high attenuation from the Muderong Shale to the Mungaroo Formation with approximate decreases in centroid frequency of 14 Hz (57 to 43) and an amplitude decay corresponding to a 10 dB decrease in energy. Guardian 1 showed similar decreases of 12 Hz (55 to 43) and 8 dB from the Muderong Shale to the Mungaroo Formation. Martell 1, which is some distance from Kentish Knock 1 and Guardian 1 showed decreases in centroid frequency and decreases in energy of 22 Hz (75 to 53) and 12 dB across Intervals 3 and 4, respectively. In relation to Kentish Knock 1 and Guardian 1 from the Muderong Shale to the Mungaroo Formation and Martell 1, which is some distance from these locations, the average decrease in centroid frequency was 16 Hz (62 to 46) with an amplitude decay that corresponded to a 10 dB decrease in energy.

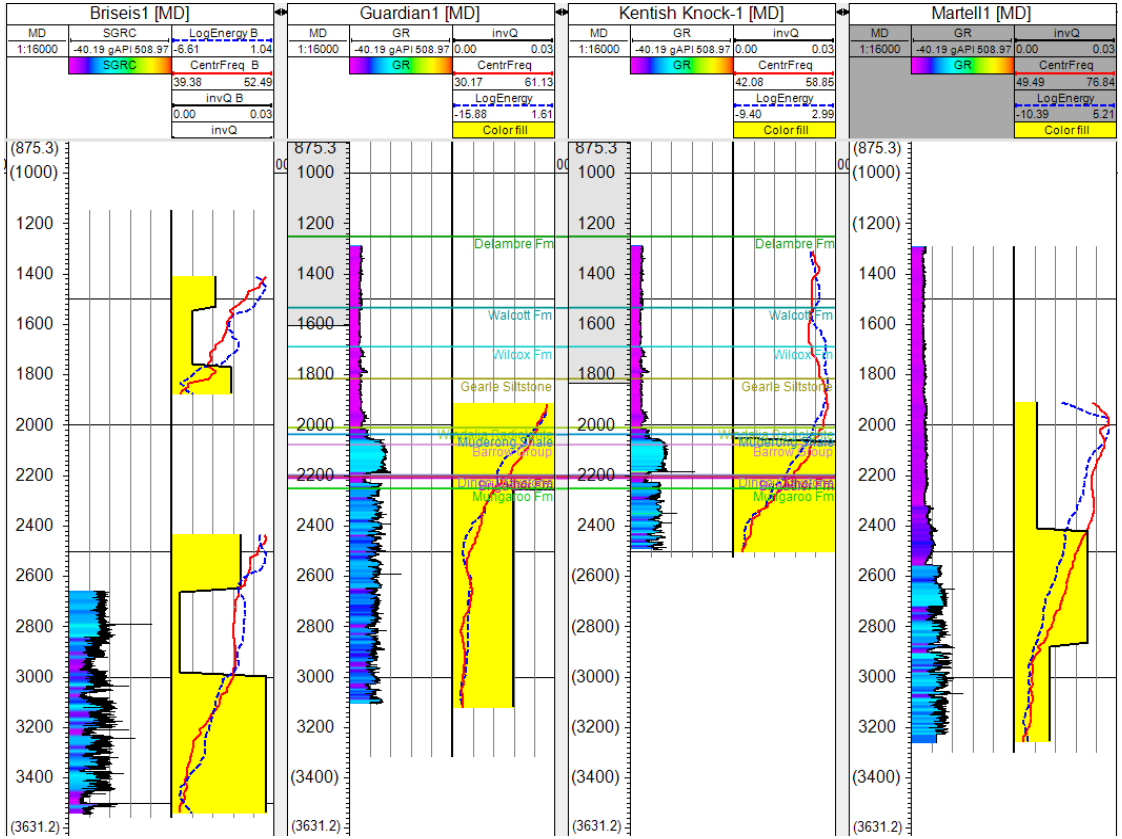

Figure 4-5. Well sections for the Briseis 1, Guardian 1, Kentish Knock 1, Martell 1 and Belicoso 1 wells. The first tract represents the gamma ray, the second tract represents the centroid frequency (the red curve) and long energy (the blue curve) and Q^{-1} (the yellow shape).

Table 4-5. The value of Q and Q^{-1} for the wells located in Area 1 at specific intervals.

Area	Well Name	VSP Data Availability (m MD)	Interval 1: Top of VSP Interval—Trealla Fm		Interval 2: Trealla Fm—Muderong Shale		Interval 3: Muderong Shale—Mungaroo Fm		Interval 4: Mungaroo Formation—End of VSP Interval	
			Q	Q^{-1}	Q	Q^{-1}	Q	Q^{-1}	Q	Q^{-1}
2	Guardian 1	1,915–3,118					24	0.04124	56	0.01785
	Kentish Knock 1	1,309–2,504			NaN	NaN	37	0.02693	35	0.02845
	Martell 1	1,909–3,255			148	0.00677	47	0.02146	97	0.01029

4.4.3 Apparent attenuation from VSP data for Area 3

Area 3 comprised the Grange 1, Brulimar 1, Brunello 1, Iago 2, Iago 3, Pluto 3, Pluto 5, Wheatstone 2 and Wheatstone 3 wells. The wells analysed (from the Trealla Formation to the Mungaroo Formation) in which the behaviour of centroid frequency reflected high attenuation. Table 4-6 sets out the estimates of apparent attenuation for the thick-layered models performed at these wells. In the majority of these wells, the centroid frequency decay and amplitude decay curves had a high reliability of *Q* estimates that were relatively equivalent. The comparable behaviour of the frequency decay curves is apparent in Iago 2, Iago 3 and Wheatstone 3.

In relation to Interval 1, the VSP data for these wells showed low attenuation with observed *Q* values between 263 and 2,037. For Interval 2, Pluto 5 and Wheatstone 2 showed significant attenuation, with *Q* values of 49 and 55, respectively. The other wells had moderate attenuation with *Q* values varying from 69 to 174. It should be noted that due to a lack of data five wells in this Interval had no estimates. For Interval 3 Grange 1, Brulimar 1 and Brunello 1 had high attenuation, with *Q* values between 42 and 56. Most of the other wells in this area had moderate attenuation, with *Q* values from 62 to 99. The five wells in Interval 4 had high attenuation, with *Q* values ranging from 34 to 64, and most of the remaining wells showed moderate attenuation.

Figure 4.6 to Figure 4.8 display the results of wells that analysed in this area. Grange 1 showed high attenuation from the Trealla Formation (~1,500 m) to beyond the Mungaroo Formation (3,500 m) with approximate decreases in centroid frequency of 18 Hz (53 to 35 Hz) and a large amplitude decay decreasing by approximately 12 dB. Iago 2 and Iago 3 had similar centroid frequency profiles from above the Trealla Formation to below the Mungaroo Formation, with approximate attenuation decreases of 24 Hz (62 to 38) and 16 Hz (58 to 42) and amplitude decreases of 17 dB and 14 dB, respectively. Wheatstone 2 had an approximate decrease in attenuation of 32 Hz (69 to 37) and an amplitude decay of 16 dB from above the Trealla Formation to below the Mungaroo Formation, while Wheatstone 3 had decreases of 19 Hz (59 to 40) and 16 dB from above the Trealla Formation to below the Mungaroo Formation. The average decreases in centroid frequency were 22 Hz (60 to 38) with an amplitude decay corresponding to a 15 dB decrease in energy.

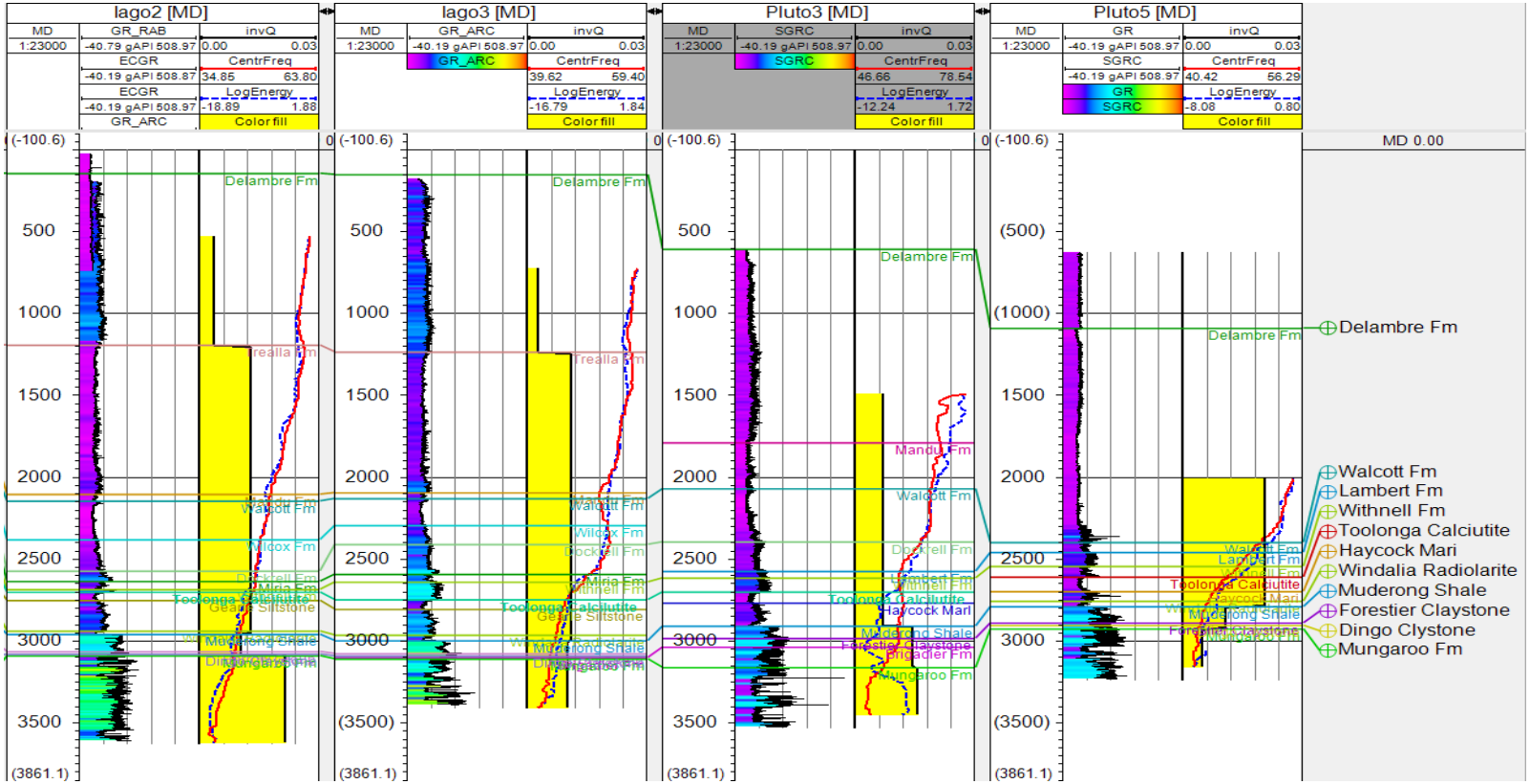

Figure 4-6. Well sections for the Iago 2, Iago 3, Pluto 3 and Pluto 5 wells. The first tract represents the gamma ray, the second tract represents the centroid frequency (the red curve) and long energy (the blue curve) and Q^{-1} (the yellow shape).

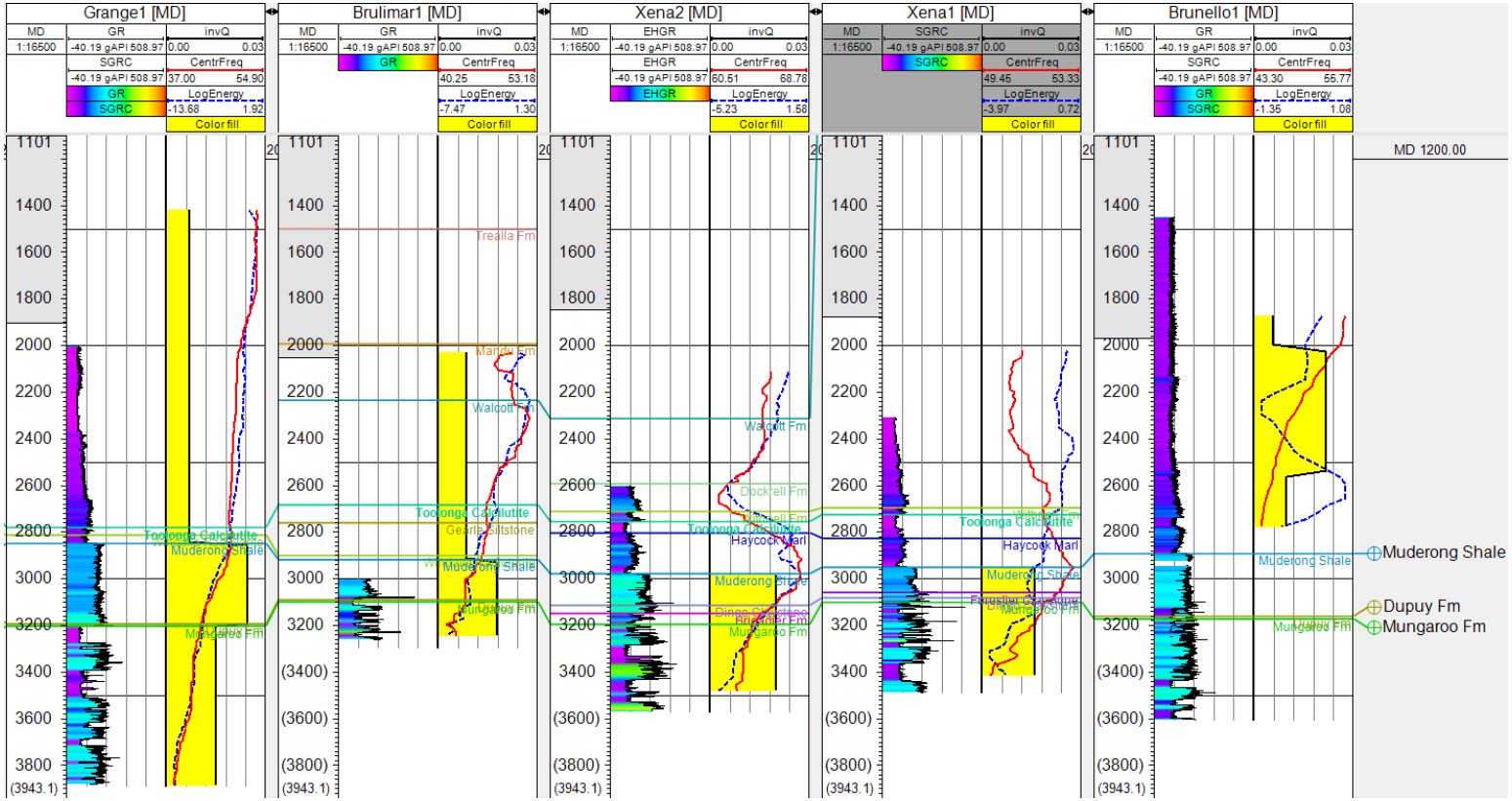

Figure 4-7. Well sections for the Grange 1, Brulimar 1, Xena 1, Xena 2 and Brunello 1 wells. The first tract represents the gamma ray, the second tract represents the centroid frequency (the red curve) and long energy (the blue curve) and Q^{-1} (the yellow shape).

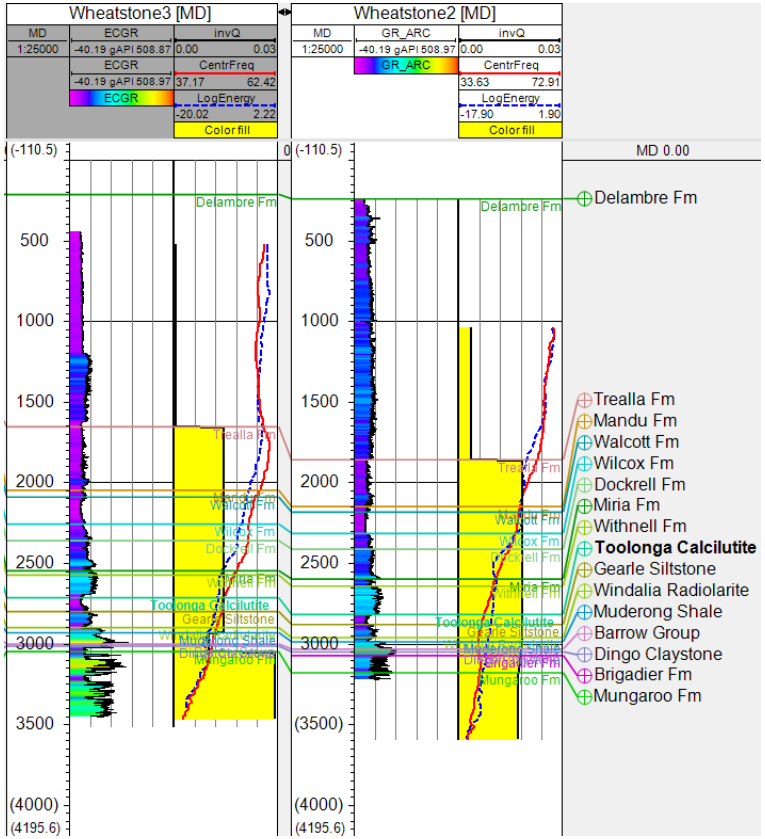

Figure 4-8. Well sections for the Wheatstone 2 and Wheatstone 3 wells. The first tract represents the gamma ray, the second tract represents the centroid frequency (the red curve) and long energy (the blue curve) and Q^{-1} (the yellow shape).

Table 4-6. The value of Q and Q^{-1} for the wells located in Area 3 at specific intervals.

Area	Well Name	VSP Data Availability	Interval 1: Top of VSP Interval—Trealla Fm		Interval 2: Trealla Fm—Muderong Shale		Interval 3: Muderong Shale—Mungaroo Fm		Interval 4: Mungaroo Formation—End of VSP Interval	
			Q	Q^{-1}	Q	Q^{-1}	Q	Q^{-1}	Q	Q^{-1}
3	Grange 1	1,420–3,885			144	0.00695	41	0.02436	67	0.01497
	Brulimar 1	2,028–3,243			118	0.00846	56	0.01777	57	0.01769
	Brunello 1	1,845–3,354			174	0.00574	46	0.02185	103	0.00975
	Iago 2	529.8–3,620	263	0.0038	77	0.013	96	0.0104	46	0.02156
	Iago 3	724.5–3,409	374	0.00267	90	0.01114	98	0.01023	99	0.01006
	Pluto 3	1,489–3,453			142	0.00704	70	0.01429	64	0.01558
	Pluto 5	2,010–3,159			49	0.02046	94	0.01067	207	0.00484
	Wheatstone 2	1,039–3,589	273	0.00366	55	0.01823	NaN	NaN	59	0.017
	Wheatstone 3	522.9–3,463	2,037	0.00049	69	0.01445	99	0.01008	34	0.02904
	Xena 1	2,023–3,416			NaN	NaN	62	0.01603		
	Xena 2	2,113–3,481			NaN	NaN	62	0.01603		

4.4.4 Apparent attenuation from VSP data for Area 4

Area 4 comprised the Barberry 1, Bath 1, Halyard 1, Rosella 2 and Salsa 1 wells. Five wells showed centroid frequency decay and amplitude decay curves indicating a relatively high reliability of the easily comparable *Q* estimates. Table 4-7 presents the estimates of the apparent attenuation for the thick-layered models performed at these wells. Further, similar behaviour of the frequency decay curves was observed for these wells.

Interval 1 and 4 had no results due to a lack of VSP data and neither interval had any significant attenuation comparing to other wells that have the same intervals. However, for Interval 2, Rosella 2 showed high attenuation with a *Q* value of 47 and the remaining wells (except Halyard 1) had a moderate attenuation with *Q* values ranging from 70 to 11. Halyard 1 had low attenuation with a *Q* value of 267. Interval 3 showed high attenuation for Salsa 1 with a *Q* value of 53. Four wells in this area had a moderate attenuation with *Q* values of 73 to 136 except Bath 1 which had low attenuation with a *Q* value of 1,481.

Figure 4.9 displays the results of the wells analysed in this area. Salsa 1 had an approximate decrease in attenuation of 16 Hz (44 to 28) for a VSP of 1,100 m to 3,500 m and its amplitude decreased by 12 Hz between 1,100 m and 2,900 m. Barberry 1 had an approximate decrease in attenuation of 16 Hz (48 to 31) for a VSP of 500 m to 2,300 m and its amplitude displayed erratic fluctuations of 0 dB to -9 dB. Bath 1 had an approximate decrease in attenuation of 6 Hz (40 to 34) and its amplitude decreased by 5 dB from below the Gearle Sandstone to the Muderong Shale. Halyard had an approximate decrease in attenuation of 5 Hz (38 to 33) and its amplitude decreased by 5 dB between the Gearle and Halyard Sandstone. The average decrease in attenuation was 11 Hz (42 to 31) with an 8 dB decrease in amplitude decay.

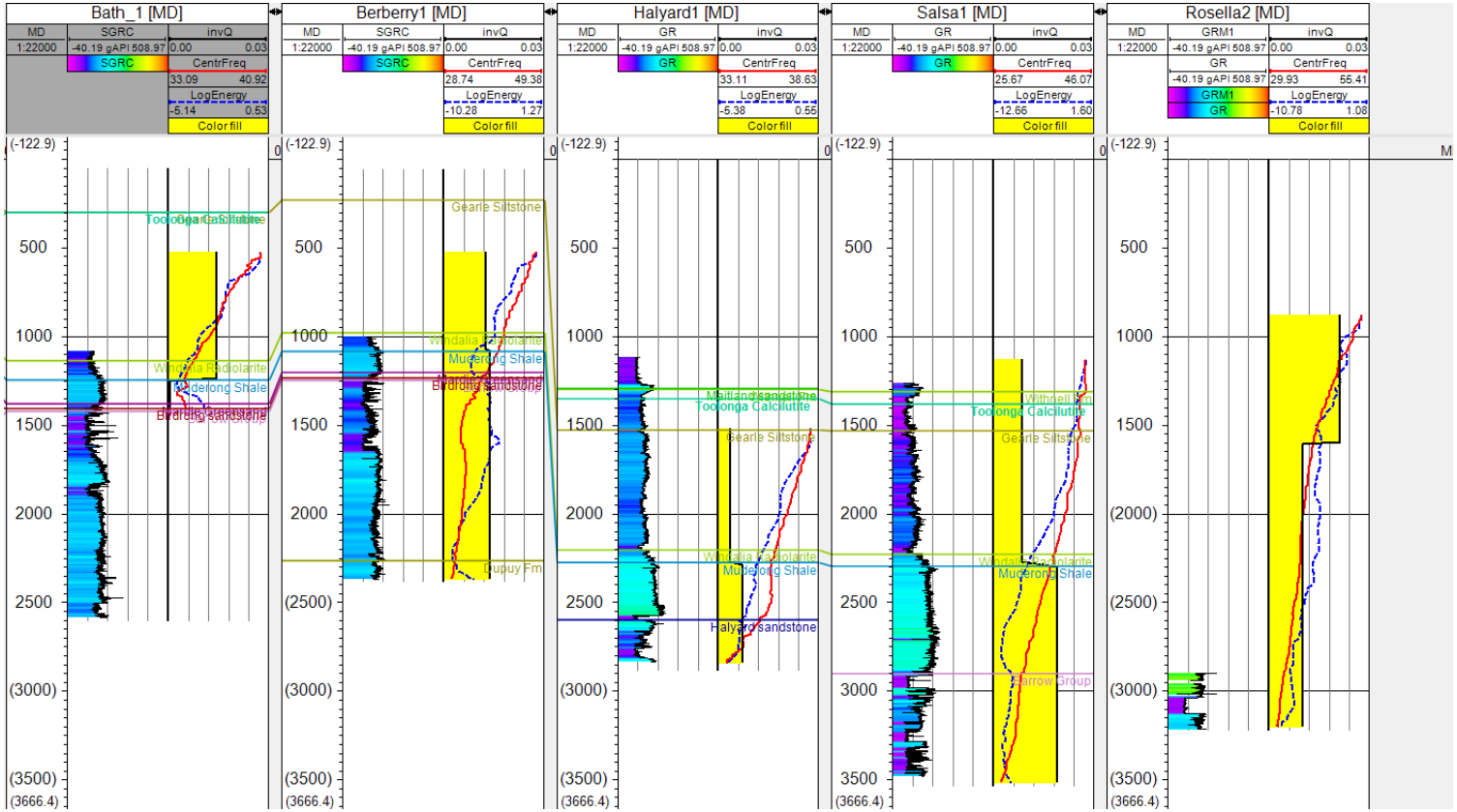

Figure 4-9. Well sections for the Bath 1, Barberry 1, Halyard 1, Salsa 1 and Rosella 2 wells. The first tract represents the gamma ray, the second tract represents the centroid frequency (the red curve) and long energy (the blue curve) and Q^{-1} (the yellow shape).

Table 4-7. The value of Q and Q^{-1} for the wells located in Area 4 through specific intervals.

Area	Well Name	VSP Data Availability	Interval 1: Top of VSP Interval—Trealla Fm		Interval 2: Trealla Fm—Muderong Shale		Interval 3: Muderong Shale—Mungroo Fm		Interval 4: Mungaroo Formation—End of VSP interval	
			Q	Q^{-1}	Q	Q^{-1}	Q	Q^{-1}	Q	Q^{-1}
4	Barberry 1	525–2,370			80	0.0125	73	0.01371		
	Bath 1	523–1,400			70	0.01424	1481	0.00068		
	Halyard 1	1,520–2,840			267	0.00375	136	0.00735		
	Maitland 2	753.2–1,263			NaN	NaN	79	0.01266		
	Rosella 2	879.3–3,203			47	0.02123	98	0.01025		
	Salsa 1	1,130–3,515			117	0.00852	53	0.01888		

4.4.5 Apparent attenuation from VSP data for Area 5

Area 5 comprised the Adams 1, Dixon 2, Fletcher 1, Lambert 8, PER 01 and Tidepole 2 wells. The wells analysed from the Trealla Formation to the Muderong Shale were those in which the behaviour of centroid frequency reflected high attenuation. Table 4-8 presents the estimates of apparent attenuation for the thick-layered models performed at these wells. These wells showed a sound match between centroid frequency decay and amplitude decay curves indicating relatively high reliability of the *Q* estimates. The frequency decay curves of these wells displayed similar behaviours.

The results of Interval 1 and 4 are not displayed (with the exception of Tidepole 2), as they did not demonstrate any attenuation due to a lack of reliable VSP data. Tidepole 2 had unreliable estimation. For Interval 2, Tidepole 2 had high attenuation with a *Q* value of 56. However, all of the other wells in this area had moderate attenuations, with *Q* values from 70 to 128. For Interval 3, Fletcher had an unreliable estimation, but Dixon 2 and Lambert 8 had high attenuation, with *Q* values of 45 and 38, respectively. The remaining two wells, Adams 1 and PER 01, had moderate attenuation with *Q* values of 66 and 83, respectively.

Figure 4.10 displays the results of the wells analysed in this area. Each had a different shape in terms of centroid frequency and energy curves. Between a VSP interval of 2,500 m and 3,700 m, the attenuation of Dixon 2 decreased by approximately, 20 Hz (65 to 45) with an amplitude decay corresponding to a 14 dB decrease in energy. The attenuation of Lambert 8 decreased by 32 Hz (68 to 36) between a VSP of 1,400 m and 4,000 m, with an amplitude decay corresponding to a 13 dB decrease in energy. The attenuation of Adams 1 decreased by approximately 16 Hz (55 to 39) between a VSP of 1,200 m and 3,100 m, and it had a 10 dB drop in energy. PER 01 exhibited an 11 Hz decrease (61 to 50) in attenuation and a 9 dB decrease in energy between a VSP of 1,500 m and 2,500 m, before stabilising at 3,000 m. Fletcher 1 provided reliable data with a VSP between 1,700 m and 3,000 m for Interval 2, with attenuation decreasing by approximately 10 Hz (55 to 45) and an amplitude decay of approximately 6 dB. The average decrease in attenuation was 18 Hz (61 to 43) with an average energy decrease of 10 dB.

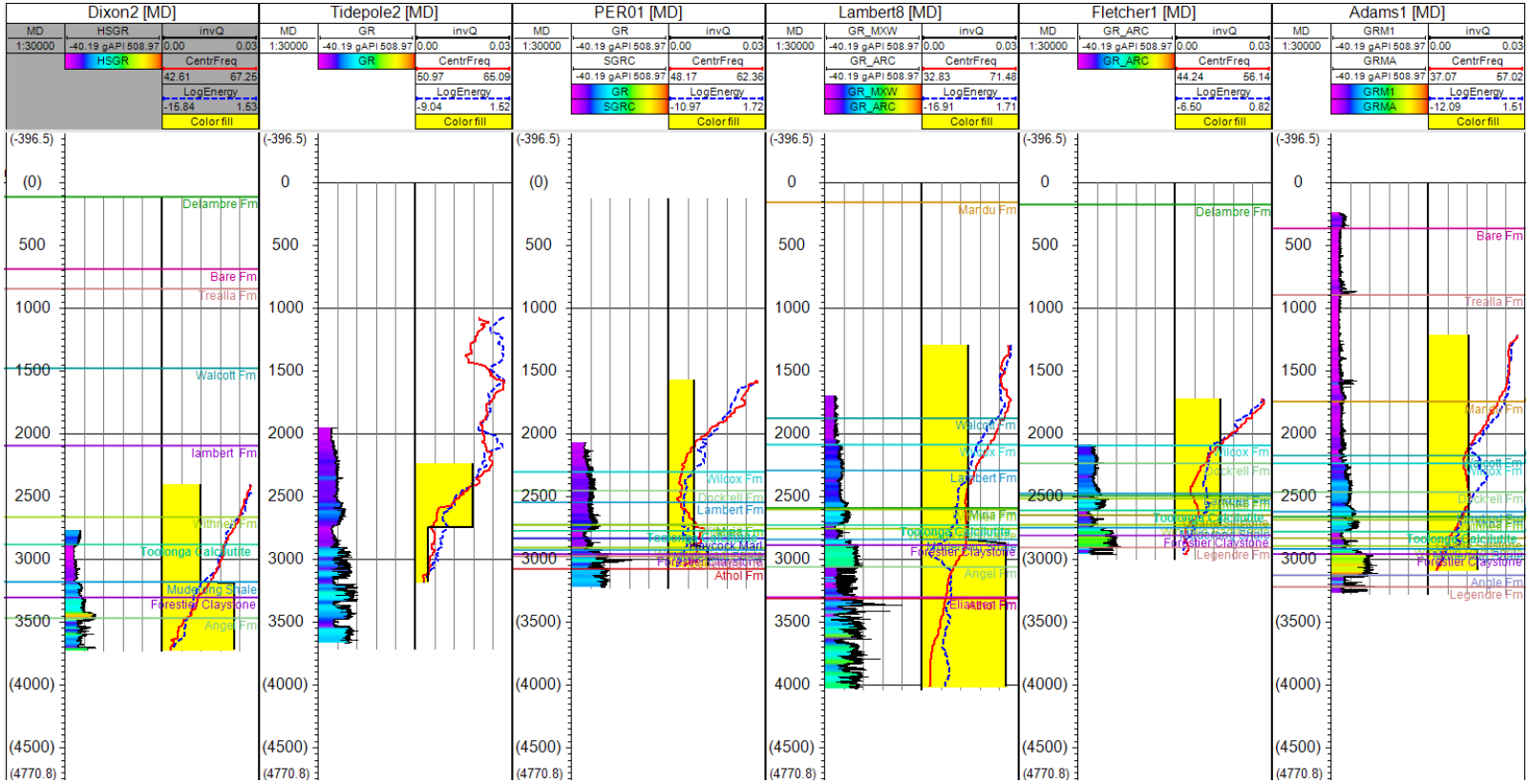

Figure 4-10. Well sections for the Dixon 2, Tidepole 2, PER 01, Lambert 8, Fletcher 1 and Adams 1 wells. The first tract represents the gamma ray, the second tract represents the centroid (the red curve) and long energy (the blue curve) and Q^{-1} (the yellow shape) represents the North Carnarvon Basin in Area 5.

Table 4-8. The value of Q and Q^{-1} for the wells located in Area 5 at specific intervals.

Area	Well Name	VSP Data Availability	Interval 1: Top of VSP Interval—Trealla Fm		Interval 2: Trealla Fm—Muderong Shale		Interval 3: Muderong Shale—Mungaroo Fm		Interval 4: Mungaroo Formation—End of VSP Interval	
			Q	Q^{-1}	Q	Q^{-1}	Q	Q^{-1}	Q	Q^{-1}
5	Adams 1	1,215–3,090			80	0.01258	66	0.01525		
	Dixon 2	2,405–2,720			84	0.01184	45	0.02244		
	Fletcher 1	1,720–2,964			71	0.01406	NaN	NaN		
	Lambert 8	1,295–4,020			70	0.0143	38	0.02612		
	PER 01	1,595–3,080			128	0.00784	83	0.01211		
	Tidepole 2	1,070–3,185	NaN	NaN	56	0.01788	247	0.00405		

4.4.6 Apparent attenuation from VSP data for Area 6

Area 6 comprised the Torosa 2, 3, 5 and 6 wells and was located at a considerable distance (i.e., 796 km) from Area 3. The Jamieson and Johnson Formations were considered the main interval for the estimation of attenuation. Table 4-9 presents the estimates of apparent attenuation for the thick-layered models performed at these wells. Between the centroid frequency decay and amplitude decay curves (that can indicate relatively high reliability of the *Q* estimates) no comparable alignment was observed. Additionally, the frequency decay curves of the wells did not demonstrate any similar behaviour.

Interval 1 had no applicable reliable data; thus, the results are not displayed. In relation to Interval 2, Torosa 6 had significant attenuation, with a Q value of 35. Torosa 3 had moderate attenuation, with a *Q* value of 92. Torosa 5 had low attenuation, with a *Q* value of 235. Torosa 2 had an unreliable estimation. For Interval 3, three of the wells had moderate attenuation, with *Q* values varying from 93 to 130. Torosa 6 also had an unreliable estimation; thus, its results are not displayed. Finally, for Interval 4, Torosa 2 and Torosa 6 had high attenuation, with *Q* values of 35 and 36, respectively and Torosa 3 and Torosa 5 had moderate attenuation, with *Q* values of 62 and 109, respectively.

Figure 4.11 displays a well section of Torosa 2. There were approximate decreases in attenuation of 11 Hz (62 to 51) and an amplitude decay corresponding to a 9 dB decrease between 3,100 m and 4,700 m.

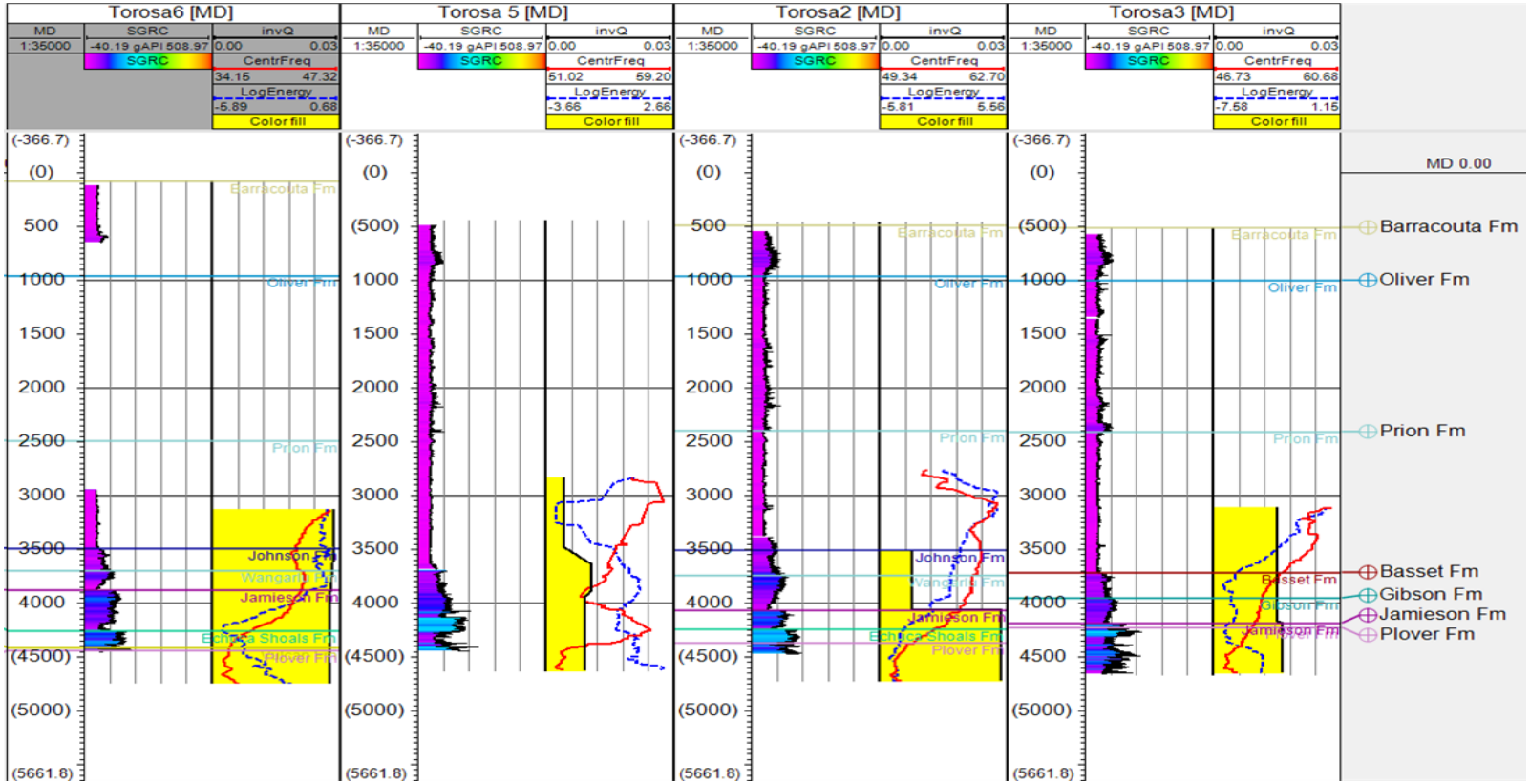

Figure 4-11. Well sections for the Torosa group 6, 5, 2 and 3 wells. The first tract represents the gamma ray, the second tract represents the centroid frequency (the red curve) and long energy (the blue curve) and Q^{-1} (the yellow shape) represents the Browse Basin in Area 6.

Table 4-9. The value of Q and Q^{-1} for the wells located in Area 6 through specific intervals.

Area	Well Name	VSP Data Availability	Interval 1: Top of VSP interval—Johnson Fm		Interval 2: Johnson Fm—Jamieson Fm		Interval 3: Jamieson Fm—Pkover Fm		Interval 4: Plover Fm—End of VSP Interval	
			Q	Q^{-1}	Q	Q^{-1}	Q	Q^{-1}	Q	Q^{-1}
6	Torosa 2	2,762–4,727			NaN	NaN	130	0.0077	35	0.2838
	Torosa 3	3,110–4,651			92	0.01088	107	0.00934	62	0.01617
	Torosa 5	2,837-4,633			235	0.00426	93	0.01076	109	0.00914
	Torosa 6	3,130-4,746			35	0.02836	NaN	NaN	36	0.02744

4.4.7 Distribution of apparent attenuation in NWSWA as seen from Zero-offset VSP data analysis.

Figure 4.12 shows the distribution of apparent attenuation at four selected intervals within the wells studied.

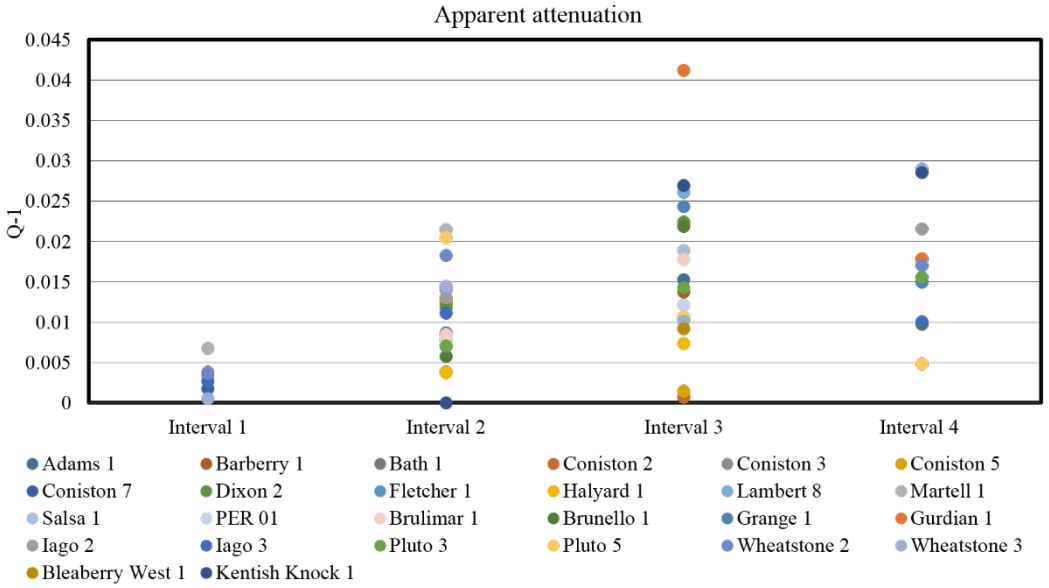

Figure 4-12. The distribution of seismic attenuation in the study area (apparent attenuation was estimated for a thick-layered model).

The four-layered model was assumed to have boundaries based on the formation tops provided. Estimation for the first interval was computed from the top of the centroid frequency curve to the formation boundary of Trealla and the estimation for the last interval was computed from the formation of the Mungaroo boundary to the end of the centroid frequency curve.

There was a clear trend of increased attenuation in relation to formation age. Unreliable results were excluded from the analyses and retained so that variations in attenuation could be further assessed. The behaviour of the centroid frequency decay curve and the amplitude (energy) decay curve were examined; attenuation estimation is thought to be robust in cases where these curves follow each other. The significant divergence between these curves or the opposite phase behaviour was then used as

criteria to filter out the corresponding attenuation values. Only reliable values of Q^{-1} were analysed.

The 63 Q^{-1} values analysed ranged from 0.00049 to 0.04124 and were categorised as follows:

- Low: Q^{-1} below 0.005 (corresponding to Q values above 200);
- Moderate: Q^{-1} between 0.005 and 0.015 (corresponding to Q Values between 65 and 200); and
- High: Q^{-1} above 0.015 (corresponding to Q values below 65).

Figure 4.13 shows the distribution of the apparent attenuation in the study area within different stratigraphical intervals. .

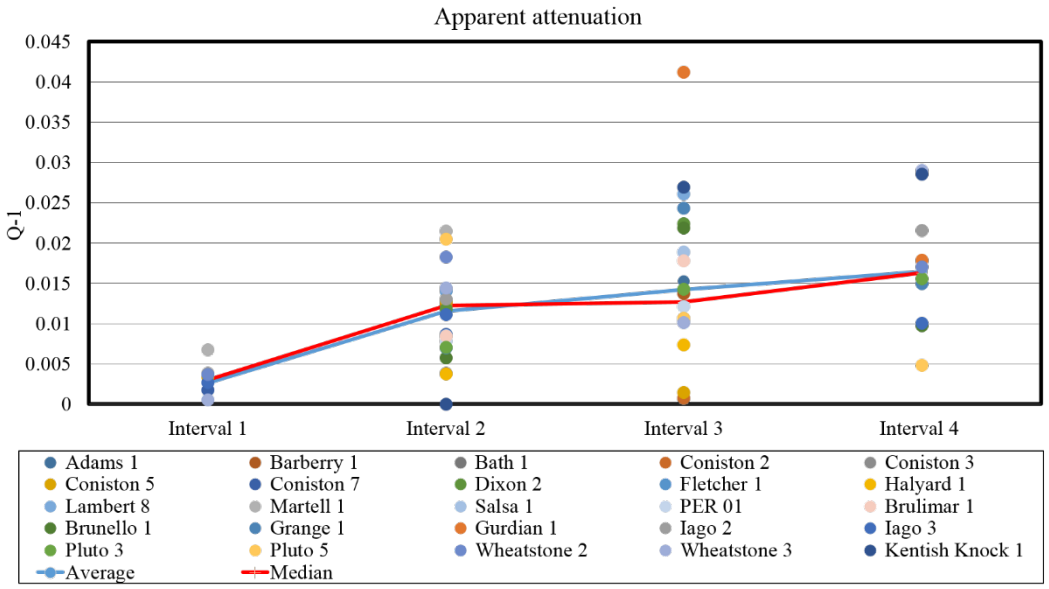

Figure 4-13. The distribution of the seismic attenuation in the study area. Unreliable estimates of apparent attenuation were excluded. The blue line represents the average distribution of Q^{-1} and the red line represents the median distribution of Q^{-1}.

In Figure 4.13 the red and blue curves are the average and median values respectively, and any alignment of these lines reflects a robust estimation of the attenuation parameter. The results, which can be interpreted in geological age terms, showed an increase of attenuation with depth. The young formations (i.e., from the Neogene to Palaeogene periods) were represented mainly by carbonate successions

and were related to the passive margin that experienced low seismic attenuation (i.e., a *Q* value of more than 200). The attenuation behaviour within the older formations (i.e., from the Cretaceous to Triassic periods) is more complicated. Figure 4.14 demonstrates this behaviour within the studied wells. Two different attenuation trends are apparent.

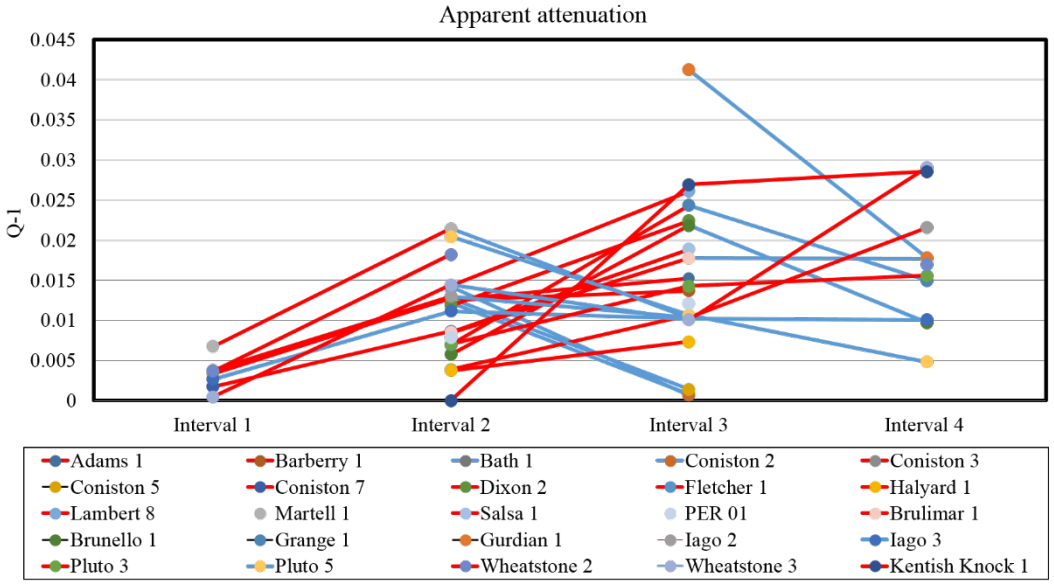

Figure 4-14. The behaviour of seismic attenuation within the wells of the study area.

In Figure 4.14, the red lines indicate increases and the blue lines indicate decreases in the behaviour of seismic attenuation at intervals in the North Carnarvon Basin. It is apparent that attenuation mostly increased from Interval 1 to 2 and from Intervals 2 to 3. Overall, there are more ‘red lines’ than ‘blue lines’. An increasing trend was noted from Intervals 2 to 3; however, in relation to depth, a decreasing trend was observed in both Intervals 2 to 3 and Intervals 3 to 4.

As Figure 4.14 shows there was high attenuation, normal (moderate attenuation) and low attenuation. If the values of the Q^{-1} estimations had high attenuation, they fell outside this trend and were likely to decrease. However, if the values of the Q^{-1} estimations fell within a moderate range, the trend was likely to increase.

Figure 4.15, 4-17, 4-19 and 4-21 show the lateral distribution of apparent attenuation for the four intervals. These intervals represent the sediments of the

Neogene period in Interval 1; the Neogene, Palaeogene and Cretaceous periods in Interval 2; the Cretaceous and Jurassic periods in Interval 3; and the Triassic period in Interval 4. A *Q* value of 65 was set as the colour limit. Zonation was found in the attenuation distribution; however, at this point it is difficult to relate these lateral variation behaviours to a particular cause. A comparison of the structural information and an extension of the study to a larger number of wells would provide further information.

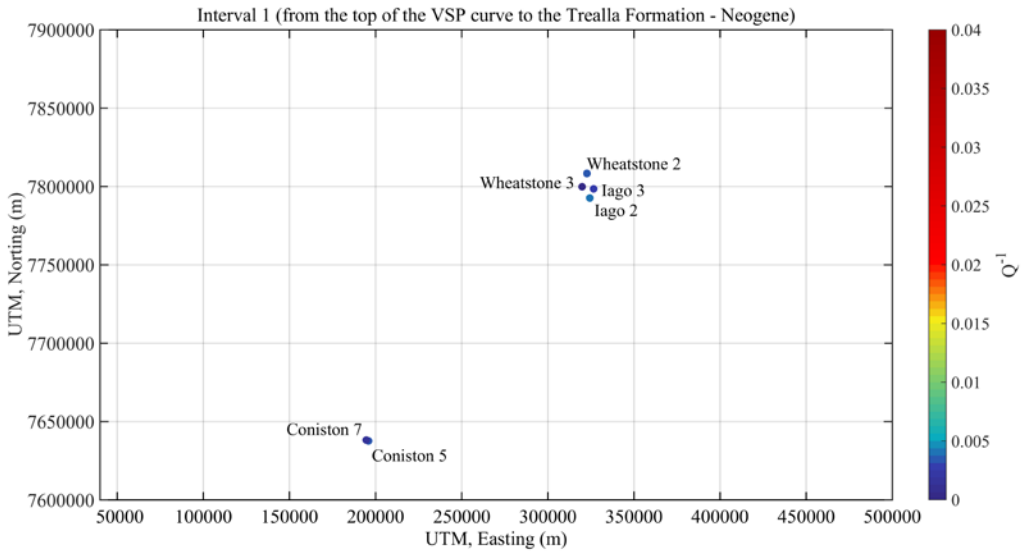

Figure 4-15. Lateral distribution of seismic attenuation within the formation boundaries of Interval 1 (from the top of the VSP data curve to the Trealla Formation).

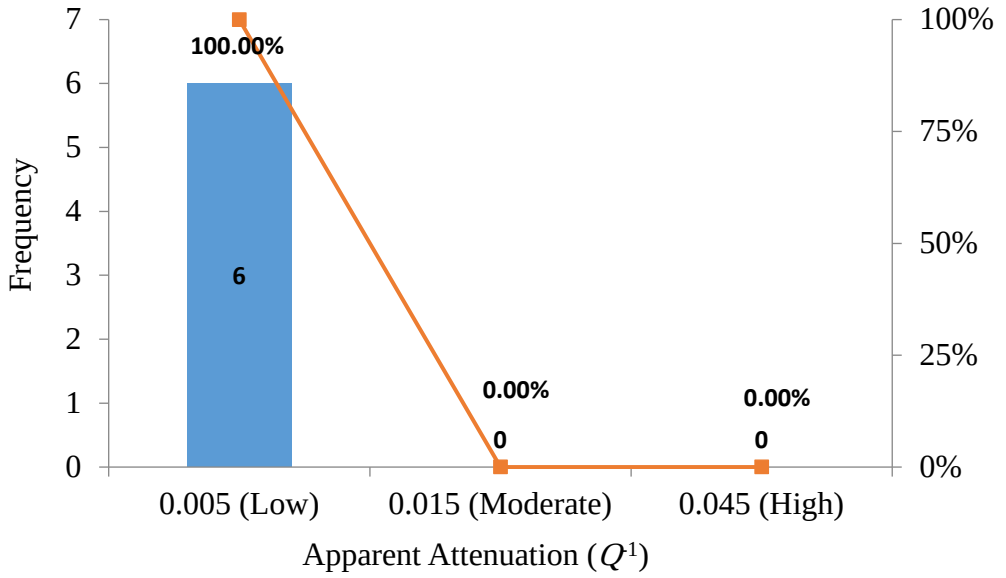

Figure 4-16. Interval 1: apparent attenuation values for the wells in Areas 1–5 (n = 6).

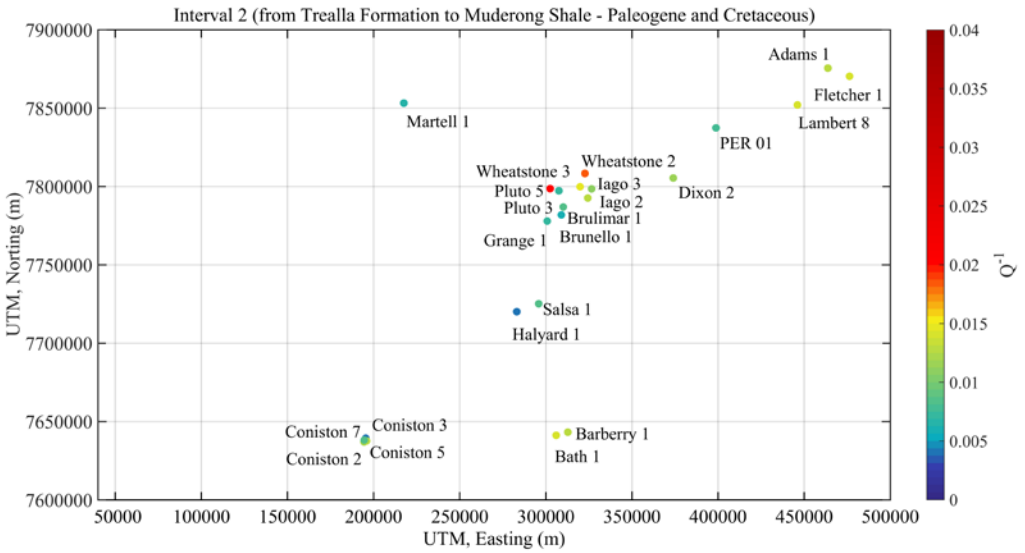

Figure 4-17. Lateral distribution of seismic attenuation within the formation boundaries of Interval 2 from the Trealla Formation to the Muderong Shale.

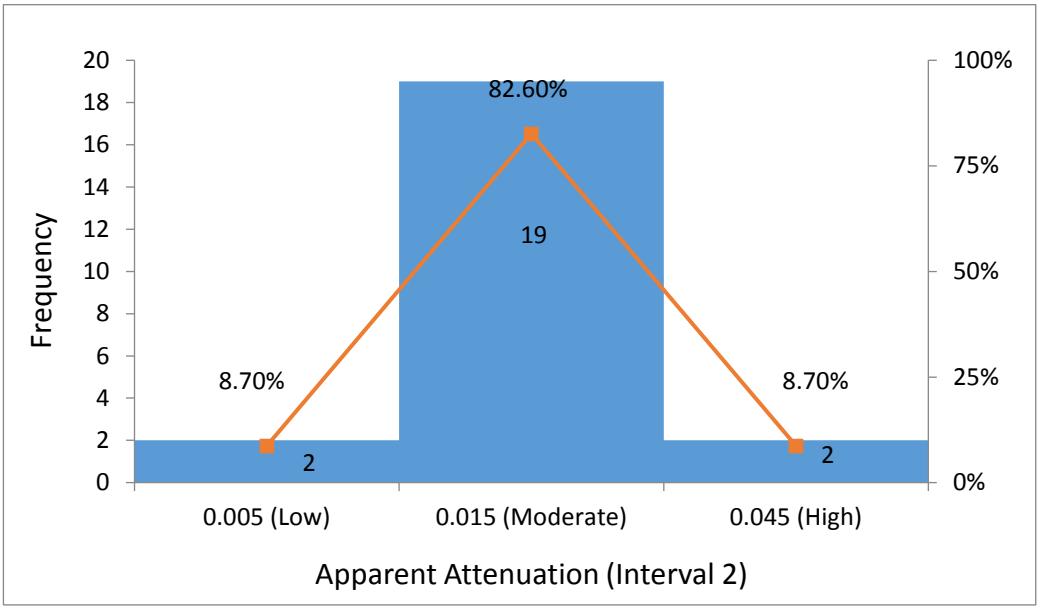

Figure 4-18. Interval 2: apparent attenuation values for the wells in Areas 1–5 (n = 23)

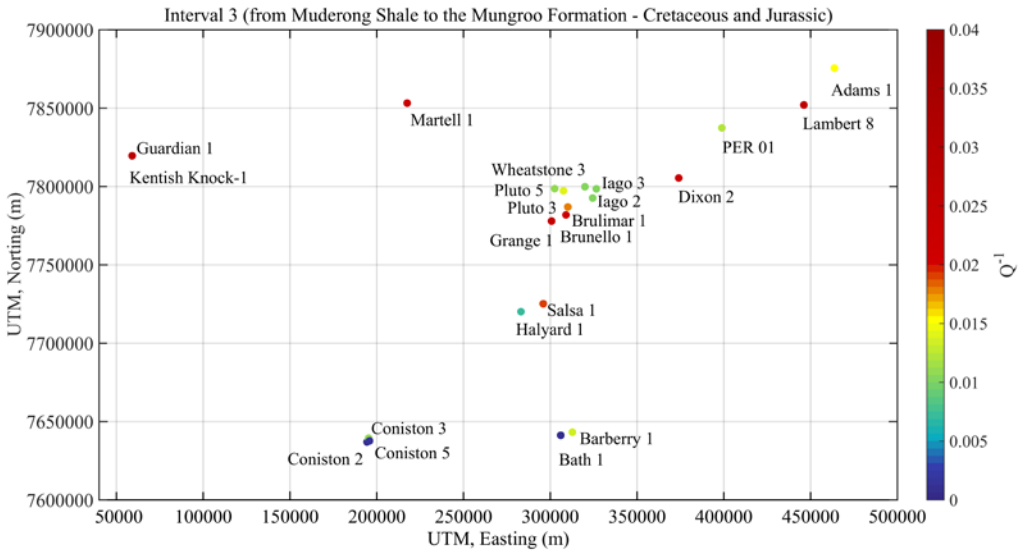

Figure 4-19. Lateral distribution of seismic attenuation within the formation boundaries of Interval 3 from the Muderong Shale to the Mungaroo Formation.

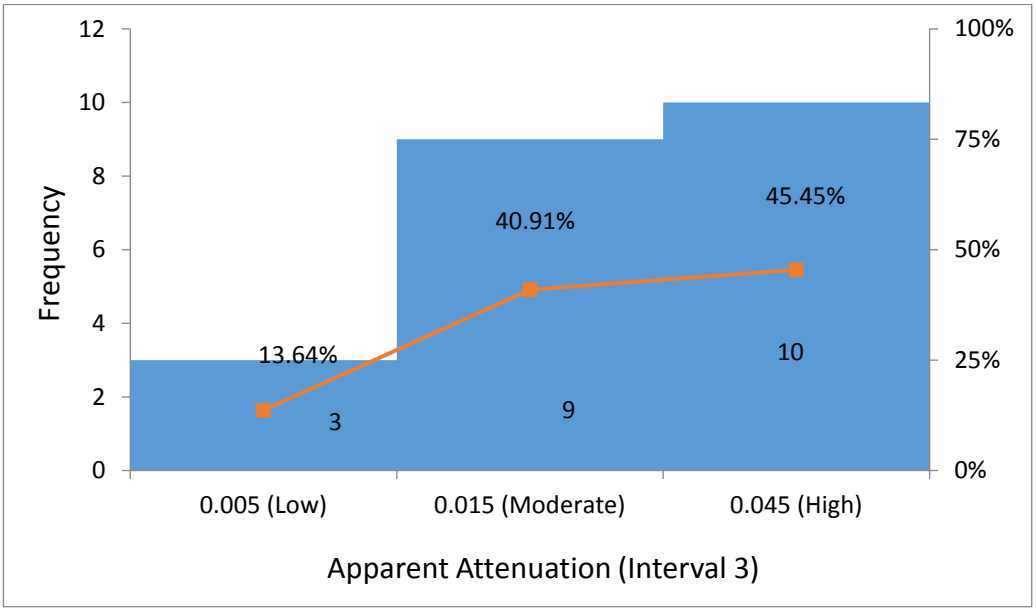

Figure 4-20. Interval 3: apparent attenuation values for the wells in Areas 1–5 (n = 22).

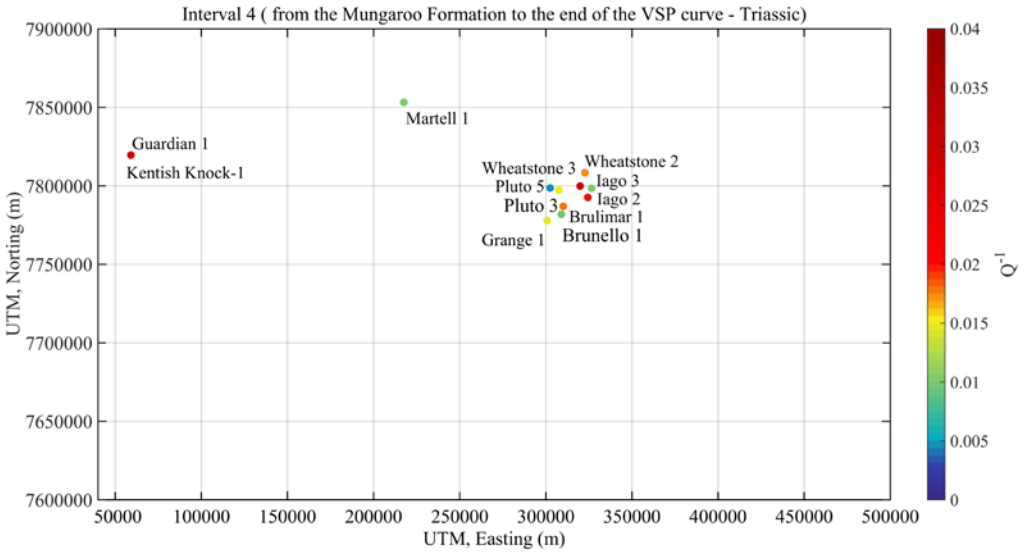

Figure 4-21. Lateral distribution of seismic attenuation within the formation boundaries of Interval 4 from the Mungaroo Formation to the end of the VSP data curve.

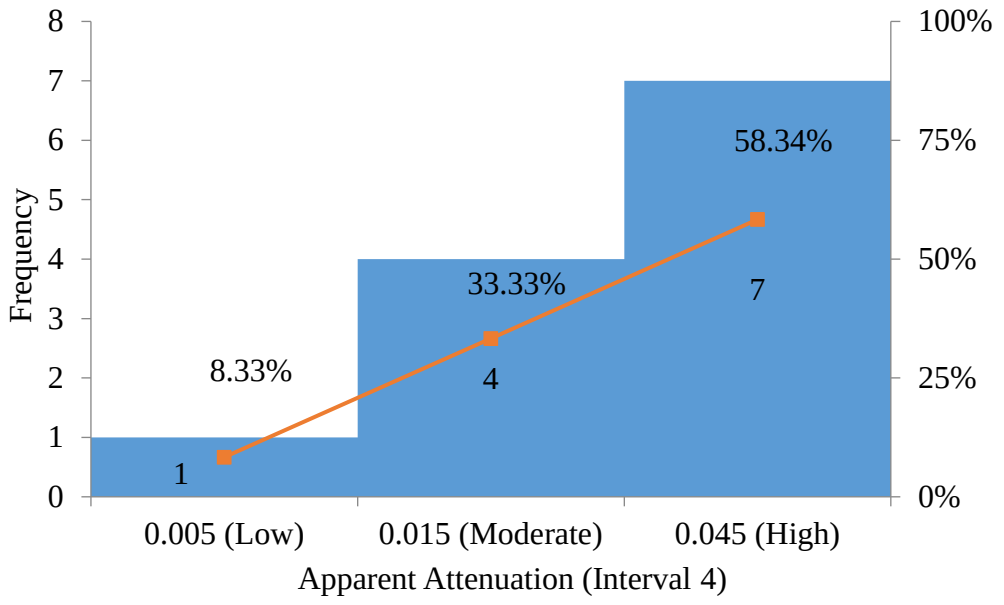

Figure 4-22. Interval 4: apparent attenuation values for the wells in Areas 1–5 (n = 12).

In summary, the results of the analysis of the North Carnarvon Basin wells showed that the apparent attenuation values were relatively greater at greater depths. The 63 *Q* values were classified on an interval basis (see Table 4-9 for a summary of the data).

Table 4-10. Apparent attenuation classifications versus Interval (n = 63).

Interval	**Attenuation (number of measurements)**			**Total**
	Low (Q>200)	**Moderate (65<Q<200)**	**High (Q<65)**	
1	6	0	0	6
2	2	19	2	23
3	3	9	10	22
4	1	4	7	12
Total	12	32	19	63

A number of observations were made in relation to the *Q* values for each interval.

Observation 1

In relation to Interval 1, all *Q* values were high. However, attenuation was often not observed near the ground surface. The data for Interval 1 are displayed in Figure 4-15. In relation to Interval 2, the majority of *Q* values were moderate (i.e., 82.60 %); however, only 8.70 % were low and high (see Figure 4.16 and Figure 4.18).

In Interval 3, there were more high *Q* values (i.e., 45.45 %) than moderate *Q* values (i.e., 40.91 %) and, proportionately, more low values (i.e., 13.64 %) than in Interval 2 (see Figure 4-19). In Interval 4, the majority of *Q* values (i.e., 58.34 %) were high and only one *Q* value was low (i.e., 8.33 %) (see Figure 4.20 and Figure 4.22).

Observation 2

In relation to the apparent attenuation values estimated from Areas 1–5 (and taking into consideration the overall *Q* value of 72), the Intervals showed that almost half of the *Q* values (i.e., 32 or 50.79 %) had moderate apparent attenuation. However there were more high *Q* values (i.e., 30.16 %) than low *Q* values (i.e., 19.05 %); (see Table 4-11).

Table 4-11. Apparent attenuation values for the wells in Areas 1-5 (n = 63).

Interval Endpoint	Frequency	Frequency %
0.005 (Low)	12	19.05
0.015 (Moderate)	32	50.79
0.045 (High)	19	30.16
Total	63	100.00

4.5 Contribution of scattering attenuation

For the purpose of estimating the relative contribution of scattering, three wells from the North Carnarvon Basin were examined (i.e., Wheatstone 2 and Wheatstone 3 from Area 3 and PER 01 from Area 5). The well log data enabled a finely layered elastic model to be built to generate synthetic VSP seismogram and estimate the quality factor (the same workflow was used as described in Chapter 3). Figure 3.23 Figure 4.23 shows the wells analysed in this area. The values are also displayed in Table 4-12.

4.5.1 Scattering attenuation from synthetic data for Area 3

In relation to PER 01, the centroid frequency and energy decay curves moved in opposite directions. Centroid frequency decreased between the Lambert Formation and the Miria Formation by approximately 0.5 Hz from a VSP of 2,550 m to 2,700 m. Energy decreased consistently by 3 dB from a VSP of 1,600 m to 3,100 m. There was no significant attenuation in Intervals 1 and 4; however, the corresponding synthetic well exhibited moderate attenuation in Intervals 2 and 3, with *Q* values of 128 and 83, respectively.

In relation to Wheatstone 2, the centroid frequency and energy decay curves aligned between 1,500 m and 2,600 m; however, no significant attenuation was observed in this well. Centroid frequency decreased by approximately 3.5 Hz (i.e., from 70.5 to 67) and from 2,600 m to 3,100 m, between the Miria and Mungaroo Formations and energy fell by approximately 2 dB across the same range. There was significant moderate attenuation in Interval 3 ($Q = 140$); however, attenuation was low in the other three intervals, ranging from a *Q* value of 1,362 in Interval 4 to 472,495 in Interval 1.

In relation to Wheatstone 3, the centroid frequency and energy decay curves exhibited very similar behaviour from 500 m above the Trealla Formation to 3,500 m below the Mungaroo Formation. The centroid frequency decreased by approximately 1 Hz (68.4 to 67.4) and energy fell by approximately 3 dB. There was significant attenuation; however, attenuation was low across Intervals 1 to 4, with *Q* value ranging between 288 (Interval 2) and 7,836 (Interval 1).

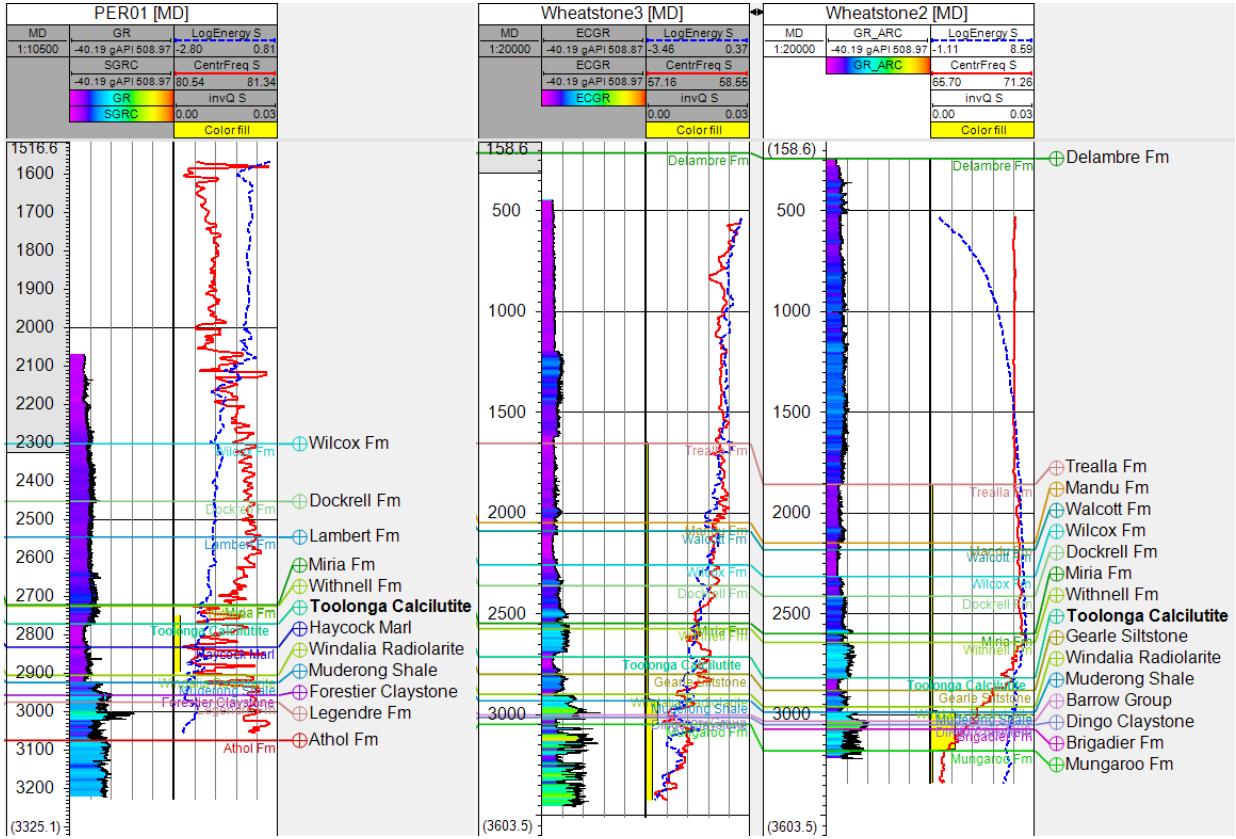

Figure 4-23. The PER 01, Wheatstone 2 and Wheatstone 3 wells. The first tract represents the gamma ray, the second tract represents the centroid frequency (the red curve) and long energy (the blue curve) and the Synthetic Q^{-1} data (the yellow shape), respectively.

Table 4-12. The value of Q and Q^{-1} synthetic data for the wells located in Area 3 at specific intervals.

Well Name	Interval 1: Top of VSP interval - Trealla Fm		Interval 2: Trealla Fm - Muderong Shale		Interval 3: Muderong Shale - Mungraoo Fm		Interval 4: Mungaroo Formation – end of VSP interval	
	Q	Q^{-1}	Q	Q^{-1}	Q	Q^{-1}	Q	Q^{-1}
PER 01 **(S)**			128	0.00784	83	0.01211		
Wheatstone 2 **(S)**	47,2495	0.00000	1,666	0.00060	140	0.00714	1,362	0.00073
Wheatstone 3 **(S)**	7,836	0.00013	1,911	0.00052	288	0.00347	592	0.00169

Chapter 5. Layering-induced Attenuation and VTI Anisotropy in the Middle East

This chapter presents the findings of the research undertaken in the Middle East, including geological settings, VSP and well log data availability. Additionally, the estimation of apparent attenuation and the contribution of scattering are verified. The estimated VTI anisotropy parameters and principal observations are also presented.

As discussed in the previous chapters, seismic attenuation can be caused by two principal mechanisms: scattering (O'Doherty and Anstey, 1971) and absorption, or the transfer of the energy into heat, most likely due to liquid friction (Müller and Shapiro, 2001). In many cases, absorption is the dominant mechanism (see the NWS study presented in Chapter 4 and (Galvin et al., 2013). However, at least two published studies document high attenuation from scattering. In the first case, the presence of shallow, stiff carbonate layers is responsible for the deterioration of seismic data quality (Maitland 1, NWSWA) (Pevzner, Müller, Bona and Gurevich, 2014). The second case shows that where there exists environments where the contrasts reach 100%, such as coal and carbonate shale layers, which can cause significant layered-induced anisotropy and attenuation (Encounter 1, Cooper Basin, South Australia) (Gurevich et al., 2015).

Layering is known to be one of the mechanisms responsible for the presence of anisotropy (Backus, 1962). However, strong velocity contrasts between horizontal layers in some carbonate sections, or sections containing stacks of coal seams, could result in significantly larger (VTI) anisotropy. This was recently reported in the case of coals (Pevzner, Müller, Bona and Gurevich, 2014).

This chapter presents a case study from a typical setting in the Middle East, where a strong contrast between relatively soft siliciclastic sediments and evaporites significantly deteriorates the quality of seismic images. Previously, significant attenuation or the presence of a strong transverse isotropy (VTI) anisotropy were rarely considered the principal impediments to imaging in this area. A dataset comprising a high-quality zero-offset (VSP) and well log data from a well in the

Middle East are used to estimate seismic attenuation and VTI (Thomsen, 2002) within the carbonate overburden.

First, I demonstrate the presence of a high level of seismic scattering attenuation and layering-induced anisotropy in the area. A robust workflow based on the modified CFS method provides reliable estimates of apparent Q from offset VSP data. The scattering component of the attenuation is then quantified with the help of seismic forward modelling.

5.1 Geological settings in the Middle East

The regional geology of the Arabian Plate comprises two main regions: the Arabian Shield to the west and the Arabian Shelf to the east. The Shield is generally composed of Precambrian igneous and metamorphic rocks, while the Shelf is made up of sedimentary rock ranging in age from Cambrian to (Recent) Holocene. The Shelf forms the Greater Arabian Basin. The Palaeozoic succession is dominated by continental clastic rocks and minor marine carbonates and shales. These rocks are exposed as a belt around the eastern edge of the Shield. The Mesozoic is dominated by marine facies of carbonate, shale rocks and minor clastics. The Cenozoic is formed of clastics and carbonates.

The sedimentary succession in the Middle East has been occurring since the Cambrian period and runs from the west (Arabian Shield) to the east (Arabian Shelf). Palaeozoic rocks are clastic, whereas Mesozoic and Cenozoic rocks are carbonates. The continental and shallow Marine strata constitute an area that is historically known as the Eastern Province, and the exposed Palaeozoic, Mesozoic and Lower Tertiary sediments constitute a belt bordering the Arabian Shield. The central and eastern parts of the surface area of the Middle East are composed of Upper Mesozoic and Cenozoic sediments, respectively.

Upper Cretaceous and Eocene rocks are mainly carbonates. The Quaternary sequence is composed of predominantly non-marine sandstones and sandy limestones, which dip subtly in the east and north east under the Zagros Mountains (Steineke et al., 1958; Powers et al., 1966; Al Sayari and Zotl, 1978; Vaslet et al., 1991). The Palaeocene and Lower Eocene Umm Er Radhuma Formations are exposed as a belt

60–120 km wide extends approximately 1,200 km from the south to the north carbonate region (Powers, Ramirez, Redmond and Elberg, 1966; Al Sayari and Zotl, 1978). The youngest sediments are *sabkhas* (in Arabic this means salt deposits), which are composed of sand, silt and salt.

The pre-Early Miocene to post-Miocene seafloor spreading of the Red Sea caused the major tectonic events of the Arabian Plate (Coleman, 1974). The collision of the Arabian and Eurasian Plates (Turkish and Iranian Plates) is considered the most significant episode in the eastern Arabian Gulf along the Zagros–Bitlis Thrust Belt. The uplift and exposure of the Precambrian basement rocks in the west formed major structural features (Schmidt et al., 1978; Ayres et al., 1982; Husseini, 1989; Al-Husseini, 2000), whereas the Phanerozoic succession occurred through five major tectonic events.

5.2 VSP and well-log data available for the study

A single vibroseis with an offset of 50.6 m was used as the seismic source, and a 3C four-level VSP tool was used as a receiver. At depths of 85.04–3,404.60 m with a 15.24 m receiver spacing, 653 traces were acquired with a 1 ms sampling rate. The top ~985 m of data show the effect of strong surface casing reverberations. Figure 5.1 shows the raw VSP data—the right panel shows the vertical component Z, while the middle and left panels show the horizontal components X (inline) and Y (crossline), respectively. High-quality P and S sonic and density logs were available for approximately the entire depth of the well.

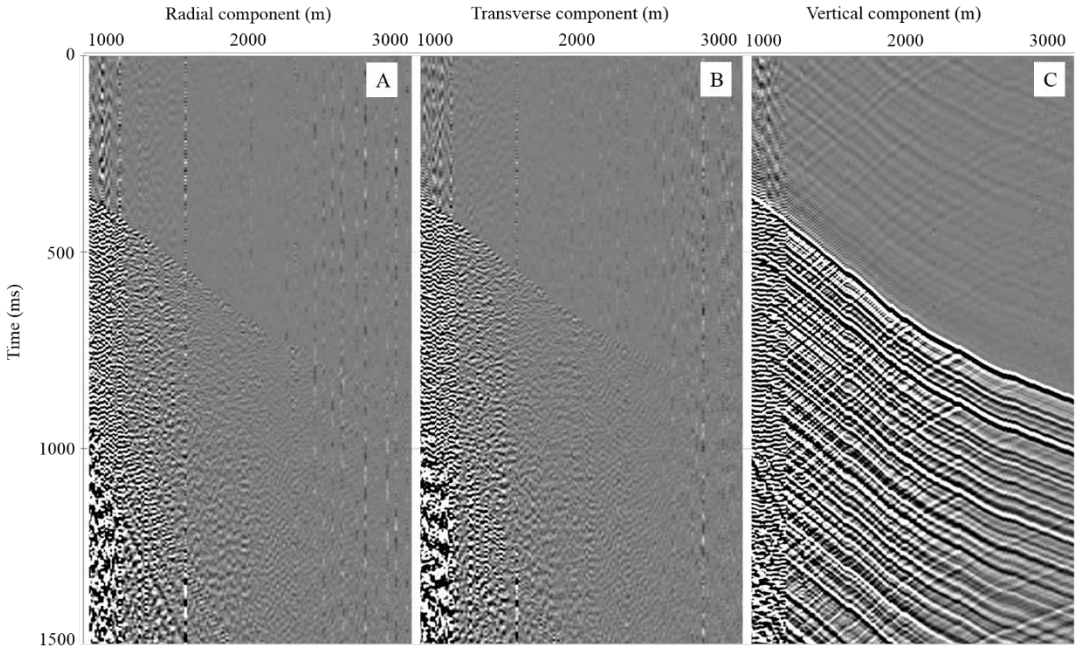

Figure 5-1. ME1 raw zero-offset field VSP data. The right panel (C) shows the vertical component (Z), and the middle (B) and left (A) panels show the horizontal (X and Y) components, respectively.

5.3 Apparent attenuation from field VSP data

The workflow for the estimation of the apparent attenuation from the field VSP data is described in Chapter 3. As the geological settings and VSP data characteristics in the Middle East are different from those in the NWSWA, all of the results (including the intermediate ones) are provided below.

To prepare the data for analysis I suppressed all waves, except the downgoing direct waves, by employing FX deconvolution (Hauge, 1981; Canales, 1984) (see Figure 5.2). First, a static correction is applied to the first arrival direct waves to flatten them. Upgoing waves are supressed using FX deconvolution as random noise, thus removing them from the seismogram. It is assumed that FX deconvolution has been applied correctly when, for example, the upgoing energy is suppressed without damaging the shape of the downgoing waves. The residuals are obtained by subtracting raw data from the data after FX deconvolution is applied. Amplitudes are also compensated for by the wavefront divergence.

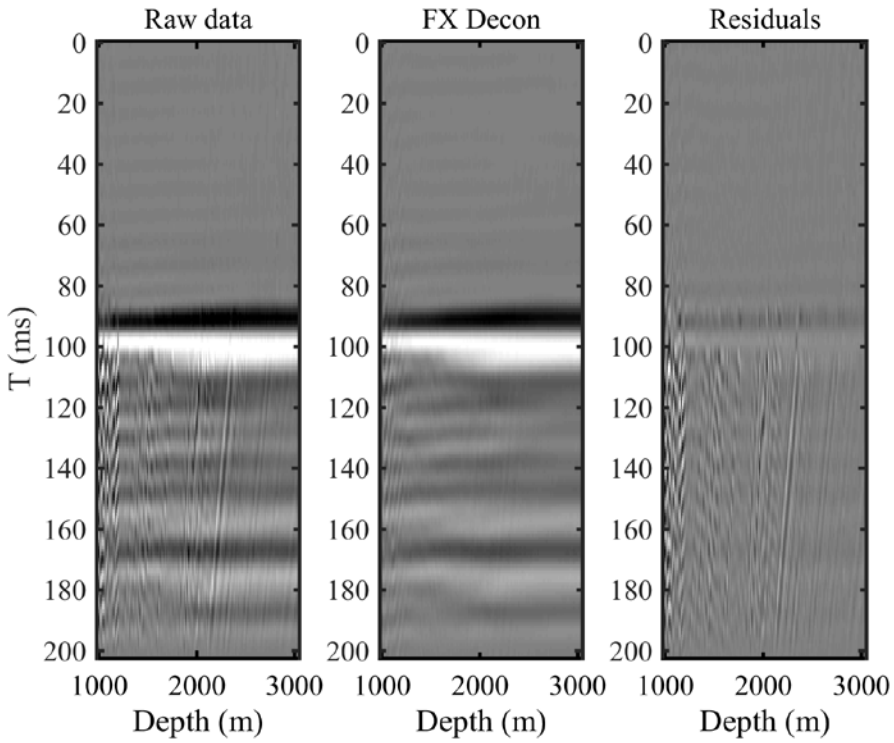

Figure 5-2. ME1 field data. Results of the suppression of upgoing waves using FX deconvolution. The left panel shows the original data, the middle panel shows the results of FX deconvolution and the right panel shows the difference.

The second stage is to transform time-domain traces to amplitude spectra by applying an FFT in the time window over the direct wave. Several studies have produced different window assessments, from a window of 50–100 ms (Shaw, Worthington, White, Andersen and Petersen, 2008) to a window of 1,000 ms (Blias, 2011). This case uses a time window of 300–400 ms, as it provides an acceptable spectral resolution. However, records with a poor S/N ratio are excluded. The influence of the interference along upgoing waves is reduced further, smoothing the spectra with depth using a running average (window size = three traces x one sample), as shown in Figure 5.3.

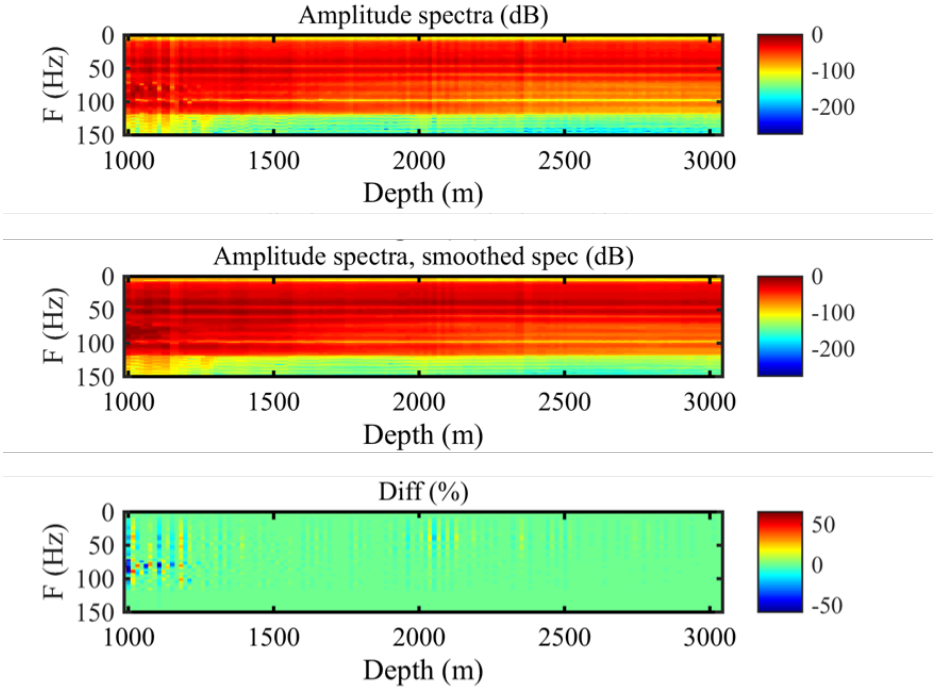

Figure 5-3. ME1 results of the estimation of amplitude spectra. Amplitude spectra (top), smoothed amplitude spectra (middle) and the relative difference (bottom) from field data.

After applying FX deconvolution, a Fourier transform is applied to the direct arrivals to calculate the amplitude spectra. The next phase uses a ‘sinc’ function to interpolate the amplitude spectrum, which smooths the amplitude spectrum of the direct wave. The divergence correction is applied as proposed by Newman (1973) (see Equation (2-2)). Newman’s formula describes the process of correcting the decay of amplitude for the direct wave. As velocity information is required for this correction, first break picks are used to estimate interval and (RMS) velocity.

Amplitude decay in the different frequencies is analysed at this stage, followed by the estimation of the centroid frequency and the square root of its variance. The square root of the variance can be defined as a ‘deviation’, as it has the same units. Figure 5-4 (top) indicates that the centroid frequency abruptly decreases at around 1,000 m, as displayed within the apparent Q values (Figure 5-5) measured on the field data, which range from over 62 Hz at the top of the well to 44 Hz at the bottom. Figure 5.4 (middle) shows the deviation of the centroid frequency in the same depth range. The spectra clearly narrow from approximately 25 Hz to 20 Hz. Figure 5-4 (bottom)

represents the corresponding amplitude decay curve at a depth interval of 1,000–2,100 m, while it stabilises between 2,200 m and 3,044 m. The stable nature of the curve indicates that there is no further attenuation. The overall amplitude decay is 1 dB as a result of the attenuation.

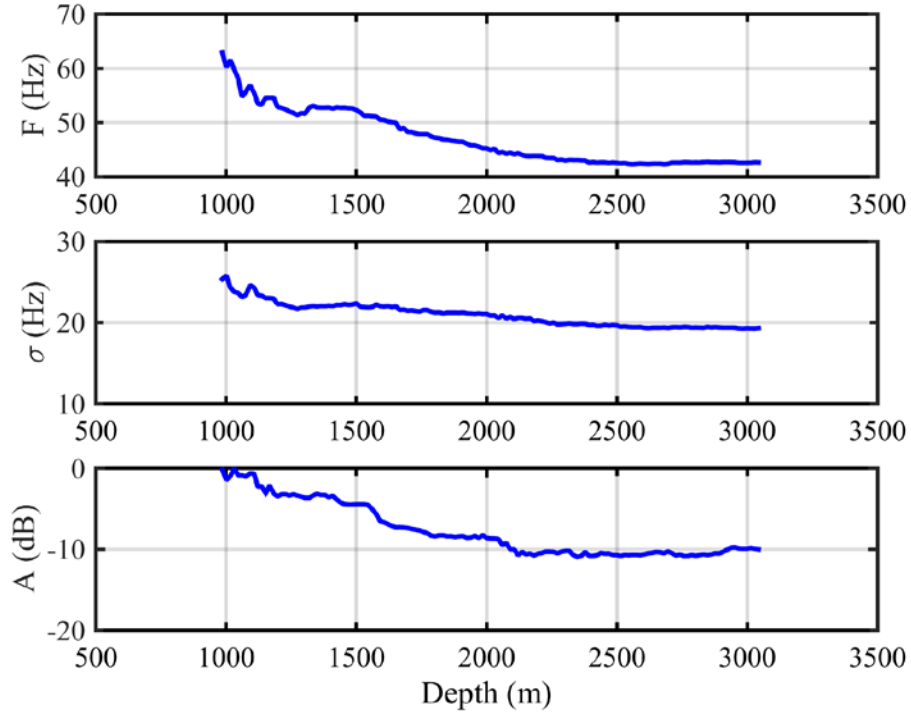

Figure 5-4. ME1 zero-offset VSP data analysis. Centroid frequency (top), deviation of the spectra (middle) and amplitude of the main peak in the wavelet (bottom), which is corrected for the divergence of the wavefront.

The centroid frequency at each depth is used to estimate Q values in the intervals, which are then used to compensate for attenuation in the amplitude decay curve. The centroid frequency decay curve is split into five interval layers, taking into account the lithology boundaries and the slope of the curve (see Figure 5.5). This leads to the application of the modified CFS method, which allows estimation apparent attenuation. It is clear that, from a centroid frequency decay of ~8 Hz, the energy decay almost doubles in the interval of 1,001–1,198 m. From this, I can estimate an apparent attenuation (Q) of 16 for the depth range of 1,000-1,198 m..

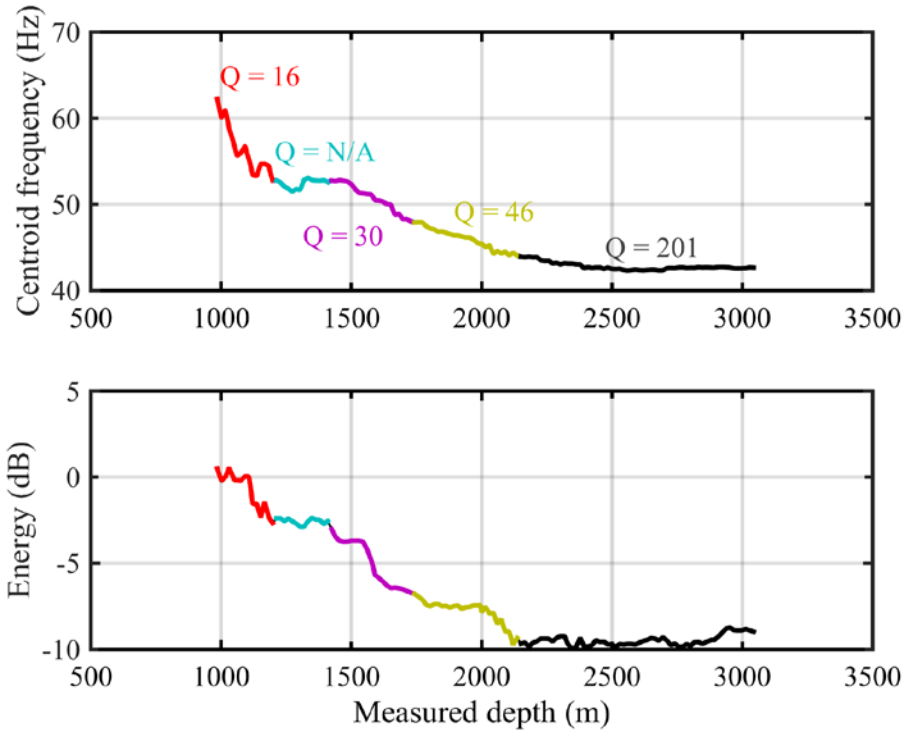

Figure 5-5. ME1 centroid frequency decay curve split into five intervals. Intervals are defined by their linear behaviour in the top display. Lower display show energy decay.

5.4 Synthetic VSP data analysis for estimating the contribution of scattering attenuation

The reasonable sonic and density log coverage of ME1 is used to build the elastic model, which is upscaled to a 1 m regular grid by employing Backus averaging (Backus, 1962). It is deduced that the averaging to a 1–2 m layer thickness will not generate any measurable effect on the amplitudes of direct waves in the synthetic seismograms. The missing density can be reconstructed using Gardner's equation (Gardner, Gardner and Gregory, 1974).

The elastic model logs are shown in Figure 5.6. The shallow carbonate layers in the 250–550 m interval depict appreciable contrasts in the elastic properties (Vp, Vs and density). Significant variation can also be observed within the depth intervals of 1,000–1,600 m and 2,000–2,500 m. Synthetic seismograms are computed for a walk-away VSP geometry using the MIT OASES global matrix algorithm code (Schmidt and Jensen, 1985). Principal modelling parameters are shown in Table 5-1.

Table 5-1. Principle parameters for the modelling. Free surface was not taken into account.

Frequency range	0.1–250 Hz
Receiver interval	0–3,270 m
Receiver step	10 m
Source offsets	50–4,525 m
Source step	25 m
Record length	16 s (to avoid wraparound)
Sampling interval	1 ms
Sampling interval	from first arrivals of zero-offset VSP data

The zero-offset VSP is a subset of the walk-away VSP synthetic data. It is used to analyse the scattering attenuation, while the entire walk-away VSP dataset is used to estimate cumulative anisotropy in the overburden.

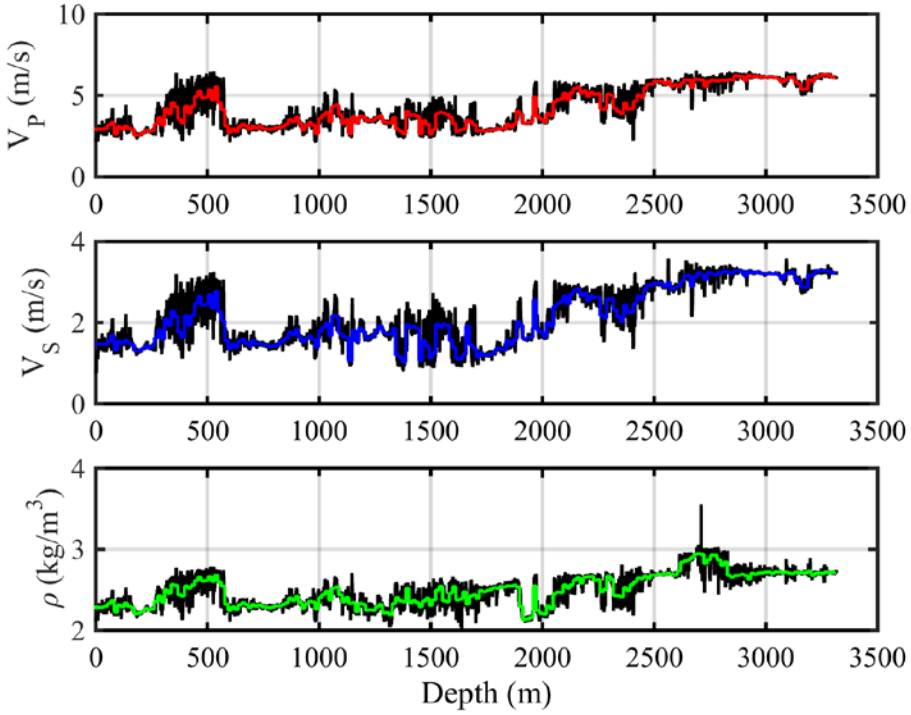

Figure 5-6. ME1 elastic model. The black curve represents log data, and the coloured curves are the results of Backus averaging.

To evaluate the amplitude decay and scattering attenuation as a result of 1D scattering, the same workflow is implemented to estimate the quality factor, as described above in conjunction with the field data analysis.

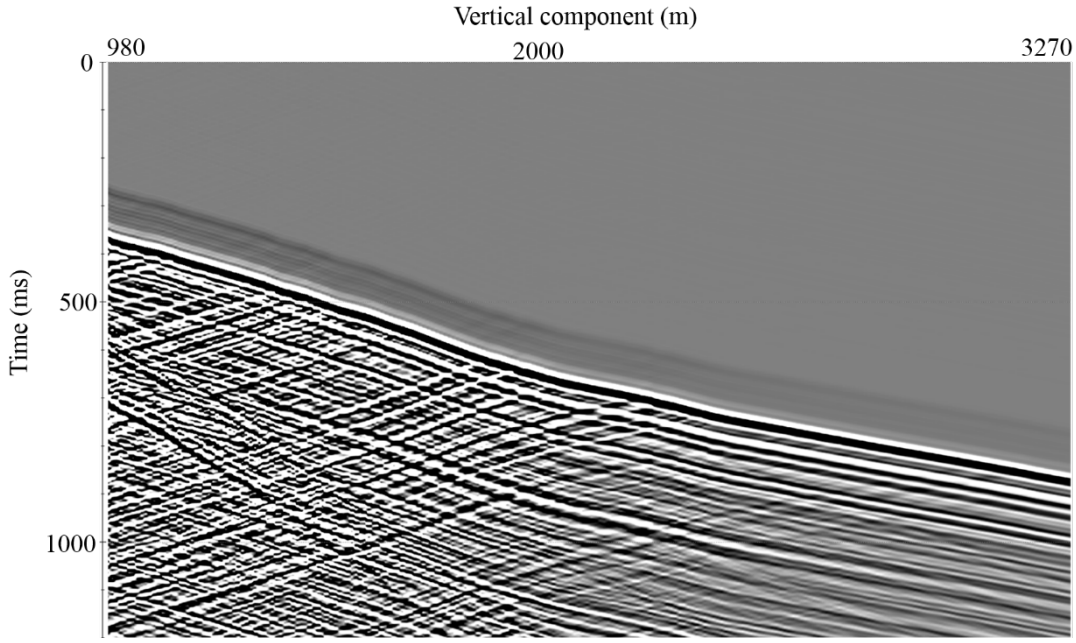

Figure 5-7. ME1 synthetic zero-offset VSP seismogram.

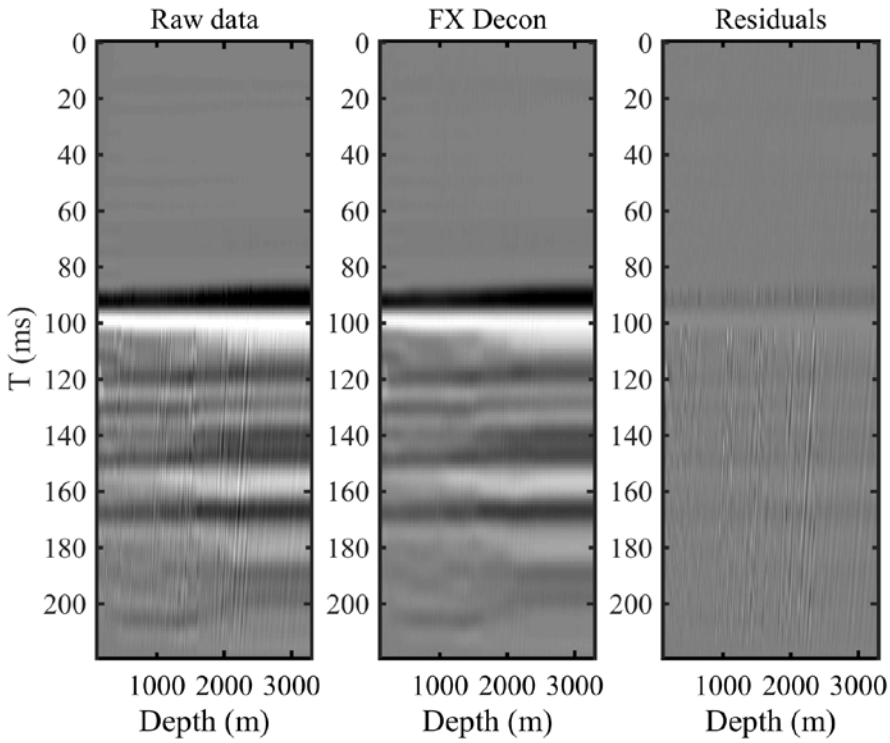

Figure 5-8. ME1 synthetic data. Results of the suppression of upgoing waves using FX deconvolution. The left panel shows the synthetic data, the middle panel shows the results of FX deconvolution and the right panel shows the difference.

Upon review, a significant variation of the wavelet at around 2,000 m is evident in both the field and synthetic data. This points towards an increase in the width of the wavelet in both datasets (see Figure 5.2 and Figure 5.8).

The primary result of $Q_{\text{scattering}}$ is shown in Figure 5.9. Obtained Q values are predicted to reflect scattering attenuation as they were generated by the synthetic seismogram using an elastic model for all layers.

In the interval at about 365–600 m, the centroid frequency decays to approximately 12 Hz while wave energy decays by a factor of two. In the upper part of the well, $Q_{\text{scattering}}$ attenuation reaches a maximum value of 46.

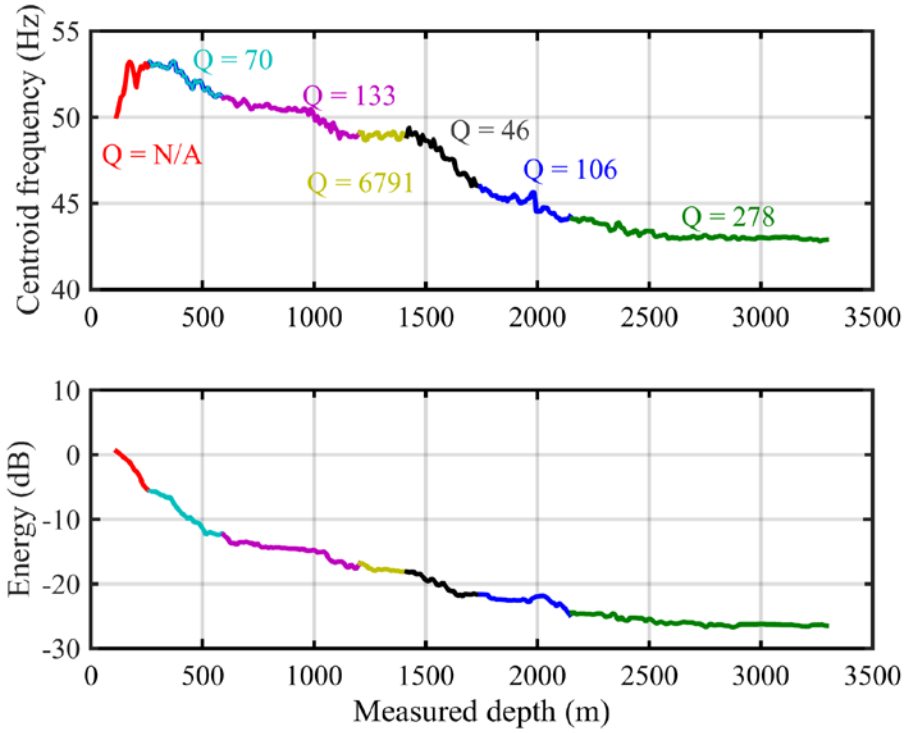

Figure 5-9. The centroid frequency and energy decay curve are displayed, and Q values are plotted above the top curve.

Figure 5.10 shows the centroid frequency and amplitude decay curves. The field (red) and synthetic (blue) data curves are identical at the bottom of the well, representing only attenuation scattering. The red curve shifts down compared to the blue curve, which indicates that the attenuation effect was greater in the field data (red curves). This is different in the upper part of the well, likely due to the casing effect.

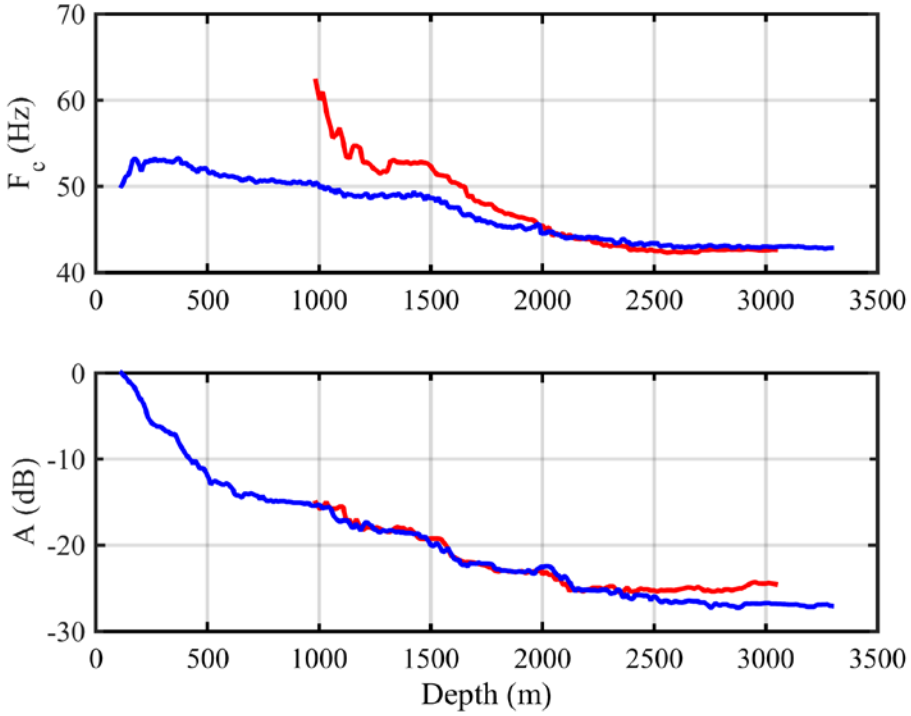

Figure 5-10. Amplitude and centroid frequency decay, field data (red curve) and synthetic data (blue curve).

Figure 5.11 (top) displays the variation of *Q* with depth. The blue curve represents the apparent attenuation from the VSP data. The red curve represents scattering attenuation from the modelling. An anomalous high value (1,000–1,200 m) is evident in the field data and is assumed to be due to changes in the well condition. The blue and red curves exhibit similar behaviour. In the shallow part of the well, scattering is considered important.

Figure 5.11 (bottom) confirms that strong attenuation arises because of a significant contrast in elastic properties. Scattering attenuation is significantly larger, with a value of 0.014 at a depth of 285–586 m, and 0.009 at a depth of 1,740–2,150 m.

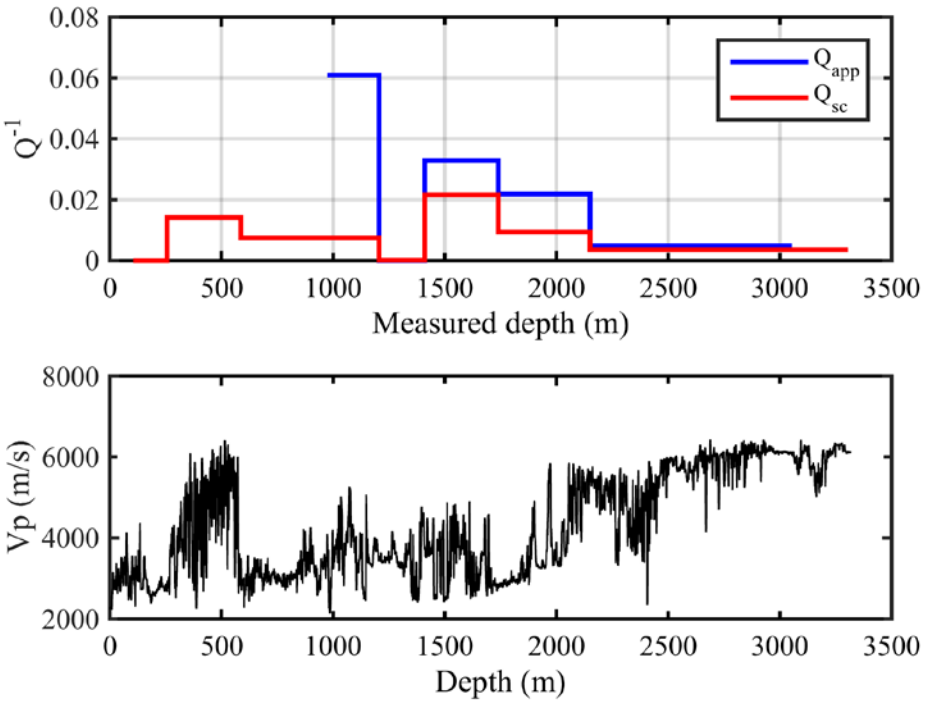

Figure 5-11. Middle East apparent (blue) and scattering (red) attenuation curves (top), Vp velocity (bottom).

5.5 Prediction of VTI anisotropy parameters

As seen in the previous sections, fine layering in the area of the ME1 well causes significant scattering attenuation. Thin layering can also cause long-wave seismic anisotropy, resulting in an apparent anisotropic medium with VTI symmetry (Backus, 1962). Usually this anisotropy is mild (Bakulin, 2003). However, in cases of strong compressibility contrasts between the layers, this bedding-induced anisotropy can become significant. Therefore, I anticipate that strong scattering attenuation may also associated with strong polar anisotropy.

Seismic anisotropy is a variation of elastic properties with the direction of propagation or polarisation of the wave (Sheriff, 2002). Horizontally layered media exhibit a special case of anisotropy; namely, these media exhibit vertical transverse isotropy or VTI. That is, such media are transversely isotropic about the vertical axis of symmetry, and the velocity only varies with the angle between the direction of propagation (or polarisation) and the vertical, but is independent of the azimuth of that direction.

In exploration seismology, it is convenient to express the degree of VTI anisotropy using anisotropy parameters γ, δ and ε proposed by Thomsen (1986). The parameter ε is used to characterise the relative difference between horizontal and vertical P-wave velocities:

$$\varepsilon = \frac{C_{11} - C_{33}}{2C_{33}}. \tag{5-1}$$

$$\gamma = \frac{C_{66} - C_{44}}{2C_{44}}. \tag{5-2}$$

$$\delta = \frac{(C_{13} + C_{44})^2 - (C_{33} + C_{44})^2}{2C_{33}(C_{33} - C_{44})}. \tag{5-3}$$

C_{ii} are components of the elastic modulus matrix constructed from the stiffness tensor using Voigt's notation (Thomsen, 1986).

To describe a VTI medium, P- and S-wave vertical velocities are also required:

$$V_{P0} = \sqrt{\frac{C_{33}}{\rho}}; \tag{5-4}$$

and

$$V_{S0} = \sqrt{\frac{C_{44}}{\rho}}. \tag{5-5}$$

Alkhalifah and Tsvankin (1995) introduce the anellipticity defined η as:

$$\eta = \frac{\varepsilon - \delta}{1 + 2\delta}, \tag{5-6}$$

The anellipticity parameter describes the deviation of a P-wavefront from an ellipse and the deviation of an SV-wavefront from a circle. Alkhalifah (1997) demonstrated that all time-related processing of P-waves, including NMO, dip moveout, and poststack and prestack time migration, requires knowledge of the small-offset NMO velocity and η alone. Alkhalifah and Tsvankin (1995) introduced an approximation for the traveltime curve of a reflected wave in the VTI medium:

$$T = \sqrt{T_0^2 + \frac{x^2}{{V_{NMO}}^2} - \frac{2\eta\, x^4}{{V_{NMO}}^2\,(\,T_0^2\,{V_{NMO}}^2 + (1+2\eta)x^2\,)}}. \tag{5-7}$$

where T and T_0 are the traveltime and traveltime at zero offset, respectively. x is offset, V_{NMO} *is* moveout velocity and η is the unellipticity parameter. In this approximation, η is the main parameter describing the seismic anisotropy (Alkhalifah and Tsvankin, 1995). This essentially means that, for a moderate range of offsets, η will be one of the main property affecting traveltime curves and consequently, imaging.

5.5.1 Estimation of interval anisotropy parameters from Backus averaging

To estimate interval anisotropy parameters, the thickness of the layer is increased by applying the Backus formulas (Backus, 1962). These formulas are employed to estimate seismic anisotropy from thick layers by using log data with Backus averaging to 15 m. Figure 5.12 shows the results of the calculated Thomsen's anisotropy parameters and the unellipticity parameter η. Strong anisotropy is observed in the uppermost section, which is composed of carbonate layers of high impedance contrasts.

Significant anisotropy can be observed in large intervals of this well where a strong contrast of properties occurs. High-contrast carbonate layers at the top of the section display strong anisotropy, a low positive value of γ (26%) and an intermediate positive value of η (~20%). The δ curve does not exhibit any variation and is therefore considered stable. At a depth of approximately 1,508 m, γ and η display a large positive magnitude of ~17% and 29% respectively. ε shows a lower positive value, and δ depicts a large negative value of ~10%.

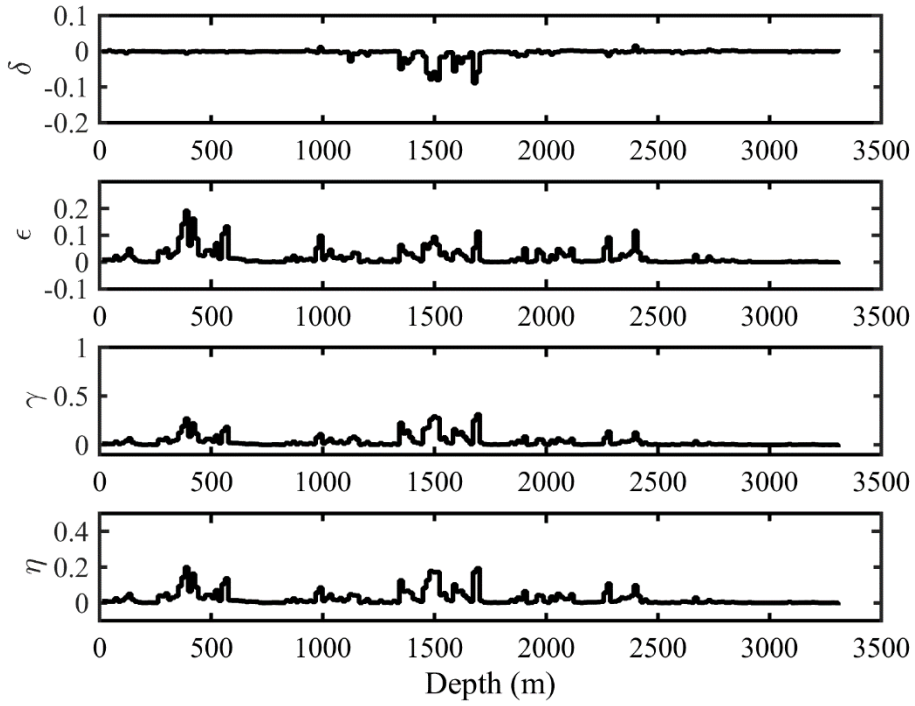

Figure 5-12. Middle East Thomsen's anisotropy parameters from Backus averaging.

5.5.2 Layer-induced cumulative anisotropy in the overburden from a synthetic walk-away vertical seismic profile analysis

To verify the anisotropy estimates from Backus averaging, travel time curves of the direct arrival wave acquired for the synthetic walk-away VSP are used. Figure 5.13 shows synthetic walk-away data. The wavefield was recorded by keeping the receiver at a depth of 960 m. The travel time curves of the direct wave were generated by applying the anisotropy moveout equation (5-7) from Alkhalifah and Tsvankin (1995). Travel time *with* η is represented by a blue curve for isotropic media, and a red curve for anisotropic media. The direct wave indicates an anisotropy moveout with η = 0.07 and V_{NMO} = 3.411 m/s. The prediction from Backus averaging shows an identical value of η.

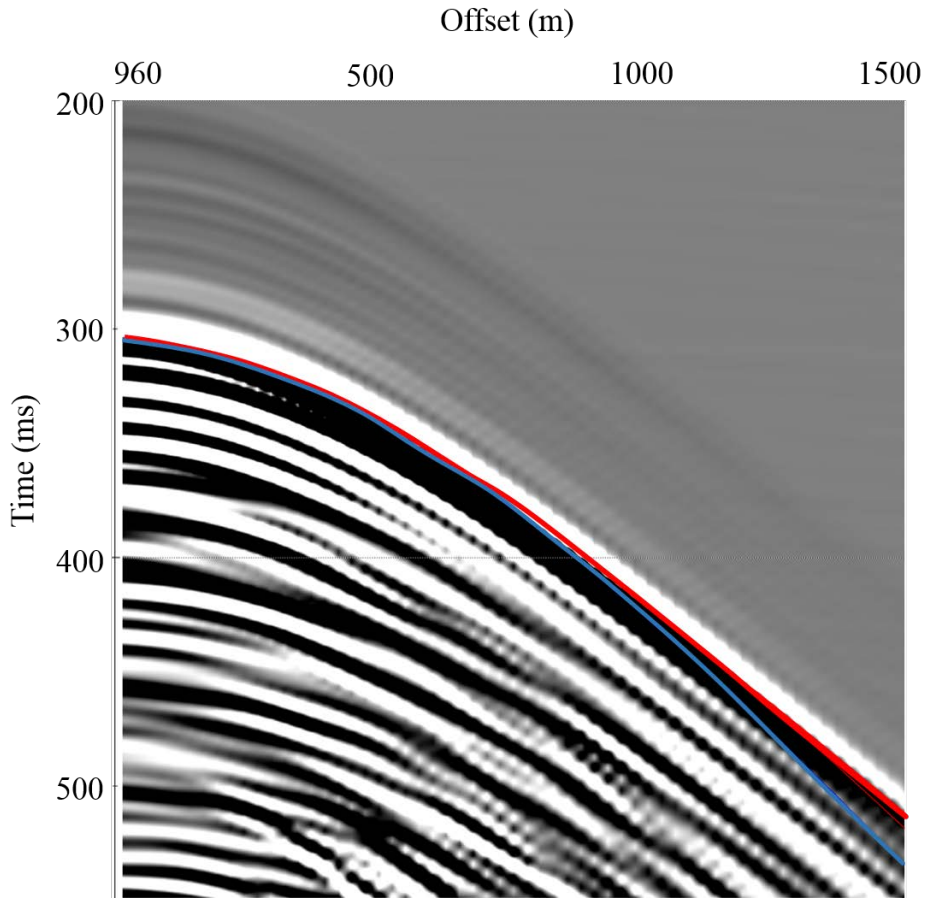

Figure 5-13. ME1 walk-away VSP data for the 960 m receiver level. The red curve is the fitted direct wave travel times for the anisotropic model with η = 0.07, and the blue curve corresponds to the isotopic case.

To quantify cumulative V_{nmo} and η from synthetic data, first breaks are automatically picked for the whole depth range. In the next step, I fitted the Alkhalifa and Tsvankin equation to these travel time curves. The resulting V_{nmo} and η are shown in Figure 5.14 (blue curves). The presence of a velocity gradient can also result in the anellipticity of the travel time curve. The velocity gradient in the ME1 well is estimated by fitting a straight line to the log Vp data, the results of which are used to predict the anellipticity (seen in the red curve in the bottom panel). It is clear that the anellipticity of the traveltime curves is caused almost entirely by the layering-induced anisotropy, with η reaching values of ~0.1. This is a significant level of VTI anisotropy, which may affect seismic imaging.

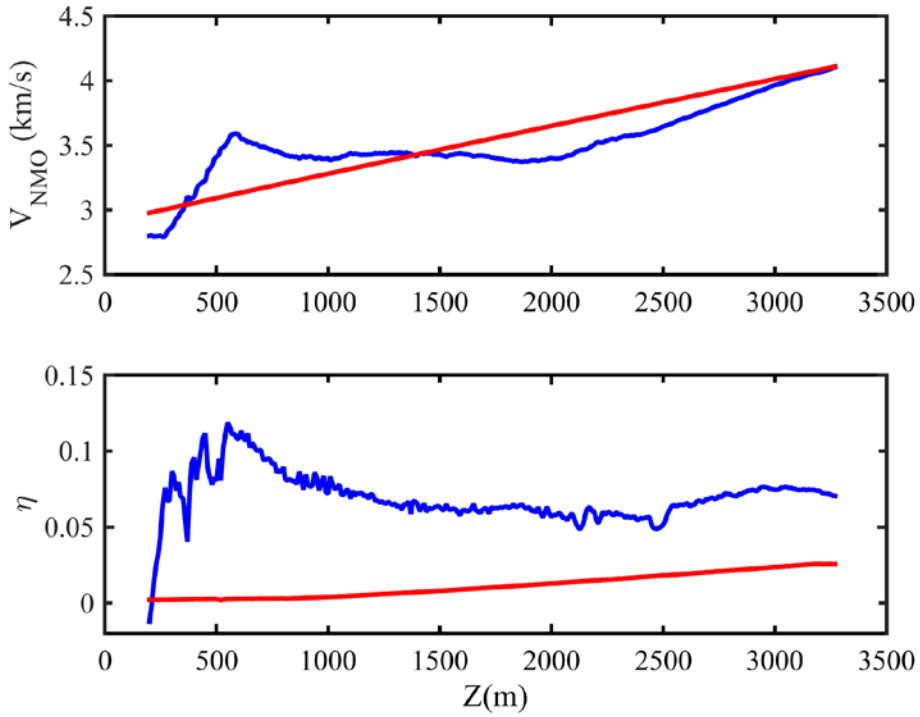

Figure 5-14. Middle East Vnmo and cumulative η from walk-away VSP data.

5.6 Layering-induced anisotropy and attenuation—principal observations

To investigate the causes and magnitude of the seismic attenuation and anisotropy affecting seismic image quality in the presence of a thinly layered carbonate overburden, a field dataset composed of VSP and log data from a well in the Middle East was studied.

Zero-offset VSP data were used to investigate apparent attenuation along the well. In figure 5-5, the magnitude of the attenuation corresponded to a Q value range of 16–201. The main part of the section had a Q value of 40 and below. This means that seismic attenuation has a very significant effect on seismic image quality.

To investigate the contribution of scattering to apparent attenuation, seismic modelling was conducted on the log-based fine-layered model. Attenuation arising from purely 1D scattering was as low as $Q_{sc} = 46$ due to the strong contrast between the elastic properties of evaporites and relatively soft sediments.

The scattering attenuation and apparent attenuation curves exhibited a similar depth profile in figure 5-11, which may indicate that the discrepancy between scattering and apparent attenuation can be attributed to both intrinsic attenuation and underestimation of the scattering component by not taking into account scattering on 3D inhomogeneities.

Backus averaging and seismic modelling (VSP geometry) were used to estimate anisotropy parameters. This demonstrates that the same layering may be responsible for a significant portion of VTI anisotropy. The seismic anisotropy magnitude corresponded to η values exceeding 0.1.

However, further research is required to obtain detailed insights into the exact correlation between layering-induced attenuation and anisotropy. Due to the noteworthy effect of large values of attenuation and anisotropy on seismic image quality, I propose that both phenomena should be accounted for during data acquisition for planning and processing.

Chapter 6. Conclusions

This chapter summarises the research outcomes and presents the conclusions drawn from the research in relation to the research objectives.

6.1 Conclusions

The main objectives of this study were to use a robust methodology to estimate the vertical and lateral distribution of seismic attenuation from borehole seismic data, and to evaluate the relative contribution of anelastic absorption and scattering. To analyse the data a robust workflow was constructed to understand the behaviour and nature of the spatial distribution of attenuation in two different regions, based on a modified CFS method. This was followed by an estimation of the contribution of scattering from full-wave synthetic VSP data (for selected wells). The robust technique used in this research can be applied in future investigations across a wide spectrum of locations and formations.

Previous studies have been limited to one well or a small number of wells, thereby providing limited information. In this research, I investigated the behaviour of seismic attenuation using a significant number of wells with zero-offset VSP and a suite of well logs from two areas: the North West Shelf of Western Australia and the Middle East. The dataset for the NWSWA was built from borehole data that were publicly available from the Department of Mines and Petroleum of Western Australia, with a total of 37 wells used in the study. For the Middle East the dataset comprised four wells, however, after initial screening, the study focused on only one well with a proper set of seismic and well log data. The research outcomes showed interesting results and cleared several misconceptions, as I summarise below.

For the evaluation of the relative contribution of different anelastic absorption and scattering, it is necessary to separate intrinsic attenuation and scattering in order to understand the behaviour of the observed attenuation. This is achieved by first generating synthetic VSP seismograms from sonic and density log data. Scattering attenuation is then computed by applying the attenuation estimation algorithm to these synthetic seismograms. The obtained attenuation values are subtracted from the

apparent attenuation measured from the field data to obtain the anelastic absorption. Hence, the contribution of each mechanism is evaluated.

The VSP data from the 37 wells from the NWSWA and the synthetic VSP data testing revealed that the reliability of the estimation of the apparent attenuation may be affected by a number of factors related to well design, VSP data acquisition conditions and geological media. The method I used to estimate the apparent attenuation relies on two principal assumptions: 1) waves are propagating along a vertical borehole drilled in a horizontally layered medium; and 2) the source and receiver conditions are stable. Serious violations of these assumptions lead to problems with the *Q* estimates.

Well design-related issues include changing the number of casing strings, which alters the coupling conditions of the VSP tool, and the deviation of a well from a vertical trajectory.

The other principal problem is the presence of 3D inhomogeneities in the vicinity of the well bore (such as steeply deeping faults or diffractors). Often, unavoidable interference of the downgoing waves, along with the secondary wavefield generated by these inhomogeneities likely to contribute to unreliable attenuation estimates.

To detect the presence of these problems, I inspected the *Q* estimates from the amplitude decay and centroid frequency decay trends simultaneously. if the *Q* estimates from these trends reflected fundamentally different behaviour, the well was excluded from the study.

In this study, I observed a range of *Q* values from 16 and above. The upper limit of *Q* values is impossible to estimate, as the reliability of *Q* estimates decreases with the increased value of *Q*, and it is limited by the sensitivity and spatial resolution of the method. It is not possible to estimate $Q > 500$ robustly from the field VSP data.

6.1.1 North West Shelf of Western Australia

In the NWSWA case study, all intervals were divided into three types in order to try to understand the spatial distribution of attenuation; low attenuation (Q value of 200 and above); moderate attenuation: (*Q* values between 65 and 200); and high attenuation (*Q* values of 65 and below). For the distribution of interval *Q* values undertaken, both the vertical and lateral analysis revealed several significant observations.

By analysing the distribution of *Q* values throughout the area, I found that 65% of all observations showed moderate attenuation, 25% high attenuation, and the remaining 10% low attenuation. Based on the four stratigraphic intervals in Table 4-3, the first observation revealed that from Interval 1, all six Q^{-1} values were low with attenuation often not evident near the ground surface. In Interval 2, the majority (82.60%) of Q^{-1} values were moderate, with just 8.70% being low and high. In Interval 3, there were more high (45.45%) Q^{-1} values than moderate (40.91%), and proportionally more low values (13.64%) than in Interval 2. Interval 4 reflected that the majority (58.34%) of Q^{-1} values were high, with just one low value (8.33%). The second observation demonstrated that apparent attenuation values estimated from Areas 1-5, taking into consideration 72 of the value Q^{-1} over all of the intervals, reflected that almost half (32, 50.79 %) of the Q^{-1} values indicated moderate apparent attenuation, with more high (30.16%) values than low (19.05%).

One objective of the study was to examine the variation of attenuation with depth. However, since there are significant dips in the area and the wells cover a large area, different formations appear at different depths in different wells. Hence, I attempted to examine the behaviour of the attenuation as a function of geologic age as a proxy for the burial depth. It was observed that as a general trend, attenuation shows an increase with geologic age as well as depth, with deeper and older formations showing a larger spread of attenuation (inverse *Q*) values. This observation was unexpected, as conventional wisdom and anecdotal experience suggests that young and soft sediments should have higher attenuation. However, as my observations were obtained by applying a consistent methodology to a large number of wells, I believe it is significant. Therefore, further studies in different areas are required in order to understand the typical behaviour of attenuation.

Two principal mechanisms were identified as being responsible for the attenuation: scattering and absorption. The use of seismic modelling to study the contribution of 1D scattering (using MIT OASES reflectivity code) showed that in most cases, scattering *Q* was over 200. This means that scattering did not cause significant seismic attenuation in the NWSWA data.

It was noted that there were several special cases where this was not true. If severe contrasts between the earth materials are present (stacks of coal seams interlaid with stiff sandstones or stiff carbonate rocks mixed with softer materials), scattering attenuation may be the dominant mechanism. For the NWSWA, this could occur in the carbonate section and has been previously reported from a synthetic VSP study (Pevzner et al., 2015), that was conducted using the Madeleine 1 well; however, no field VSP data confirming this was available for this study.

At the beginning of the research project, I expected that the relationship between the lithology and the value of attenuation would be unique, and that each formation would have a specific range of values in a similar manner to velocity. This would enable me to use a relatively sparse set of wells with the VSP data available to study the regional distribution of seismic attenuation. However, the spatial variability of the seismic attenuation is significant, so only some trends and special relationships were apparent but uncertain. For example, I observed that young sediments (younger than the Trealla Formation) exhibit very little attenuation (Q >200).

In summary, in the NWSWA, young shallow sediments have shown low attenuation, and hence have limited influence on seismic image quality (and reflection amplitudes) for deeper intervals. The range of the *Q* values of the formations varies from low to high, with a general trend of increasing seismic attenuation with depth. In addition, the behaviour of seismic attenuation in old sediments was found to be more complex**.** Scattering attenuation was found to be insignificant, unless abnormally high contrasts between adjacent layers were present.

6.1.2 Middle East

The magnitude of the apparent attenuation observed in the ME1 (this is a pseudonym, as the true name of the well cannot be disclosed) dataset showed *Q* values in the range of 16 to 201, with the major part of the section having a *Q* value of 40 and below. This indicates that seismic attenuation has a significant effect on seismic image quality in the area. Attenuation arising from purely 1D scattering was shown to be as low as $Q_{sc} = 46$ as obtained from modelling. The presence of a strong contrast in elastic properties between evaporites and relatively soft sediments was responsible for this high scattering attenuation. For instance, in the ME1 well, it was observed that carbonate layers can cause significant attenuation. Further, such a contrast between alternating layers is expected to cause significant layering-induced VTI anisotropy.

To evaluate the magnitude of the VTI anisotropy caused by layering, the VTI anisotropy was calculated using Backus averaging and seismic modelling (walk- away VSP geometry). The result demonstrated the presence of significant VTI anisotropy caused by the same layering, with seismic anisotropy magnitude corresponding to η values exceeding 0.1. However, further research is required in order to obtain detailed insights into the exact correlation between the layering-induced attenuation and anisotropy. Given the noteworthy effect on seismic image quality rendered by large values of attenuation and anisotropy, it is proposed that both phenomena should be accounted for during the planning of data acquisition and processing.

Bibliography

Aki, K., and B. Chouet, 1975, Origin of Coda Waves - Source, Attenuation, and Scattering Effects: Journal of Geophysical Research, **80**, 3322-3342.

Aki, K., and P. Richards, 1980, Quantitative Seismology: Theory and Methods: Volume I: WH Freeman & Co.

Aki, K., and P. Richards, 1980, Quantitative seismology: Theory and methods: San Francisco.

Al-Husseini, M., 2000, Origin of the Arabian Plate structures: Amar collision and Najd rift: Geoarabia-Manama-, **5**, 527-542.

Al Sayari, S. S., and J. G. Zotl, 1978, Quaternary Period in Saudi Arabia. 1. Sedimentological, hydrogeological, hydrochemical, geomorphological, and climatological investigations in central and eastern Saudi Arabia: Springer Verlag.

Alkhalifah, T., 1997, Velocity analysis using nonhyperbolic moveout in transversely isotropic media: Geophysics, **62**, 1839-1854.

Alkhalifah, T., and I. Tsvankin, 1995, Velocity analysis for transversely isotropic media: Geophysics, **60**, 1550-1566.

Amundsen, L., and R. Mittet, 1994, Estimation of phase velocities and Q-factors from zero-offset, vertical seismic profile data: Geophysics, **59**, 500-517.

Asch, M., W. Kohler, G. Papanicolaou, M. Postel, and B. White, 1991, Frequency Content of Randomly Scattered Signals: Siam Review, **33**, 519-625.

Ayres, M., M. Bilal, R. Jones, L. Slentz, M. Tartir, and A. Wilson, 1982, Hydrocarbon habitat in main producing areas, Saudi Arabia: AAPG bulletin, **66**, 1-9.

Backus, G. E., 1962, Long‐wave elastic anisotropy produced by horizontal layering: Journal of Geophysical Research, **67**, 4427-4440.

Barber, P., Year, The Exmouth Plateau deep water frontier: a case history: The North West Shelf, Australia: Proceedings Petroleum Exploration Society Australia Symposium, 173-188.

Batzle, M., R. Hofmann, and D. Han, 2006, Heavy oils—seismic properties: The Leading Edge, **25**, 750-756.

Bentley, J., Year, The Candace Terrace—a geological perspective: The North West Shelf, Australia: Proceedings of Petroleum Exploration Society, Australia Symposium, Perth, 157-171.

Blias, E., Year, Optimization Approach to Q-factor Estimate from VSP Data: 73rd EAGE Conference & Exhibition.

Blias, E., 2011, Optimization Approach to Q-Factor Estimation From VSP Data: Google Patents.

Bradshaw, M., J. Bradshaw, A. Murray, D. Needham, L. Spencer, R. Summons, J. Wilmot, and S. Winn, Year, Petroleum systems in West Australian basins: The Sedimentary Basins of Western Australia, Proceedings of the Petroleum Exploration Society of Australia Symposium, Perth, 93-118.

Bradshaw, M., A. Yeates, R. Beynon, A. Brakel, R. Langford, J. Totterdell, and M. Yeung, Year, Palaeogeographic evolution of the North West Shelf region: The North West Shelf, Australia: Proceedings of the Petroleum Exploration Society of Australia Symposium, Perth, 29-54.

Burridge, R., G. S. Papanicolaou, and B. S. White, 1988, One-dimensional wave propagation in a highly discontinuous medium: Wave motion, **10**, 19-44.

Canales, L. L., Year, Random noise reduction: 1984 SEG Annual Meeting, Society of Exploration Geophysicists.

Castagna, J. P., M. L. Batzle, and R. L. Eastwood, 1985, Relationships between compressional-wave and shear-wave velocities in clastic silicate rocks: Geophysics, **50**, 571-581.

Cheng, P., and G. F. Margrave, 2011, Estimation of Q: a comparison of different computational methods.

Cheng, P., and G. F. Margrave, Year, Q estimation by a match-filter method: 2012 SEG Annual Meeting, Society of Exploration Geophysicists.

Coleman, R. G., 1974, Geologic background of the Red Sea: Springer.

Dasgupta, R., and R. A. Clark, 1998, Estimation of Q from surface seismic reflection data: Geophysics, **63**, 2120-2128.

Delfos, E., and R. DEDMAN, 1988, The petroleum potential of the Peedamullah Shelf: The North West Shelf, Australia: Proceedings of the Petroleum Exploration Society of Australia, Perth, 147-156.

Dietrich, M., and M. Bouchon, 1985, Measurements of attenuation from vertical seismic profiles by iterative modeling: Geophysics, **50**, 931-949.

Dunkin, J. W., 1965, Computation of modal solutions in layered, elastic media at high frequencies: Bulletin of the Seismological Society of America, **55**, 335-358.

Engelhard, L., 1996, Determination of seismic-wave attenuation by complex trace analysis: Geophysical Journal International, **125**, 608-622.

Forman, D. J., D. W. Wales, and R. V. Burne, 1981, Geological evolution of the Canning Basin, Western Australia: Australian Government Pub. Service.

Fryer, G. J., and L. N. Frazer, 1987, Seismic waves in stratified anisotropic media—II. Elastodynamic eigensolutions for some anisotropic systems: Geophysical Journal International, **91**, 73-101.

Fuchs, K., and G. Müller, 1971, Computation of synthetic seismograms with the reflectivity method and comparison with observations: Geophysical Journal International, **23**, 417-433.

Futterman, W. I., 1962, Dispersive body waves: Journal of Geophysical Research, **67**, 5279-5291.

Gal′perin, E. I., 1974, Vertical seismic profiling: Society of Exploration Geophysicists.

Galvin, R., T. Müller, R. Pevzner, and B. Gurevich, 2013, Estimation of Scattering Attenuation from Zero-offset VSP Data: CO2CRC Otway Project Case Study.

Ganley, D., and E. Kanasewich, 1980, Measurement of absorption and dispersion from check shot surveys: Journal of Geophysical Research: Solid Earth (1978–2012), **85**, 5219-5226.

Gardner, G., L. Gardner, and A. Gregory, 1974, Formation velocity and density-the diagnostic basics for stratigraphic traps: Geophysics, **39**, 770-780.

Gladwin, M. T., and F. Stacey, 1974, Anelastic degradation of acoustic pulses in rock: Physics of the Earth and Planetary Interiors, **8**, 332-336.

Goloshubin, G., and I. Bayuk, Year, Application of amplitude and spectral ratio methods for estimation of attenuation from VSP: 2010 SEG Annual Meeting, Society of Exploration Geophysicists.

Group, A. N. W. S. S., Year, Deep reflections on the North West Shelf: changing perceptions of basin formation: The Sedimentary Basins of Western Australia: Proceedings of the Western Australian Basins Symposium, Perth, WA, PESA, 63-76.

Gurevich, B., R. Pevzner, and A. Bona, Year, Anisotropy from Fine Layering in Coal- and Carbonate-rich Sequences: Well Log Based Modelling Study: Seismic Driven Reservoir Characterization and Production Management.

Haskell, N. A., 1953, The dispersion of surface waves on multilayered media: Bulletin of the Seismological Society of America, **43**, 17-34.

Hatton, L., M. H. Worthington, and J. Makin, 1986, Seismic data processing: theory and practice: Merlin Profiles Ltd.

Hauge, P. S., 1981, Measurements of attenuation from vertical seismic profiles: Geophysics, **46**, 1548-1558.

Hocking, R., Year, Regional geology of the northern Carnarvon Basin: The North West Shelf, Australia: Proc. Pet. Expl. Soc. Aust. Symp, 97-114.

Hu, W., 2011, Q tomography method: Google Patents.

Husseini, M. I., 1989, Tectonic and deposition model of late Precambrian-Cambrian Arabian and adjoining plates: AAPG bulletin, **73**, 1117-1131.

Jannsen, D., J. Voss, and F. Theilen, 1985, Comparison of methods to determine Q in shallow sediments from vertical reflection seismograms: Geophysical Prospecting, **33**, 479-497.

Keep, M., I. LONGLEY, and R. JONES, 2002, The Sumba enigma and its effect on Australia's northwest margin, *in* R. R. M. HILLIS, R.D.,, ed., The Evolution and Dynamics of the Australian Plate: Joint Special Publication of Geological Society of Australia and Geological Society of America.

Kennard, J., and J. B. Colwell, 1996, Petrel Sub-basin Study 1995-1996: Summary Report: Australian Geological Survey Organisation.

Kennett, B., 1974, Reflections, rays, and reverberations: Bulletin of the Seismological Society of America, **64**, 1685-1696.

Kennett, B., 2009, Seismic wave propagation in stratified media: ANU E Press.

Levin, F. K., and R. D. Lynn, 1958, Deep-hole geophone studies: Geophysics, **23**, 639-664.

Longley, I., C. Buessenschuett, L. Clydsdale, C. Cubitt, R. Davis, M. Johnson, N. Marshall, A. Murray, R. Somerville, and T. Spry, Year, The North West Shelf of Australia–a Woodside perspective: The Sedimentary Basins of Western Australia 3: Proceedings of the Petroleum Exploration Society of Australia Symposium, Perth, 27-88.

Makarynska, D., B. Gurevich, J. Behura, and M. Batzle, 2010, Fluid substitution in rocks saturated with viscoelastic fluids: Geophysics, **75**, E115-E122.

Markus, B., 1974, Spectral Analysis in Geophysics [M]: New York: Elsevier Scientific Publishing Company, **285**, 287.

Martín, N. W., A. Azavache, and M. S. Donati, Year, Indirect Oil Detection BY Using P-Wa V EAttenuation Analysis In Eastern Venezuela Basin: 1998 SEG Annual Meeting, Society of Exploration Geophysicists.

Matsushima, J., 2006, Seismic wave attenuation in methane hydrate‐bearing sediments: Vertical seismic profiling data from the Nankai Trough exploratory well, offshore Tokai, central Japan: Journal of Geophysical Research: Solid Earth (1978‐2012), **111**.

Matsushima, J., 2007, Seismic attenuation from VSP data in methane hydrate-bearing sediments: Exploration Geophysics, **38**, 29-36.

McClure, I., D. Smith, A. Williams, L. Clegg, and C. Ford, Year, Oil and gas fields in the Barrow Sub-basin: The North West Shelf, Australia. Proc. Pet. Expl. Soc. Aust. Symp, 371-390.

McDonal, F., F. Angona, R. Mills, R. Sengbush, R. Van Nostrand, and J. White, 1958, Attenuation of shear and compressional waves in Pierre shale: Geophysics, **23**, 421-439.

Menke, W., 1983, A formula for the apparent attenuation of acoustic waves in randomly layered media: Geophysical Journal of the Royal Astronomical Society, **75**, 541-544.

Metcalfe, I., 1995, Gondwana dispersion and Asian accretion: Journal of Geology Series B, **5**, 6.

Metcalfe, I., 2013, Gondwana dispersion and Asian accretion: tectonic and palaeogeographic evolution of eastern Tethys: Journal of Asian Earth Sciences, **66**, 1-33.

Mi, Y., and G. F. Margrave, 1998, Comparison of phase shift cascade and global matrix elastic wavefield modeling.

Mitchell, J. T., N. Derzhi, and E. Lichma, Year, Energy absorption analysis: A case study: Expanded Abstracts of 66th Annual Internat SEG Mtg, 1785-1788.

Molotkov, L., 1984, Matrix Method in the Theory of Wave Propagation in Layered Elastic and Liquid Media: Nauka, Leningrad.

Mory, A., Year, Regional geology of the offshore Bonaparte Basin: The North West Shelf Australia, Proceedings of Petroleum Exploration Society of Australia Symposium, Perth, 287-309.

Müller, T., B. Gurevich, and M. Lebedev, 2010, Seismic wave attenuation and dispersion due to wave-induced flow in porous rocks–A review Geophysics 2010; 75:; 1: A147-A164.

Müller, T., R. Pevzner, M. Lebedev, M. Urosevic, and a. B. G. R. Galvin, 2012, Estimation of attenuation from rig-source VSPs and log data, 84.

Müller, T. M., and S. A. Shapiro, 2001, Seismic scattering attenuation estimates for the German KTB Area derived from well‐log statistics: Geophysical research letters, **28**, 3761-3764.

Newman, P., 1973, Divergence effects in a layered earth: Geophysics, **38**, 481-488.

Nicoll, R. S., and C. B. Foster, 1994, Late Triassic conodont and palynomorph biostratigraphy and conodont termal maturation, North West Shelf, Australia: Journal of Australian Geology and Geophysics, **15**, 101-118.

O'Doherty, R., and N. A. Anstey, 1971, Reflections on AMPLITUDES*: Geophysical Prospecting, **19**, 430-458.

Oristaglio, M. L., 1985, A guide to current uses of vertical seismic profiles: Geophysics, **50**, 2473-2479.

Patton, S. W., 1988, Robust and least-squares estimation of acoustic attenuation from well-log data: Geophysics, **53**, 1225-1232.

Pevzner, R., R. J. Galvin, B. Gurevich, and T. M. Müller, Year, Estimation of attenuation from zero-offset VSP data: CO2CRC Otway Project case study: 2012 SEG Annual Meeting, Society of Exploration Geophysicists.

Pevzner, R., T. Muller, A. Bona, and B. Gurevich, 2015, Layer-induced scattering attenuation and VTI anisotropy-NW Shelf Australia synthetic study: ASEG Extended Abstracts, **2015**, 1-4.

Pevzner, R., T. Müller, A. Bona, and B. Gurevich, Year, Layer-induced Scattering Attenuation and VTI Anisotropy–NW Shelf Australia Synthetic Study: 2014 SEG Annual Meeting, Society of Exploration Geophysicists.

Picotti, S., and J. M. Carcione, 2006, Estimating seismic attenuation (Q) in the presence of random noise: Journal of Seismic Exploration, **15**, 165-181.

Pimentel, C., 2011, OVERBURDEN RELATED AMPLITUDE/FREQUENCY DECAY ANALYSIS USING VSP DATA (EXMOUTH PLATEAU)PhD Thesis, Curtin University.

Portsmouth, I., M. Worthington, and C. Kerner, 1993, A field study of seismic attenuation in layered sedimentary rocks—I. VSP data: Geophysical Journal International, **113**, 124-134.

Powers, R., L. Ramirez, C. Redmond, and E. Elberg, 1966, Geology of the Arabian peninsula: Geological survey professional paper, **560**, 1-147.

Pride, S. R., J. M. Harris, D. L. Johnson, A. Mateeva, K. T. Nihel, R. L. Nowack, J. W. Rector, H. Spetzler, R. Wu, and T. Yamomoto, 2003, Permeability dependence of seismic amplitudes: The Leading Edge, **22**, 518-525.

Prskalo, S., 2004, Application of relations between seismic amplitude, velocity and lithology in geological interpretation of seismic data: Journal of Hungarian Geomathematics, v. 2: ndash, **68**, 51.

Pujol, J., 2003, Elastic wave propagation and generation in seismology: Cambridge University Press.

Pujol, J., and S. Smithson, 1991, Seismic wave attenuation in volcanic rocks from VSP experiments: Geophysics, **56**, 1441-1455.

Pujol, J. M., E. Luschen, and Y. Hu, 1998, Seismic wave attenuation in metamorphic rocks from VSP data recorded in Germany's continental super-deep borehole: Geophysics, **63**, 354-365.

Quan, Y., and J. M. Harris, 1997, Seismic attenuation tomography using the frequency shift method: Geophysics, **62**, 895-905.

Raikes, S., and R. White, 1984, Measurements of Earth Attenuation from Downhole and Surface Seismic RECORDINGS*: Geophysical Prospecting, **32**, 892-919.

Rapoport, M. B., and V. I. Ryjkov, 1994, Seismic waves velocity dispersion: An indicator of hydrocarbons: Society of Exploration Geophysicists, Tulsa, OK (United States).

Ricker, N., 1953, The form and laws of propagation of seismic wavelets: Geophysics, **18**, 10-40.

Schmidt, D. L., D. G. Hadley, D. B. Stoeser, and S. Arabia, 1978, Late Proterozoic crustal history of the Arabian shield, southern Najd province, Kingdom of Saudi Arabia: US Geological Survey.

Schmidt, H., 2004, OASES version 3.1 user guide and reference manual: Department of Ocean Engineering, Massachusetts Institute of Technology.

Schmidt, H., and F. B. Jensen, 1985, Efficient numerical solution technique for wave propagation in horizontally stratified environments: Computers & Mathematics with Applications, **11**, 699-715.

Schmidt, H., and F. B. Jensen, 1985, A full wave solution for propagation in multilayered viscoelastic media with application to Gaussian beam reflection at fluid–solid interfaces: The Journal of the Acoustical Society of America, **77**, 813-825.

Schmidt, H., and G. Tango, 1986, Efficient global matrix approach to the computation of synthetic seismograms: Geophysical Journal International, **84**, 331-359.

Schoenberger, M., and F. Levin, 1974, Apparent attenuation due to intrabed multiples: Geophysics, **39**, 278-291.

Schoenberger, M., and F. Levin, 1978, Apparent attenuation due to intrabed multiples, II: Geophysics, **43**, 730-737.

Shapiro, S., and P. Hubral, 1999, Elastic Waves in Random Media, Fundamentals of Seismic Stratographic Filtering: Springer-Verlag, Berlin.

Shapiro, S. A., and P. Hubral, 1996, Elastic waves in finely layered sediments: The equivalent medium and generalized O'Doherty-Anstey formulas: Geophysics, **61**, 1282-1300.

Shapiro, S. A., and P. Hubral, 1999, Elastic waves in random media: Lecture Notes in Earth Sciences, Berlin Springer Verlag, **80**.

Shaw, F., M. Worthington, R. White, M. Andersen, and U. Petersen, 2008, Seismic attenuation in Faroe Islands basalts: Geophysical Prospecting, **56**, 5-20.

Shearer, P. M., 1999, Introduction to SeismologyCambridge University Press: Cambridge, UK.

Sheriff, R. E., 1975, Factors affecting seismic amplitudes: Geophysical Prospecting, **23**, 125-138.

Sheriff, R. E., 2002, Encyclopaedic Dictionary of Exploration Geophysics: SEG.

Sheriff, R. E., and L. P. Geldart, 1995, Exploration seismology: Cambridge university press.

Stainsby, S., and M. Worthington, 1985, Q estimation from vertical seismic profile data and anomalous variations in the central North Sea: Geophysics, **50**, 615-626.

Steineke, M., R. Bramkamp, and N. Sander, 1958, Stratigraphic relations of Arabian Jurassic oil: Presented at the American Association of Petroleum Geologists Symposium.

Sun, L. F., B. Milkereit, and D. R. Schmitt, 2009, Measuring velocity dispersion and attenuation in the exploration seismic frequency band: Geophysics, **74**, WA113-WA122.

Sun, Y.-F., and D. Goldberg, 2000, Characterization of the upper oceanic crust using high-resolution seismic amplitude modeling: SPECIAL PAPERS-GEOLOGICAL SOCIETY OF AMERICA, 203-210.

Thomsen, L., 1986, Weak elastic anisotropy: Geophysics, **51**, 1954-1966.

Thomsen, L., 2002, Understanding seismic anisotropy in exploration and exploitation: Society of Exploration Geophysicist.

Thomson, W. T., 1950, Transmission of elastic waves through a stratified solid medium: Journal of applied Physics, **21**, 89-93.

Thrower, E. N., 1965, The computation of the dispersion of elastic waves in layered media: Journal of Sound and Vibration, **2**, 210-226.

Tindale, K., N. Newell, J. Keall, and N. Smith, Year, Structural evolution and charge history of the Exmouth Sub-basin, northern Carnarvon Basin, Western Australia: The Sedimentary Basins of Western Australia 2: Proceedings of the Petroleum Exploration Society of Australia Symposium, Perth, 447-472.

Tingate, P., A. Khaksar, P. Van Ruth, D. Dewhurst, M. Raven, H. Young, R. Hillis, and K. Dodds, 2001, Geological controls on overpressure in the Northern Carnarvon Basin: APPEA Journal, **41**, 573-593.

Tonn, R., 1991, The determination of the seismic quality factor Q from VSP data: a comparison of different computational methods: Geophysical Prospecting, **39**, 1-27.

Toverud, T., and B. Ursin, 2005, Comparison of seismic attenuation models using zero-offset vertical seismic profiling (VSP) data: Geophysics, **70**, F17-F25.

Vaslet, D., M. Al-Muallem, S. Maddeh, J. Brosse, J. Fourniquet, J. Breton, and Y. Le Nindre, 1991, Explanatory notes to the geologic map of the Ar Riyad

Quadrangle, Sheet 24 I, Kingdom of Saudi Arabia. Saudi Arabian Deputy Ministry for Mineral Resources, Jeddah: Geosciences Map, **121**, 1-54.

Wang, D. Y., and D. W. McCowan, 1989, Spherical divergence correction for seismic reflection data using slant stacks: Geophysics, **54**, 563-569.

Ward, R. W., and M. N. Toksöz, 1971, Causes of regional variation of magnitudes: Bulletin of the Seismological Society of America, **61**, 649-670.

Western Australia Department of Resources, E. a. T., 2008, Release areas W08-18, W08-19 and W08-20 Exmouth Sub-Basin, Carnarvon Basin Western Australia: E. a. T. Department of Resources.

Wingo, J. R., 1981, Velocity and attenuation determinations from a vertical seismic profile.

Yang, Y., Y. Li, and T. Liu, 2009, 1D viscoelastic waveform inversion for Q structures from the surface seismic and zero-offset VSP data: Geophysics, **74**, WCC141-WCC148.

Yeates, A., M. Bradshaw, J. Dickins, A. Brakel, N. Exon, R. Langford, S. Mulholland, J. Totterdell, and M. Yeung, Year, The Westralian superbasin: an Australian link with Tethys: International symposium on Shallow Tethys 2, 199-213.

Zeitvogel, M. E., 1982, Investigation of frequency dependent attenuation in a vertical seismic profile, Texas A&M University.

Appendices

Appendix A

North West Shelf of Western Australia wells results

A.1. Adams 1 results

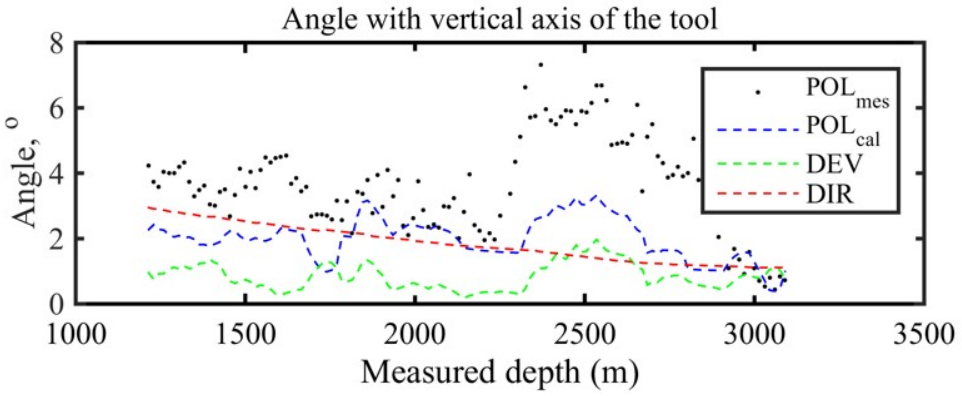

Figure A.1-1. Adams 1. Results of the orientation: measured polarization of P-wave in respect to a vertical axis of the VSP tool (black dots); calculated polarization of P-wave in respect to a vertical axis of the VSP tool (blue dash line); well inclination (green dash line); angle between a vertical direction and the direction of P-wave propagation (red dash line).

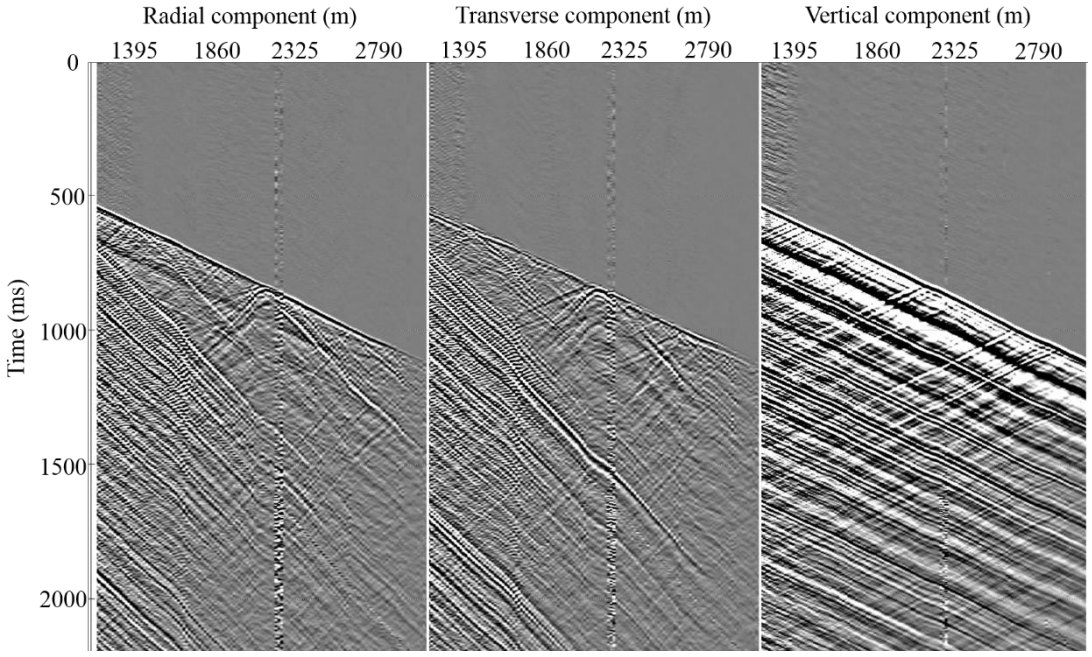

Figure A.1-2. Adams 1. 3C VSP oriented data: radial (left panel), transverse (middle panel), and vertical (right panel) components.

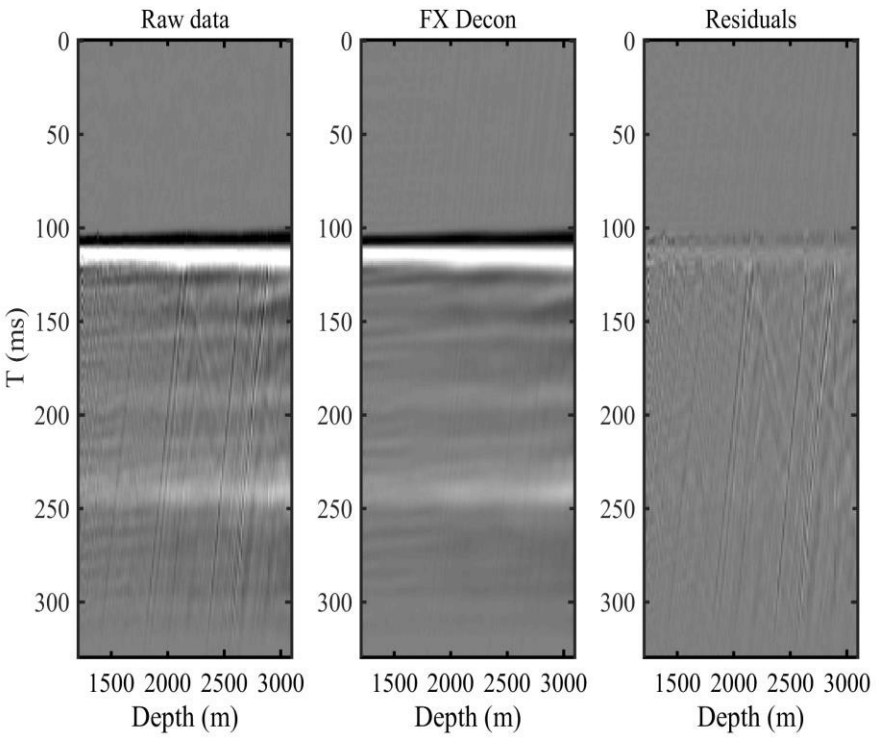

Figure A.1-3. Adams 1. Results of attenuation of upgoing wavefield by using FX deconvolution. From left to right: original data, result of FX deconvolution and the difference.

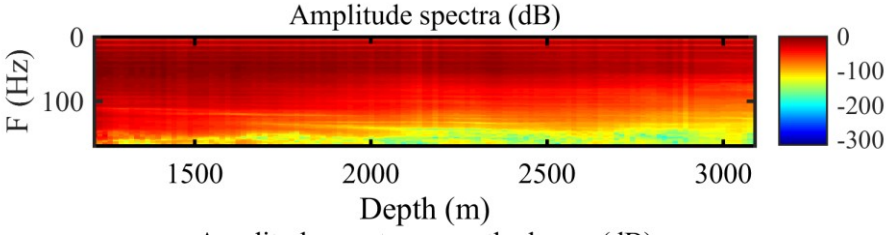

Figure A.1-4. Adams 1. Amplitude spectra after FX deconvolution.

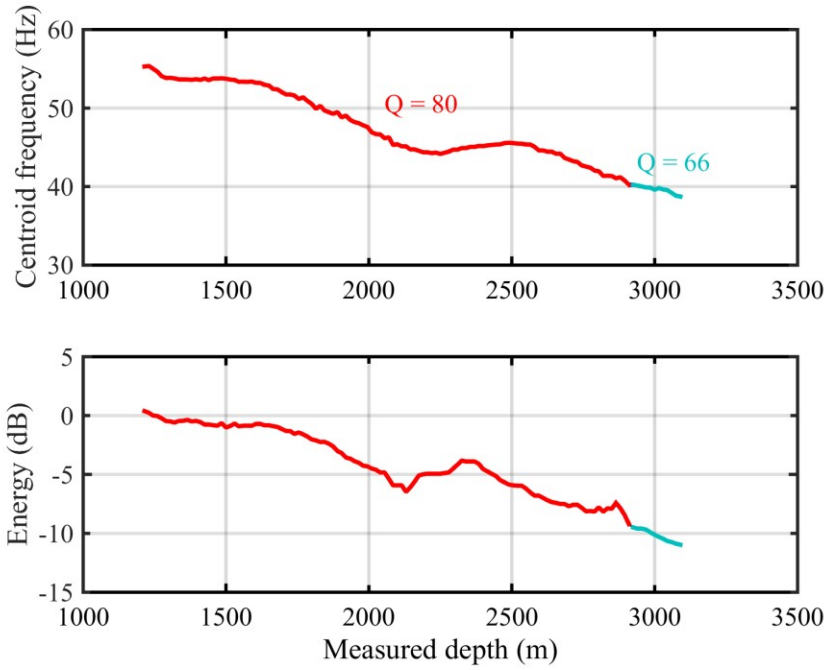

Figure A.1-5. Adams 1. Results of centroid frequency (top panel) and energy (bottom panel) decay estimation. Estimated attenuation values are derived for 2 stratigraphic intervals.

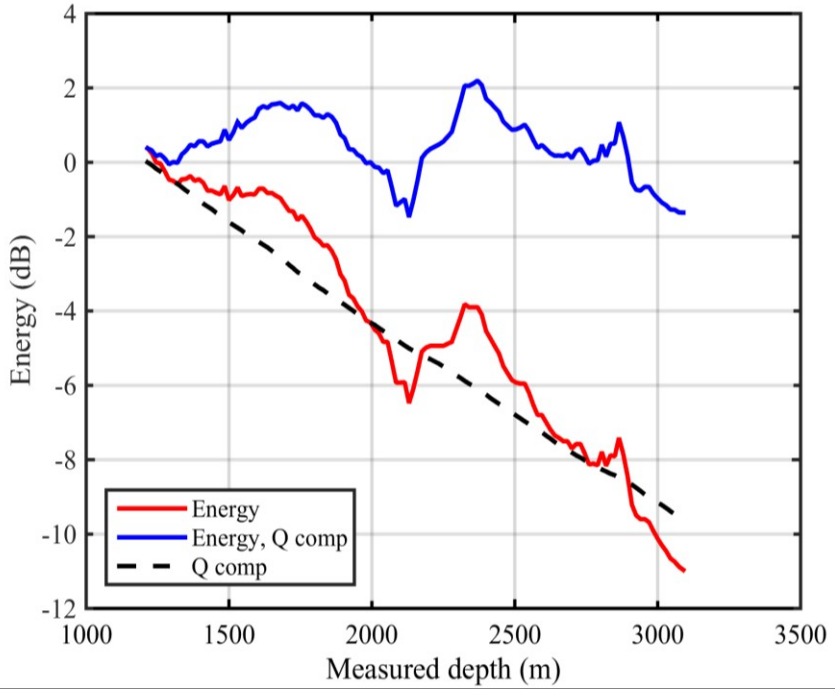

Figure A.1-6. Adams 1. Results of energy decay curve from direct wave (divergence variation is applied) (red); attenuation component of the energy decay (black) and result of the energy decay compensation (blue).

A.2. Barberry 1 results

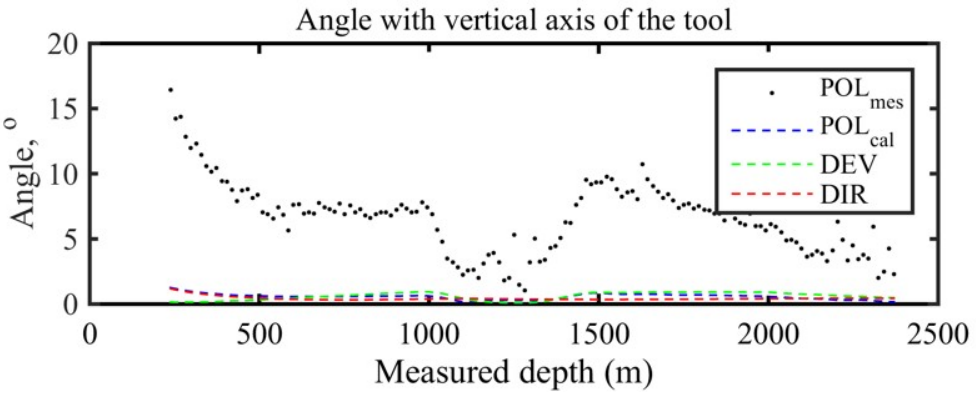

Figure A.2-1. Barberry1. Results of the orientation: measured polarization of P-wave in respect to a vertical axis of the VSP tool (black dots); calculated polarization of P-wave in respect to a vertical axis of the VSP tool (blue dash line); well inclination (green dash line); angle between a vertical direction and the direction of P-wave propagation (red dash line).

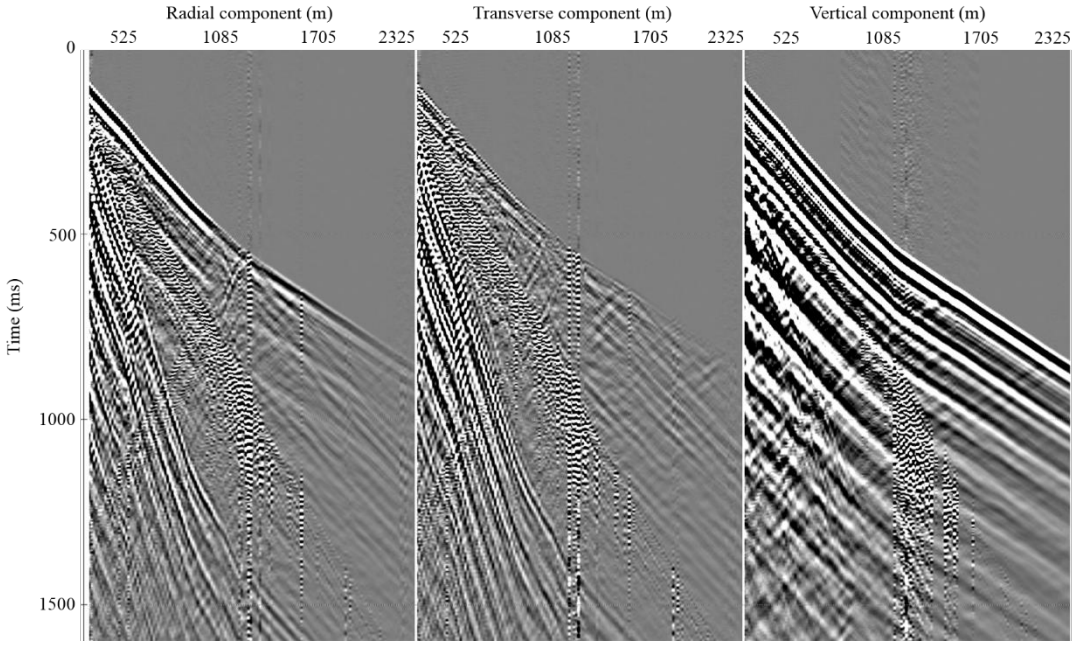

Figure A.2-2 Barberry 1 3C VSP oriented data: radial (left panel), transverse (middle panel), and vertical (right panel) components.

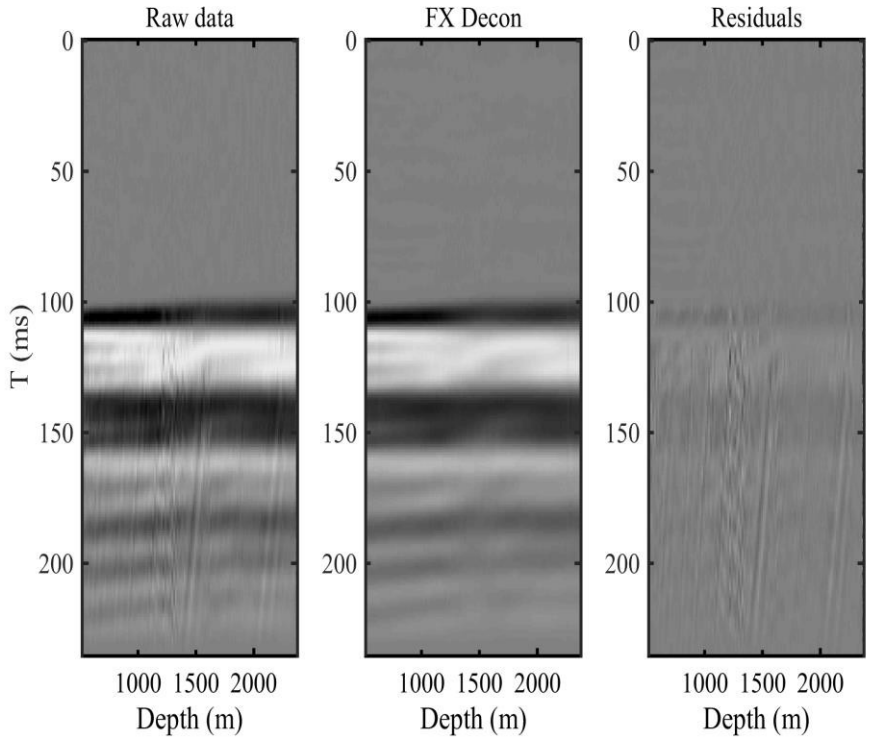

.

Figure A.2-3. Barberry 1. Results of attenuation of upgoing wavefield by using FX deconvolution. From left to right: original data, result of FX deconvolution and the difference.

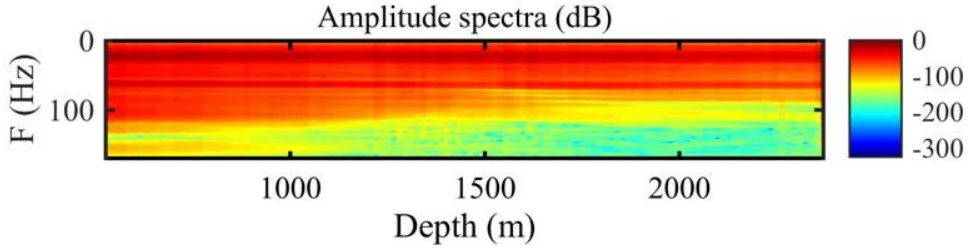

Figure A.2-4. Barberry 1. Amplitude spectra after FX deconvolution.

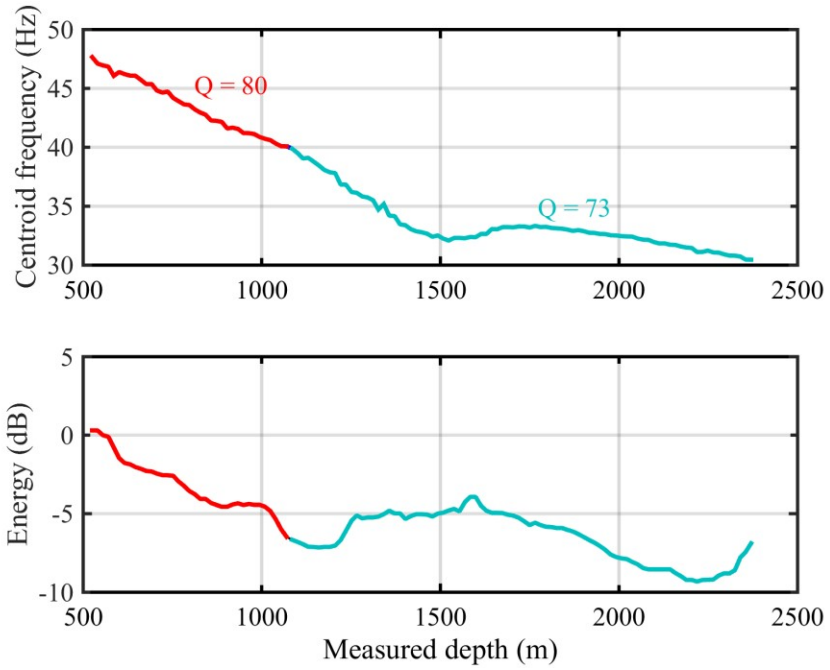

Figure A.2-5. Barberry 1. Results of centroid frequency (top panel) and energy (bottom panel) decay estimation. Estimated attenuation values are derived for 2 stratigraphic intervals.

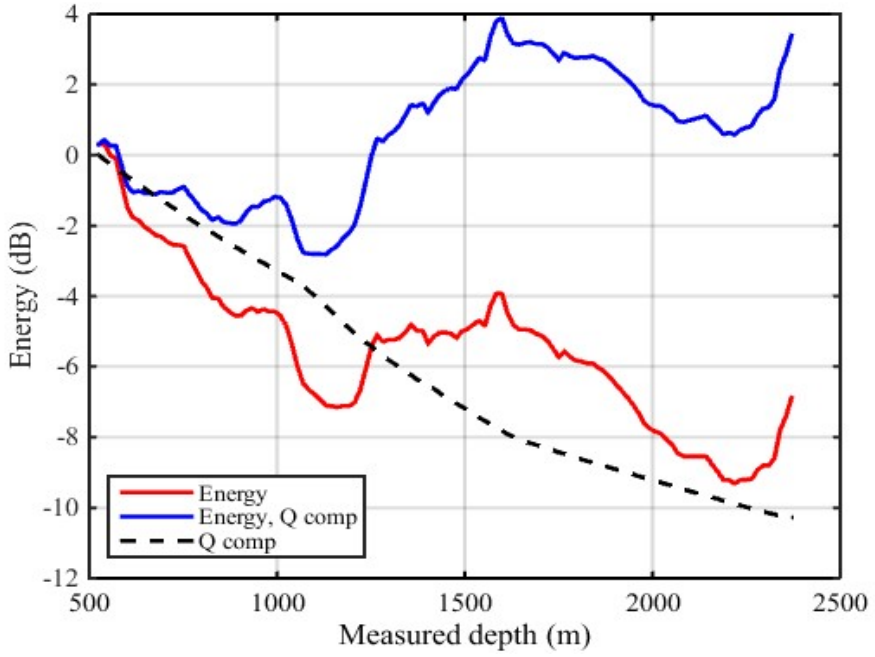

Figure A.2-6. Barberry 1. Results of energy decay curve from direct wave (divergence variation is applied) (red); attenuation component of the energy decay (black) and result of the energy decay compensation (blue).

A.3. Bath 1 results

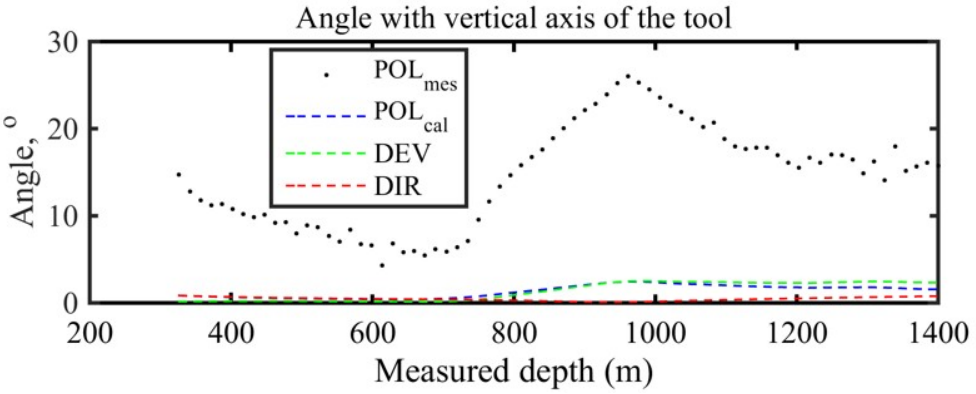

Figure A.3-1. Bath 1. Results of the orientation: measured polarization of P-wave in respect to a vertical axis of the VSP tool (black dots); calculated polarization of P-wave in respect to a vertical axis of the VSP tool (blue dash line); well inclination (green dash line); angle between a vertical direction and the direction of P-wave propagation (red dash line).

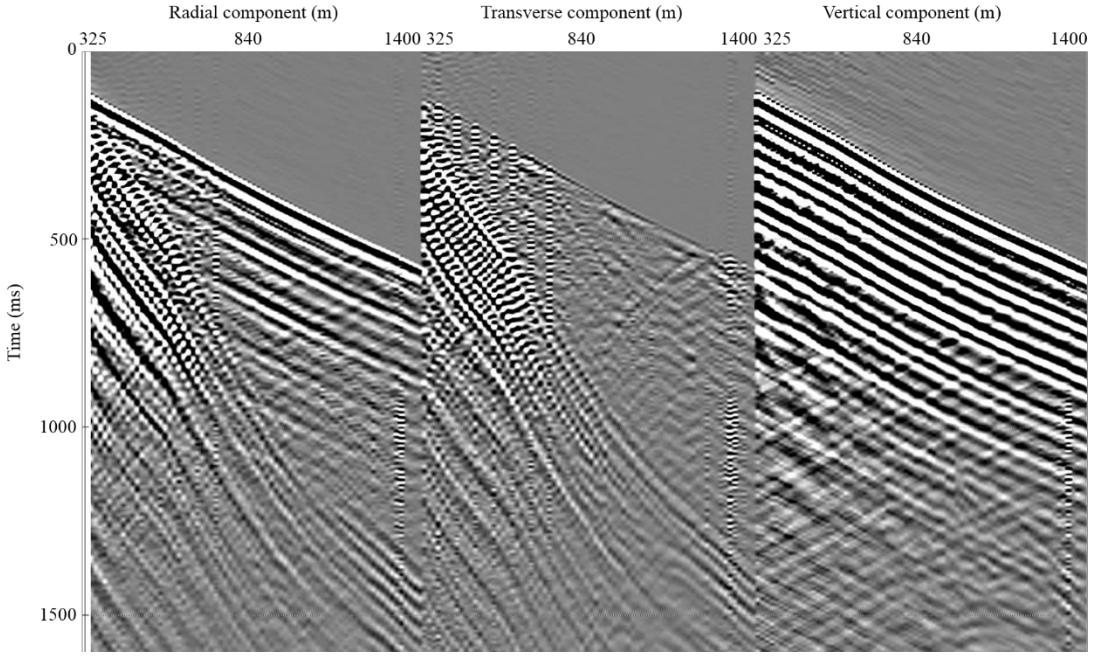

Figure A.3-2. Bath 1. 3C VSP oriented data: radial (left panel), transverse (middle panel), and vertical (right panel) components.

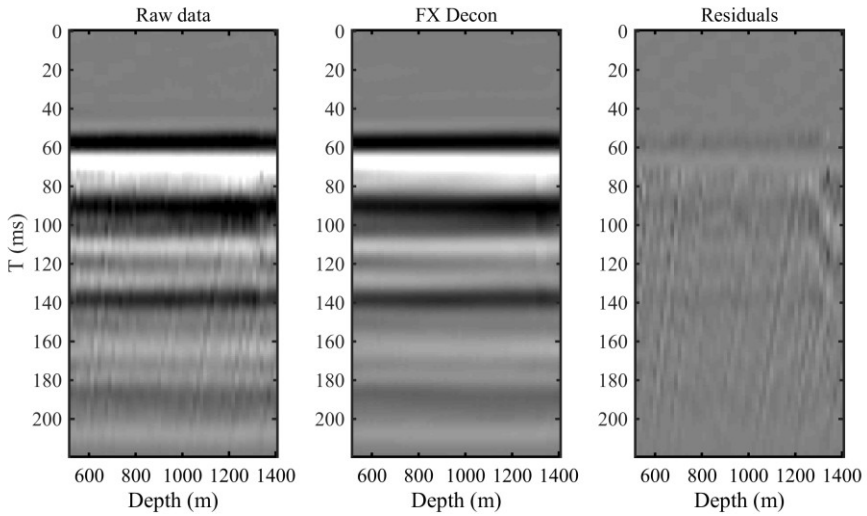

Figure A.3-3. Bath 1. Results of attenuation of upgoing wavefield by using FX deconvolution. From left to right: original data, result of FX deconvolution and the difference.

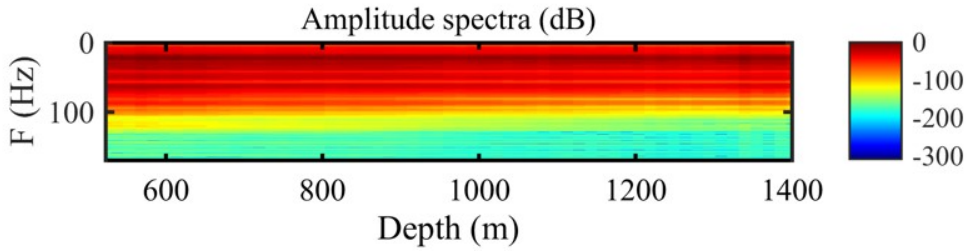

Figure A.3-4. Bath 1. Amplitude spectra after FX deconvolution.

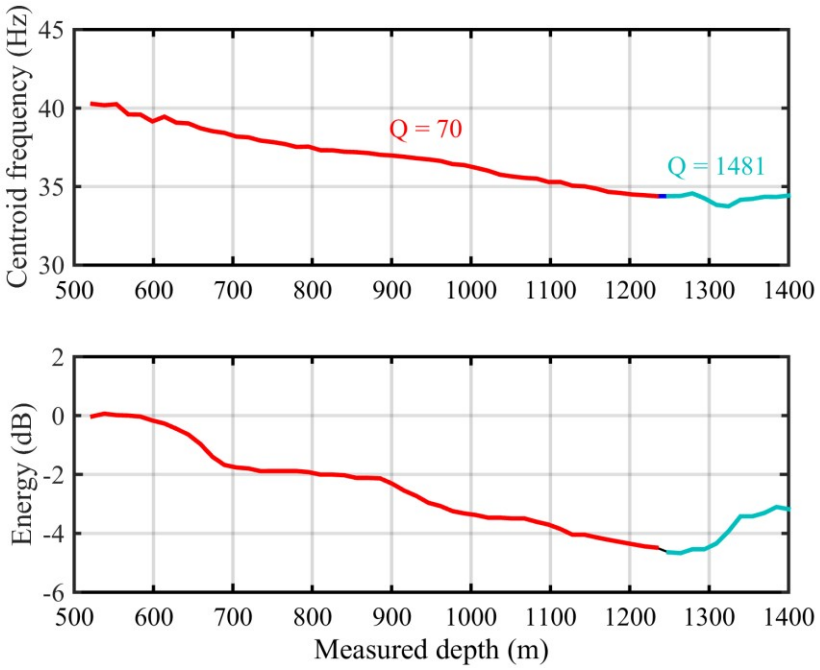

Figure A.3-5. Bath 1. Results of centroid frequency (top panel) and energy (bottom panel) decay estimation. Estimated attenuation values are derived for 2 stratigraphic intervals.

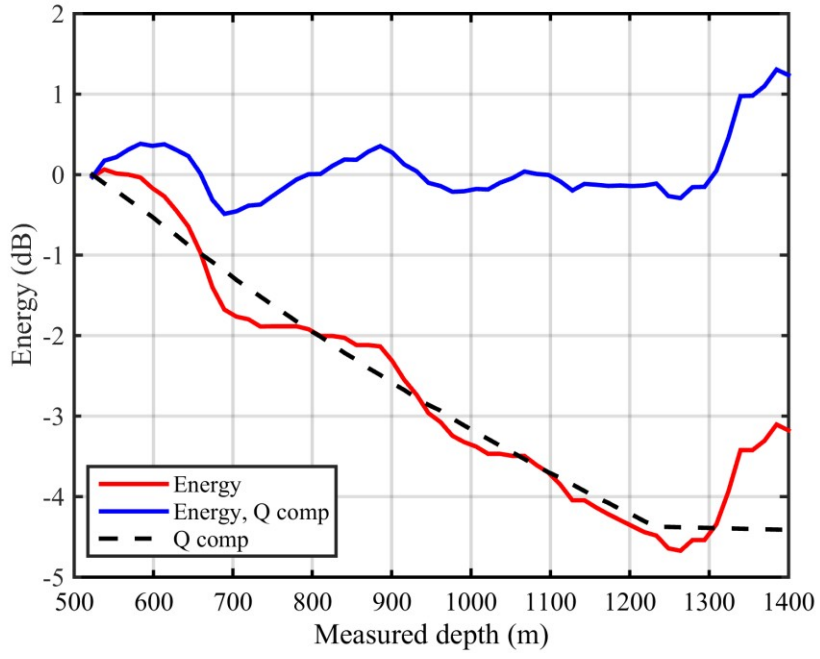

Figure A.3-6. Bath 1. Results of energy decay curve from direct wave (divergence variation is applied) (red); attenuation component of the energy decay (black) and result of the energy decay compensation (blue).

A.4. Belicoso 1 results

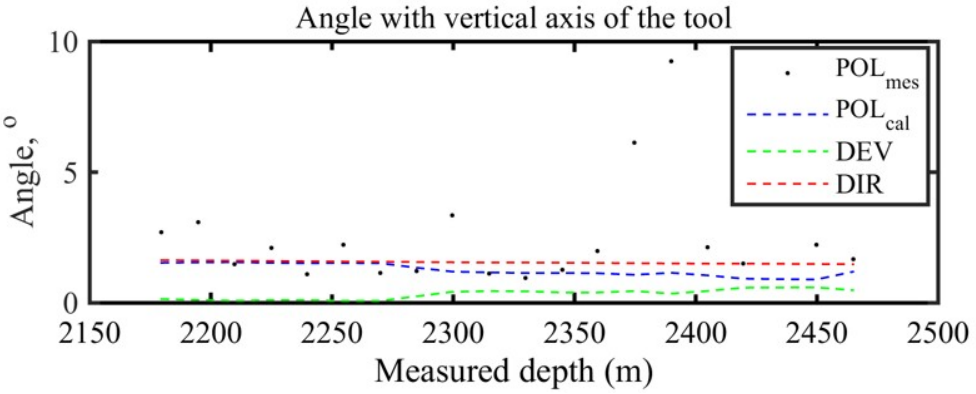

Figure A.4-1. Belicoso 1. Results of the orientation: measured polarization of P-wave in respect to a vertical axis of the VSP tool (black dots); calculated polarization of P-wave in respect to a vertical axis of the VSP tool (blue dash line); well inclination (green dash line); angle between a vertical direction and the direction of P-wave propagation (red dash line).

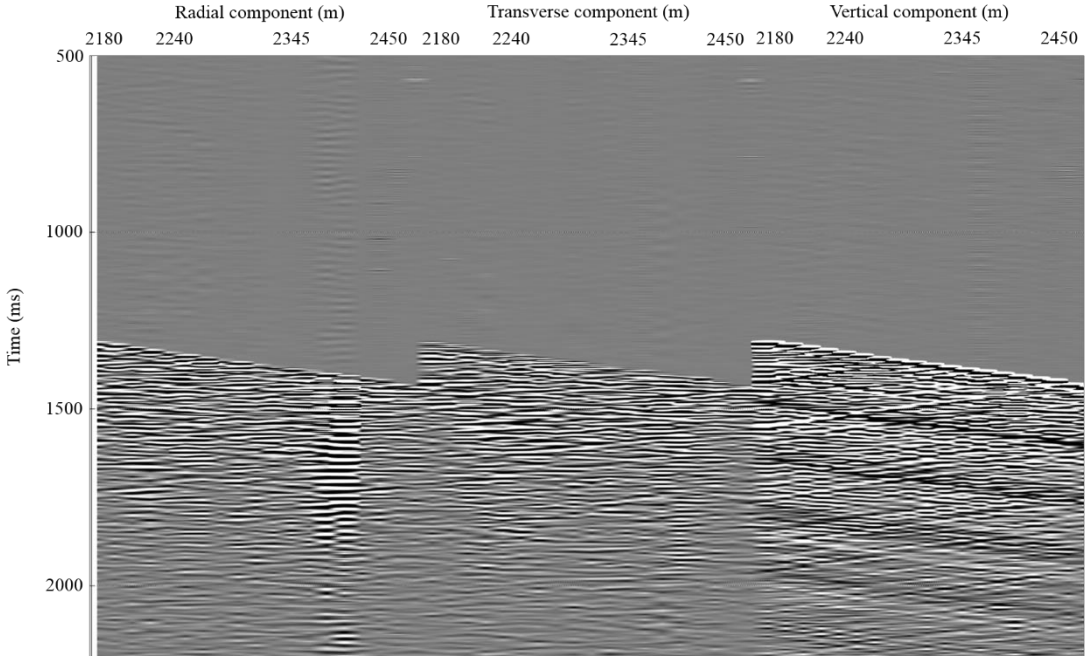

Figure A.4-2. Belicoso 1. 3C VSP oriented data: radial (left panel), transverse (middle panel), and vertical (right panel) components.

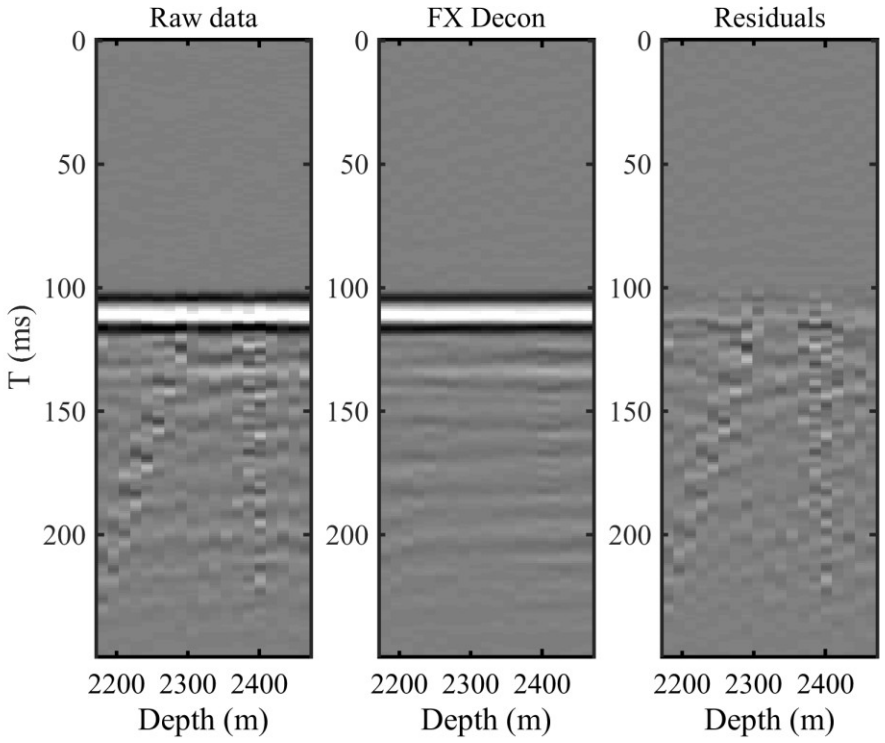

Figure A.4-3. Belicoso 1. Results of attenuation of upgoing wavefield by using FX deconvolution. From left to right: original data, result of FX deconvolution and the difference.

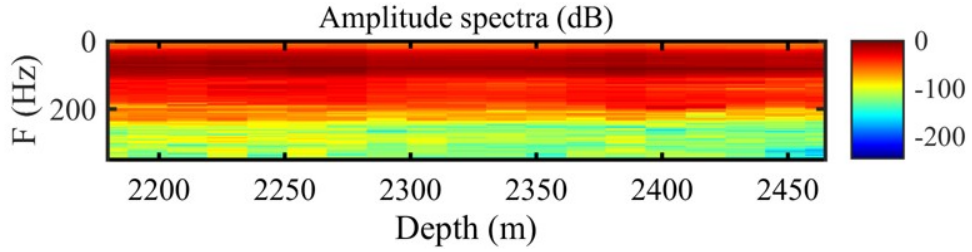

Figure A.4-4. Belicoso 1. Amplitude spectra after FX deconvolution.

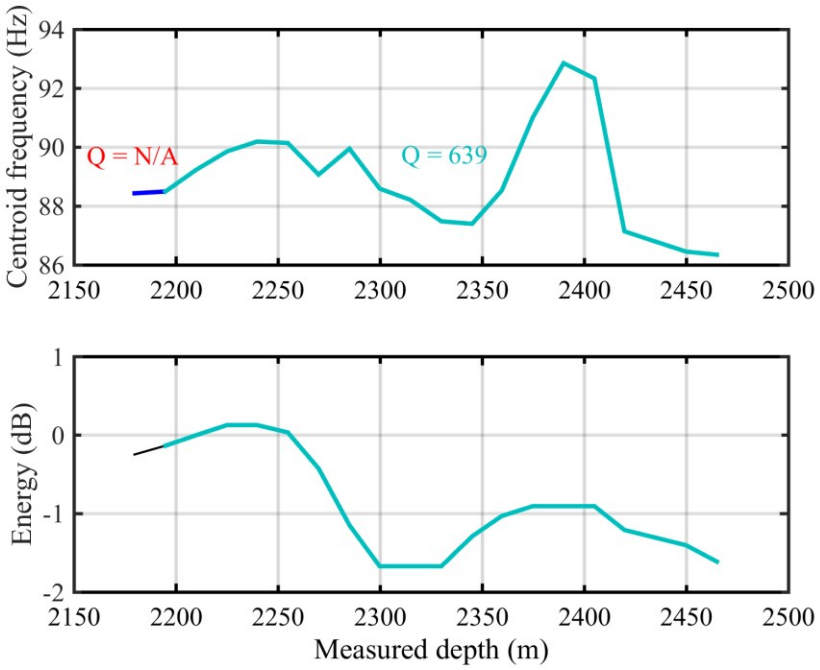

Figure A.4-5. Belicoso 1. Results of centroid frequency (top panel) and energy (bottom panel) decay estimation. Estimated attenuation values are derived for 2 stratigraphic intervals.

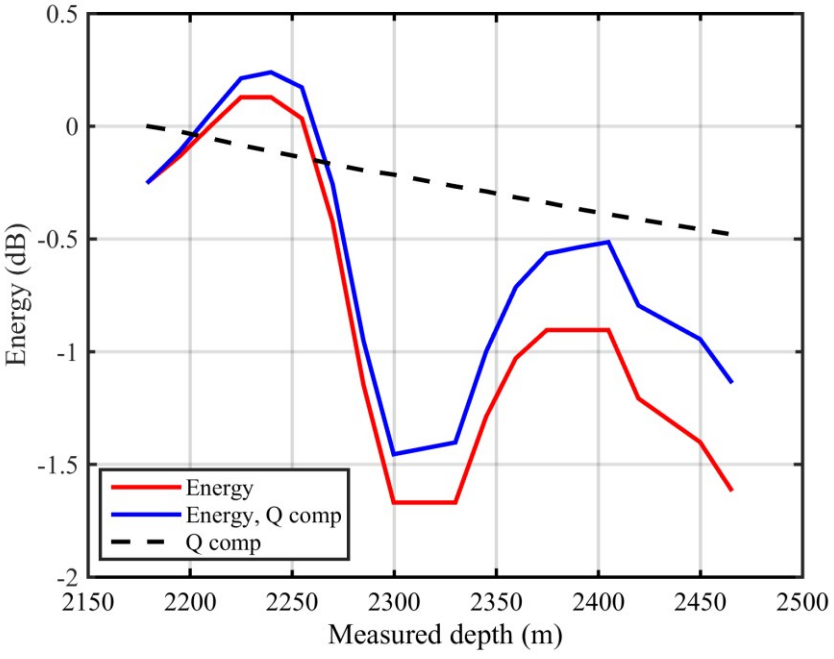

Figure A.4-6. Belicoso 1. Results of energy decay curve from direct wave (divergence variation is applied) (red); attenuation component of the energy decay (black) and result of the energy decay compensation (blue).

.

A.5. Bleaberry West 1 results

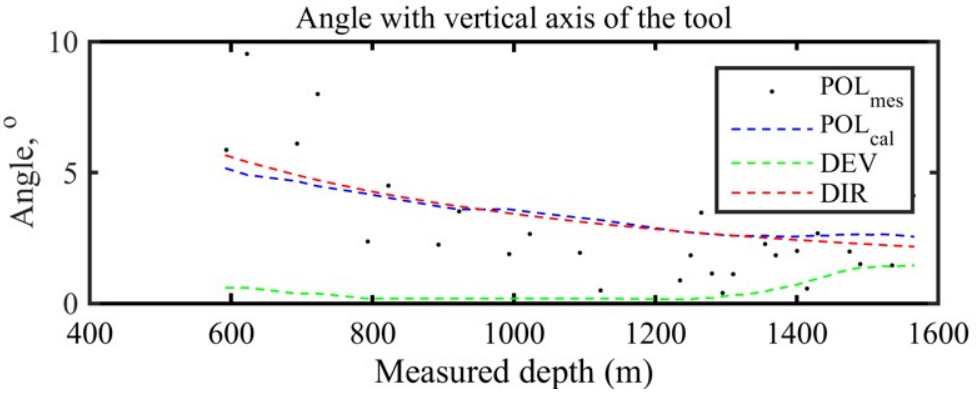

Figure A.5-1. Bleaberry west 1. Results of the orientation: measured polarization of P-wave in respect to a vertical axis of the VSP tool (black dots); calculated polarization of P-wave in respect to a vertical axis of the VSP tool (blue dash line); well inclination (green dash line); angle between a vertical direction and the direction of P-wave propagation (red dash line).

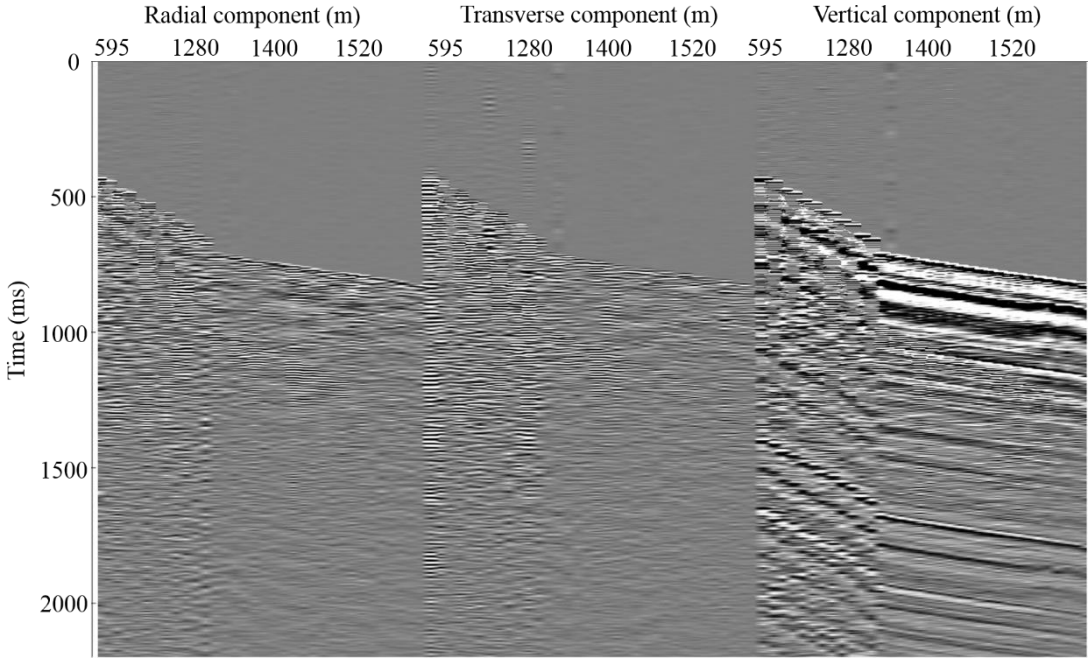

Figure A.5-2. Bleaberry west 1. 3C VSP oriented data: radial (left panel), transverse (middle panel), and vertical (right panel) components.

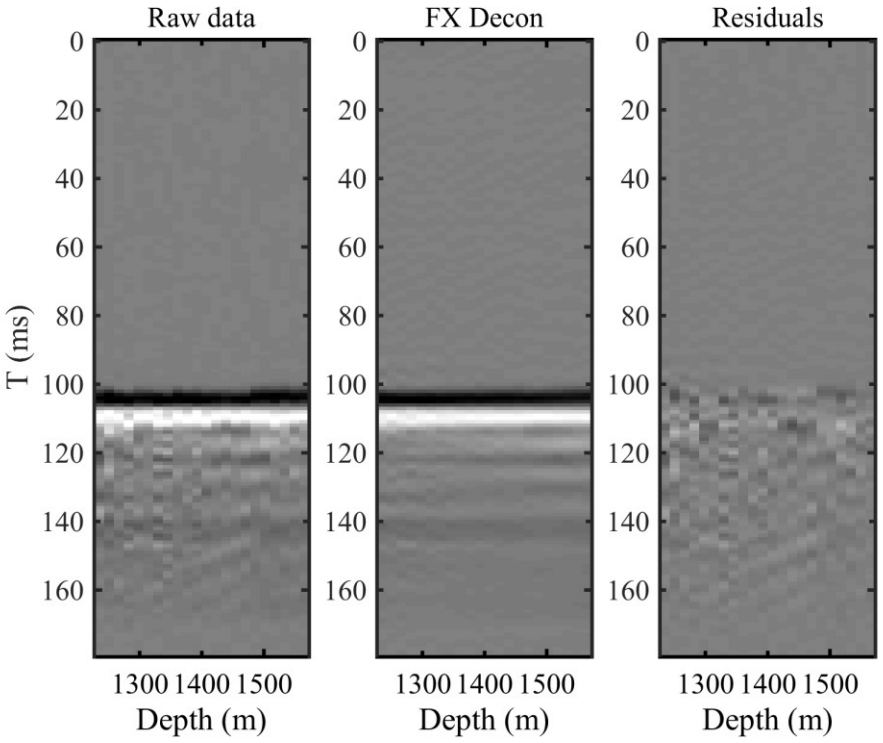

Figure A.5-3. Bleaberry west 1. Results of attenuation of upgoing wavefield by using FX deconvolution. From left to right: original data, result of FX deconvolution and the difference.

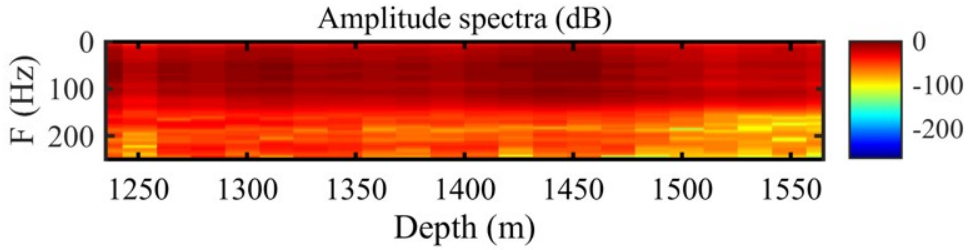

Figure A.5-4. Bleaberry west 1. Amplitude spectra after FX deconvolution.

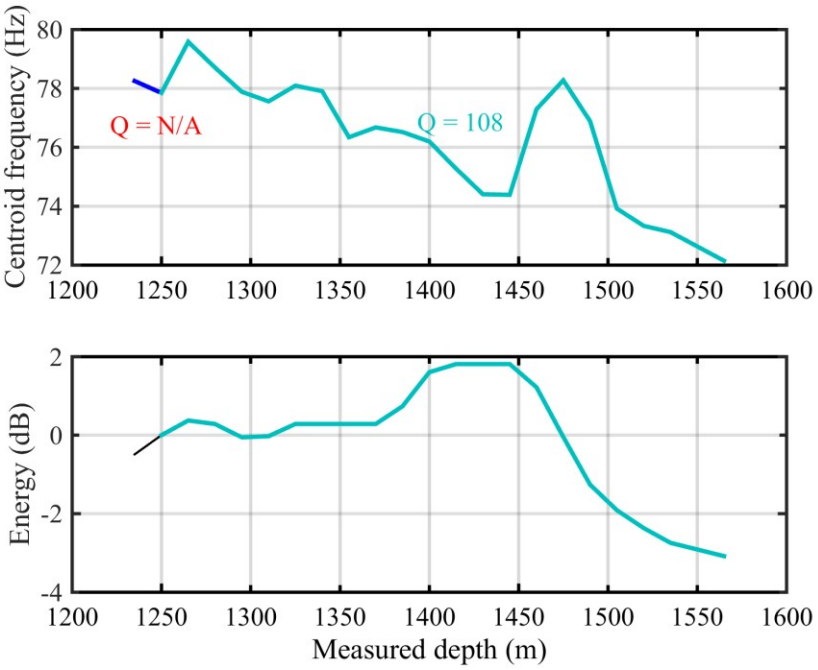

Figure A.5-5. Bleaberry west 1. Results of centroid frequency (top panel) and energy (bottom panel) decay estimation. Estimated attenuation values are derived for 2 stratigraphic intervals.

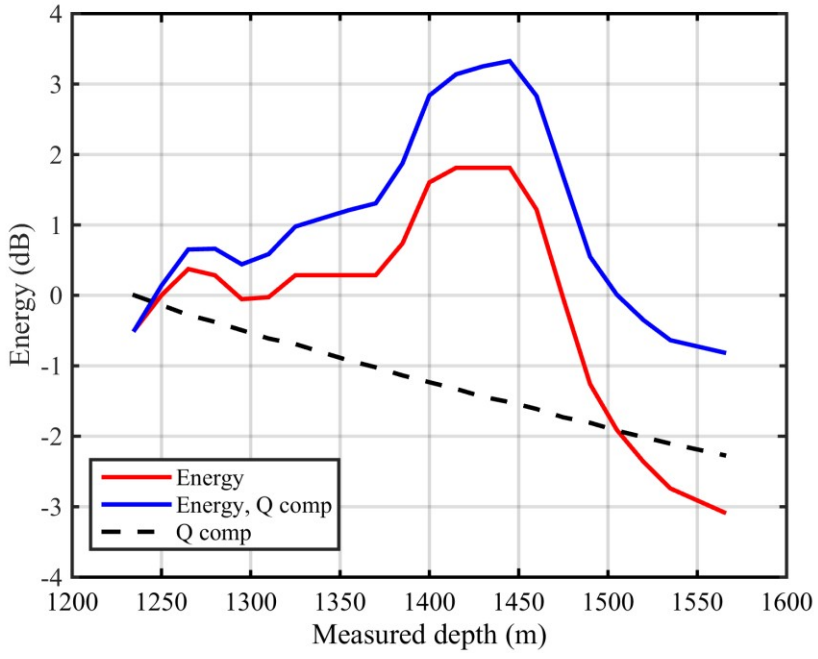

Figure A.5-6. Bleaberry west 1. Results of energy decay curve from direct wave (divergence variation is applied) (red); attenuation component of the energy decay (black) and result of the energy decay compensation (blue).

A.6. Briseis 1 results

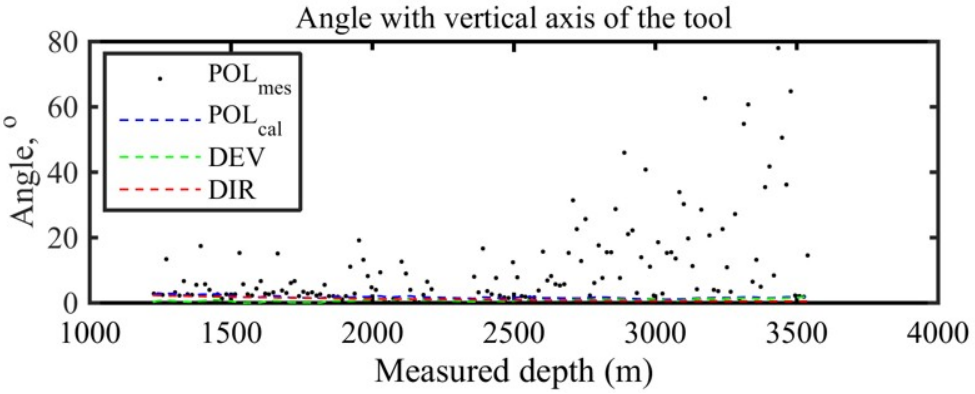

Figure A.6-1. Briseis 1. Results of the orientation: measured polarization of P-wave in respect to a vertical axis of the VSP tool (black dots); calculated polarization of P-wave in respect to a vertical axis of the VSP tool (blue dash line); well inclination (green dash line); angle between a vertical direction and the direction of P-wave propagation (red dash line).

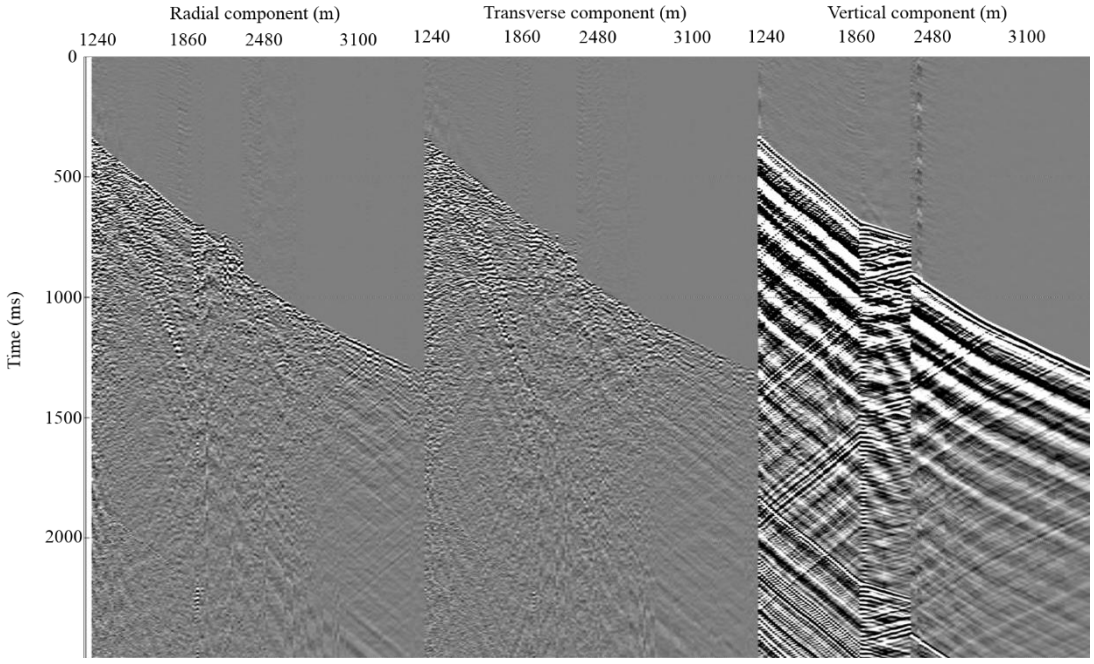

Figure A.6-2. Briseis 1. 3C VSP oriented data: radial (left panel), transverse (middle panel), and vertical (right panel) components.

.

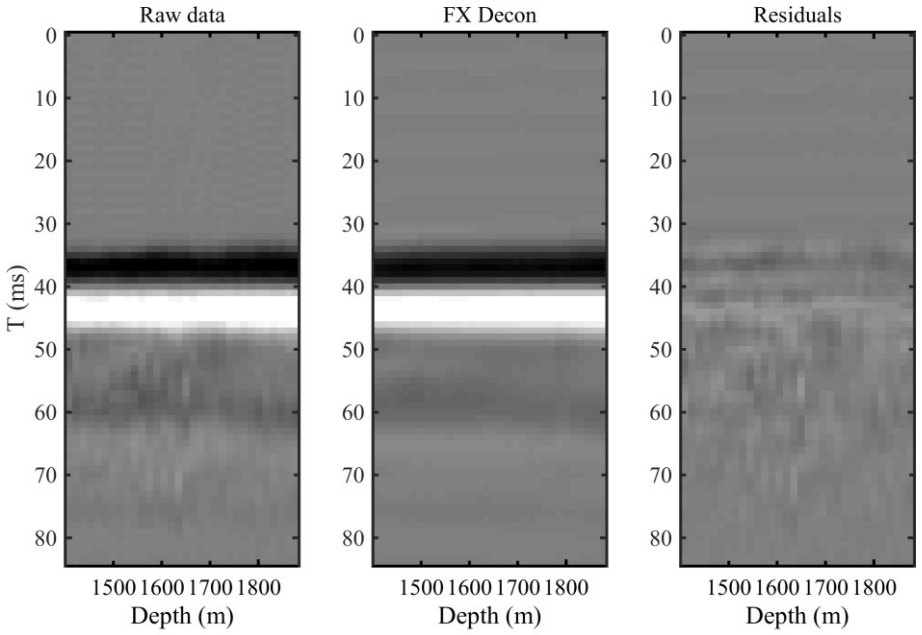

Figure A.6-3. Briseis 1. Results of attenuation of upgoing wavefield by using FX deconvolution. From left to right: original data, result of FX deconvolution and the difference.

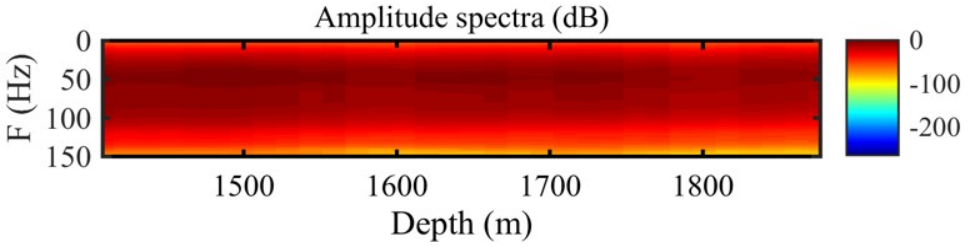

Figure A.6-4. Briseis 1. Amplitude spectra after FX deconvolution.

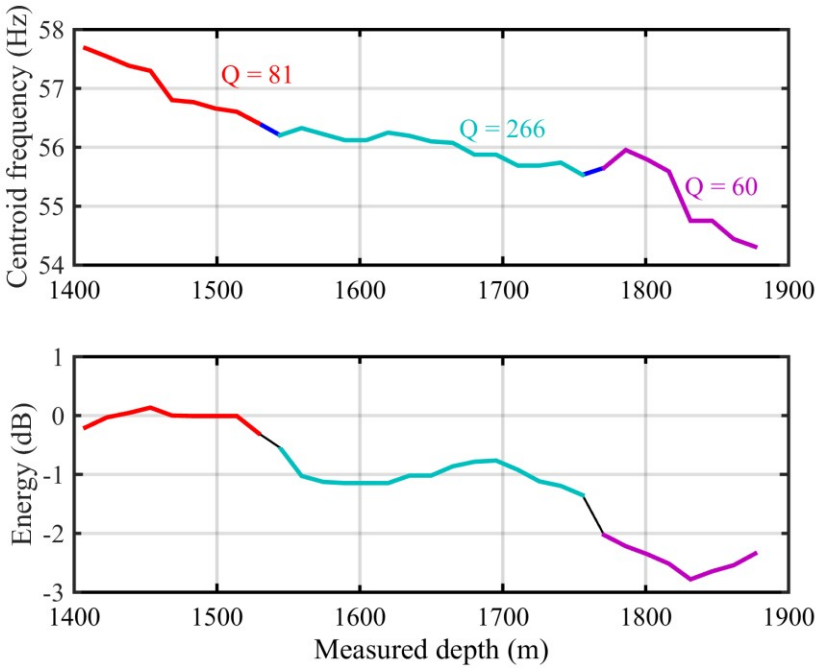

Figure A.6-5. Briseis 1. Results of centroid frequency (top panel) and energy (bottom panel) decay estimation. Estimated attenuation values are derived for 3 stratigraphic intervals.

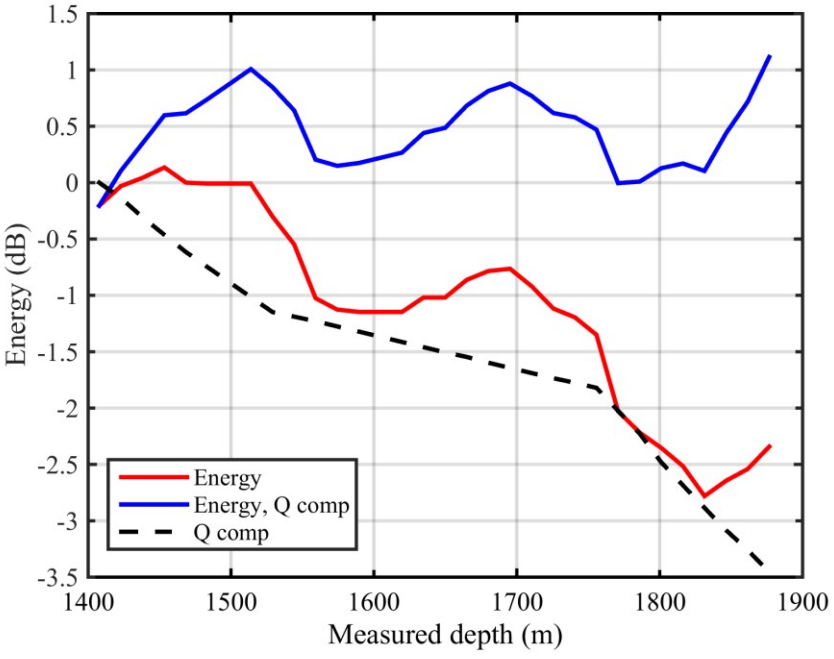

Figure A.6-6. Briseis 1. Results of energy decay curve from direct wave (divergence variation is applied) (red); attenuation component of the energy decay (black) and result of the energy decay compensation (blue).

A.7. Brulimar 1 results

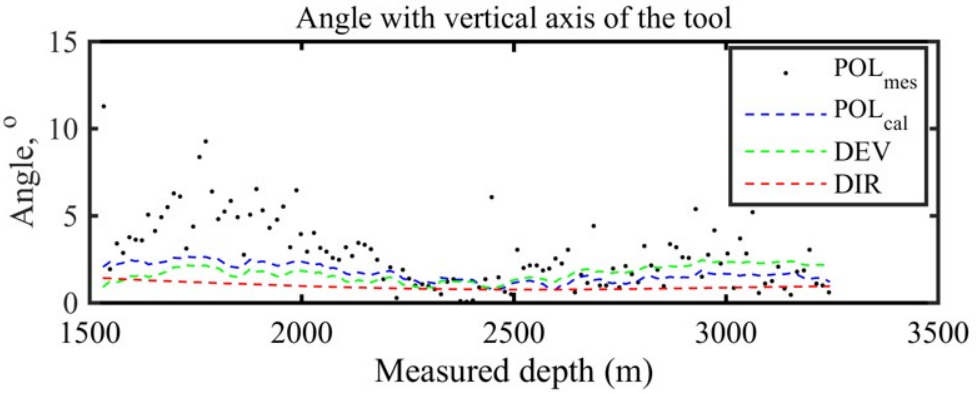

Figure A.7-1. Brulimar 1. Results of the orientation: measured polarization of P-wave in respect to a vertical axis of the VSP tool (black dots); calculated polarization of P-wave in respect to a vertical axis of the VSP tool (blue dash line); well inclination (green dash line); angle between a vertical direction and the direction of P-wave propagation (red dash line).

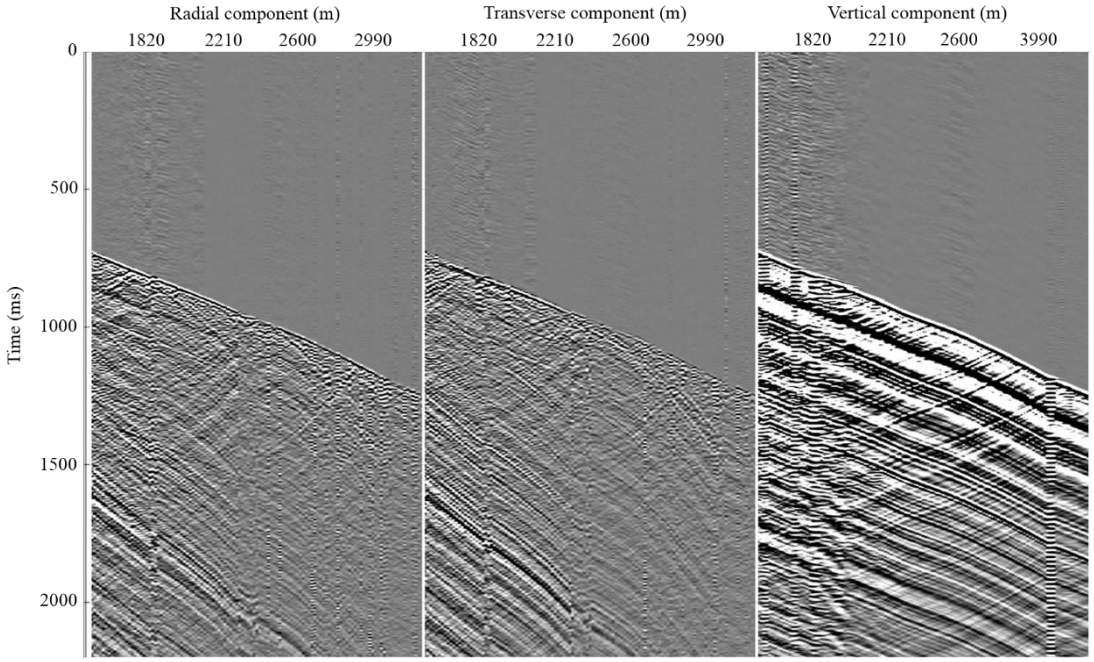

Figure A.7-2. Brulimar 1. 3C VSP oriented data Radial (left panel) transverse (middle panel), and vertical (right panel) components.

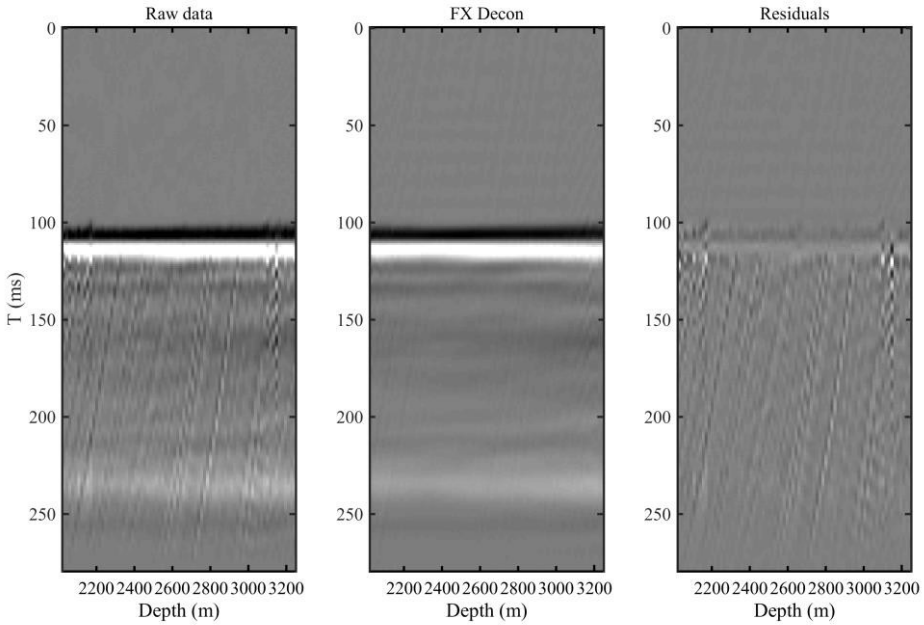

Figure A.7-3. Brulimar 1. Results of attenuation of upgoing wavefield by using FX deconvolution. From left to right: original data, result of FX deconvolution and the difference.

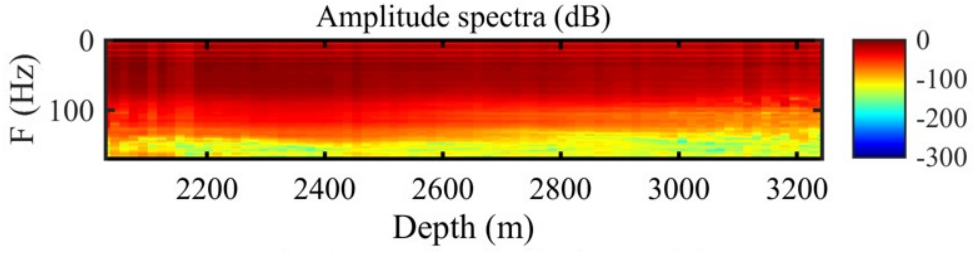

Figure A.7-4. Brulimar 1. Amplitude spectra after FX deconvolution.

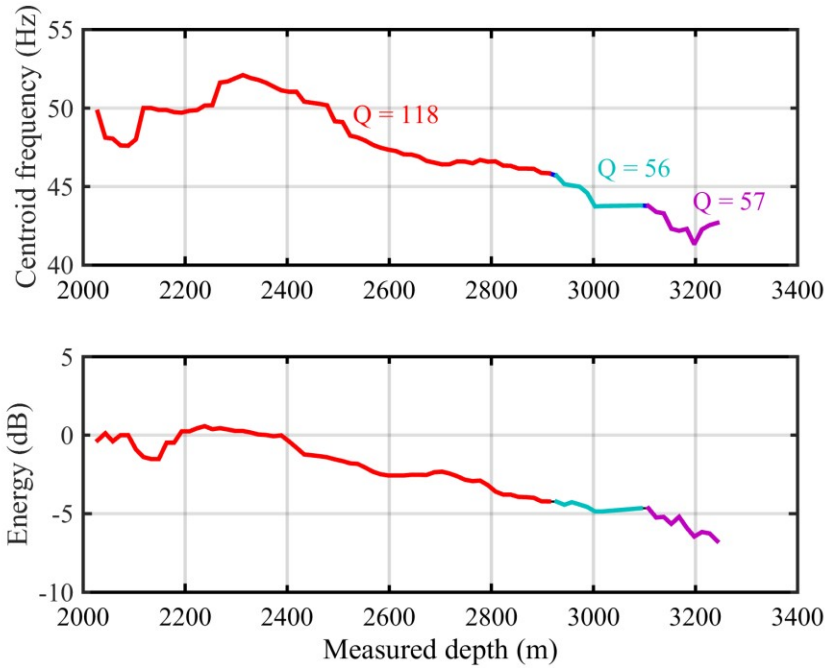

Figure A.7-5. Brulimar 1. Results of centroid frequency (top panel) and energy (bottom panel) decay estimation. Estimated attenuation values are derived for 3 stratigraphic intervals.

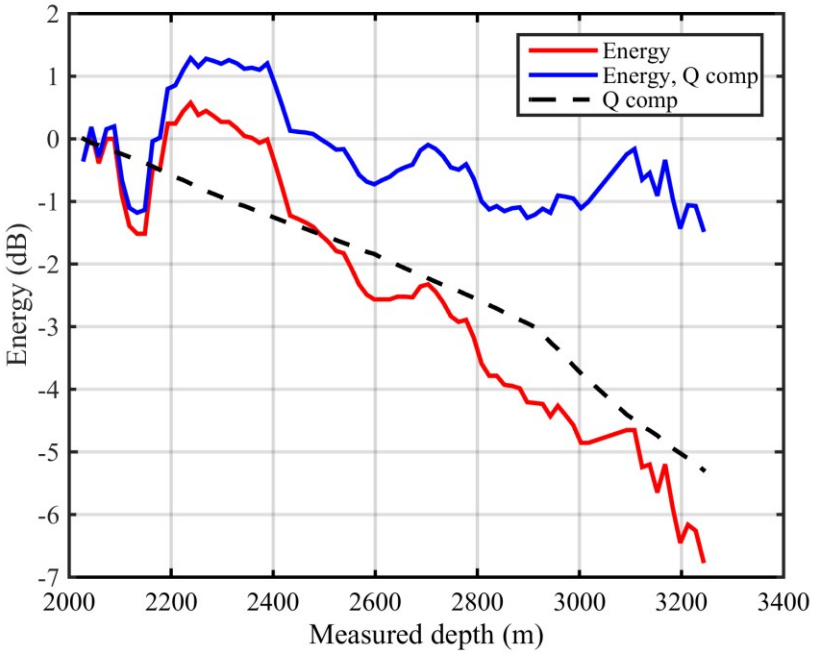

Figure A.7-6. Brulimar 1. Results of energy decay curve from direct wave (divergence variation is applied) (red); attenuation component of the energy decay (black) and result of the energy decay compensation (blue).

A.8. Brunello 1 results

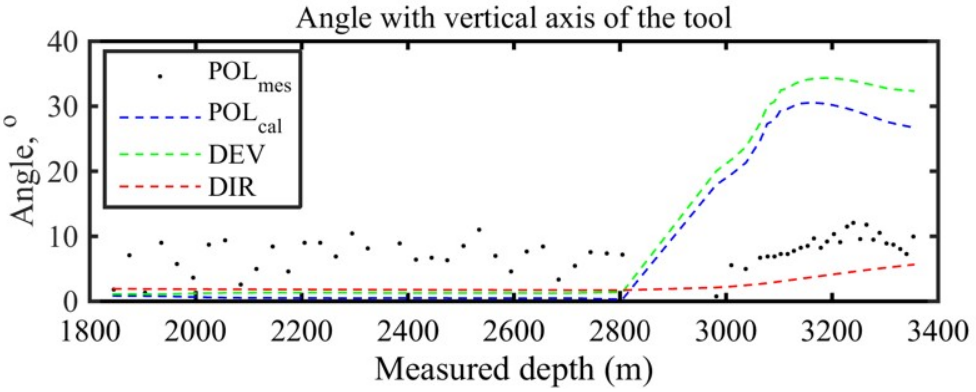

Figure A.8-1. Brunello 1. Results of the orientation: measured polarization of P-wave in respect to a vertical axis of the VSP tool (black dots); calculated polarization of P-wave in respect to a vertical axis of the VSP tool (blue dash line); well inclination (green dash line); angle between a vertical direction and the direction of P-wave propagation (red dash line).

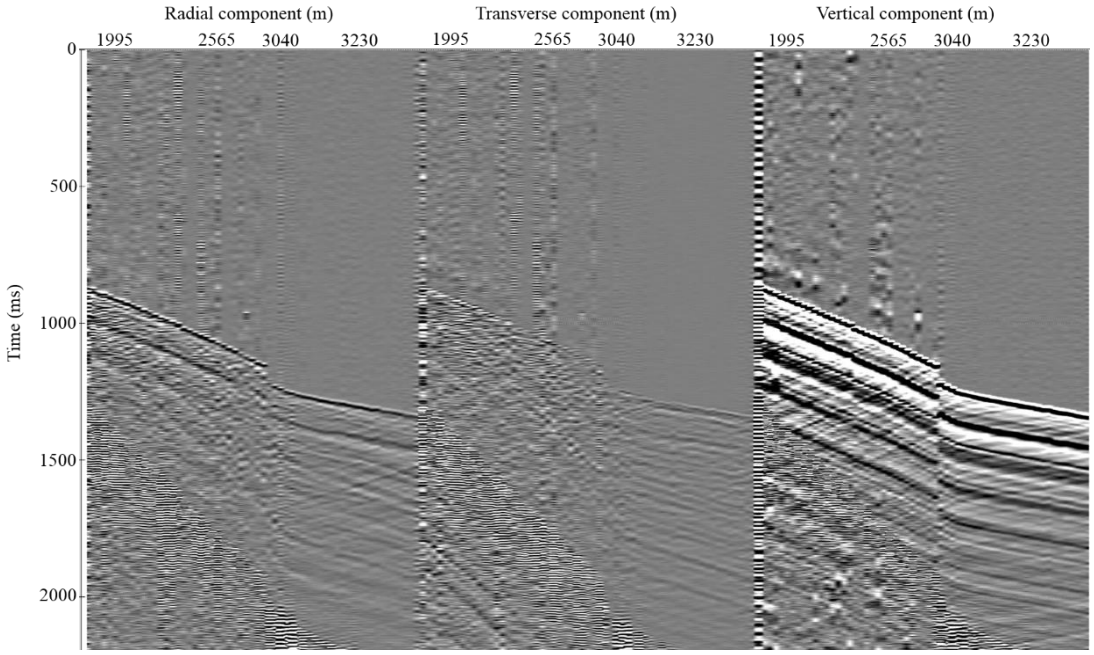

Figure A.8-2. Brunello 1. 3C VSP oriented data: radial (left panel), transverse (middle panel), and vertical (right panel) components.

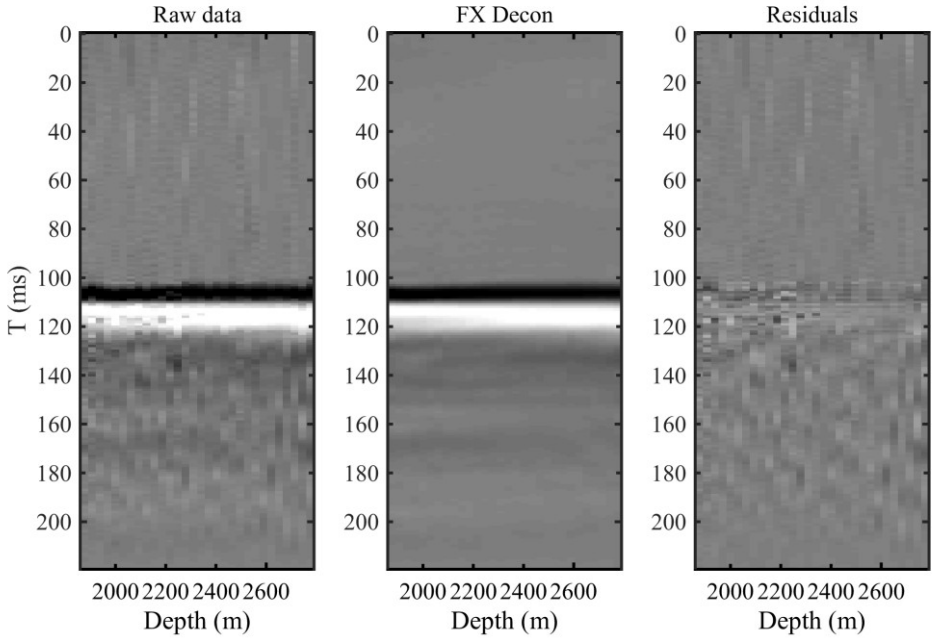

Figure A.8-3. Brunello 1. Results of attenuation of upgoing wavefield by using FX deconvolution. From left to right: original data, result of FX deconvolution and the difference.

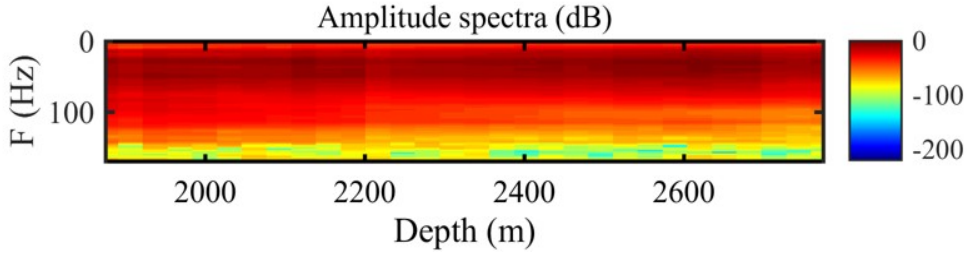

Figure A.8-4. Brunello 1. Amplitude spectra after FX deconvolution.

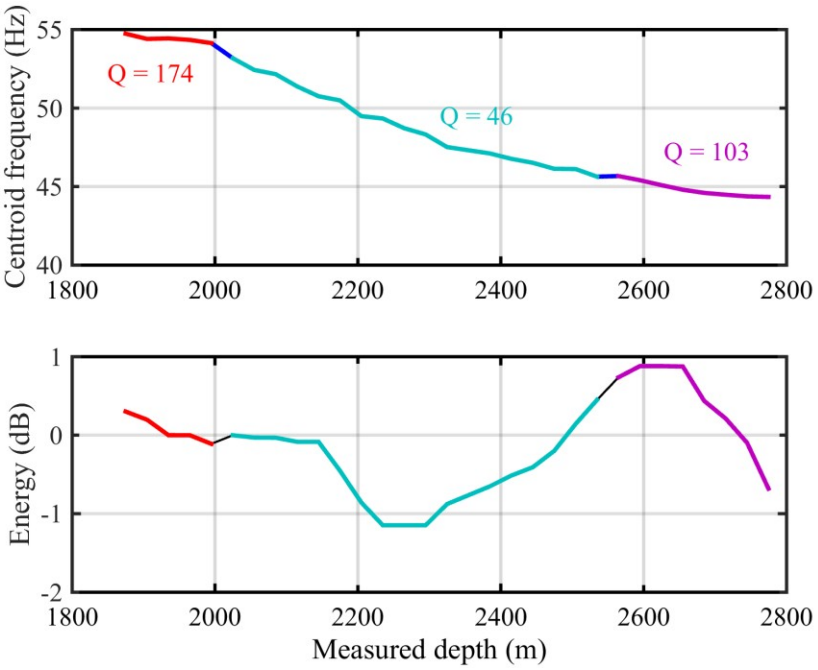

Figure A.8-5. Brunello 1. Results of centroid frequency (top panel) and energy (bottom panel) decay estimation. Estimated attenuation values are derived for 3 stratigraphic intervals.

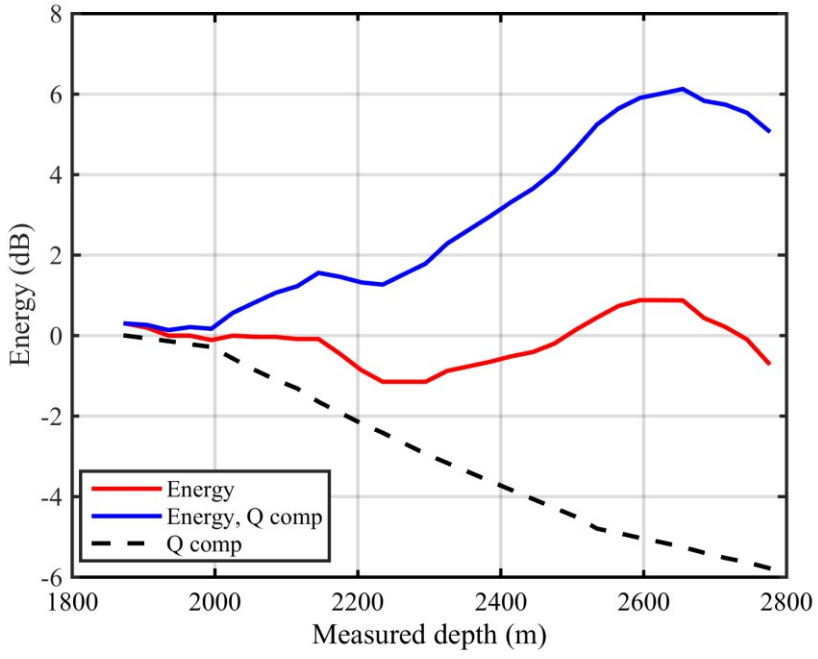

Figure A.8-6. Brunello 1. Results of energy decay curve from direct wave (divergence variation is applied) (red); attenuation component of the energy decay (black) and result of the energy decay compensation (blue).

A.9. Coniston 2 results

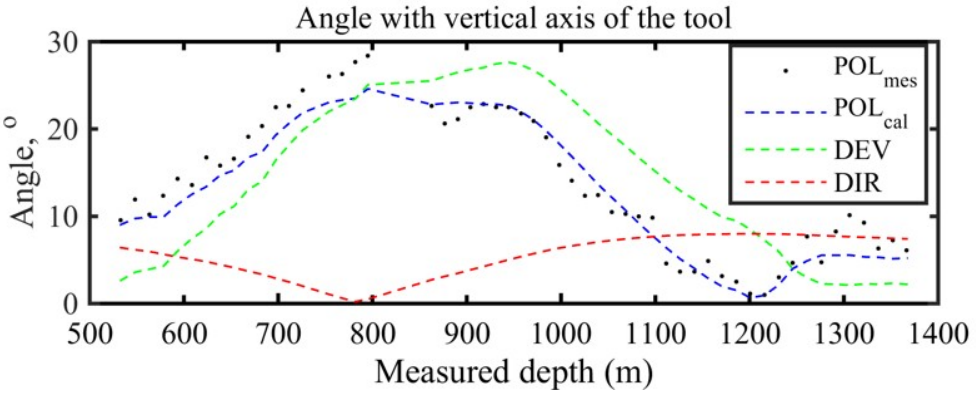

Figure A.9-1. Coniston 2. Results of the orientation: measured polarization of P-wave in respect to a vertical axis of the VSP tool (black dots); calculated polarization of P-wave in respect to a vertical axis of the VSP tool (blue dash line); well inclination (green dash line); angle between a vertical direction and the direction of P-wave propagation (red dash line).

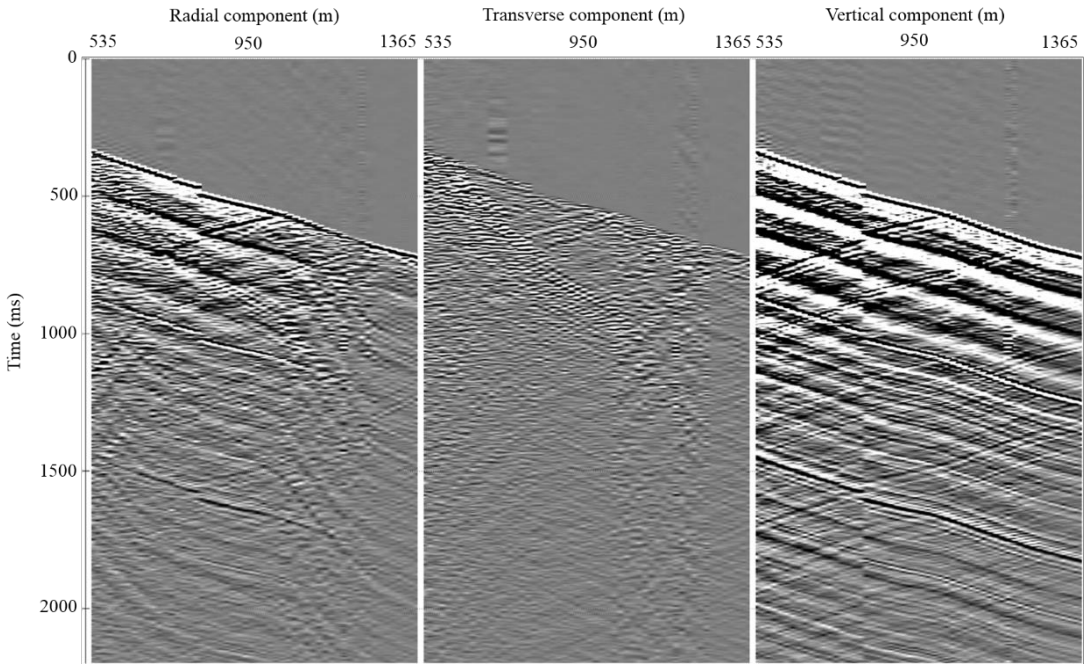

Figure A.9-2. Coniston 2. 3C VSP oriented data: radial (left panel), transverse (middle panel), and vertical (right panel) components.

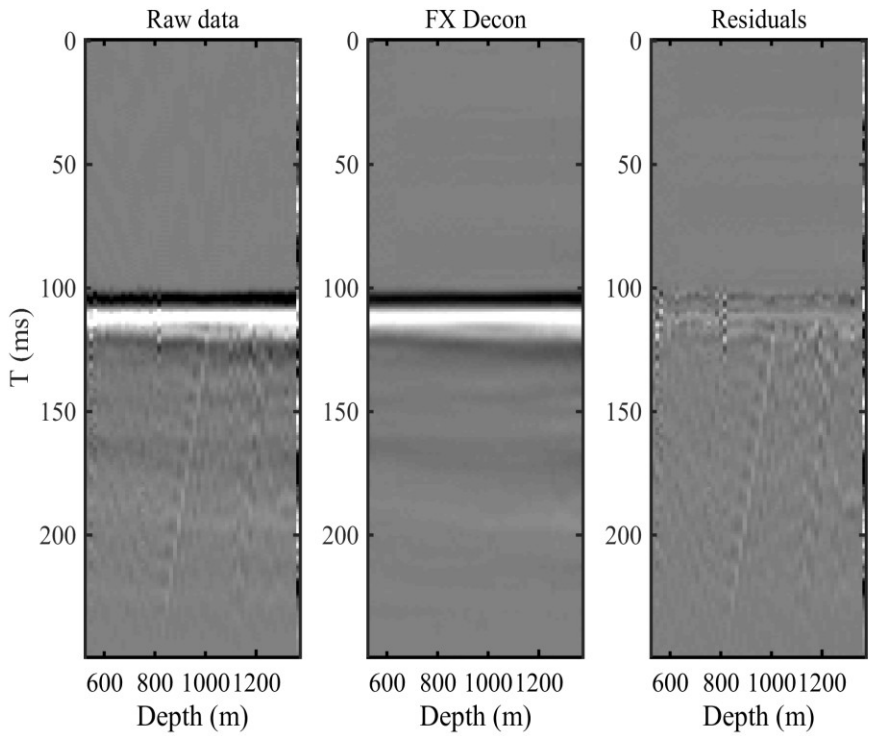

Figure A.9-3. Coniston 2. Results of attenuation of upgoing wavefield by using FX deconvolution. From left to right: original data, result of FX deconvolution and the difference.

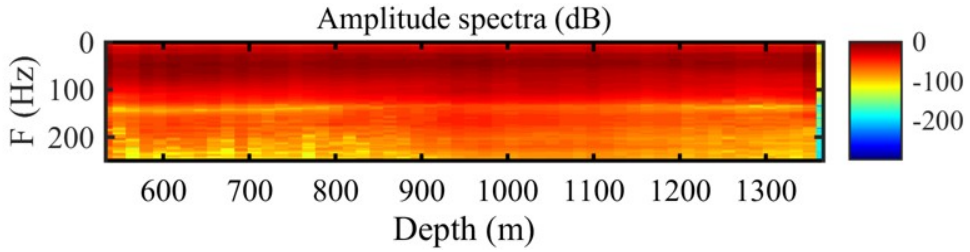

Figure A.9-4. Coniston 2. Amplitude spectra after FX deconvolution.

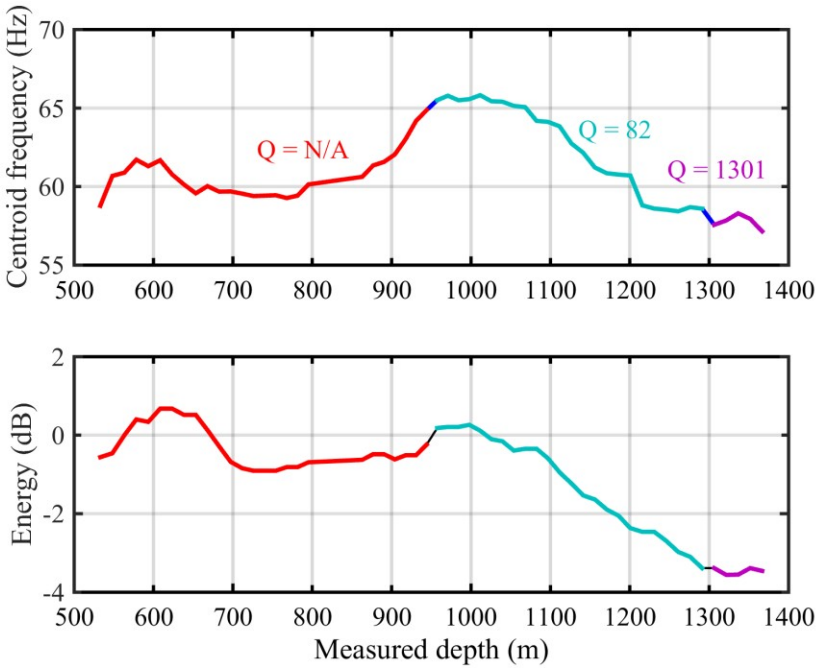

Figure A.9-5. Coniston 2. Results of centroid frequency (top panel) and energy (bottom panel) decay estimation. Estimated attenuation values are derived for 3 stratigraphic intervals.

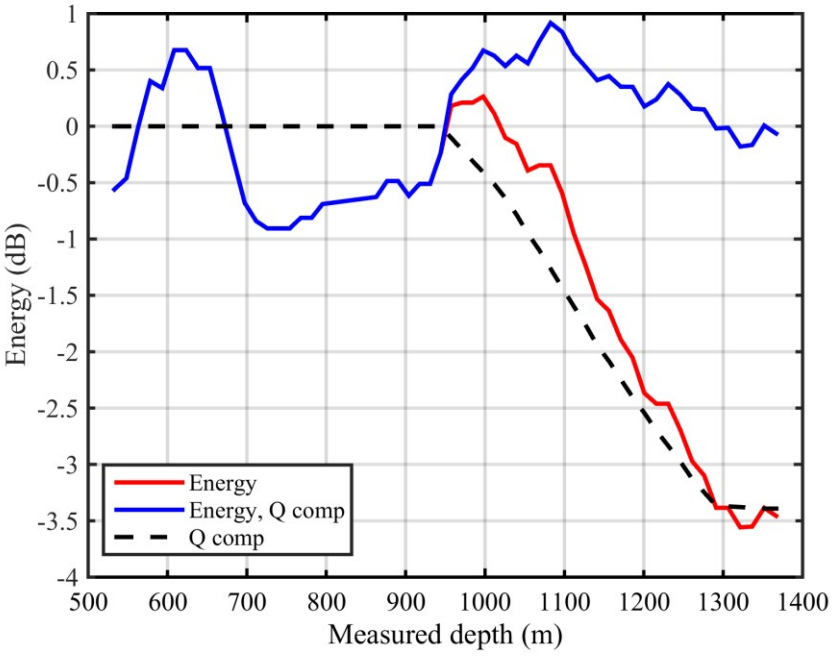

Figure A.9-6. Coniston 2. Results of energy decay curve from direct wave (divergence variation is applied) (red); attenuation component of the energy decay (black) and result of the energy decay compensation (blue).

A.10. Coniston 3 results

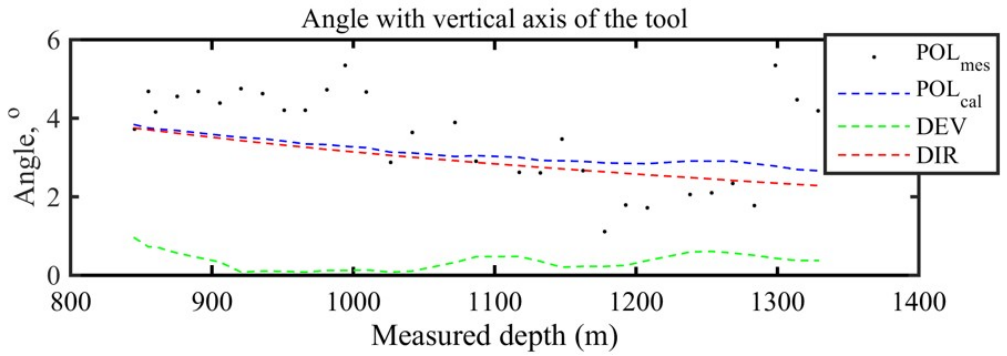

Figure A.10-1. Results of the orientation: measured polarization of P-wave in respect to a vertical axis of the VSP tool (black dots); calculated polarization of P-wave in respect to a vertical axis of the VSP tool (blue dash line); well inclination (green dash line); angle between a vertical direction and the direction of P-wave propagation (red dash line).

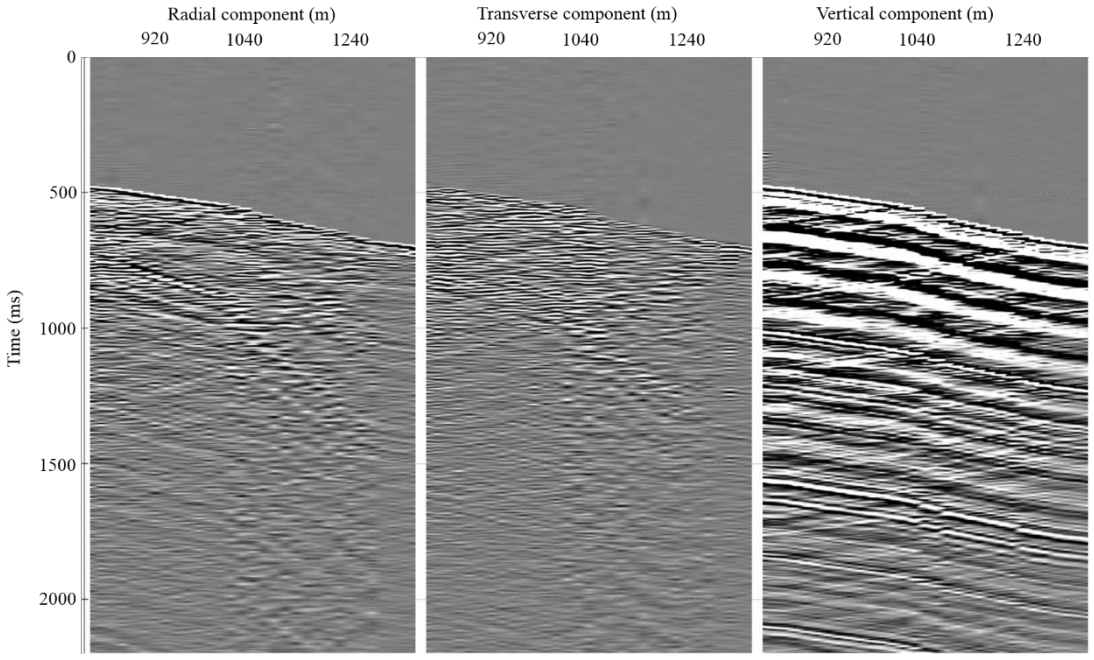

Figure A.10-2. Coniston 3. 3C VSP oriented data: radial (left panel), transverse (middle panel), and vertical (right panel) components.

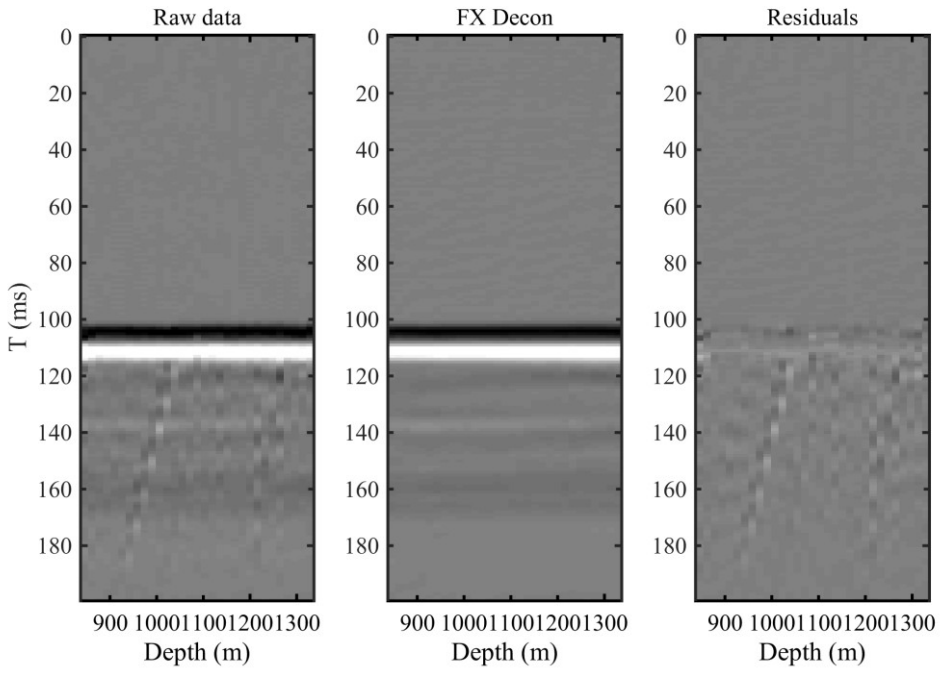

Figure A.10-3. Coniston 3. Results of attenuation of upgoing wavefield by using FX deconvolution. From left to right: original data, result of FX deconvolution and the difference.

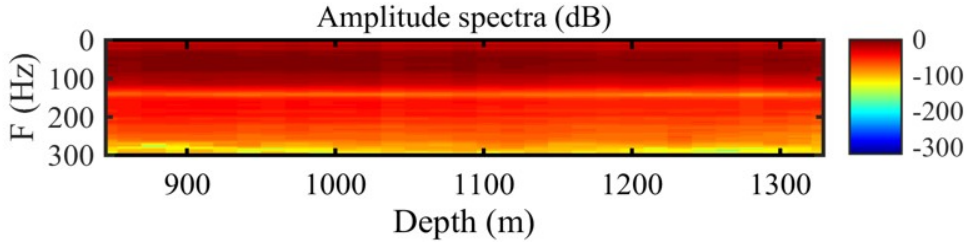

Figure A.10-4. Coniston 3. Amplitude spectra after FX deconvolution.

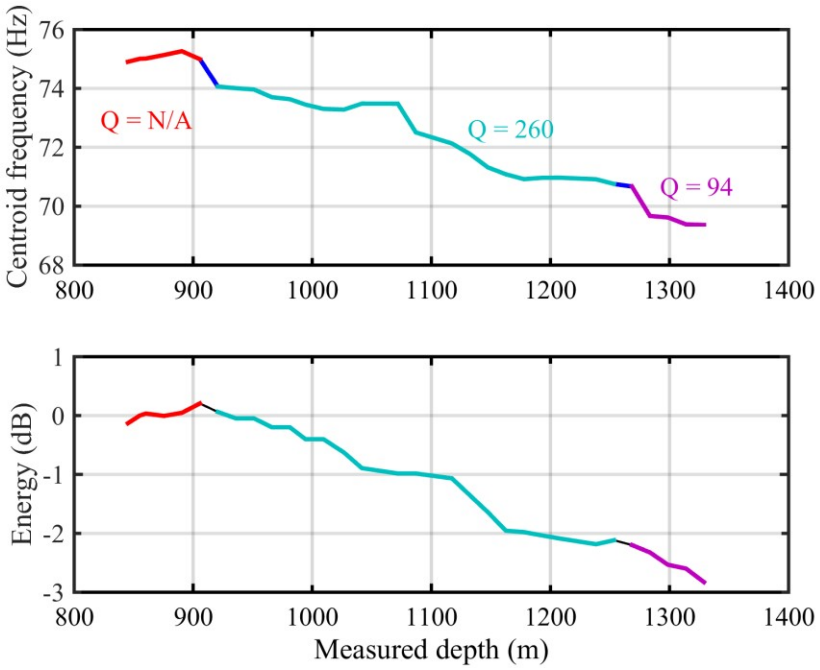

Figure A.10-5. Coniston 3. Results of centroid frequency (top panel) and energy (bottom panel) decay estimation. Estimated attenuation values are derived for 3 stratigraphic intervals.

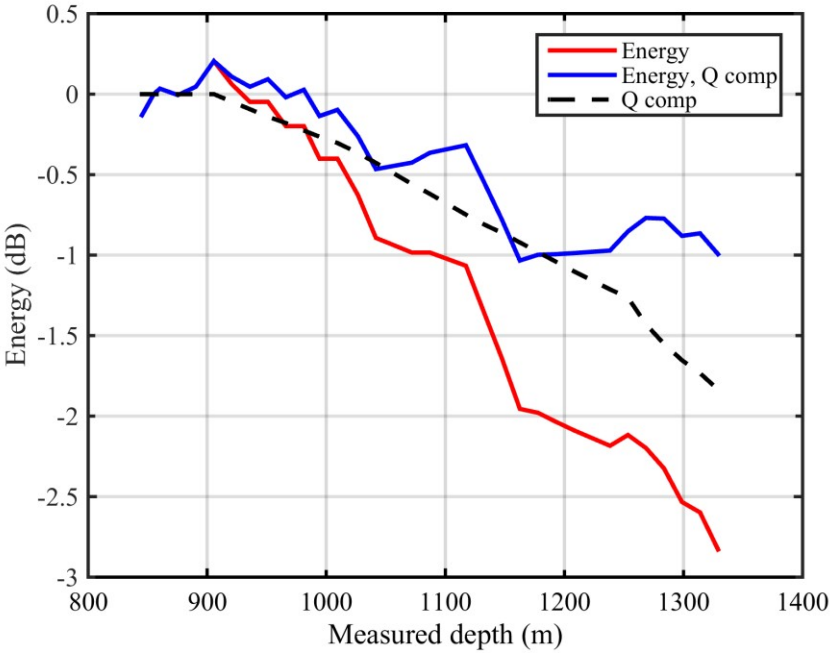

Figure A.10-6. Coniston 3. Results of energy decay curve from direct wave (divergence variation is applied) (red); attenuation component of the energy decay (black) and result of the energy decay compensation (blue).

A.11. Coniston 5 results

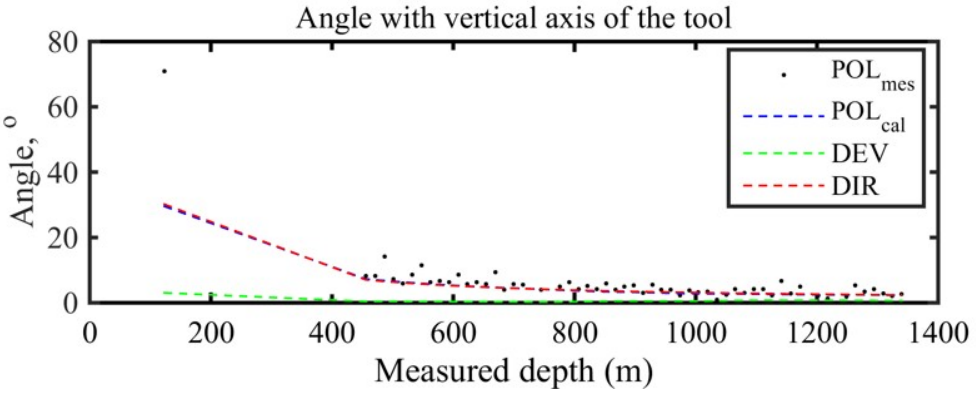

Figure A.11-1. Coniston 5. Results of the orientation: measured polarization of P-wave in respect to a vertical axis of the VSP tool (black dots); calculated polarization of P-wave in respect to a vertical axis of the VSP tool (blue dash line); well inclination (green dash line); angle between a vertical direction and the direction of P-wave propagation (red dash line).

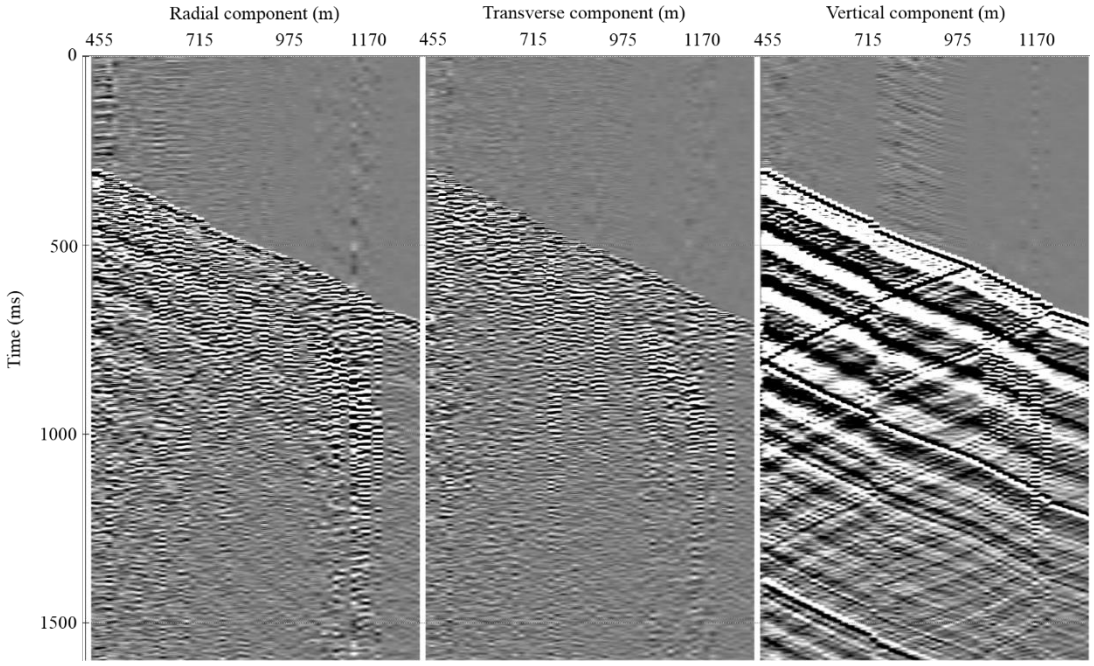

Figure A.11-2. Coniston 5. 3C VSP oriented data: radial (left panel), transverse (middle panel), and vertical (right panel) components.

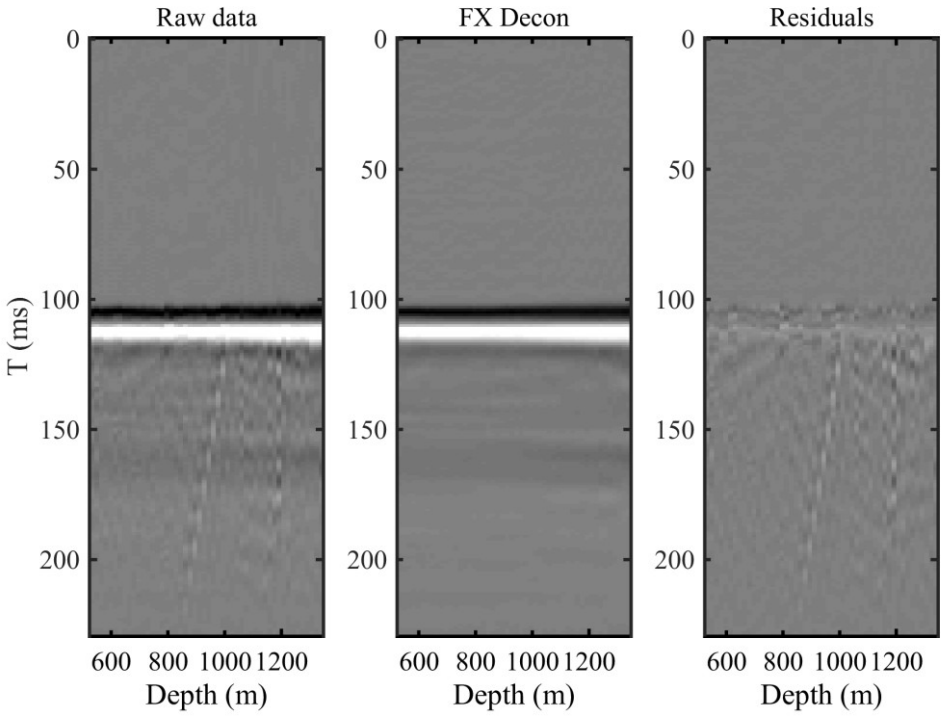

Figure A.11-3. Coniston 5. Results of attenuation of upgoing wavefield by using FX deconvolution. From left to right: original data, result of FX deconvolution and the difference.

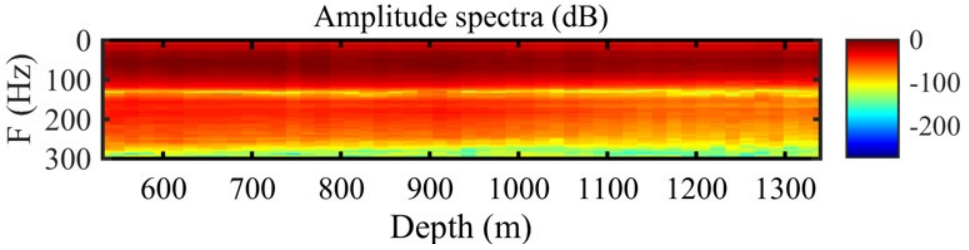

Figure A.11-4. Coniston 5. Amplitude spectra after FX deconvolution.

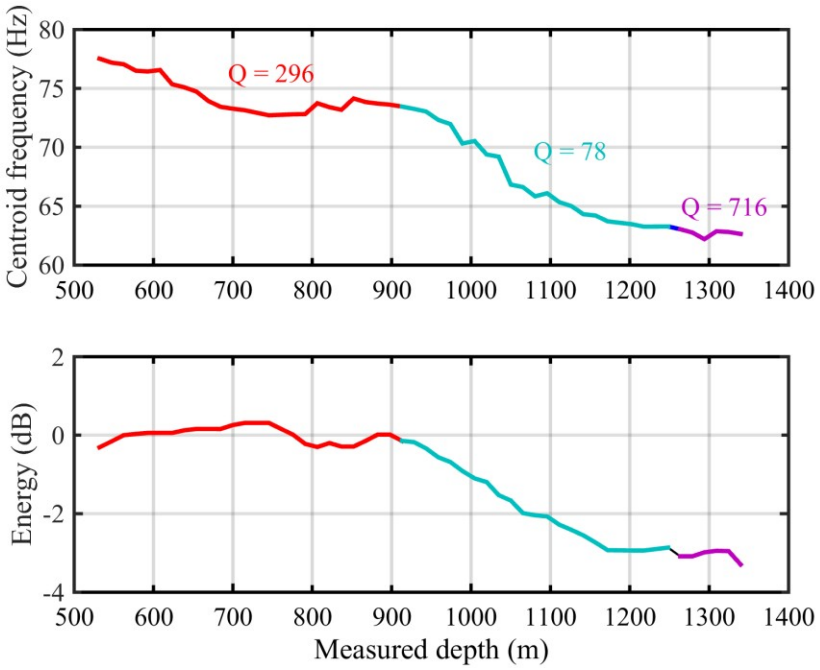

Figure A.11-5. Coniston 5. Results of centroid frequency (top panel) and energy (bottom panel) decay estimation. Estimated attenuation values are derived for 3 stratigraphic intervals.

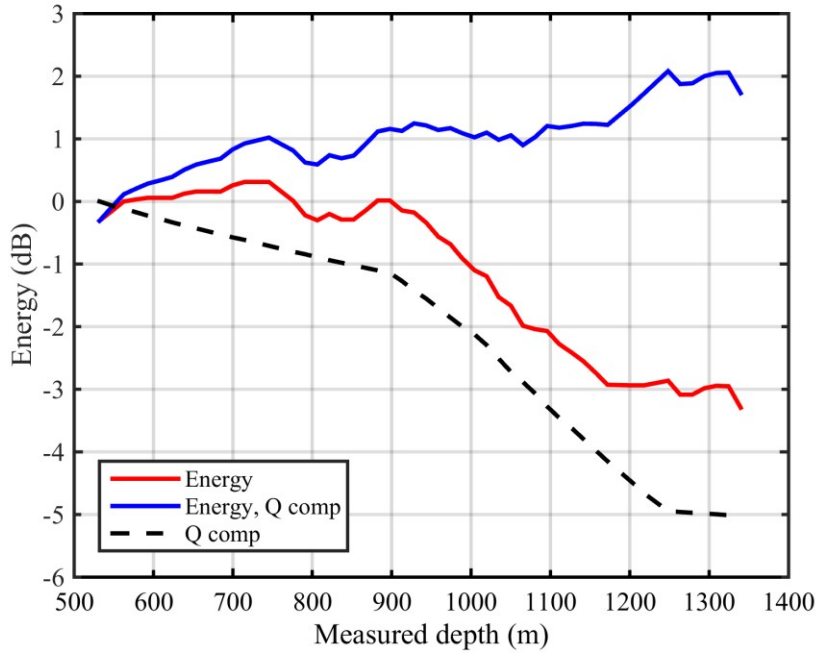

Figure A.11-6. Coniston 5. Results of energy decay curve from direct wave (divergence variation is applied) (red); attenuation component of the energy decay (black) and result of the energy decay compensation (blue).

A.12. Coniston 7 results

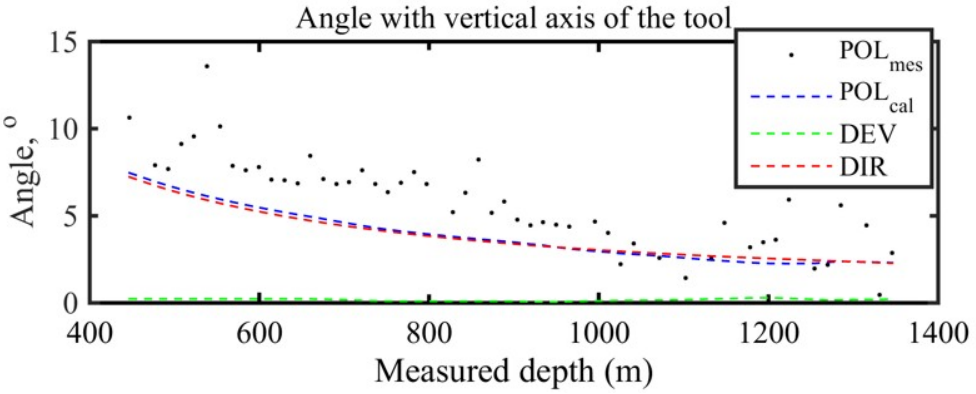

Figure A.12-1. Coniston 7. Results of the orientation: measured polarization of P-wave in respect to a vertical axis of the VSP tool (black dots); calculated polarization of P-wave in respect to a vertical axis of the VSP tool (blue dash line); well inclination (green dash line); angle between a vertical direction and the direction of P-wave propagation (red dash line).

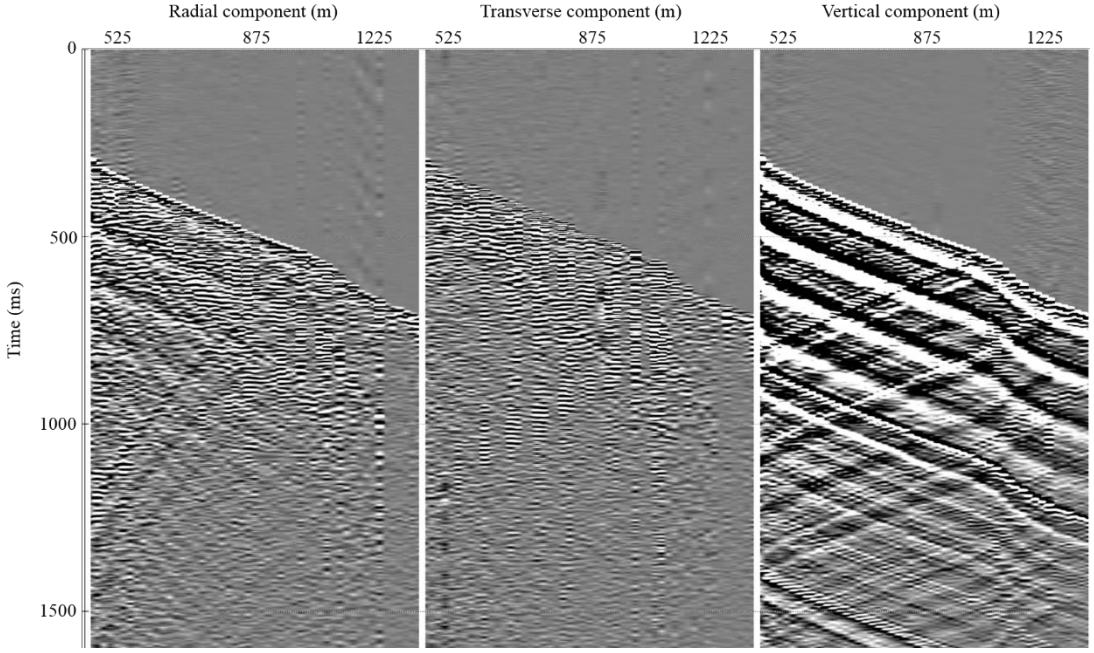

Figure A.12-2. Coniston 7. 3C VSP oriented data: radial (left panel), transverse (middle panel), and vertical (right panel) components.

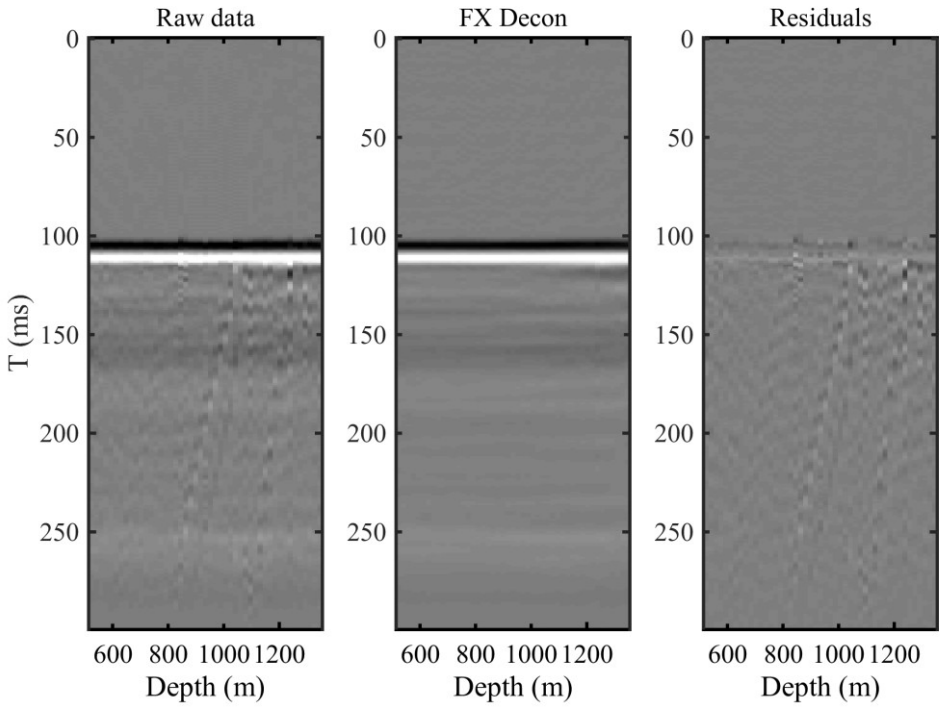

Figure A.12-3. Coniston 7. Results of attenuation of upgoing wavefield by using FX deconvolution. From left to right: original data, result of FX deconvolution and the difference.

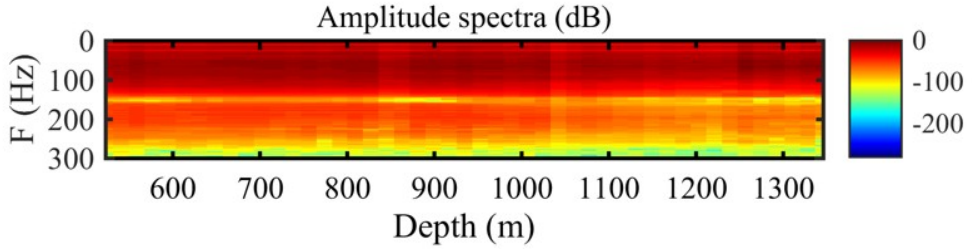

Figure A.12-4. Coniston 7. Amplitude spectra after FX deconvolution.

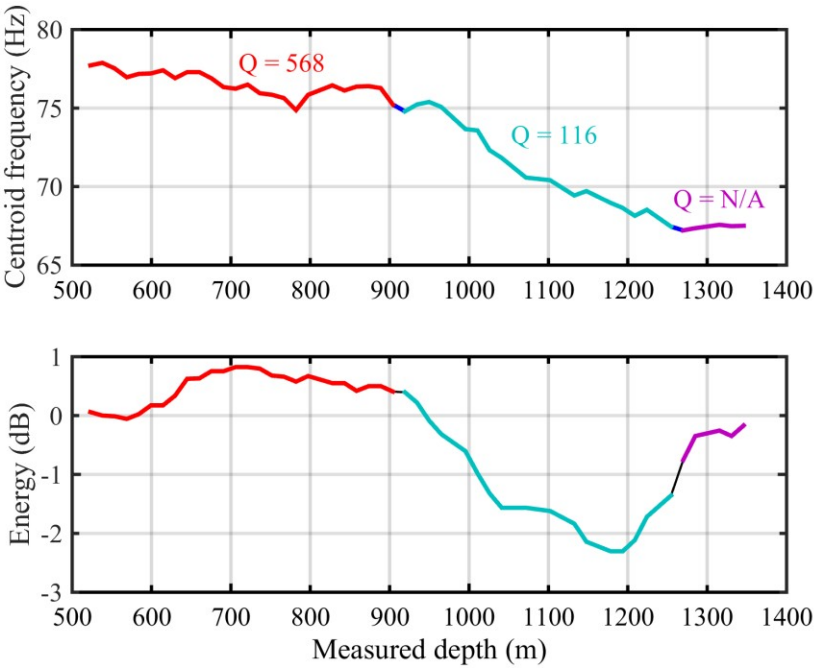

Figure A.12-5. Coniston 7. Results of centroid frequency (top panel) and energy (bottom panel) decay estimation. Estimated attenuation values are derived for 3 stratigraphic intervals.

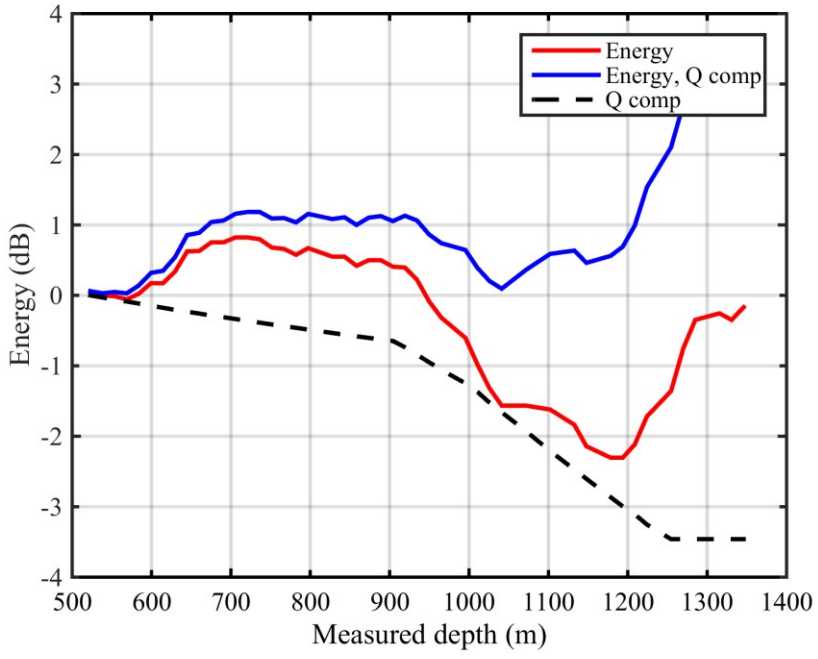

Figure A.12-6. Coniston 7. Results of energy decay curve from direct wave (divergence variation is applied) (red); attenuation component of the energy decay (black) and result of the energy decay compensation (blue).

A.13. Dixon 2 results

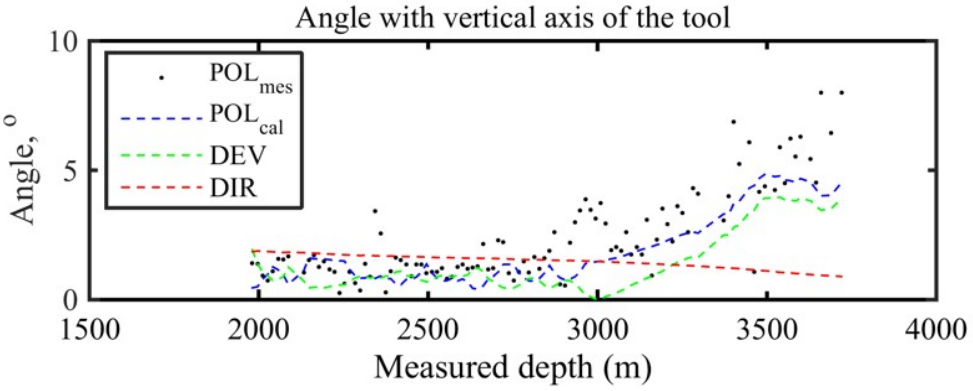

Figure A.13-1. Dixon 2. Results of the orientation: measured polarization of P-wave in respect to a vertical axis of the VSP tool (black dots); calculated polarization of P-wave in respect to a vertical axis of the VSP tool (blue dash line); well inclination (green dash line); angle between a vertical direction and the direction of P-wave propagation (red dash line).

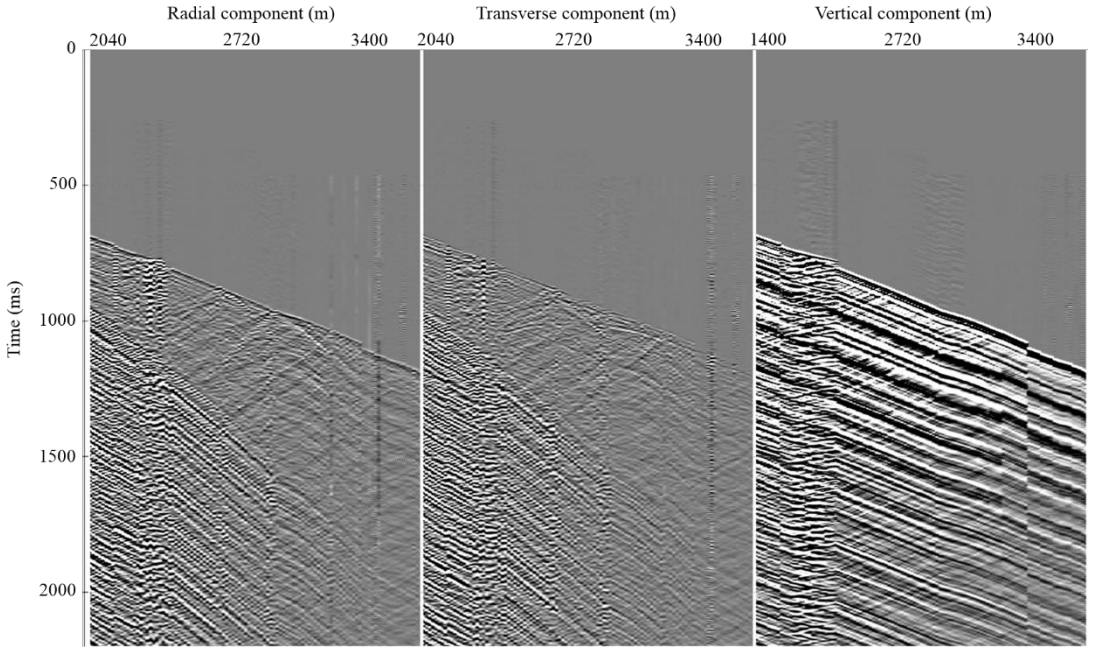

Figure A.13-2. Dixon 2. 3C VSP oriented data: radial (left panel), transverse (middle panel), and vertical (right panel) components.

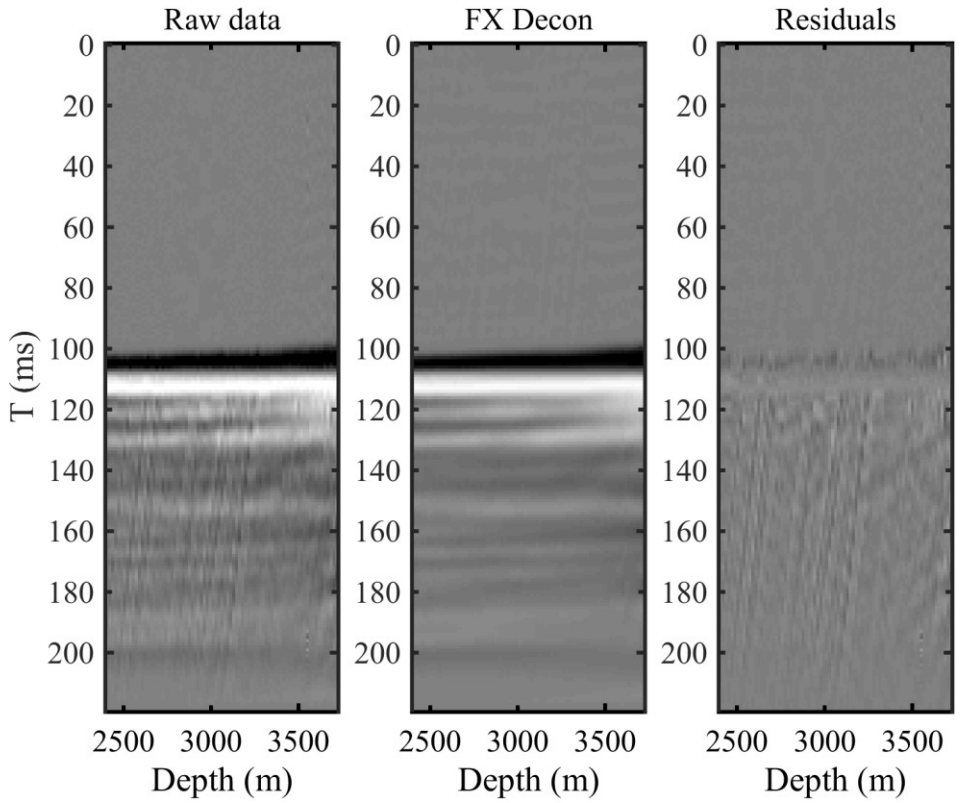

Figure A.13-3. Dixon 2. Results of attenuation of upgoing wavefield by using FX deconvolution. From left to right: original data, result of FX deconvolution and the difference.

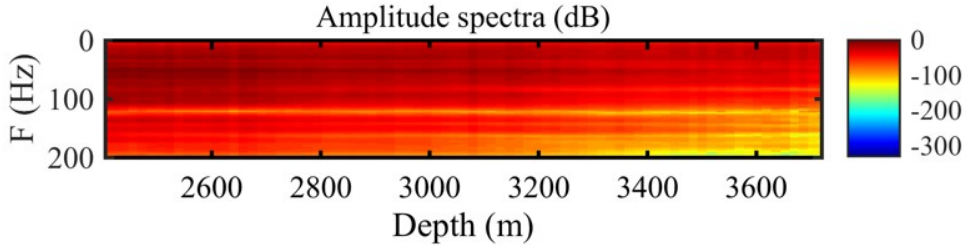

Figure A.13-4. Dixon 2. Amplitude spectra after FX deconvolution.

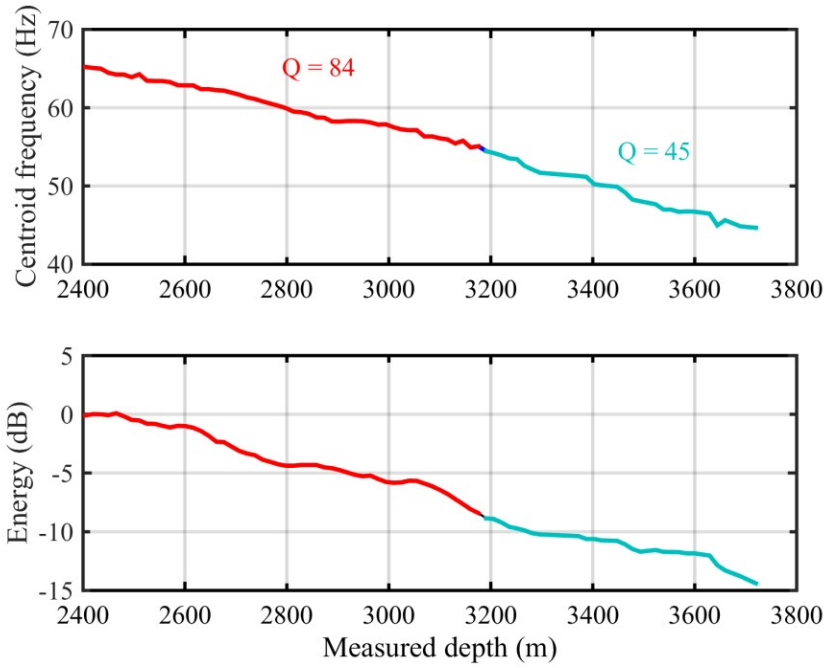

Figure A.13-5. Dixon 2. Results of centroid frequency (top panel) and energy (bottom panel) decay estimation. Estimated attenuation values are derived for 2 stratigraphic intervals.

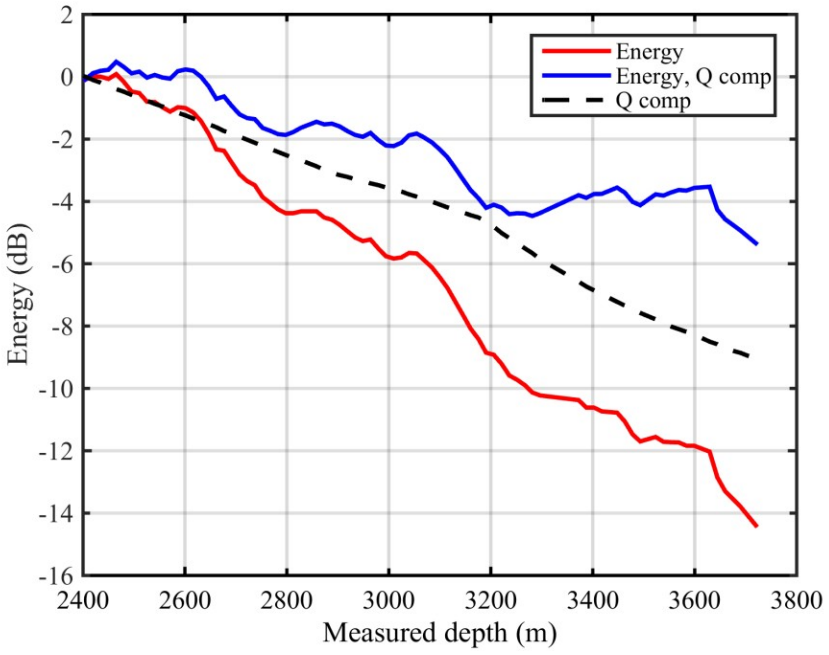

Figure A.13-6. Dixon 2. Results of energy decay curve from direct wave (divergence variation is applied) (red); attenuation component of the energy decay (black) and result of the energy decay compensation (blue).

A.14. Fletcher 1 results

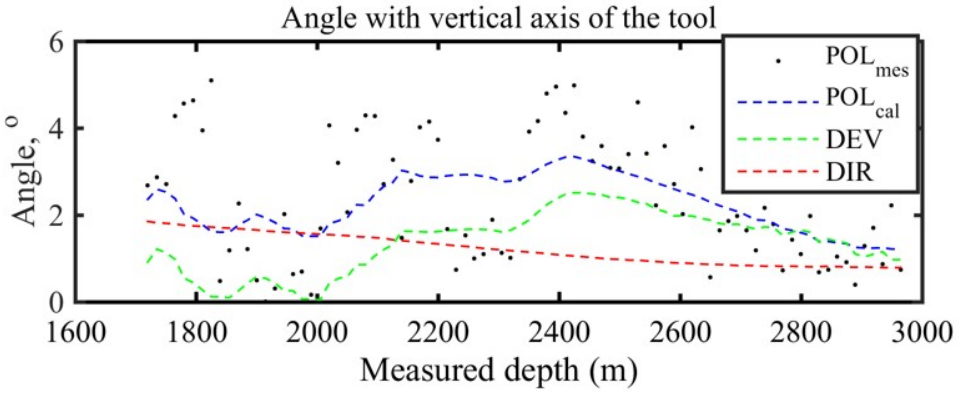

Figure A.14-1. Fletcher 1. Results of the orientation: measured polarization of P-wave in respect to a vertical axis of the VSP tool (black dots); calculated polarization of P-wave in respect to a vertical axis of the VSP tool (blue dash line); well inclination (green dash line); angle between a vertical direction and the direction of P-wave propagation (red dash line).

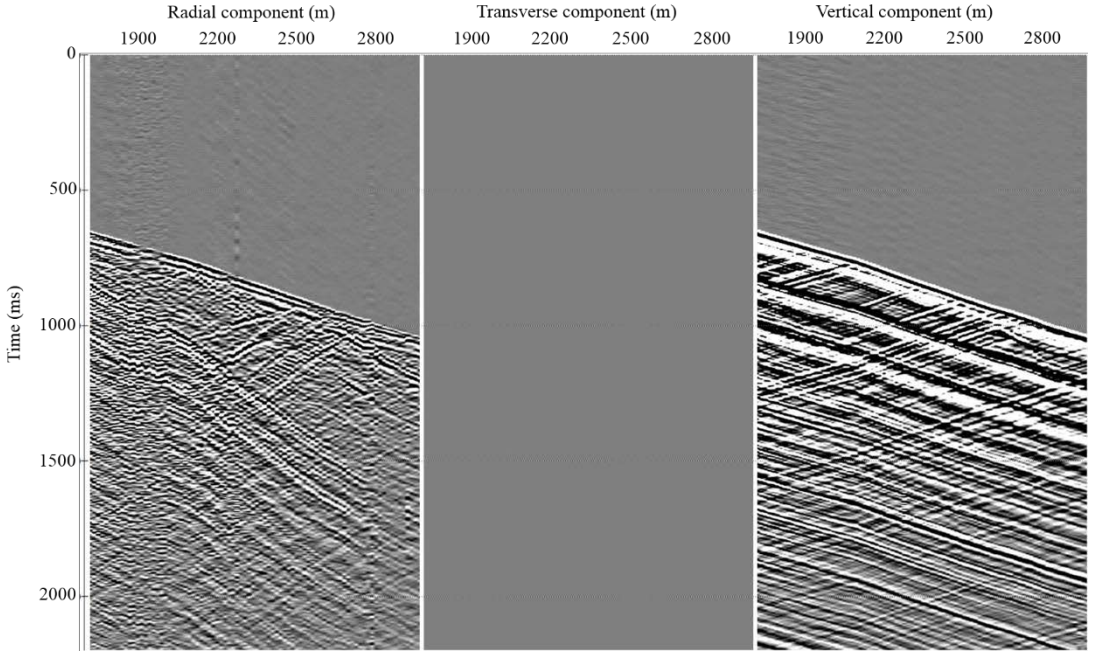

Figure A.14-2. Fletcher 1. 3C VSP oriented data: radial (left panel), transverse (middle panel), and vertical (right panel) components.

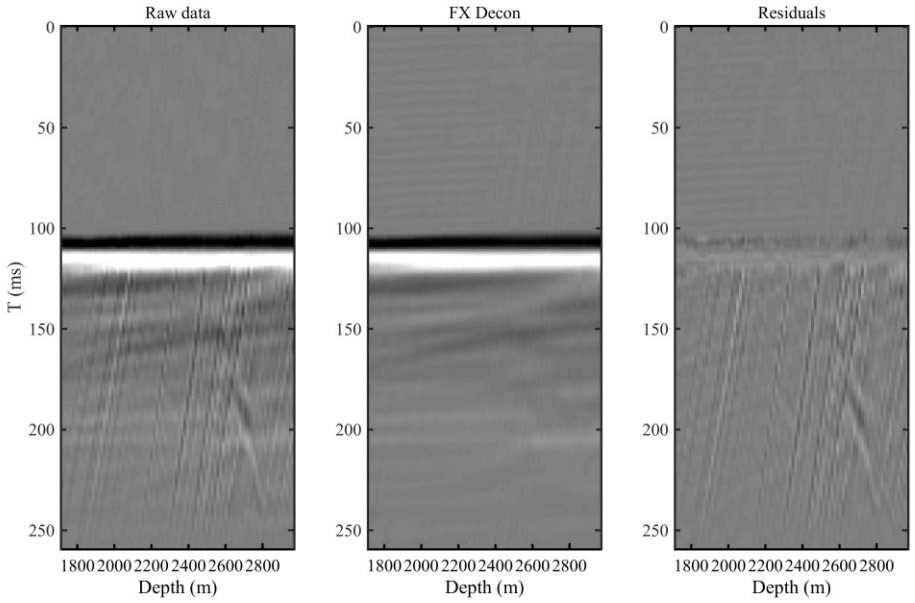

Figure A.14-3. Fletcher 1. Results of attenuation of upgoing wavefield by using FX deconvolution. From left to right: original data, result of FX deconvolution and the difference.

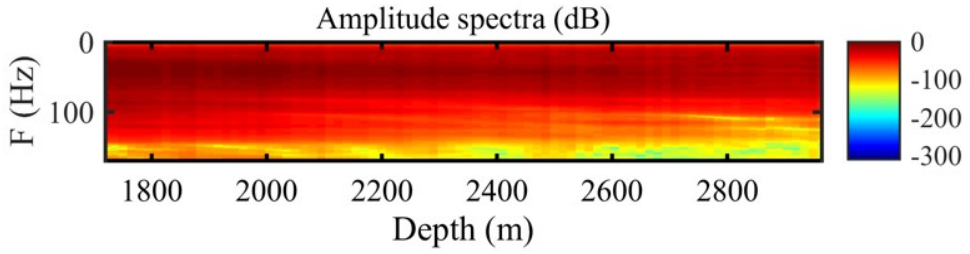

Figure A.14-4. Fletcher 1. Amplitude spectra after FX deconvolution.

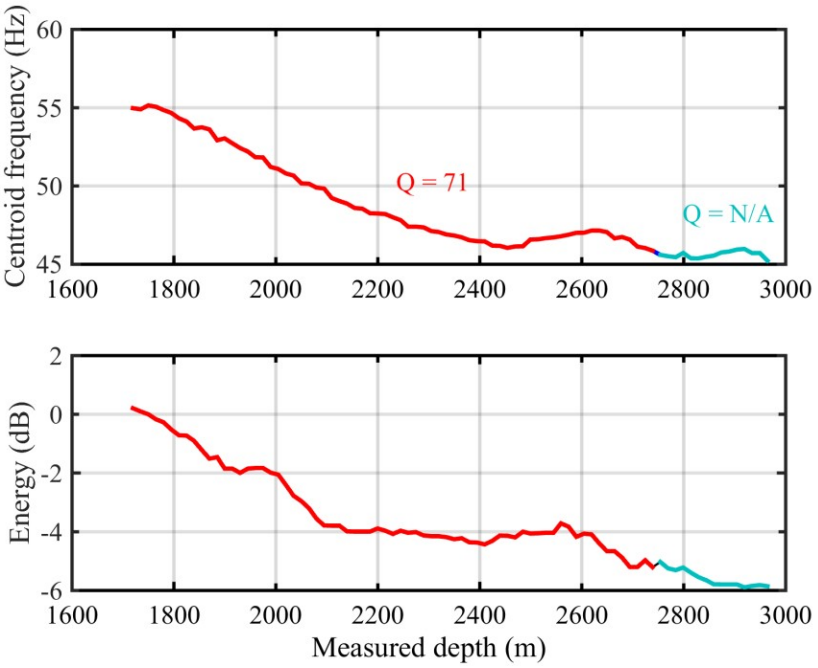

Figure A.14-5. Fletcher 1. Results of centroid frequency (top panel) and energy (bottom panel) decay estimation. Estimated attenuation values are derived for 2 stratigraphic intervals.

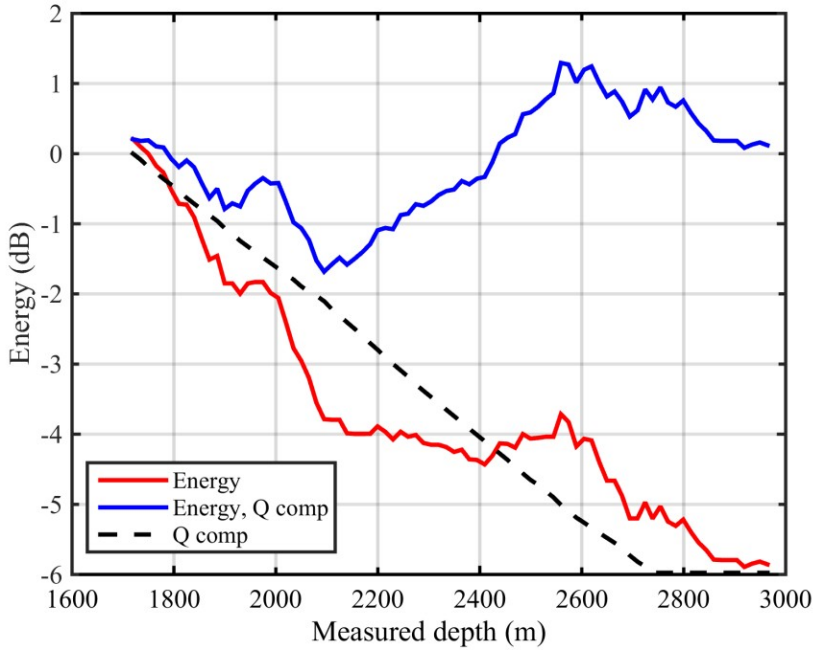

Figure A.14-6. Fletcher 1. Results of energy decay curve from direct wave (divergence variation is applied) (red); attenuation component of the energy decay (black) and result of the energy decay compensation (blue).

A.15. Grange 1 results

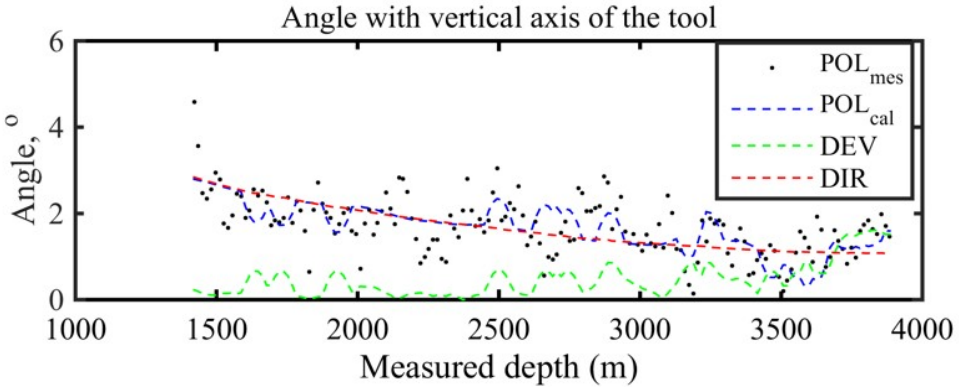

Figure A.15-1. Grange 1. Results of the orientation: measured polarization of P-wave in respect to a vertical axis of the VSP tool (black dots); calculated polarization of P-wave in respect to a vertical axis of the VSP tool (blue dash line); well inclination (green dash line); angle between a vertical direction and the direction of P-wave propagation (red dash line).

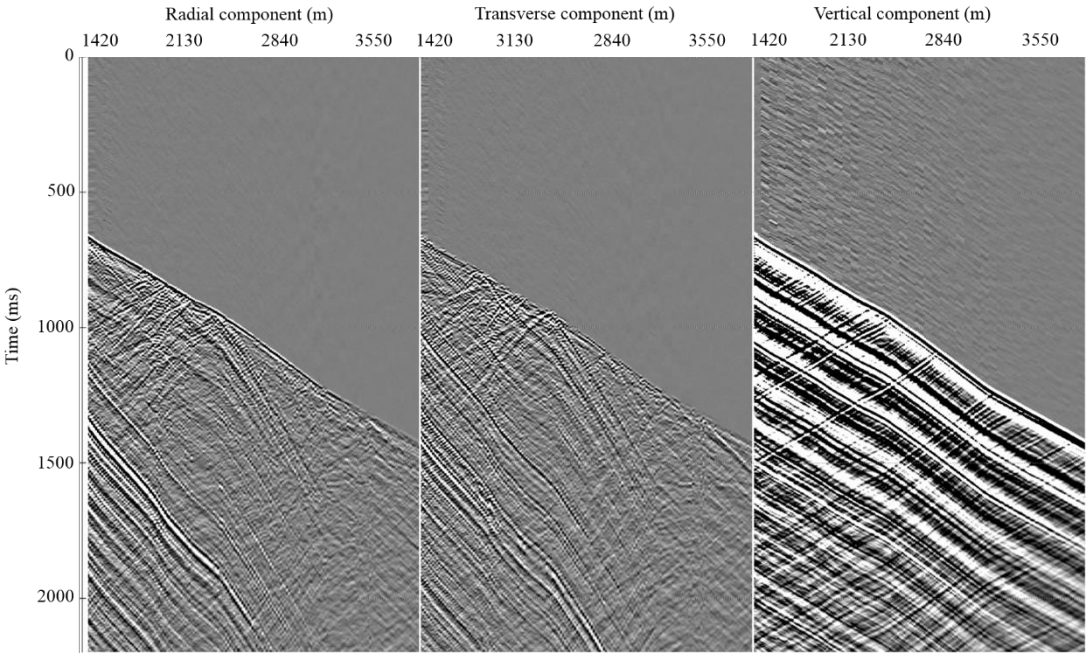

Figure A.15-2. Grange 1. 3C VSP oriented data: radial (left panel), transverse (middle panel), and vertical (right panel) components.

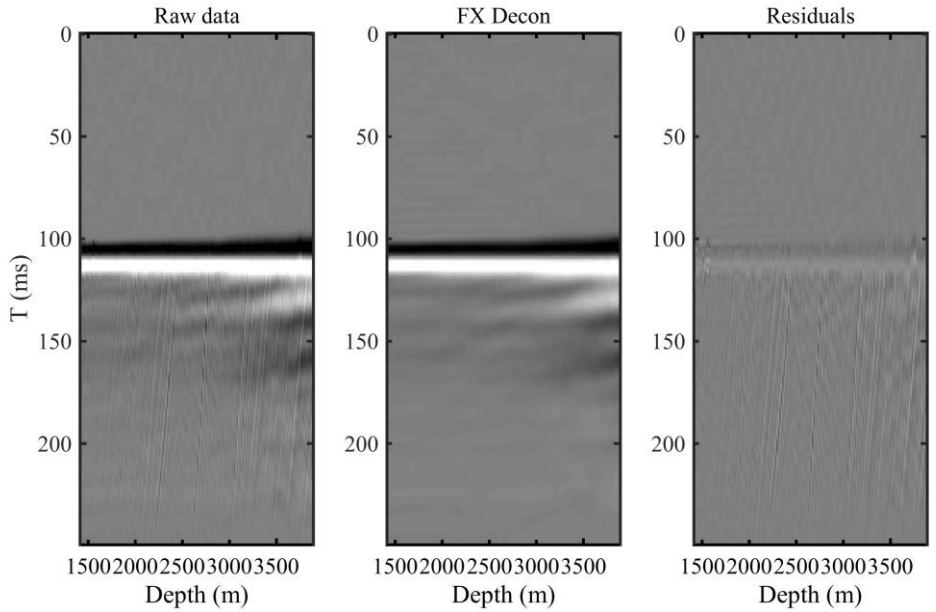

Figure A.15-3. Grange 1. Results of attenuation of upgoing wavefield by using FX deconvolution. From left to right: original data, result of FX deconvolution and the difference.

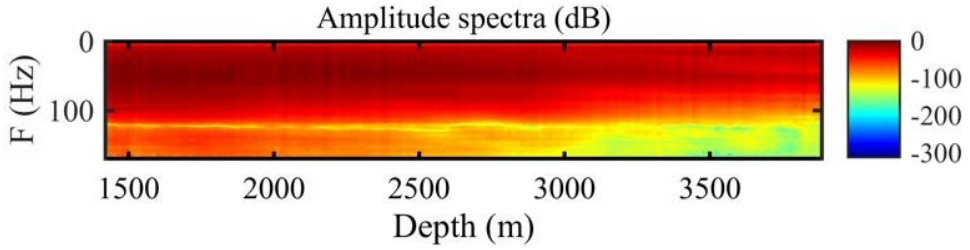

Figure A.15-4. Grange 1. Amplitude spectra after FX deconvolution.

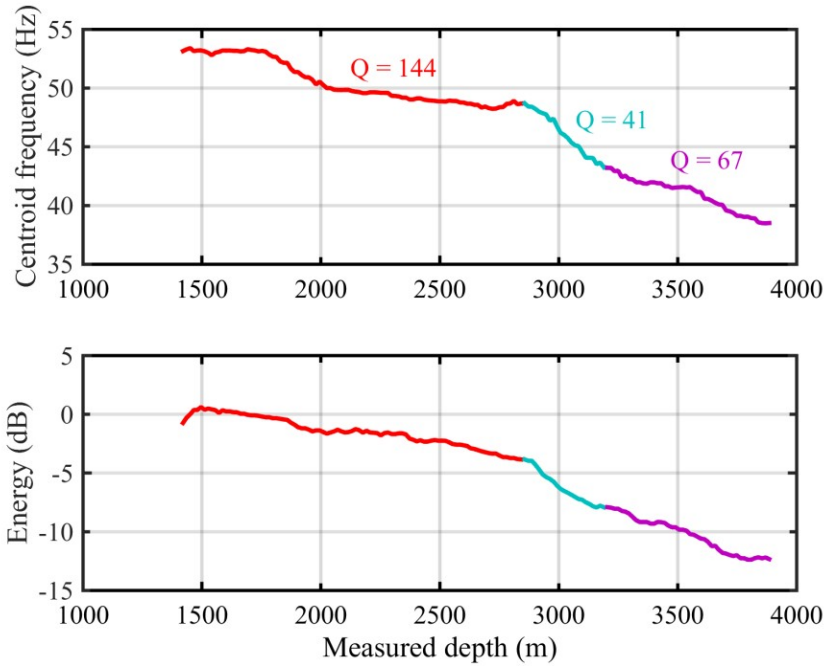

Figure A.15-5. Grange 1. Results of centroid frequency (top panel) and energy (bottom panel) decay estimation. Estimated attenuation values are derived for 3 stratigraphic intervals.

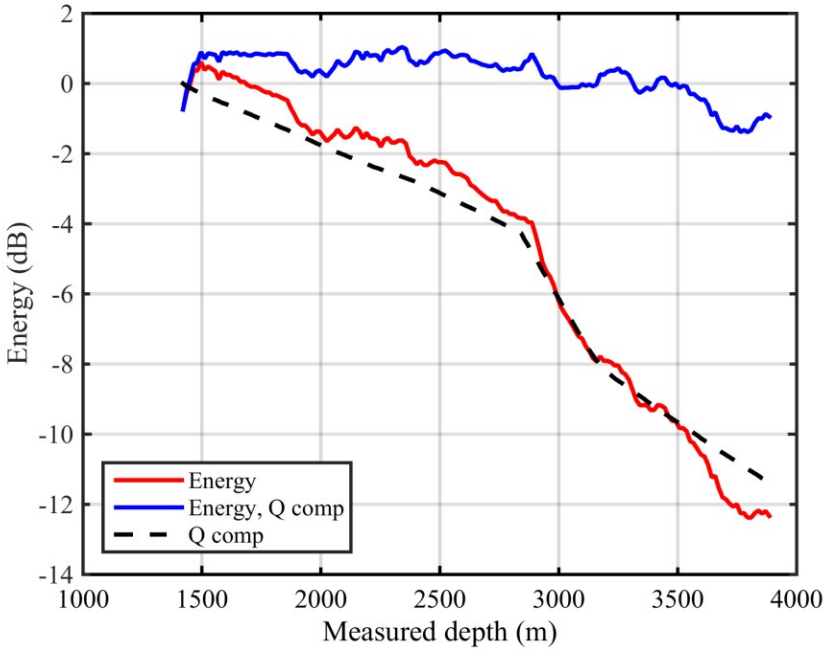

Figure A.15-6. Grange 1. Results of energy decay curve from direct wave (divergence variation is applied) (red); attenuation component of the energy decay (black) and result of the energy decay compensation (blue).

A.16. Guardian 1 results

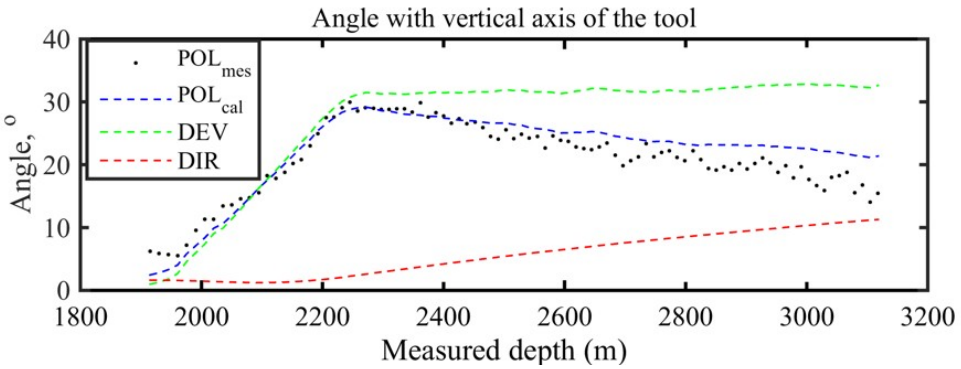

Figure A.16-1. Guardian 1. Results of the orientation: measured polarization of P-wave in respect to a vertical axis of the VSP tool (black dots); calculated polarization of P-wave in respect to a vertical axis of the VSP tool (blue dash line); well inclination (green dash line); angle between a vertical direction and the direction of P-wave propagation (red dash line).

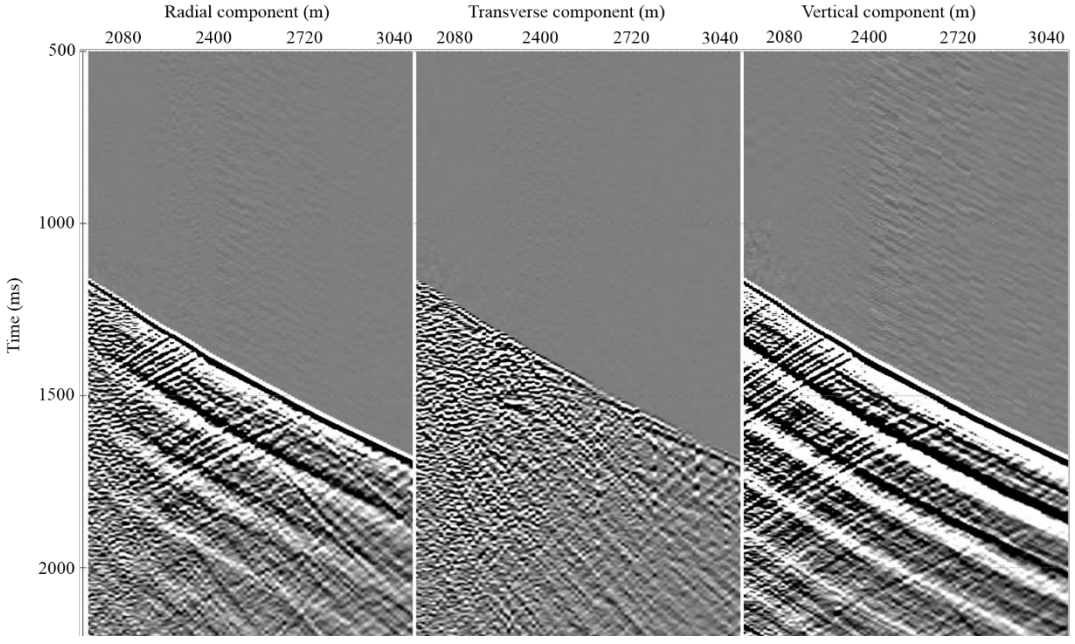

Figure A.16-2. Guardian 1. 3C VSP oriented data: radial (left panel), transverse (middle panel), and vertical (right panel) components.

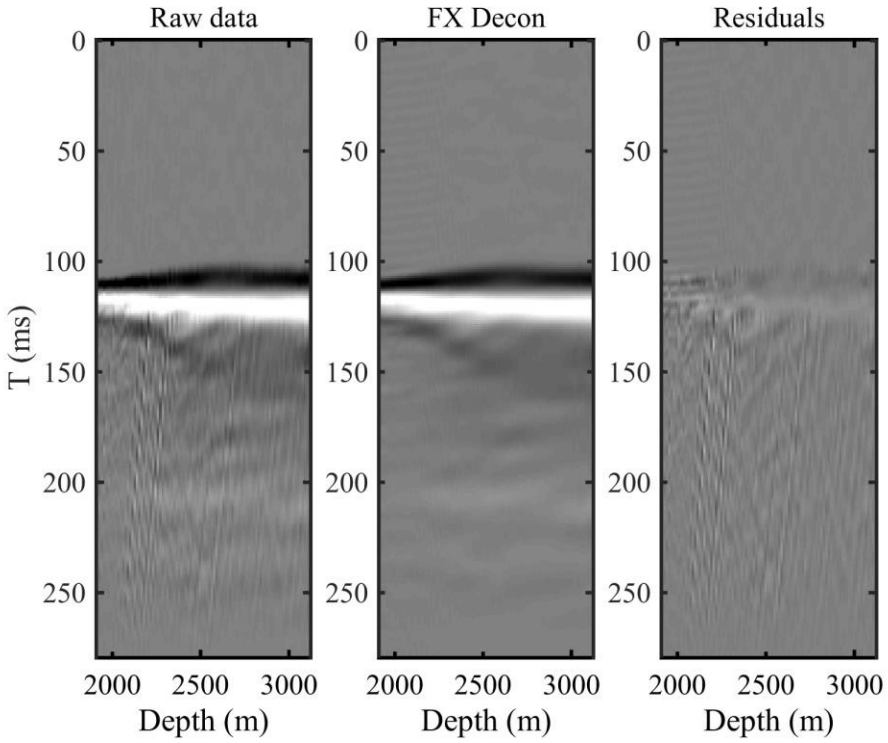

Figure A.16-3. Guardian 1. Results of attenuation of upgoing wavefield by using FX deconvolution. From left to right: original data, result of FX deconvolution and the difference.

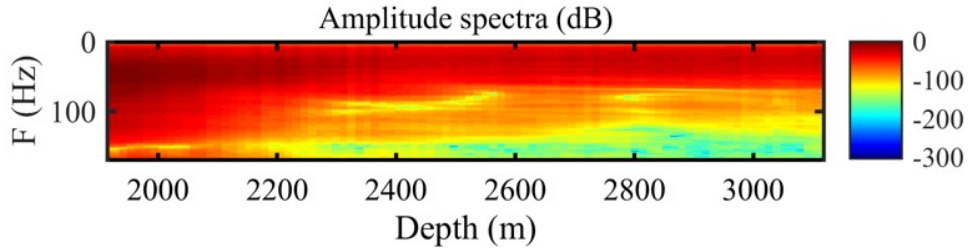

Figure A.16-4. Guardian 1. Amplitude spectra after FX deconvolution.

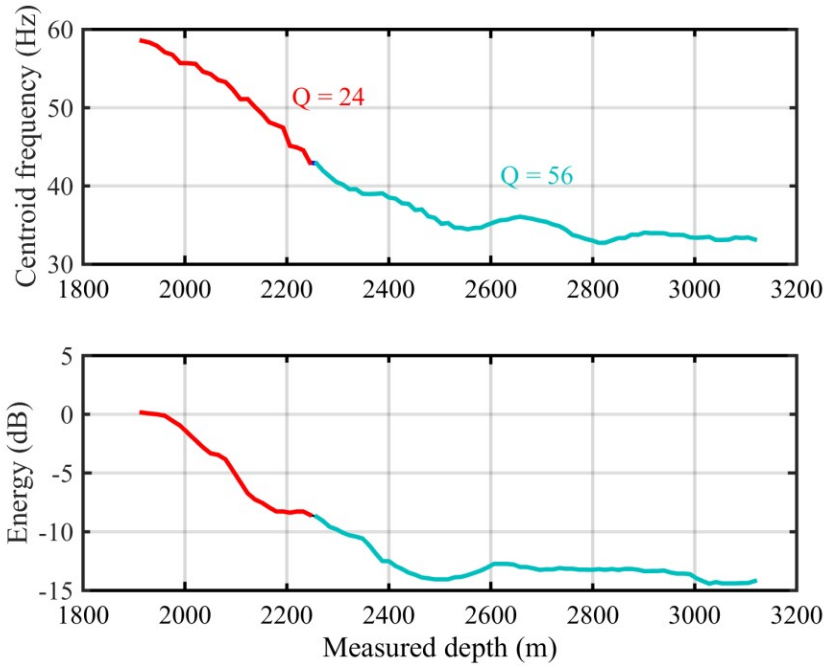

Figure A.16-5. Guardian 1. Results of centroid frequency (top panel) and energy (bottom panel) decay estimation. Estimated attenuation values are derived for 2 stratigraphic intervals.

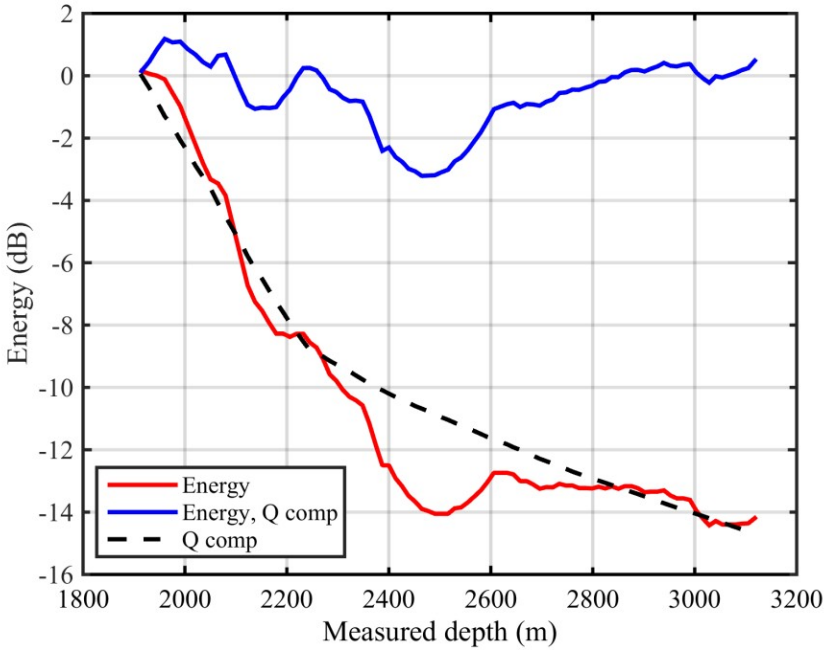

Figure A.16-6. Guardian 1. Results of energy decay curve from direct wave (divergence variation is applied) (red); attenuation component of the energy decay (black) and result of the energy decay compensation (blue).

A.17. Halyard 1 results

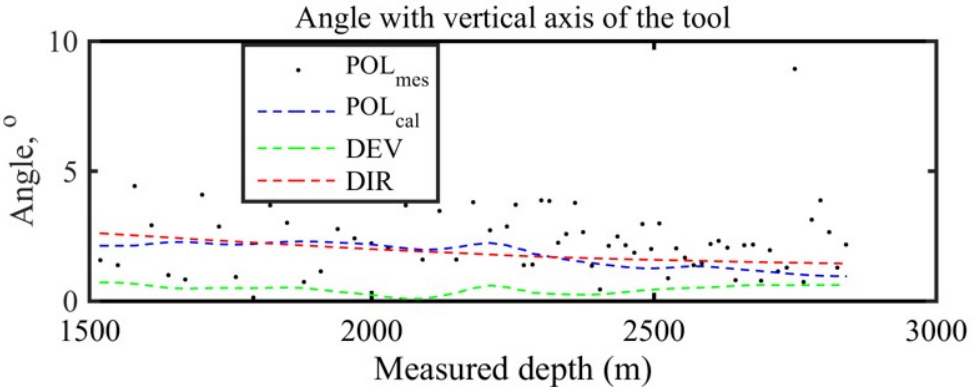

Figure A.17-1. Halyard 1. Results of the orientation: measured polarization of P-wave in respect to a vertical axis of the VSP tool (black dots); calculated polarization of P-wave in respect to a vertical axis of the VSP tool (blue dash line); well inclination (green dash line); angle between a vertical direction and the direction of P-wave propagation (red dash line).

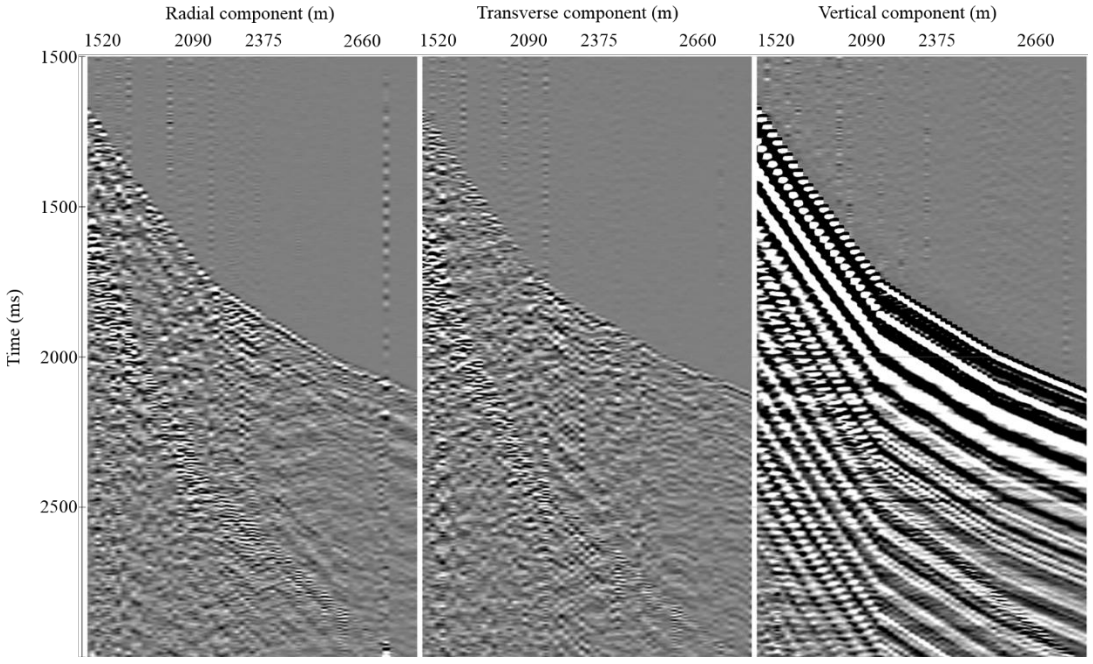

Figure A.17-2. Halyard 1. 3C VSP oriented data: radial (left panel), transverse (middle panel), and vertical (right panel) components.

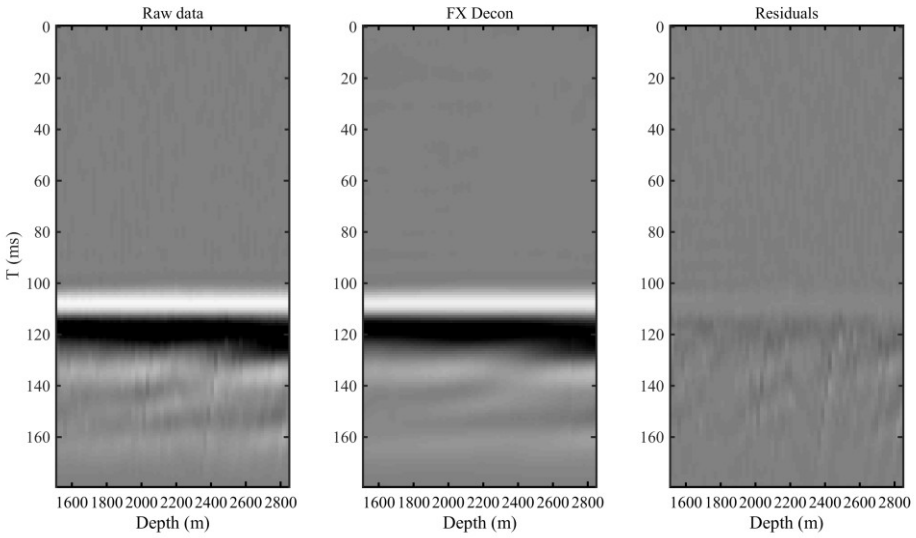

Figure A.17-3. Halyard 1. Results of attenuation of upgoing wavefield by using FX deconvolution. From left to right: original data, result of FX deconvolution and the difference.

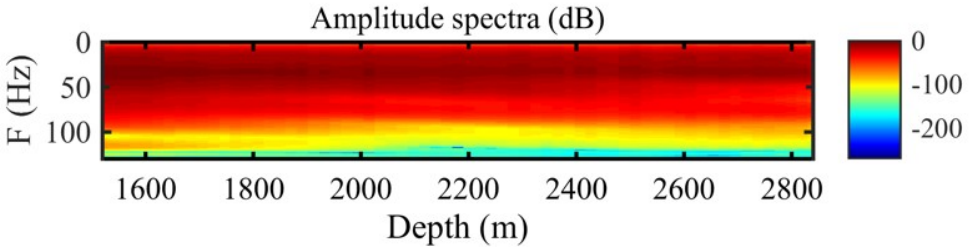

Figure A.17-4. Halyard 1. Amplitude spectra after FX deconvolution.

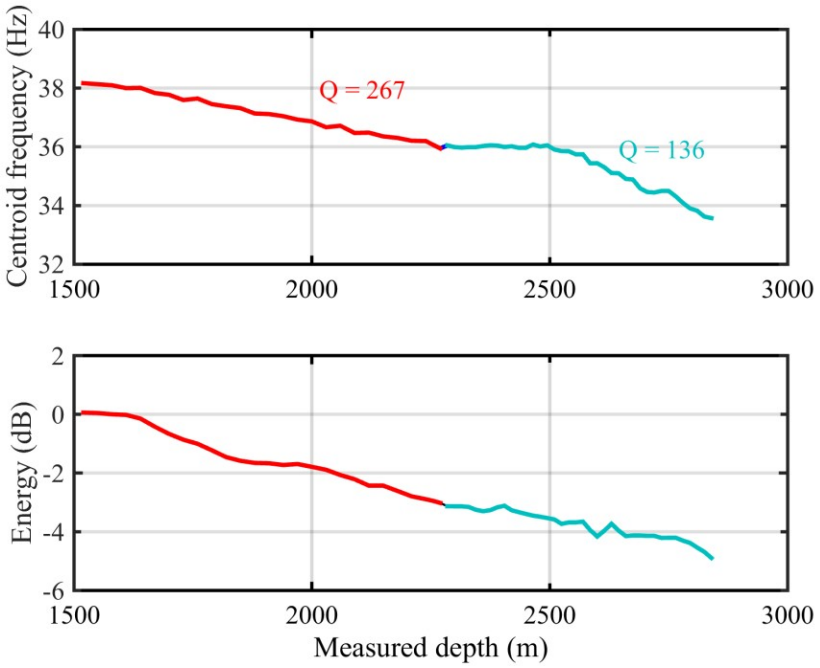

Figure A.17-5. Halyard 1. Results of centroid frequency (top panel) and energy (bottom panel) decay estimation. Estimated attenuation values are derived for 2 stratigraphic intervals.

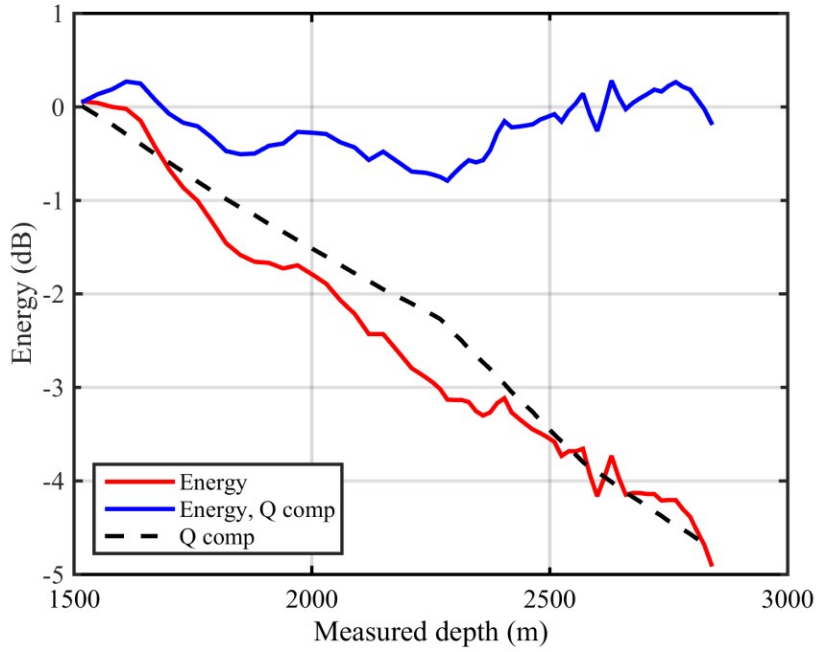

Figure A.17-6. Halyard 1. Results of energy decay curve from direct wave (divergence variation is applied) (red); attenuation component of the energy decay (black) and result of the energy decay compensation (blue).

A.18. Iago 2 results

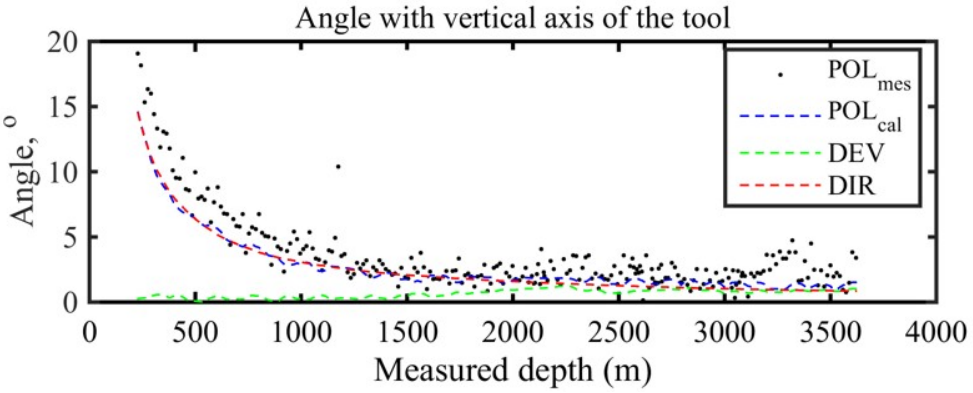

Figure A.18-1. Iago 2. Results of the orientation: measured polarization of P-wave in respect to a vertical axis of the VSP tool (black dots); calculated polarization of P-wave in respect to a vertical axis of the VSP tool (blue dash line); well inclination (green dash line); angle between a vertical direction and the direction of P-wave propagation (red dash line).

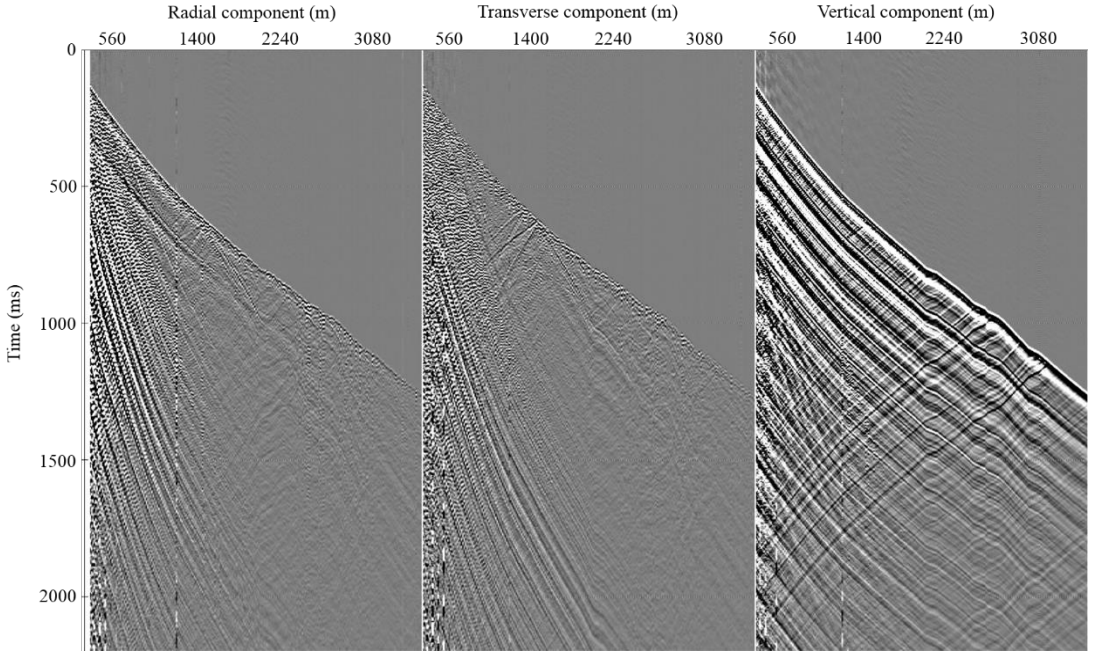

Figure A.18-2. Iago 2. 3C VSP oriented data: radial (left panel), transverse (middle panel), and vertical (right panel) components.

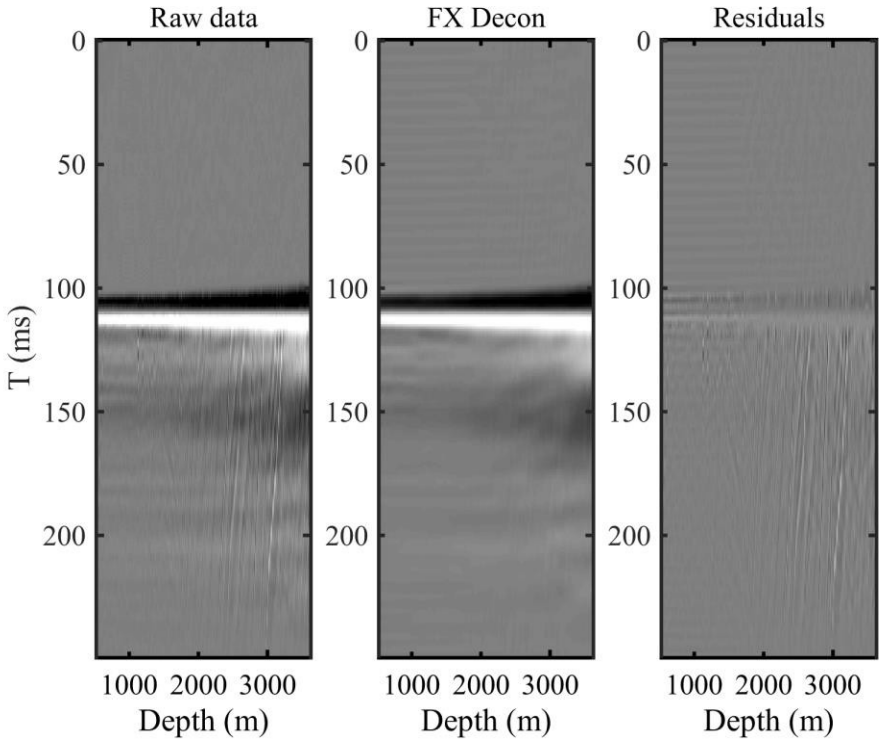

Figure A.18-3. Iago 2. Results of attenuation of upgoing wavefield by using FX deconvolution. From left to right: original data, result of FX deconvolution and the difference.

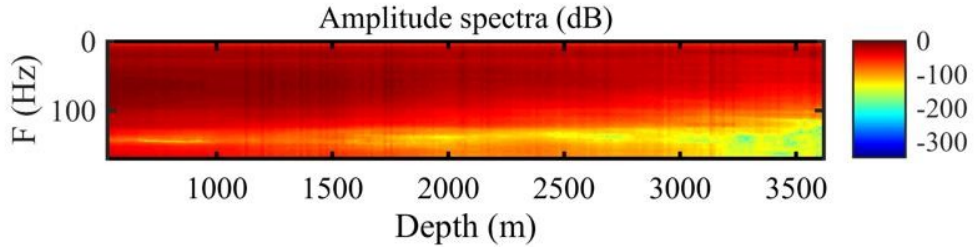

Figure A.18-4. Iago 2. Amplitude spectra after FX deconvolution.\

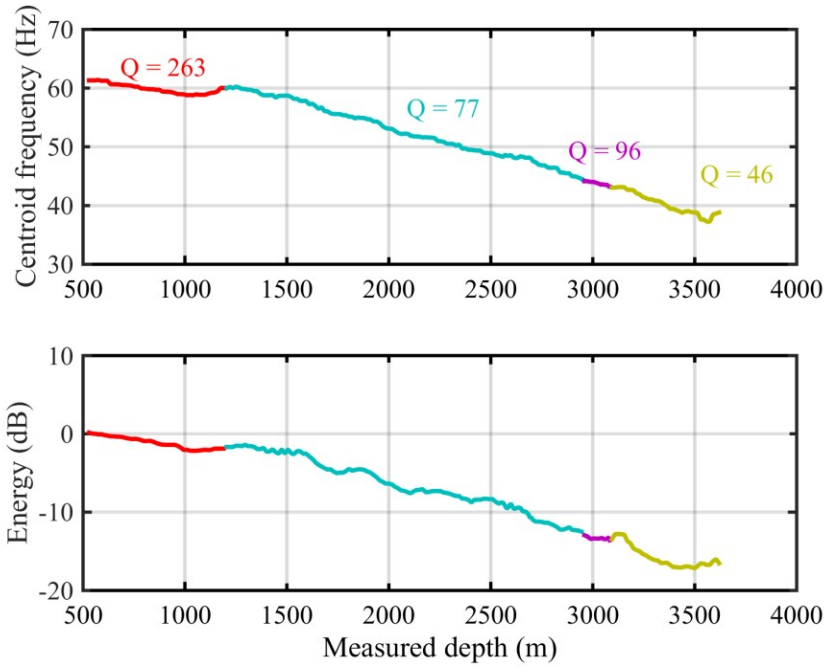

Figure A.18-5. Iago 2. Results of centroid frequency (top panel) and energy (bottom panel) decay estimation. Estimated attenuation values are derived for 4 stratigraphic intervals.

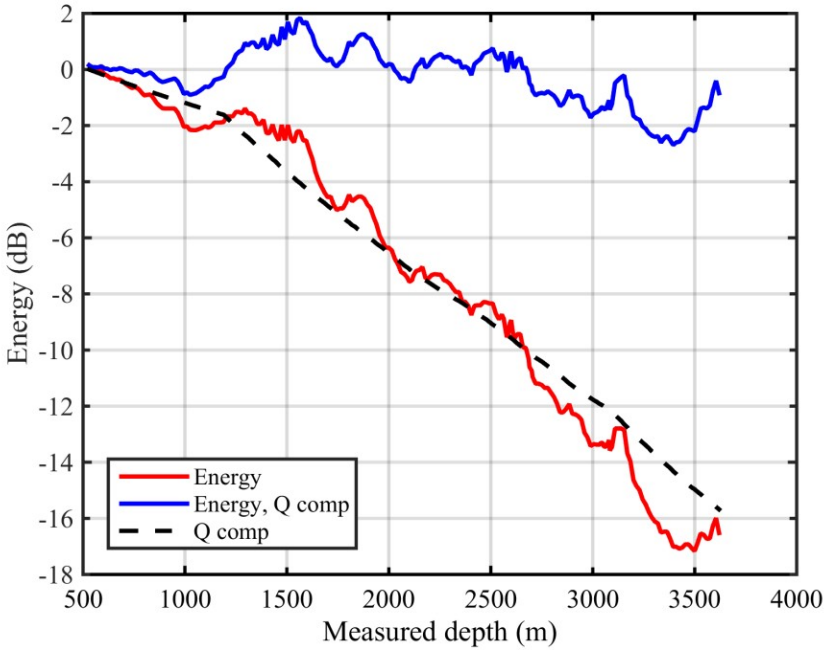

Figure A.18-6. Iago 2. Results of energy decay curve from direct wave (divergence variation is applied) (red); attenuation component of the energy decay (black) and result of the energy decay compensation (blue).

A.19. Iago 3 results

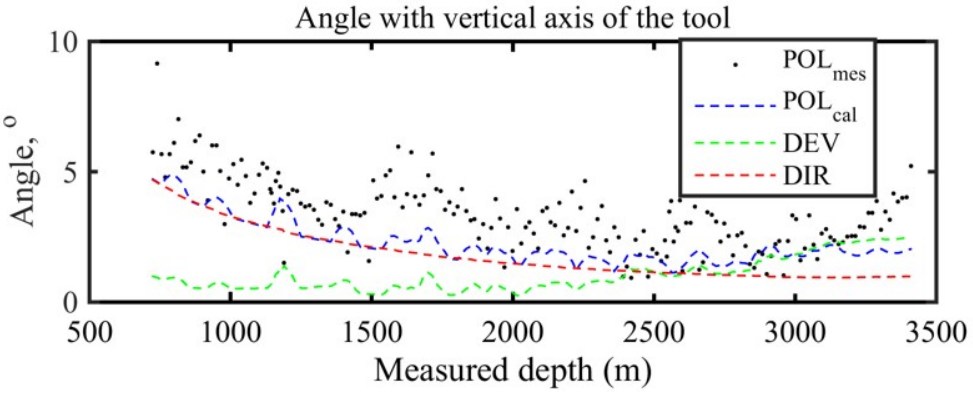

Figure A.19-1. Iago 3. Results of the orientation: measured polarization of P-wave in respect to a vertical axis of the VSP tool (black dots); calculated polarization of P-wave in respect to a vertical axis of the VSP tool (blue dash line); well inclination (green dash line); angle between a vertical direction and the direction of P-wave propagation (red dash line).

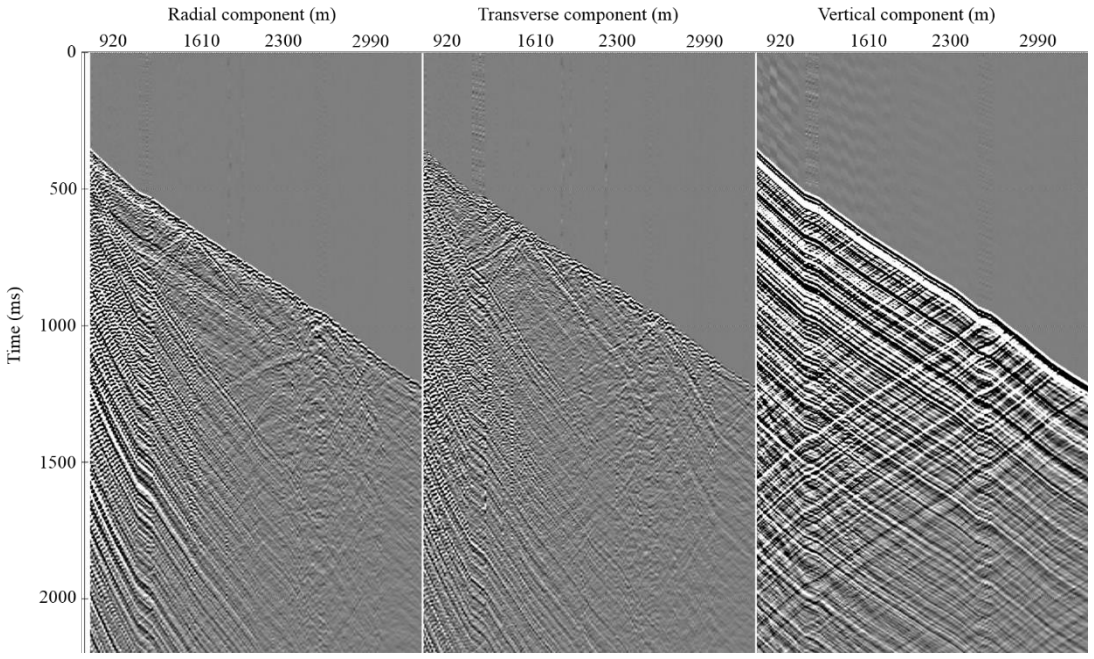

Figure A.19-2. Iago 3. 3C VSP oriented data: radial (left panel), transverse (middle panel), and vertical (right panel) components.

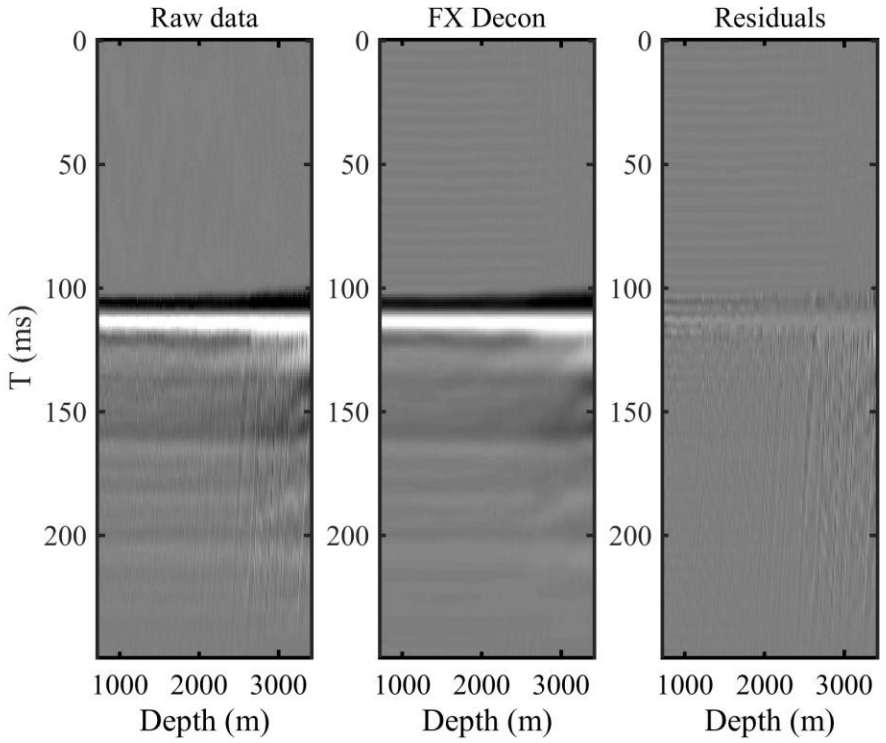

Figure A.19-3. Iago 3. Results of attenuation of upgoing wavefield by using FX deconvolution. From left to right: original data, result of FX deconvolution and the difference.

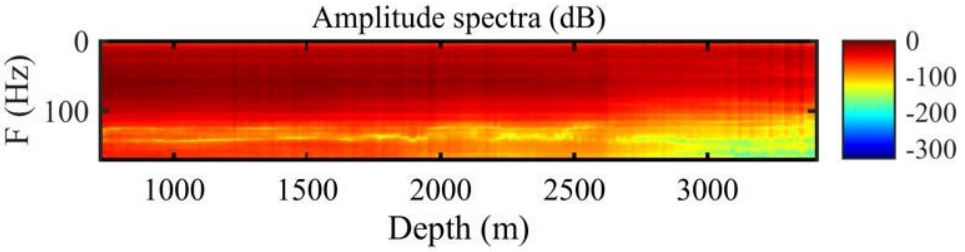

Figure A.19-4. Iago 3. Amplitude spectra after FX deconvolution.

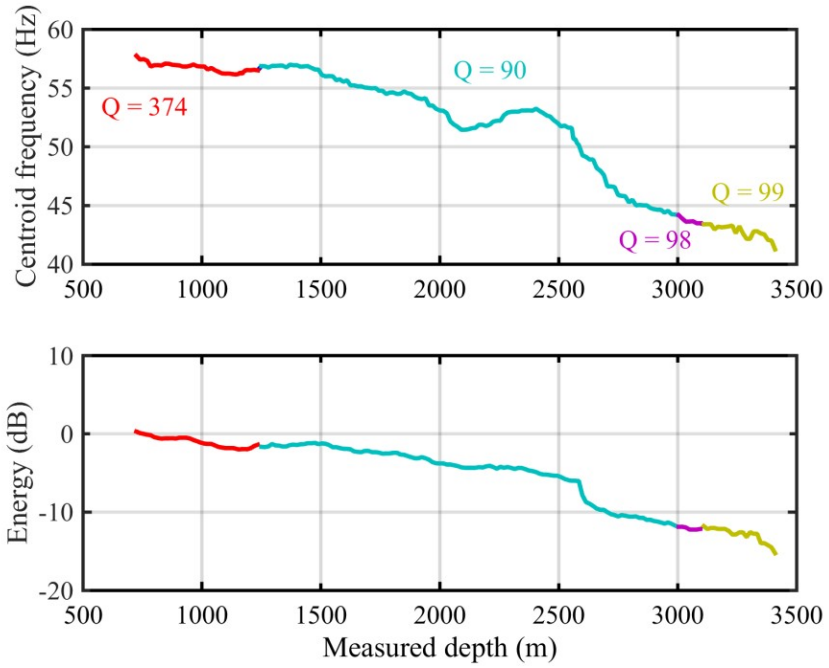

Figure A.19-5. Iago 3. Results of centroid frequency (top panel) and energy (bottom panel) decay estimation. Estimated attenuation values are derived for 4 stratigraphic intervals.

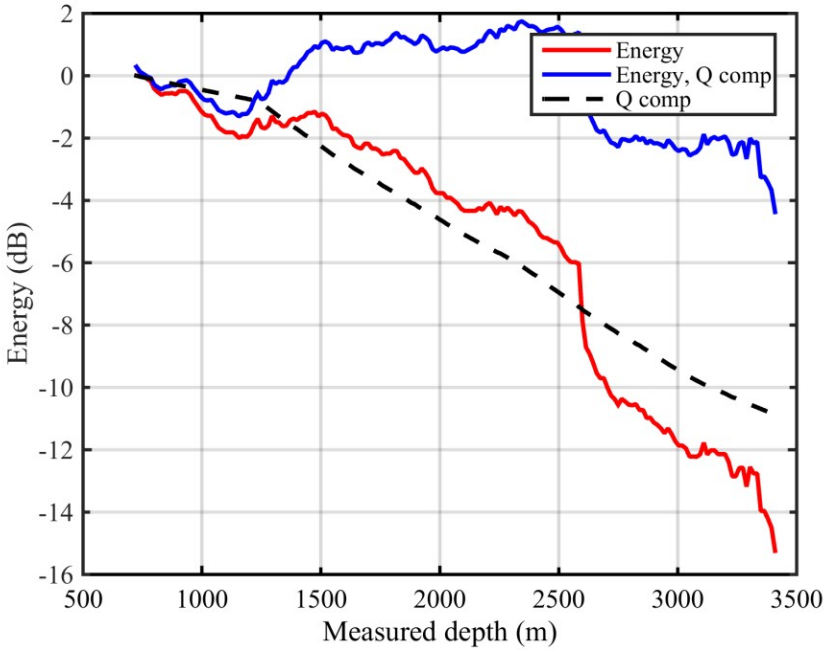

Figure A.19-6. Iago 3. Results of energy decay curve from direct wave (divergence variation is applied) (red); attenuation component of the energy decay (black) and result of the energy decay compensation (blue).

A.20. Lambert 8 results

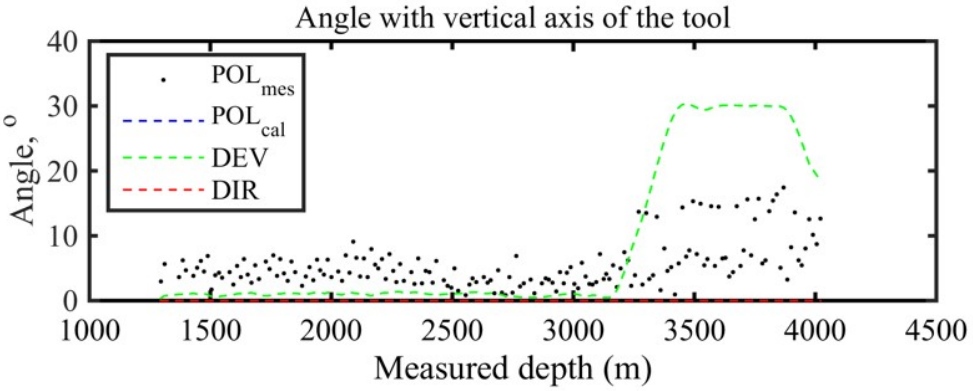

Figure A.20-1. Lambert 8. Results of the orientation: measured polarization of P-wave in respect to a vertical axis of the VSP tool (black dots); calculated polarization of P-wave in respect to a vertical axis of the VSP tool (blue dash line); well inclination (green dash line); angle between a vertical direction and the direction of P-wave propagation (red dash line).

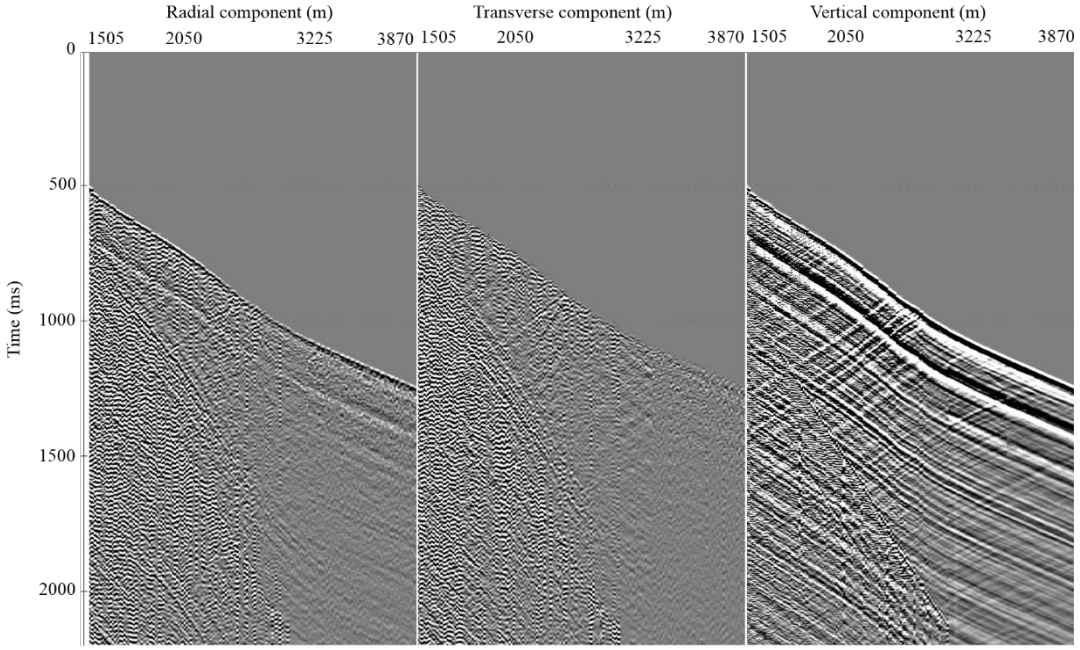

Figure A.20-2. 3C VSP oriented data: radial (left panel), transverse (middle panel), and vertical (right panel) components.

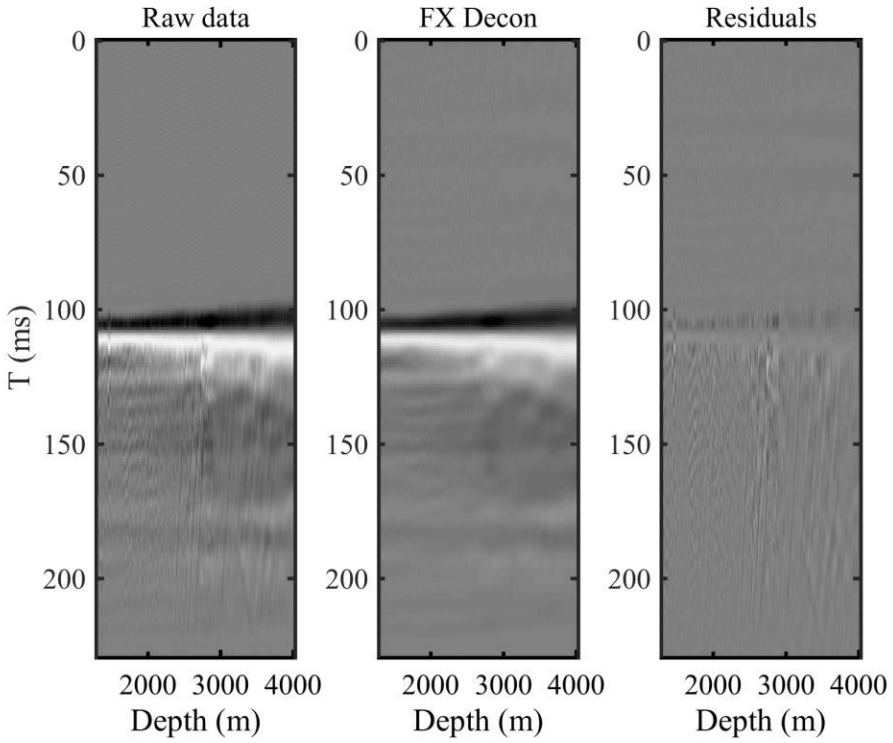

Figure A.20-3. Lambert 8. Results of attenuation of upgoing wavefield by using FX deconvolution. From left to right: original data, result of FX deconvolution and the difference.

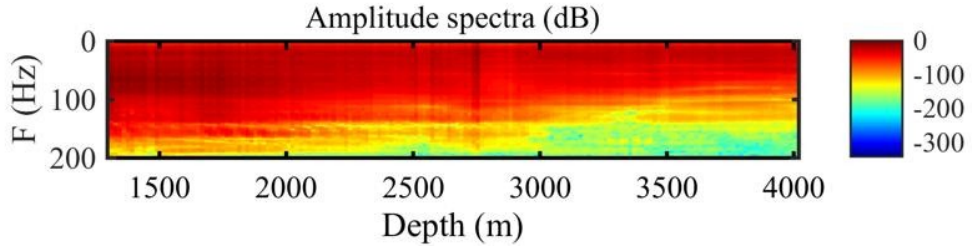

Figure A.20-4. Lambert 8. Amplitude spectra after FX deconvolution.

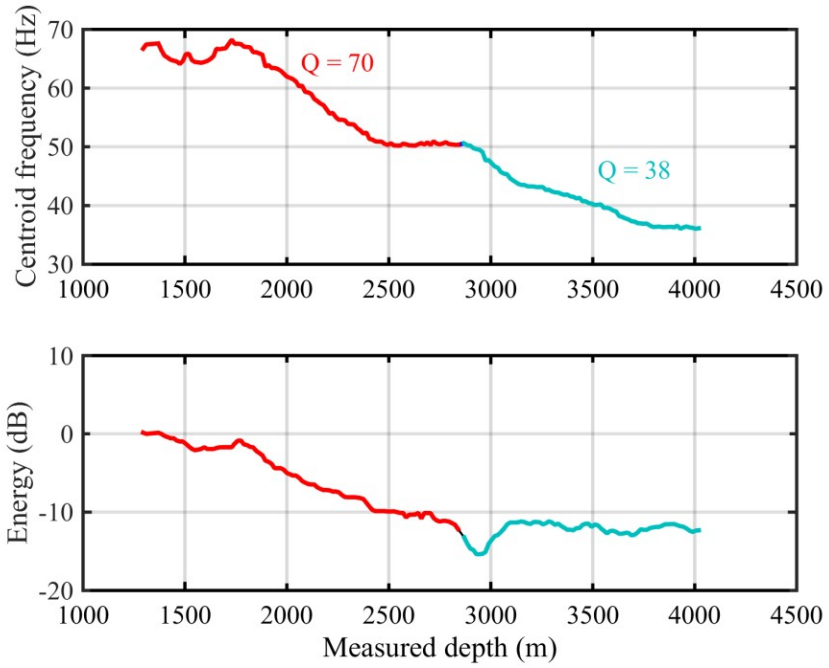

Figure A.20-5. Lambert 8. Results of centroid frequency (top panel) and energy (bottom panel) decay estimation. Estimated attenuation values are derived for 2 stratigraphic intervals.

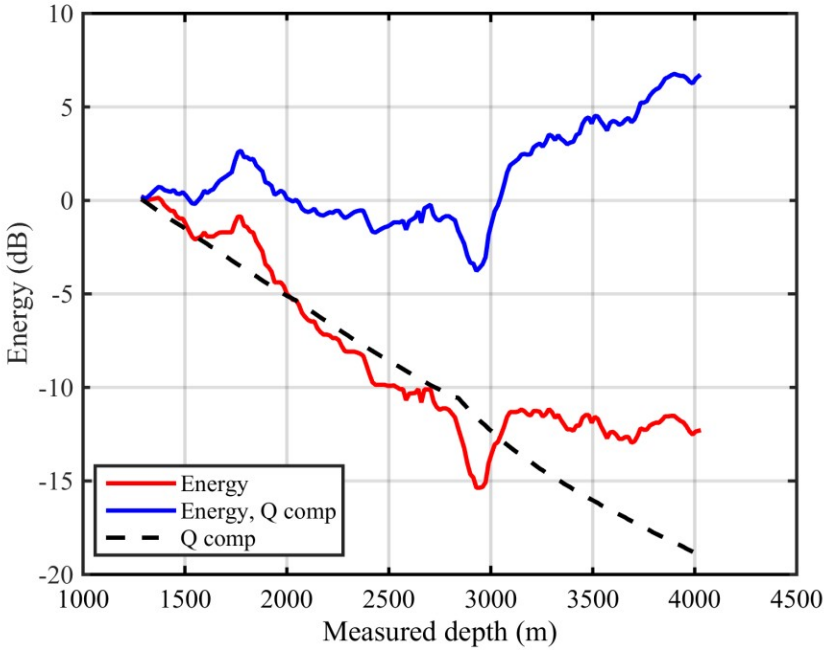

Figure A.20-6. Lambert 8. Results of energy decay curve from direct wave (divergence variation is applied) (red); attenuation component of the energy decay (black) and result of the energy decay compensation (blue).

A.21. Maitland 2 results

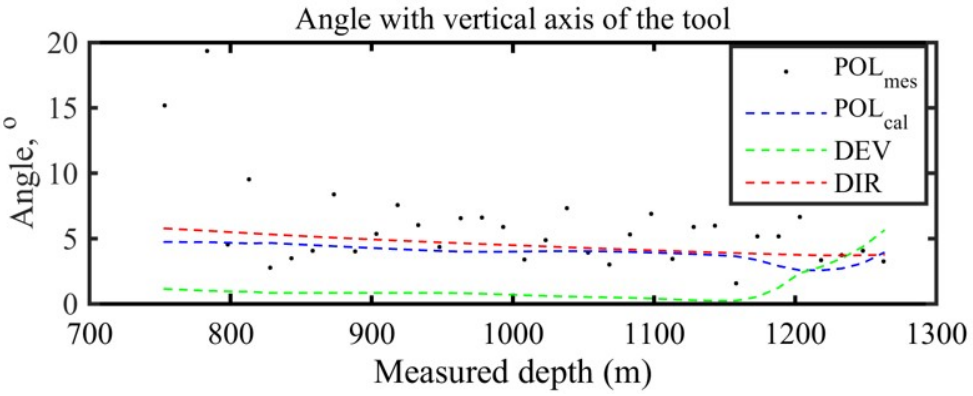

Figure A.21-1. Maitland 2. Results of the orientation: measured polarization of P-wave in respect to a vertical axis of the VSP tool (black dots); calculated polarization of P-wave in respect to a vertical axis of the VSP tool (blue dash line); well inclination (green dash line); angle between a vertical direction and the direction of P-wave propagation (red dash line).

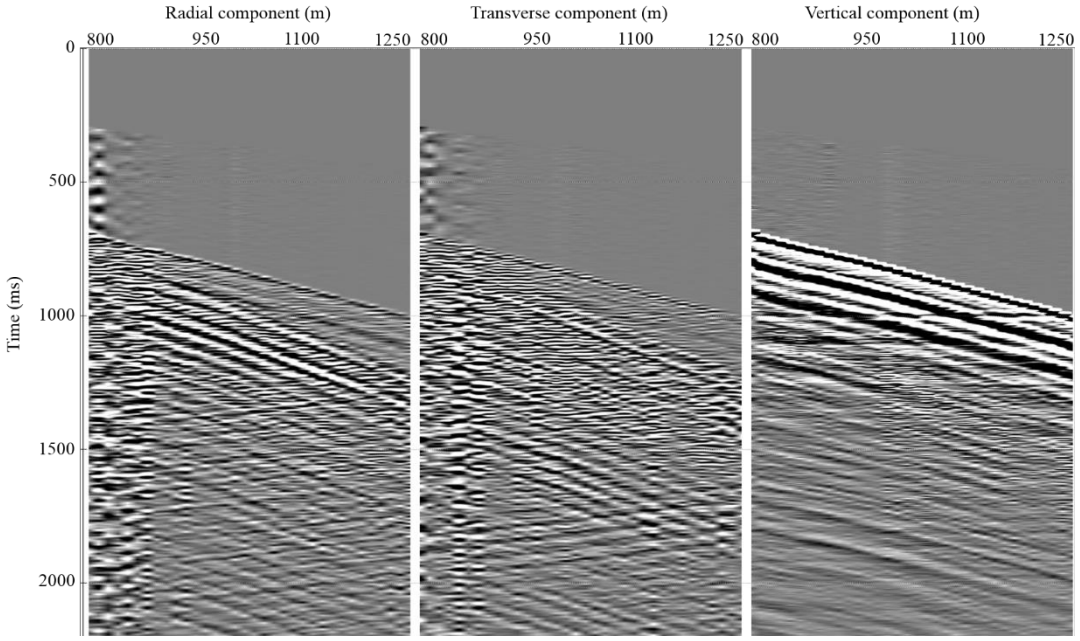

Figure A.21-2. Maitland 2. 3C VSP oriented data: radial (left panel), transverse (middle panel), and vertical (right panel) components.

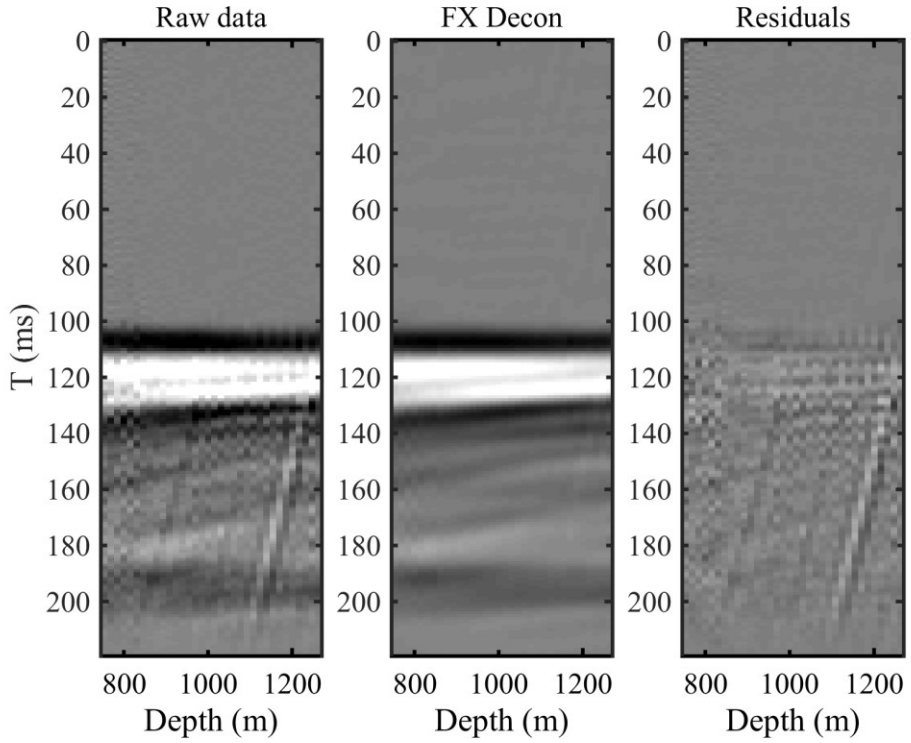

.

Figure A.21-3. Maitland 2. Results of attenuation of upgoing wavefield by using FX deconvolution. From left to right: original data, result of FX deconvolution and the difference.

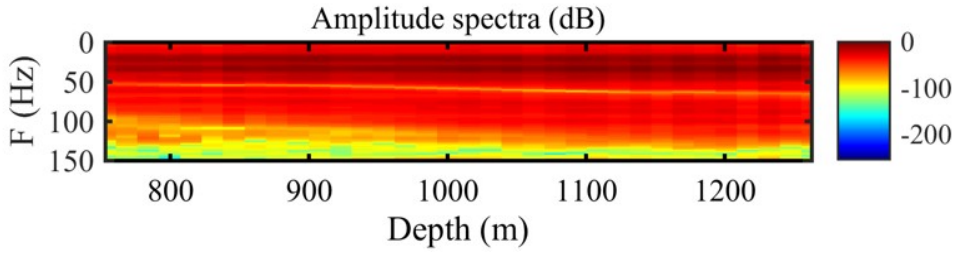

Figure A.21-4. Maitland 2. Amplitude spectra after FX deconvolution.

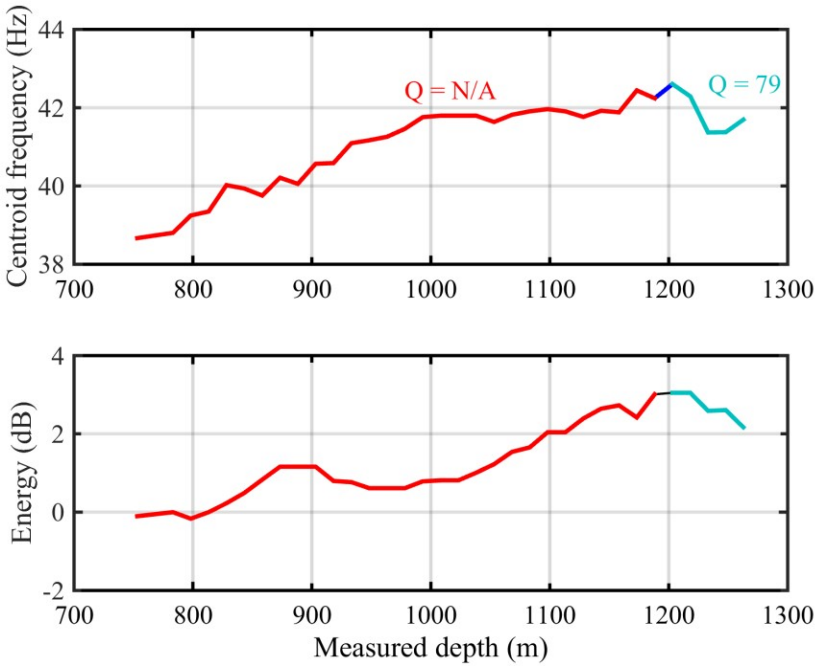

Figure A.21-5. Maitland 2. Results of centroid frequency (top panel) and energy (bottom panel) decay estimation. Estimated attenuation values are derived for 2 stratigraphic intervals.

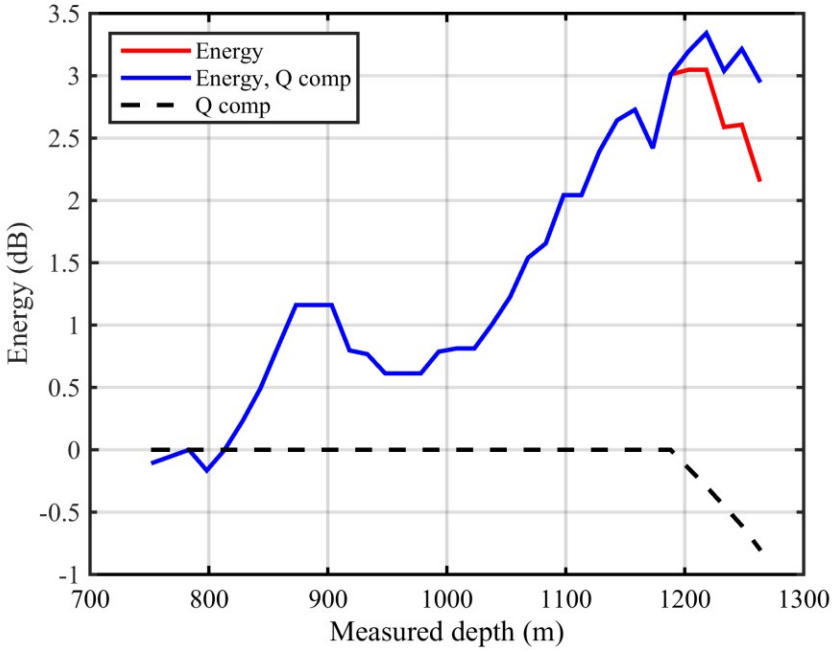

Figure A.21-6. Maitland 2. Results of energy decay curve from direct wave (divergence variation is applied) (red); attenuation component of the energy decay (black) and result of the energy decay compensation (blue).

A.22. Martell 1 results

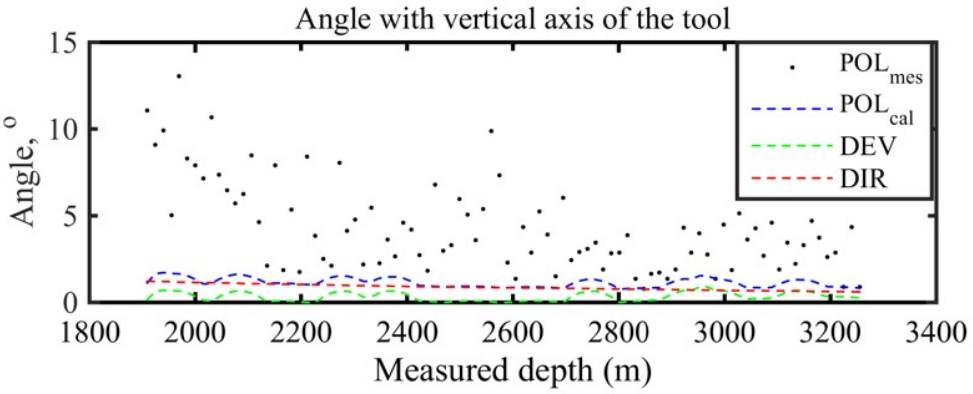

Figure A.22-1. Martell 1. Results of the orientation: measured polarization of P-wave in respect to a vertical axis of the VSP tool (black dots); calculated polarization of P-wave in respect to a vertical axis of the VSP tool (blue dash line); well inclination (green dash line); angle between a vertical direction and the direction of P-wave propagation (red dash line).

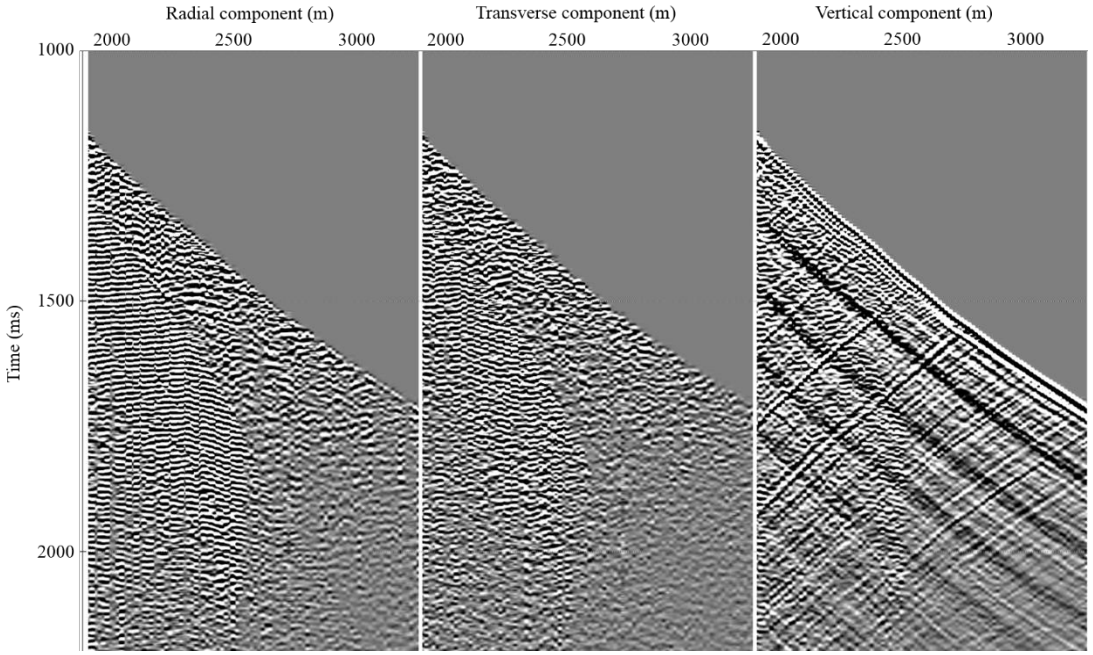

Figure A.22-2. Martell 1. 3C VSP oriented data: radial (left panel), transverse (middle panel), and vertical (right panel) components.

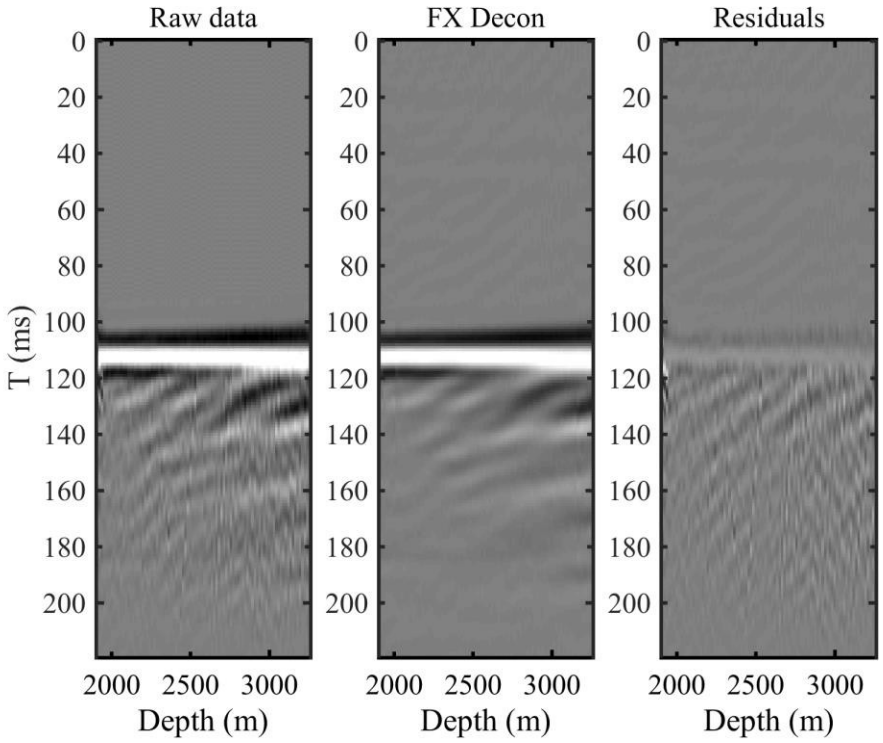

Figure A.22-3. Martell 1. Results of attenuation of upgoing wavefield by using FX deconvolution. From left to right: original data, result of FX deconvolution and the difference.

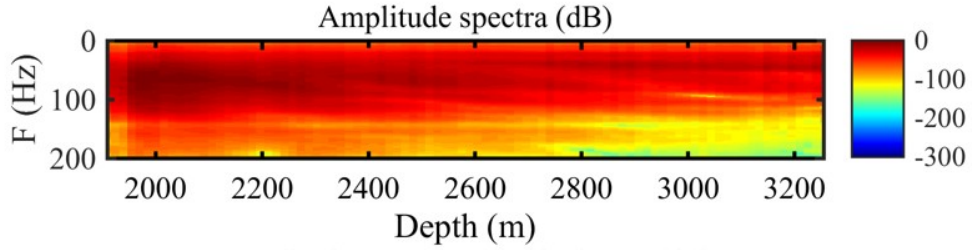

Figure A.22-4. Martell 1. Amplitude spectra after FX deconvolution.

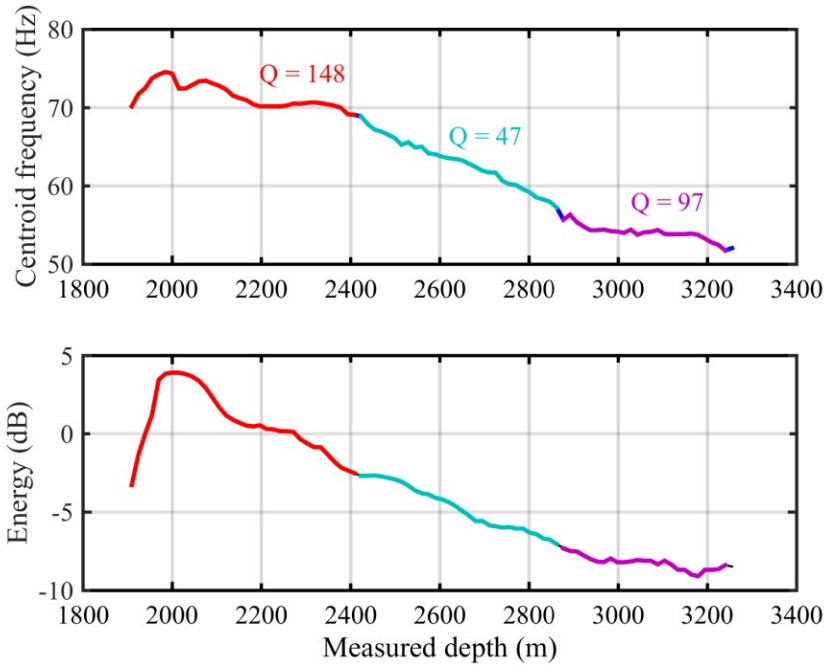

Figure A.22-5. Martell 1. Results of centroid frequency (top panel) and energy (bottom panel) decay estimation. Estimated attenuation values are derived for 3 stratigraphic intervals.

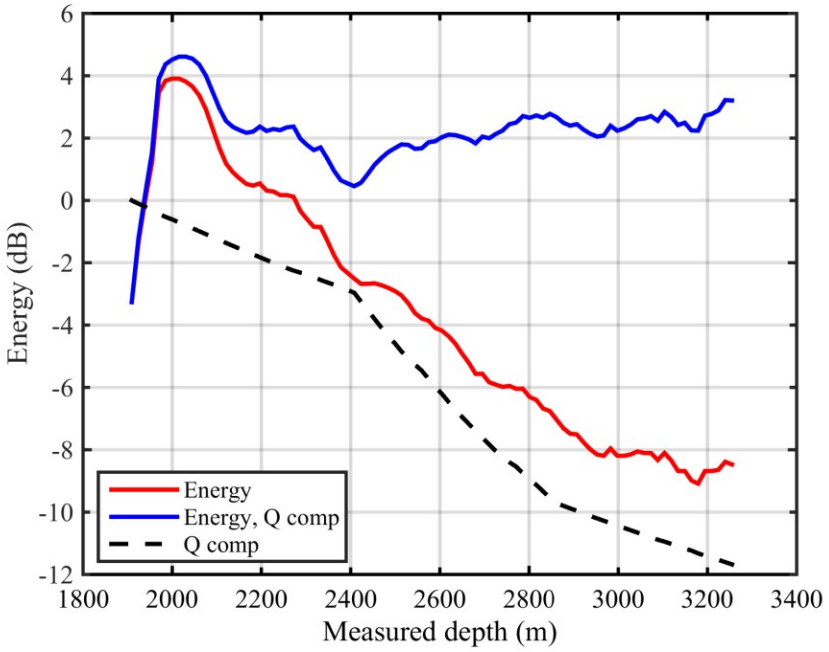

Figure A.22-6. Martell 1. Results of energy decay curve from direct wave (divergence variation is applied) (red); attenuation component of the energy decay (black) and result of the energy decay compensation (blue).

A.23. Rosella 2 results

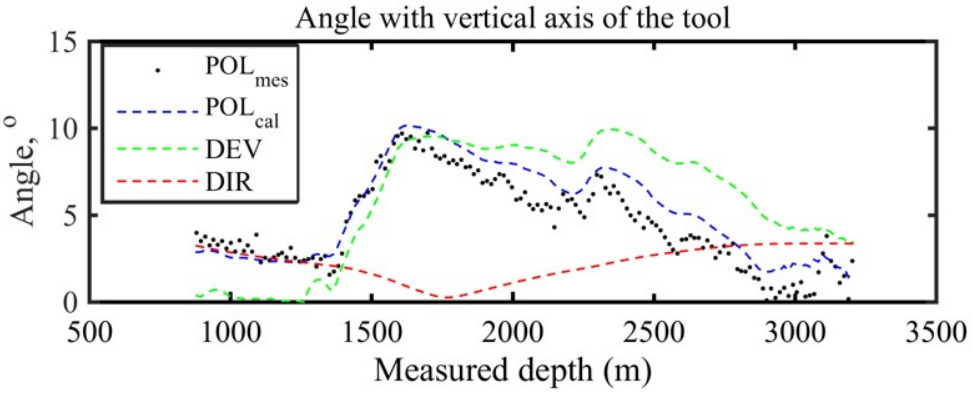

Figure A.23-1. Rosella 2. Results of the orientation: measured polarization of P-wave in respect to a vertical axis of the VSP tool (black dots); calculated polarization of P-wave in respect to a vertical axis of the VSP tool (blue dash line); well inclination (green dash line); angle between a vertical direction and the direction of P-wave propagation (red dash line).

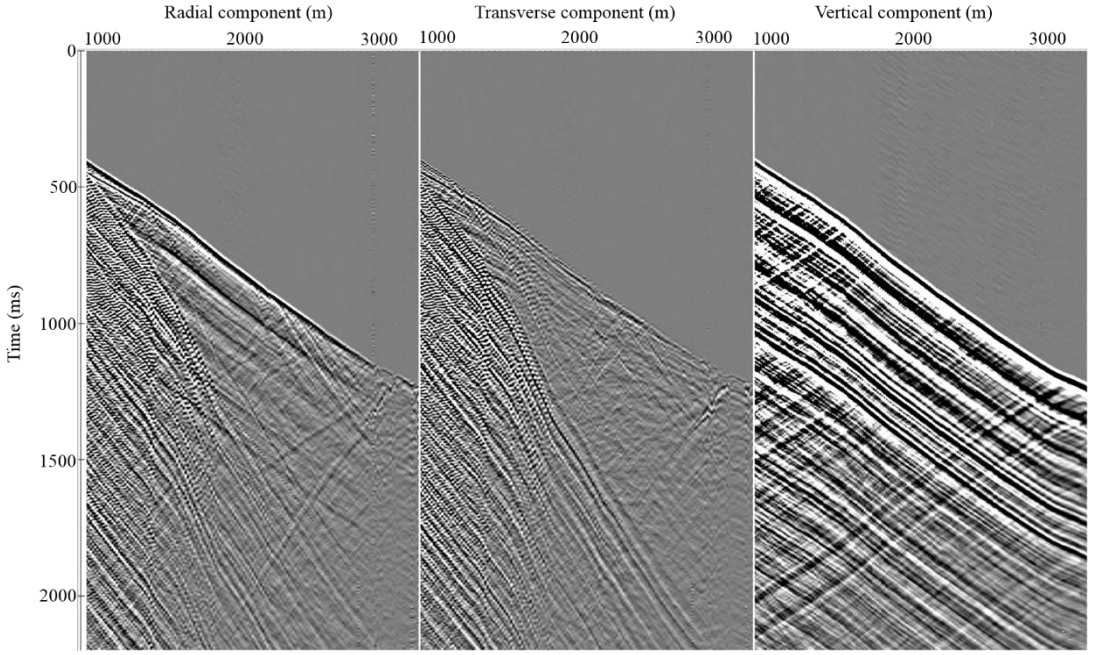

Figure A.23-2. Rosella 2. 3C VSP oriented data: radial (left panel), transverse (middle panel), and vertical (right panel) components.

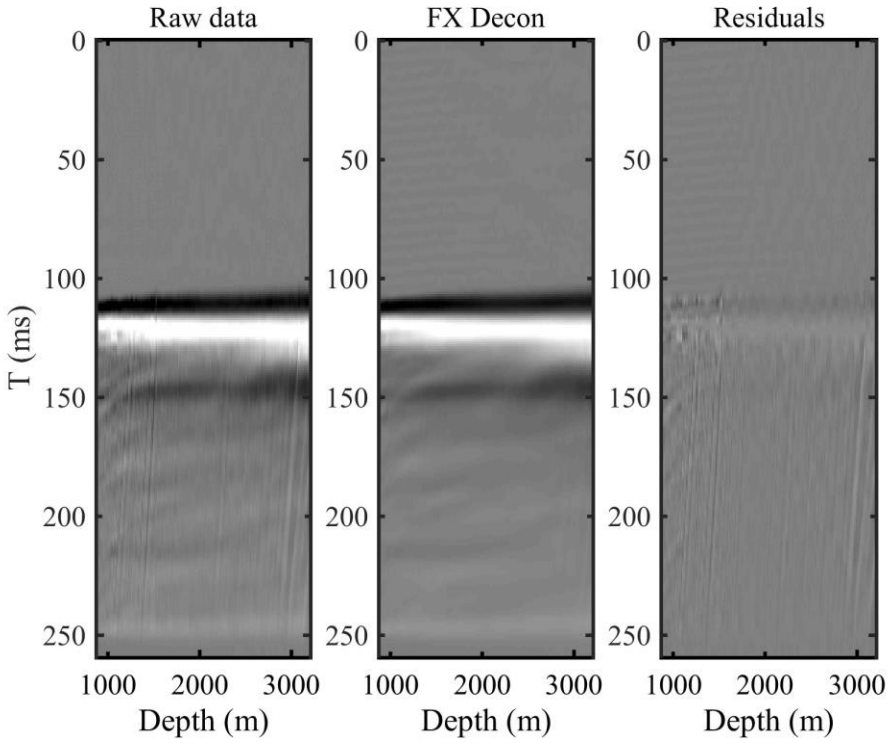

Figure A.23-3. Rosella 2. Results of attenuation of upgoing wavefield by using FX deconvolution. From left to right: original data, result of FX deconvolution and the difference.

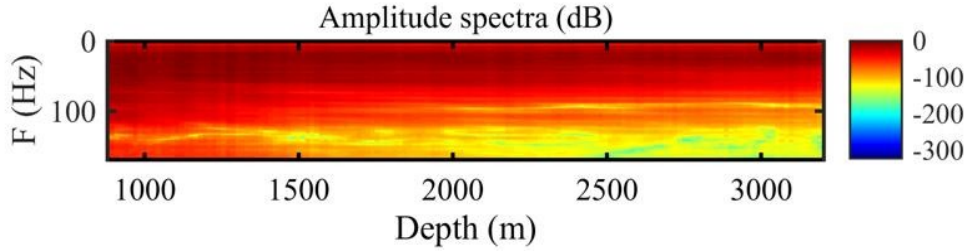

Figure A.23-4. Rosella 2. Amplitude spectra after FX deconvolution.

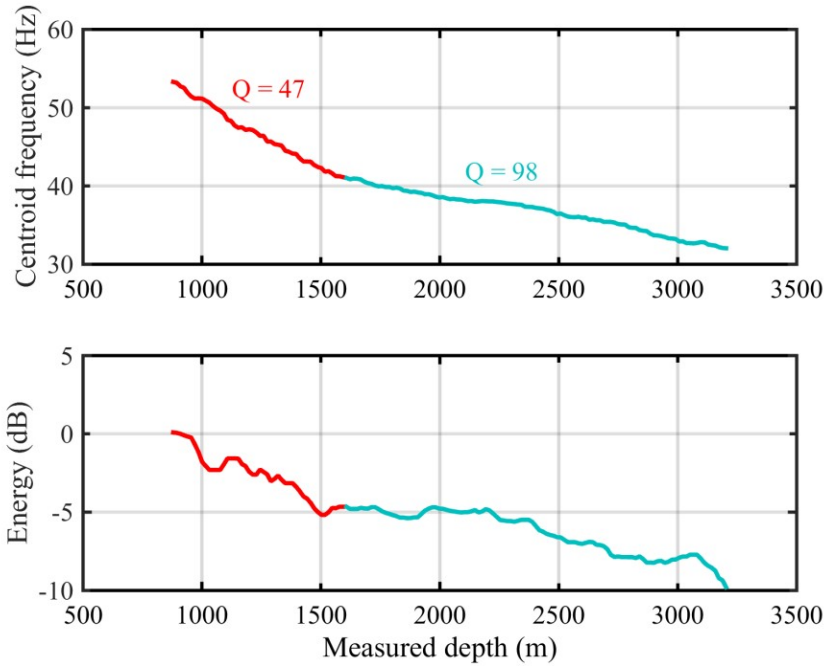

Figure A.23-5. Rosella 2. Results of centroid frequency (top panel) and energy (bottom panel) decay estimation. Estimated attenuation values are derived for 2 stratigraphic intervals.

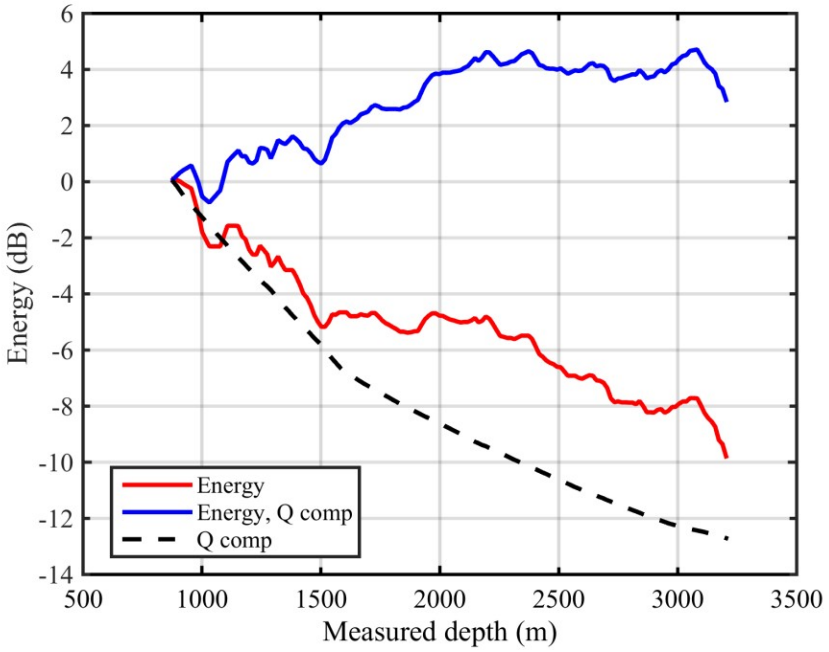

Figure A.23-6. Rosella 2. Results of energy decay curve from direct wave (divergence variation is applied) (red); attenuation component of the energy decay (black) and result of the energy decay compensation (blue).

A.24. Pluto 3 results

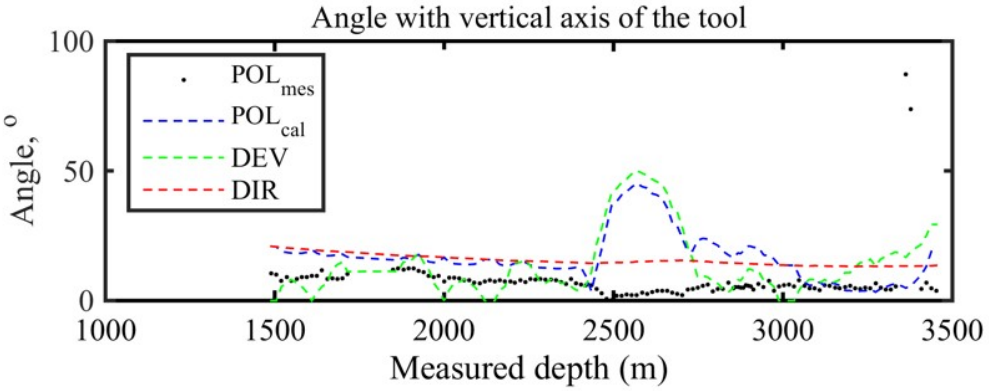

Figure A.24-1. Pluto 3. Results of the orientation: measured polarization of P-wave in respect to a vertical axis of the VSP tool (black dots); calculated polarization of P-wave in respect to a vertical axis of the VSP tool (blue dash line); well inclination (green dash line); angle between a vertical direction and the direction of P-wave propagation (red dash line).

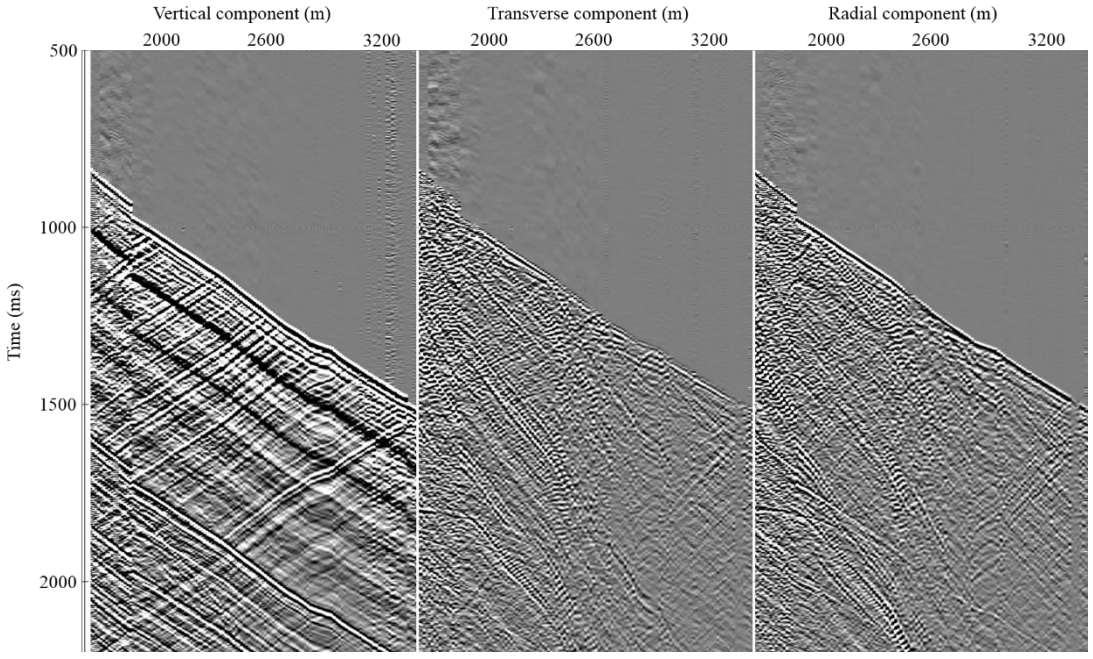

Figure A.24-2. Pluto 3. 3C VSP oriented data: radial (left panel), transverse (middle panel), and vertical (right panel) components.

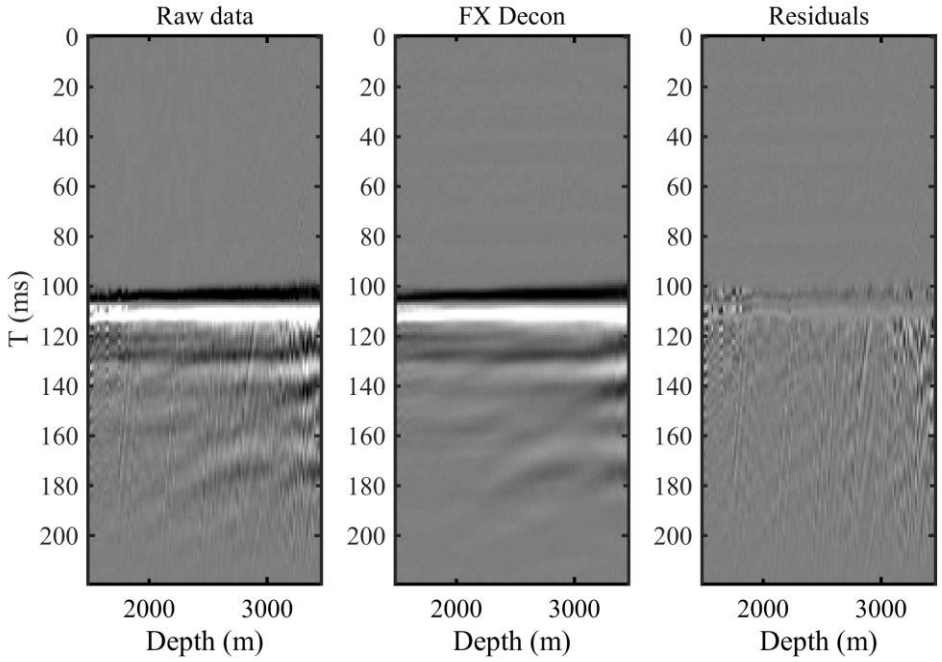

Figure A.24-3. Pluto 3. Results of attenuation of upgoing wavefield by using FX deconvolution. From left to right: original data, result of FX deconvolution and the difference.

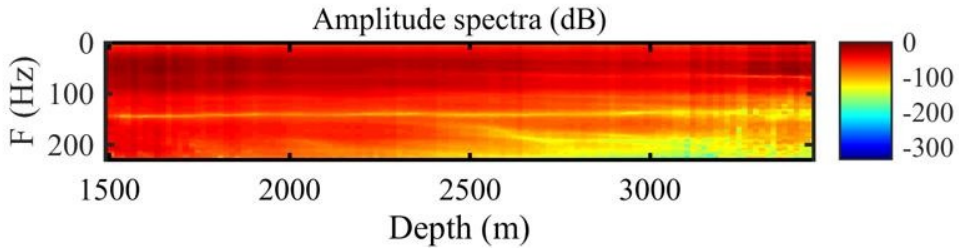

Figure A.24-4. Pluto 3. Amplitude spectra after FX deconvolution.

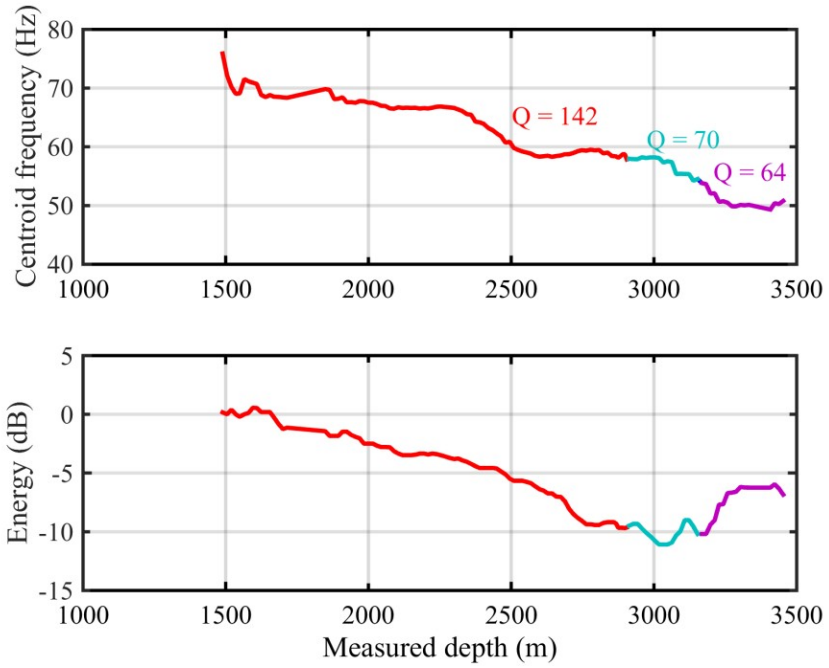

Figure A.24-5. Pluto 3. Results of centroid frequency (top panel) and energy (bottom panel) decay estimation. Estimated attenuation values are derived for 3 stratigraphic intervals.

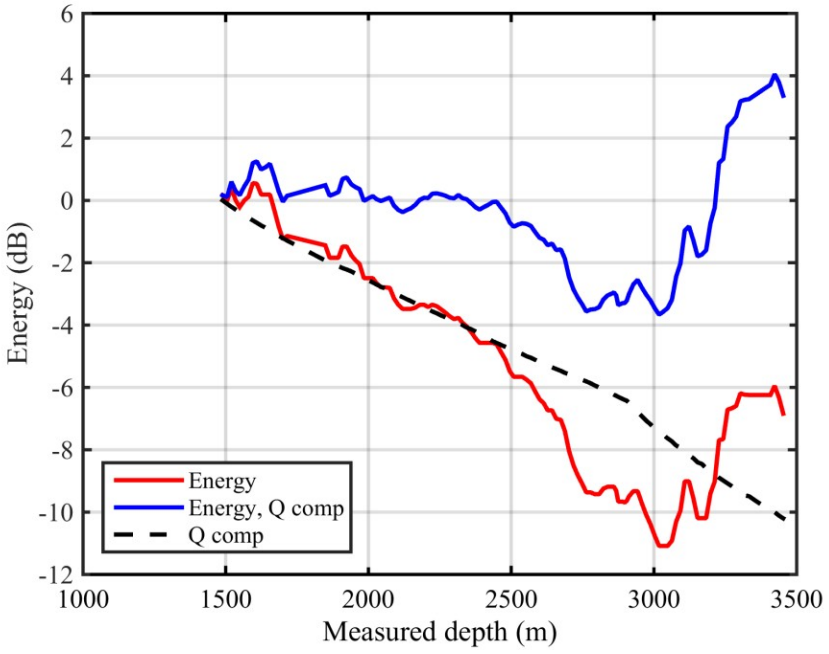

Figure A.24-6. Pluto 3. Results of energy decay curve from direct wave (divergence variation is applied) (red); attenuation component of the energy decay (black) and result of the energy decay compensation (blue).

A.25. Pluto 5 results

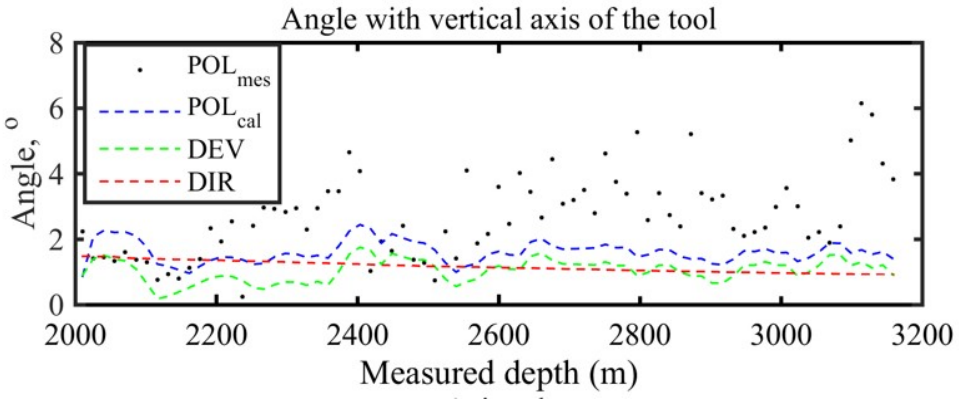

Figure A.25-1. Pluto 5. Results of the orientation: measured polarization of P-wave in respect to a vertical axis of the VSP tool (black dots); calculated polarization of P-wave in respect to a vertical axis of the VSP tool (blue dash line); well inclination (green dash line); angle between a vertical direction and the direction of P-wave propagation (red dash line).

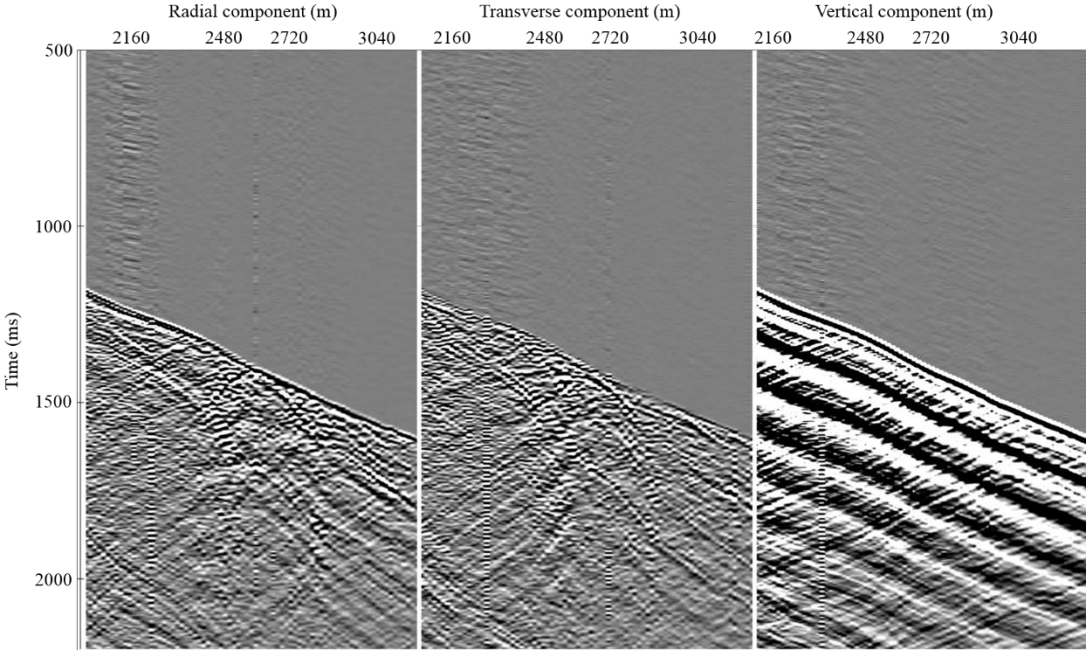

Figure A.25-2. Pluto 5. 3C VSP oriented data: radial (left panel), transverse (middle panel), and vertical (right panel) components.

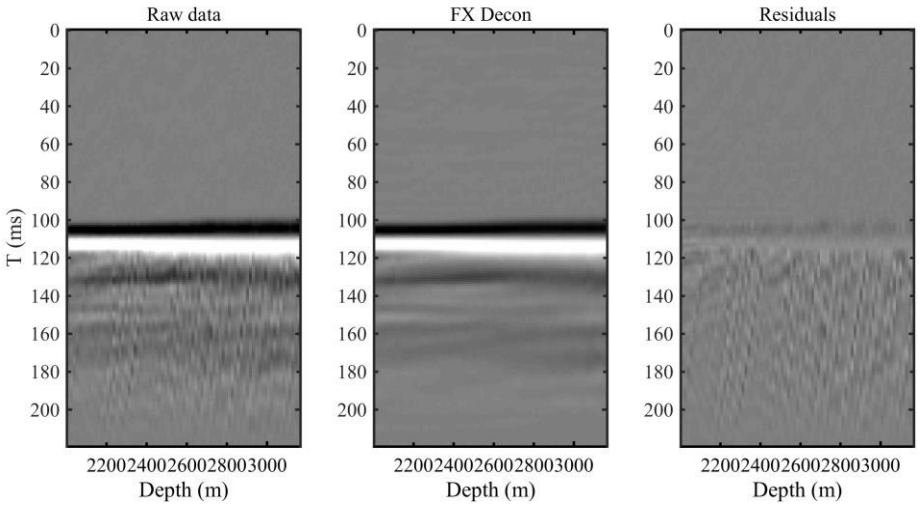

Figure A.25-3. Pluto 5. Results of attenuation of upgoing wavefield by using FX deconvolution. From left to right: original data, result of FX deconvolution and the difference.

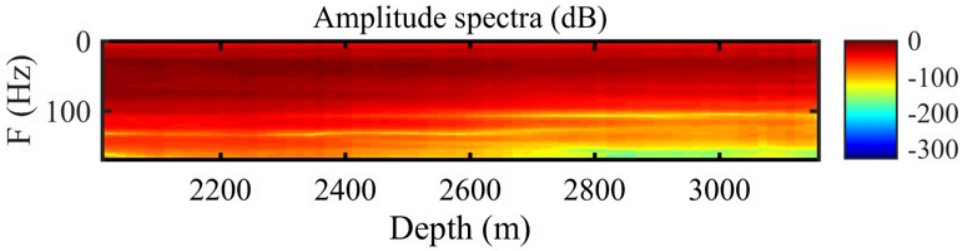

Figure A.25-4. Pluto 5. Amplitude spectra after FX deconvolution.

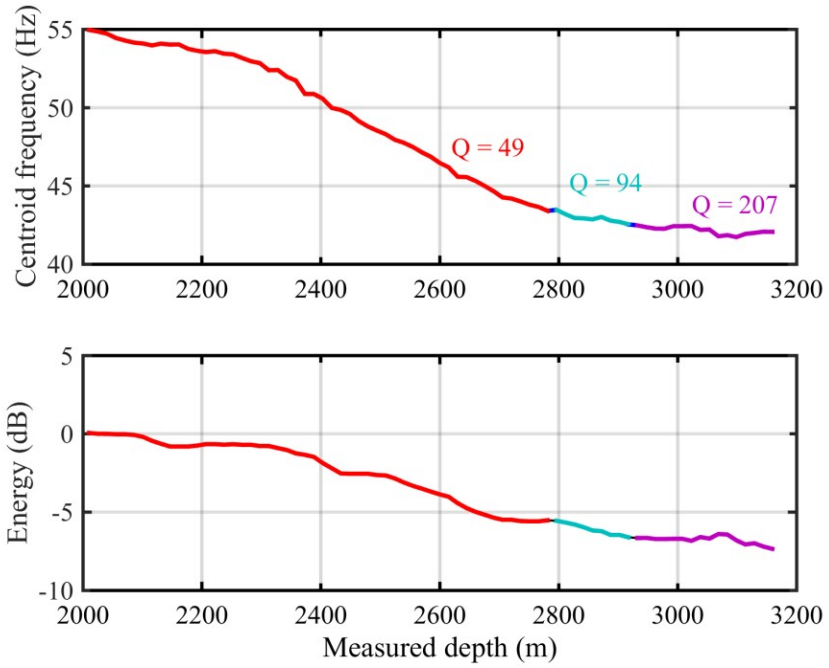

Figure A.25-5. Pluto 5. Results of centroid frequency (top panel) and energy (bottom panel) decay estimation. Estimated attenuation values are derived for 3 stratigraphic intervals.

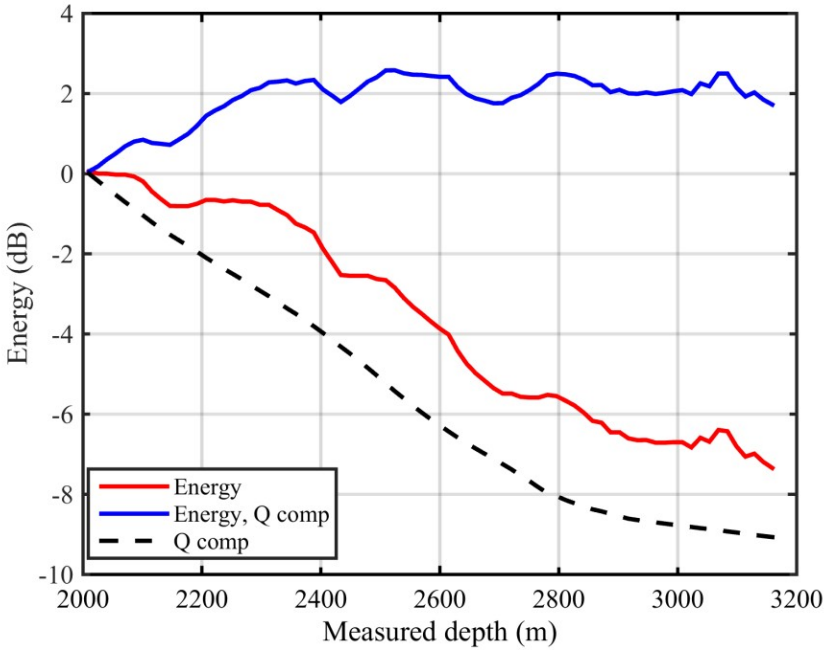

Figure A.25-6. Pluto 5. Results of energy decay curve from direct wave (divergence variation is applied) (red); attenuation component of the energy decay (black) and result of the energy decay compensation (blue).

A.26. Salsa 1 results

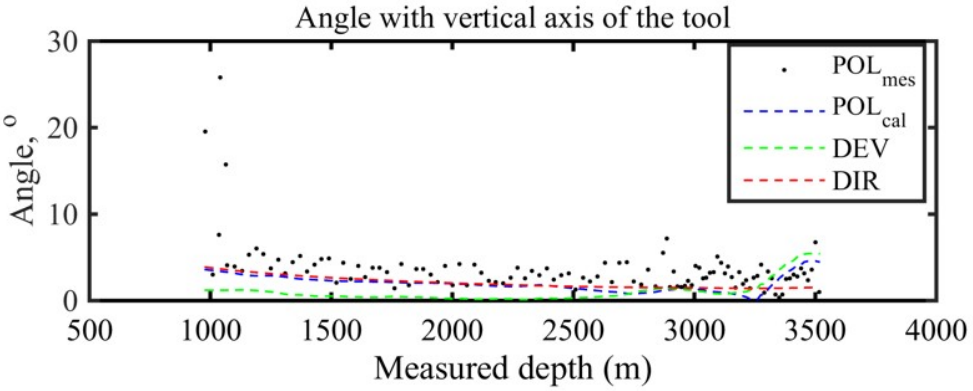

Figure A.26-1. Salsa 1. Results of the orientation: measured polarization of P-wave in respect to a vertical axis of the VSP tool (black dots); calculated polarization of P-wave in respect to a vertical axis of the VSP tool (blue dash line); well inclination (green dash line); angle between a vertical direction and the direction of P-wave propagation (red dash line).

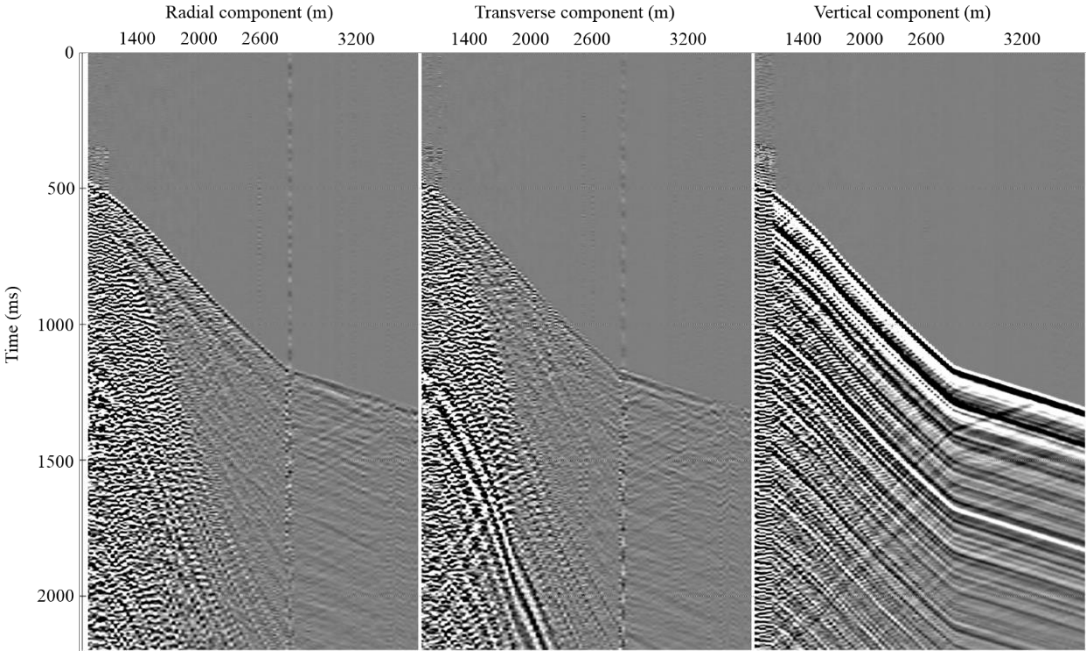

Figure A.26-2. Salsa 1. 3C VSP oriented data: radial (left panel), transverse (middle panel), and vertical (right panel) components.

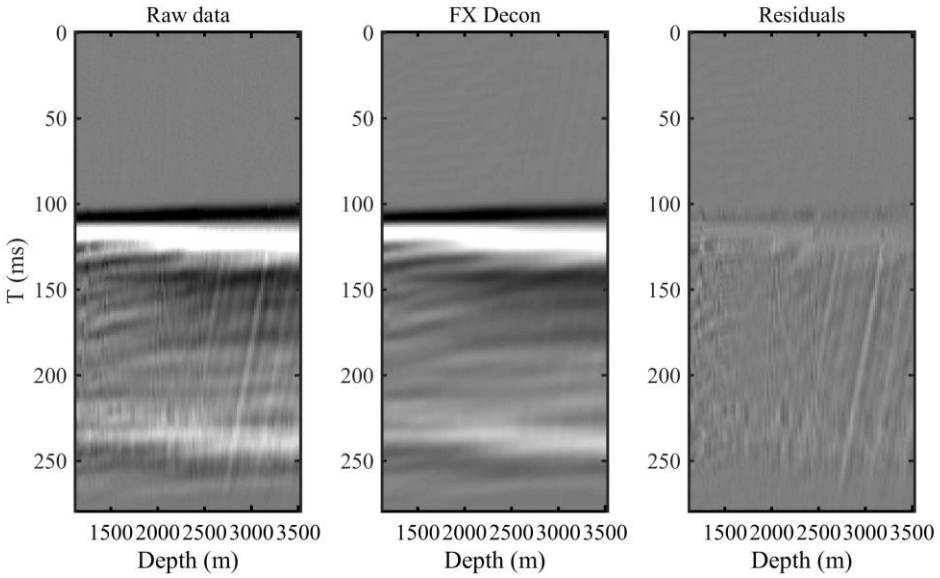

Figure A.26-3. Salsa 1. Results of attenuation of upgoing wavefield by using FX deconvolution. From left to right: original data, result of FX deconvolution and the difference.

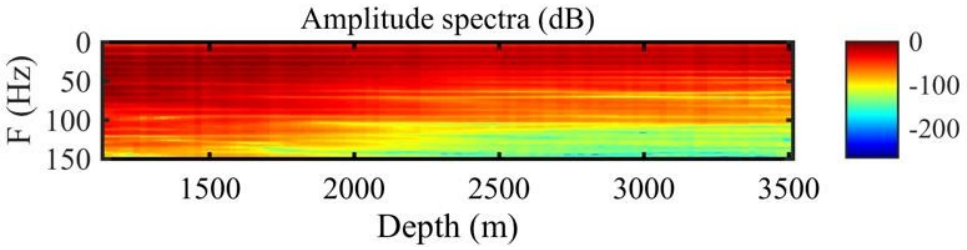

Figure A.26-4. Salsa 1. Amplitude spectra after FX deconvolution.

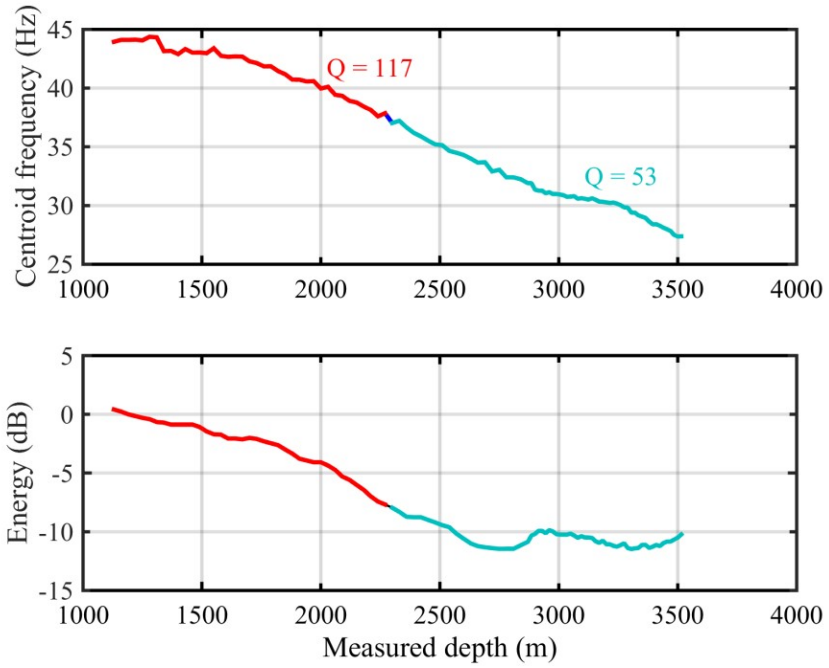

Figure A.26-5. Salsa 1. Results of centroid frequency (top panel) and energy (bottom panel) decay estimation. Estimated attenuation values are derived for 2 stratigraphic intervals.

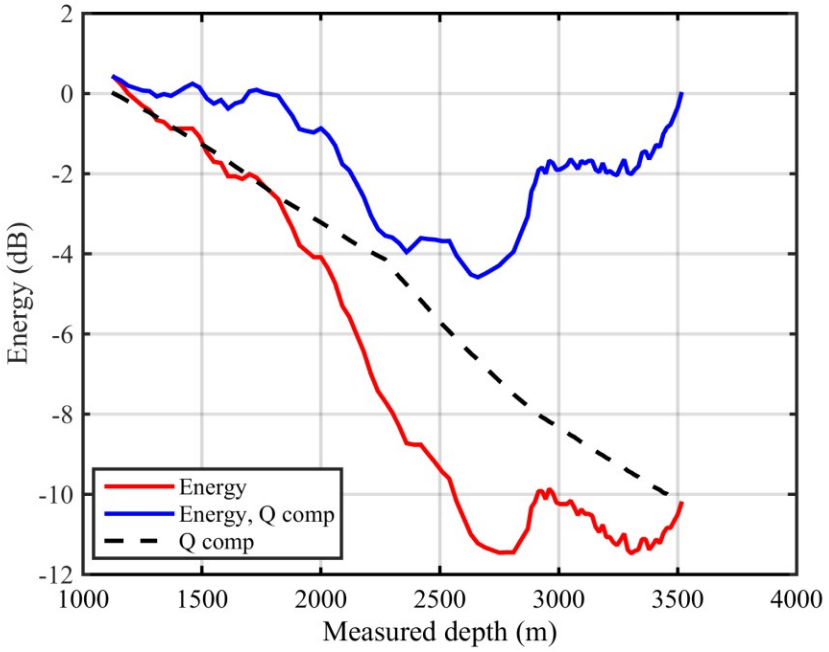

Figure A.26-6. Salsa 1. Results of energy decay curve from direct wave (divergence variation is applied) (red); attenuation component of the energy decay (black) and result of the energy decay compensation (blue).

A.27. Tidepole 2

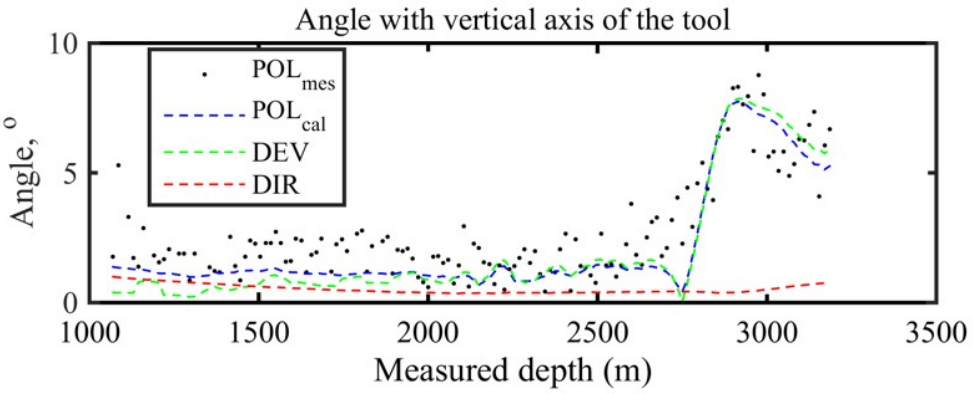

Figure A.27-1. Tidepole 2. Results of the orientation: measured polarization of P-wave in respect to a vertical axis of the VSP tool (black dots); calculated polarization of P-wave in respect to a vertical axis of the VSP tool (blue dash line); well inclination (green dash line); angle between a vertical direction and the direction of P-wave propagation (red dash line).

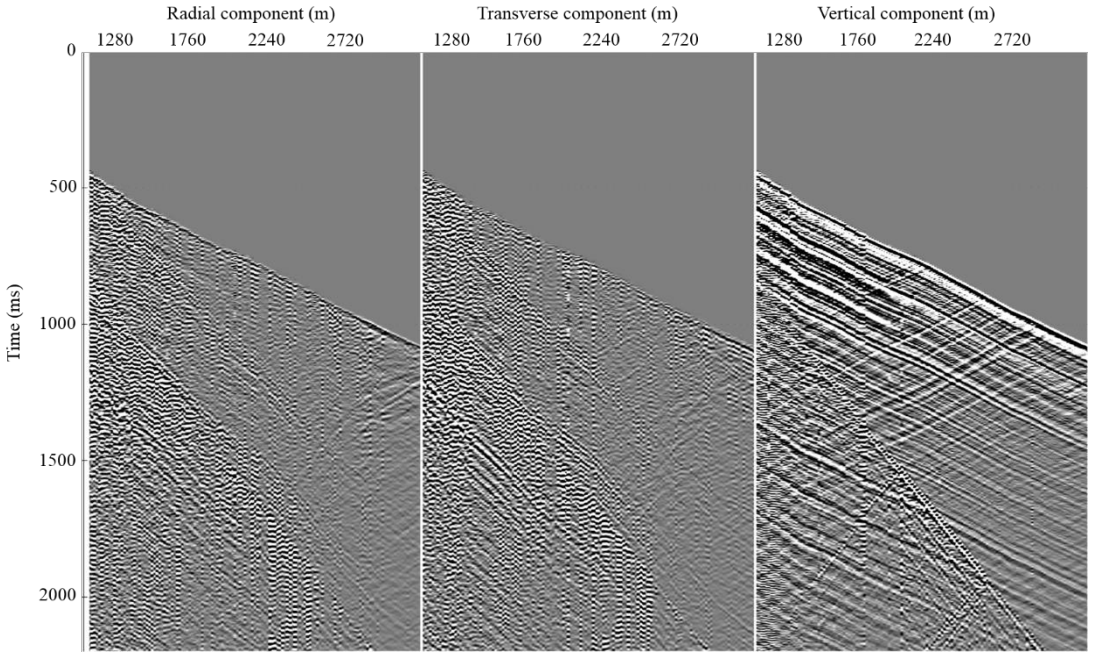

Figure A.27-2. Tidepole 2. 3C VSP oriented data: radial (left panel), transverse (middle panel), and vertical (right panel) components.

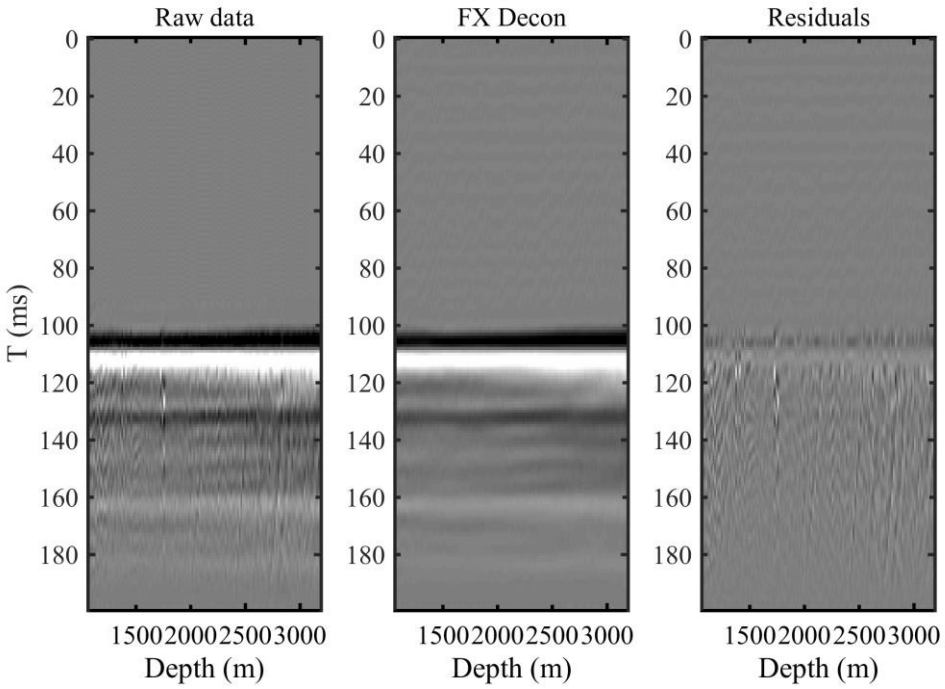

Figure A.27-3. Tidepole 2. Results of attenuation of upgoing wavefield by using FX deconvolution. From left to right: original data, result of FX deconvolution and the difference.

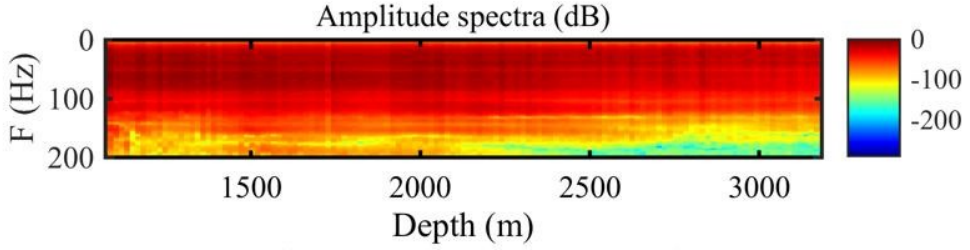

Figure A.27-4. Tidepole 2. Amplitude spectra after FX deconvolution.

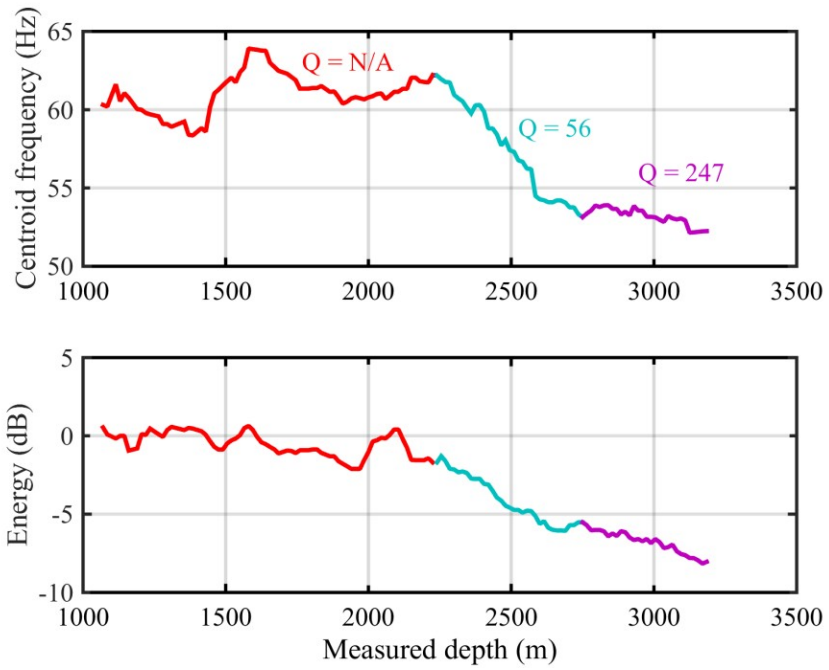

Figure A.27-5. Tidepole 2. Results of centroid frequency (top panel) and energy (bottom panel) decay estimation. Estimated attenuation values are derived for 3 stratigraphic intervals.

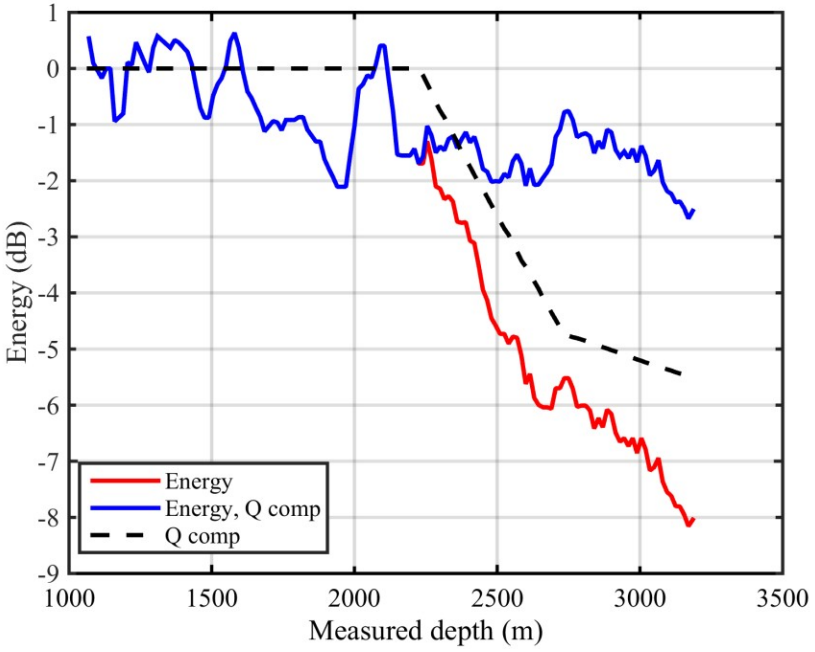

Figure A.27-6. Tidepole 2. Results of energy decay curve from direct wave (divergence variation is applied) (red); attenuation component of the energy decay (black) and result of the energy decay compensation (blue).

A.28. Torosa 2 results

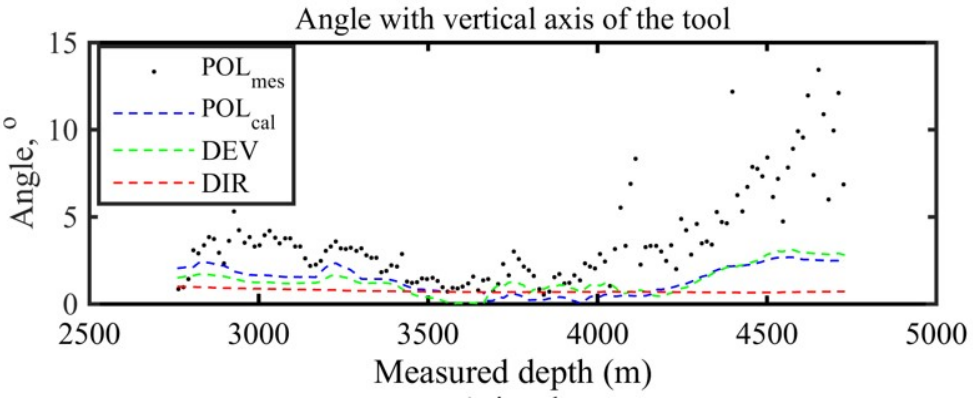

Figure A.28-1. Torosa 2. Results of the orientation: measured polarization of P-wave in respect to a vertical axis of the VSP tool (black dots); calculated polarization of P-wave in respect to a vertical axis of the VSP tool (blue dash line); well inclination (green dash line); angle between a vertical direction and the direction of P-wave propagation (red dash line).

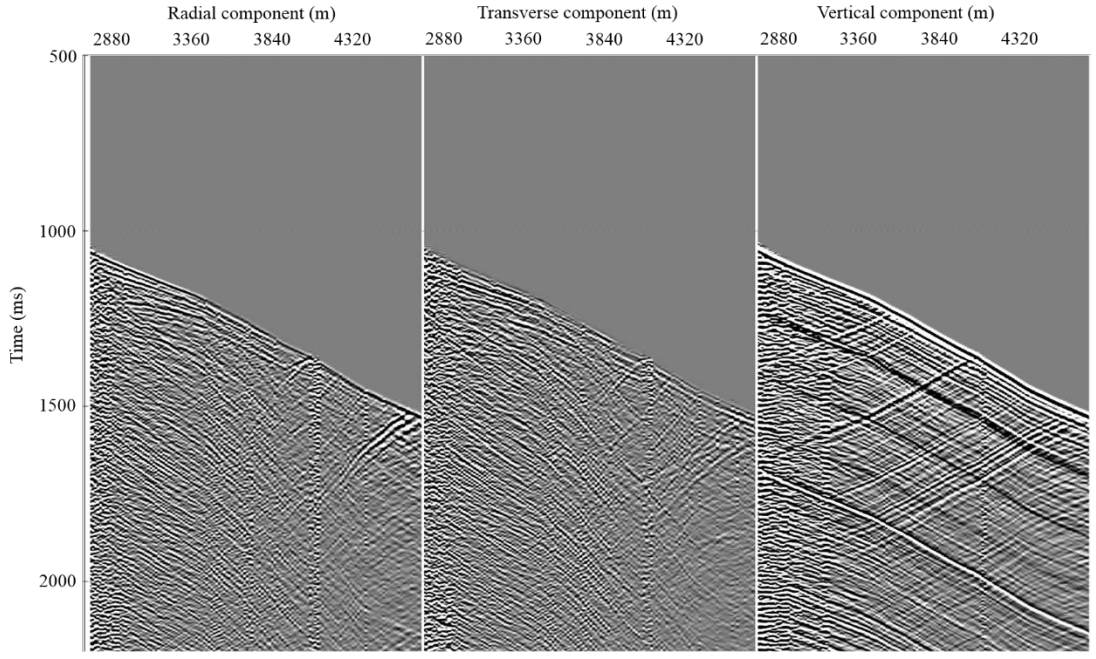

Figure A.28-2. Torosa 2. 3C VSP oriented data: radial (left panel), transverse (middle panel), and vertical (right panel) components.

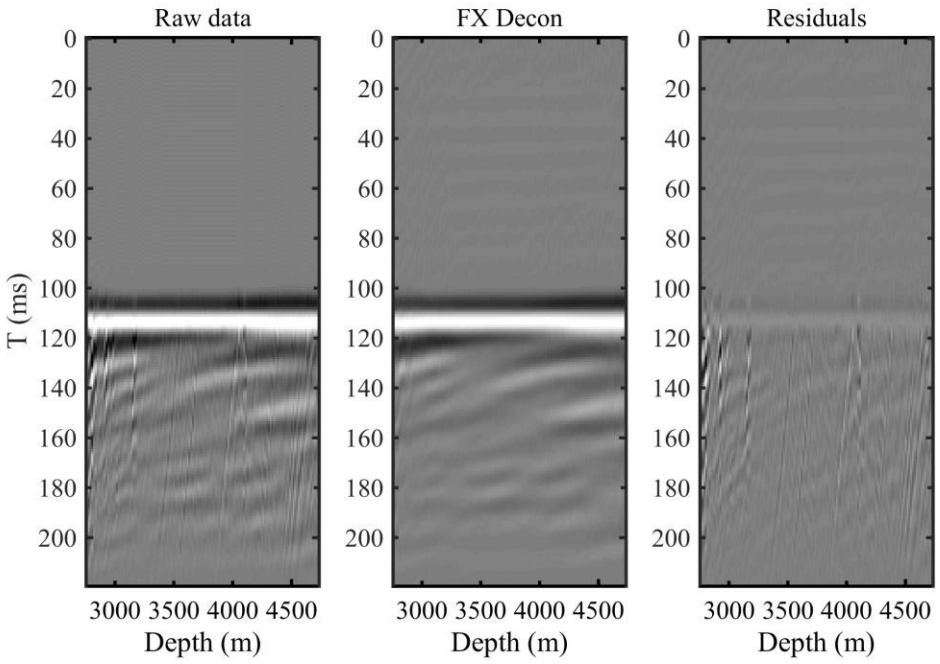

Figure A.28-3. Torosa 2. Results of attenuation of upgoing wavefield by using FX deconvolution. From left to right: original data, result of FX deconvolution and the difference.

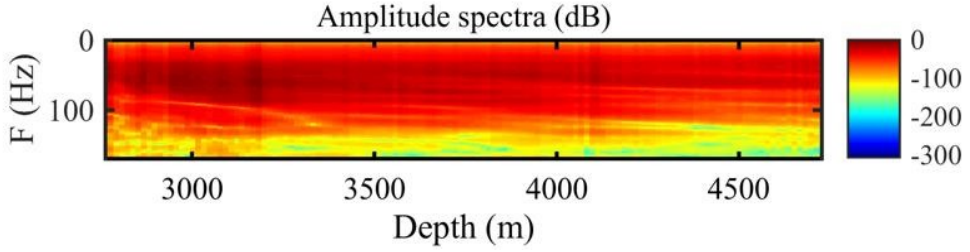

Figure A.28-4. Torosa 2. Amplitude spectra after FX deconvolution.

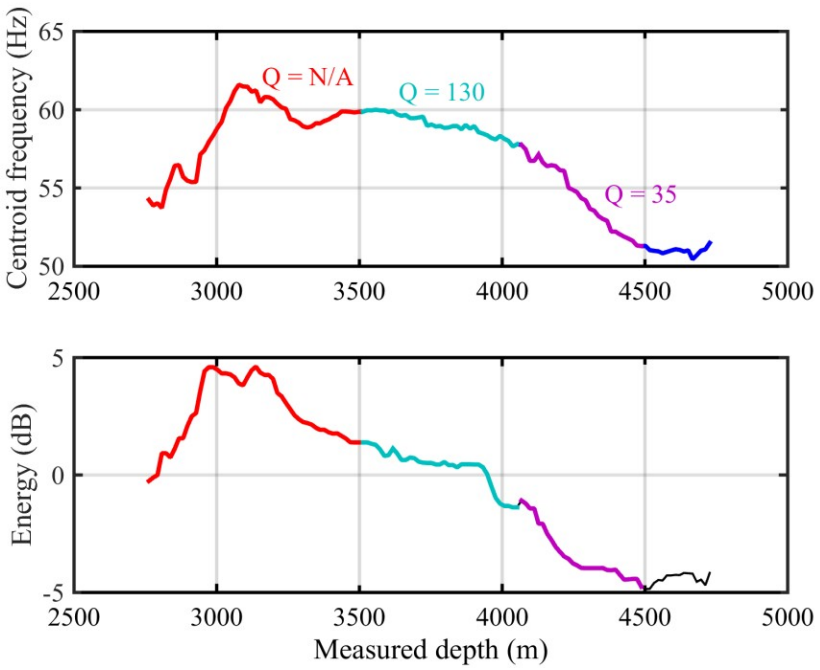

Figure A.28-5. Torosa 2. Results of centroid frequency (top panel) and energy (bottom panel) decay estimation. Estimated attenuation values are derived for 3 stratigraphic intervals.

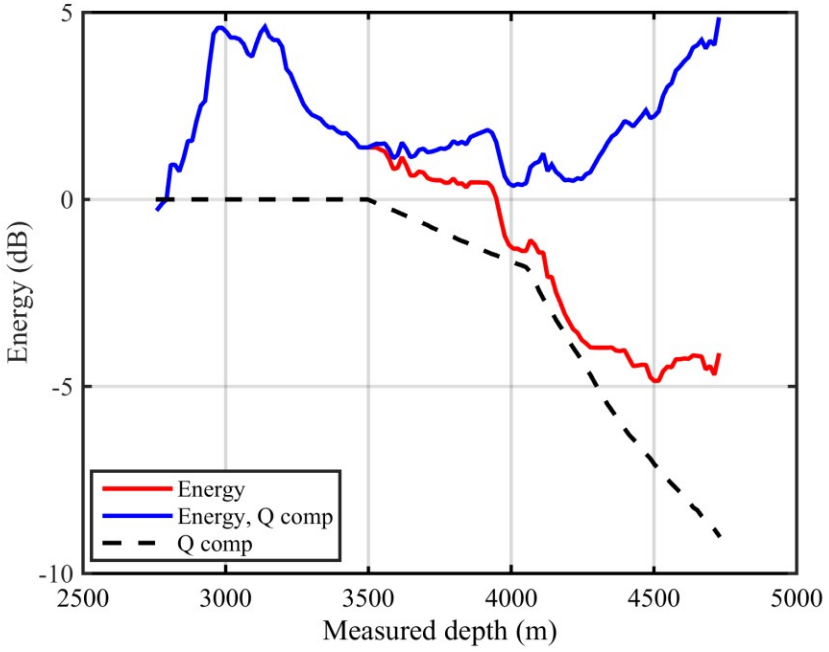

Figure A.28-6. Torosa 2. Results of energy decay curve from direct wave (divergence variation is applied) (red); attenuation component of the energy decay (black) and result of the energy decay compensation (blue).

A.29. Torosa 3 results

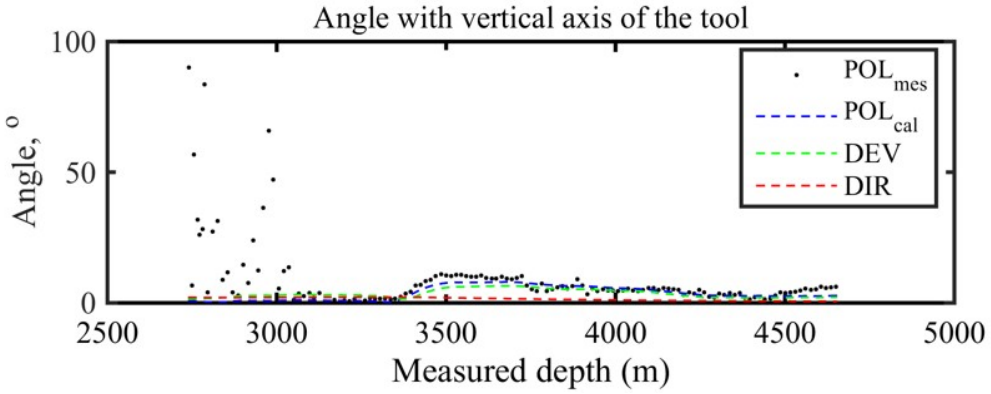

Figure A.29-1. Torosa 3. Results of the orientation: measured polarization of P-wave in respect to a vertical axis of the VSP tool (black dots); calculated polarization of P-wave in respect to a vertical axis of the VSP tool (blue dash line); well inclination (green dash line); angle between a vertical direction and the direction of P-wave propagation (red dash line).

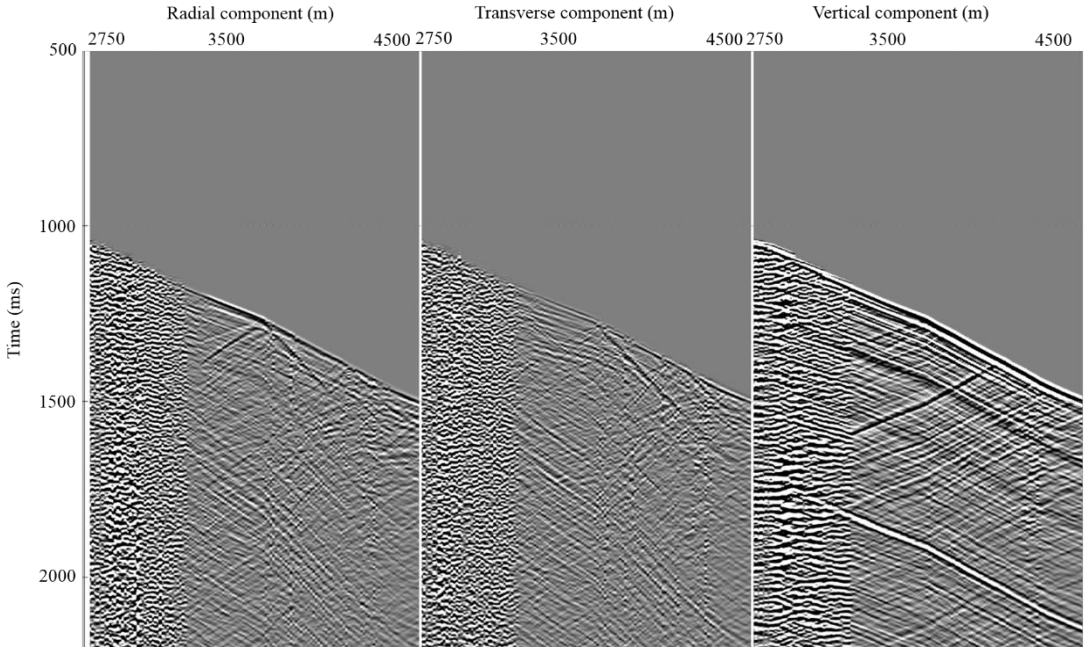

Figure A.29-2. Torosa 3. 3C VSP oriented data: radial (left panel), transverse (middle panel), and vertical (right panel) components.

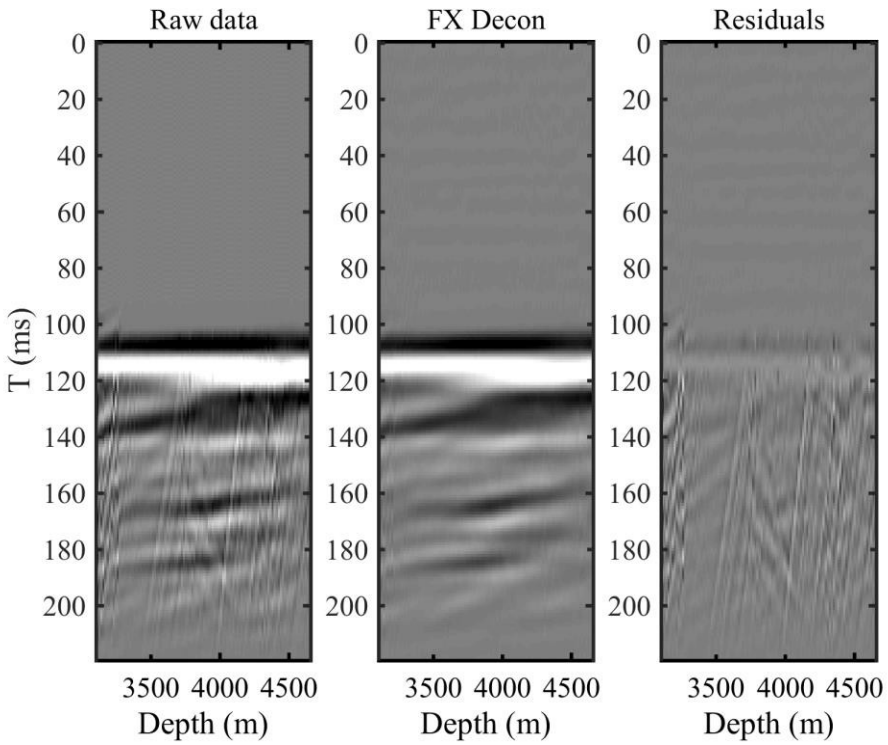

Figure A.29-3. Torosa 3. Results of attenuation of upgoing wavefield by using FX deconvolution. From left to right: original data, result of FX deconvolution and the difference.

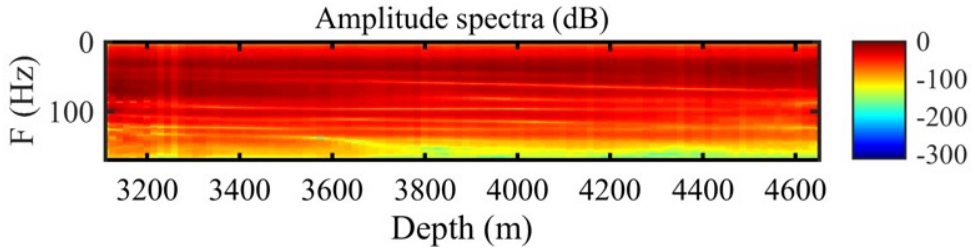

Figure A.29-4. Torosa 3. Amplitude spectra after FX deconvolution.

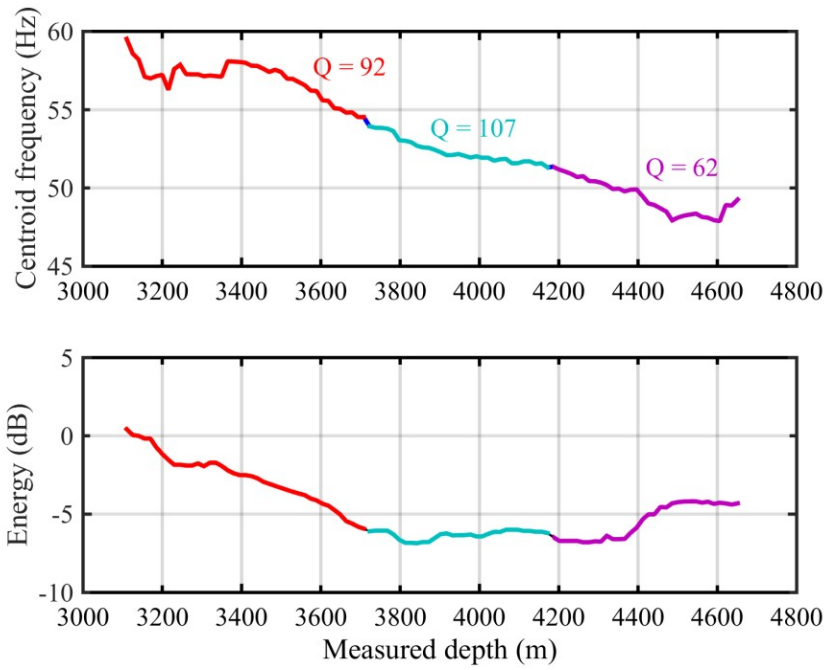

Figure A.29-5. Torosa 3. Results of centroid frequency (top panel) and energy (bottom panel) decay estimation. Estimated attenuation values are derived for 3 stratigraphic intervals.

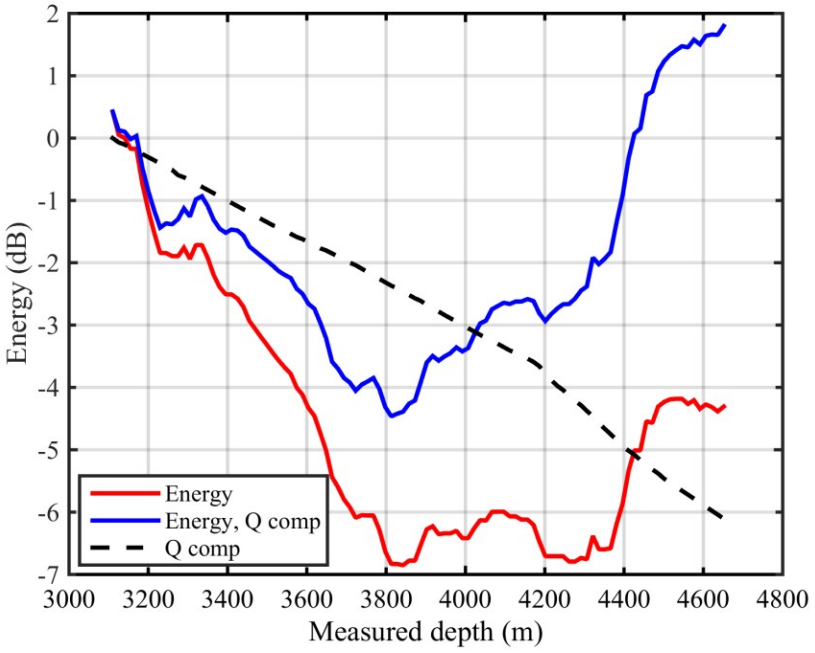

Figure A.29-6. Torosa 3. Results of energy decay curve from direct wave (divergence variation is applied) (red); attenuation component of the energy decay (black) and result of the energy decay compensation (blue).

A.30. Torosa 5 results

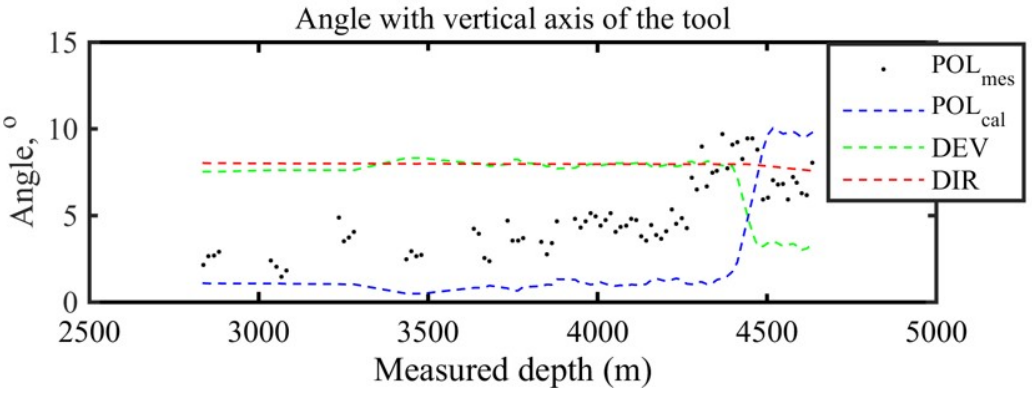

Figure A.30-1. Torosa 5. Results of the orientation: measured polarization of P-wave in respect to a vertical axis of the VSP tool (black dots); calculated polarization of P-wave in respect to a vertical axis of the VSP tool (blue dash line); well inclination (green dash line); angle between a vertical direction and the direction of P-wave propagation (red dash line).

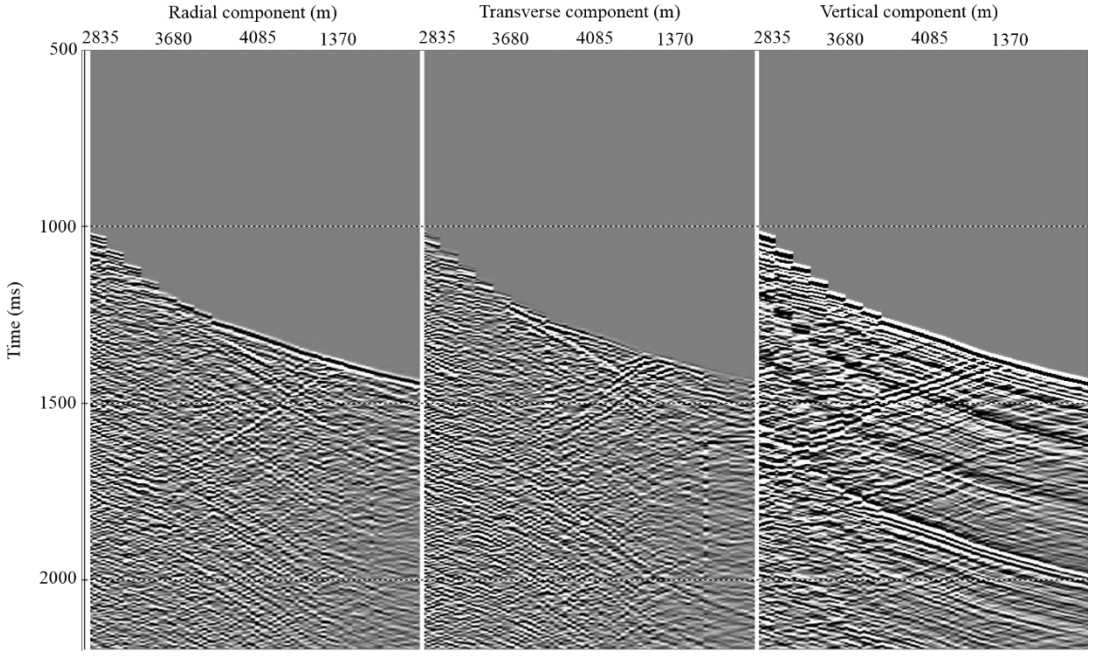

Figure A.30-2. Torosa 5. 3C VSP oriented data: radial (left panel), transverse (middle panel), and vertical (right panel) components.

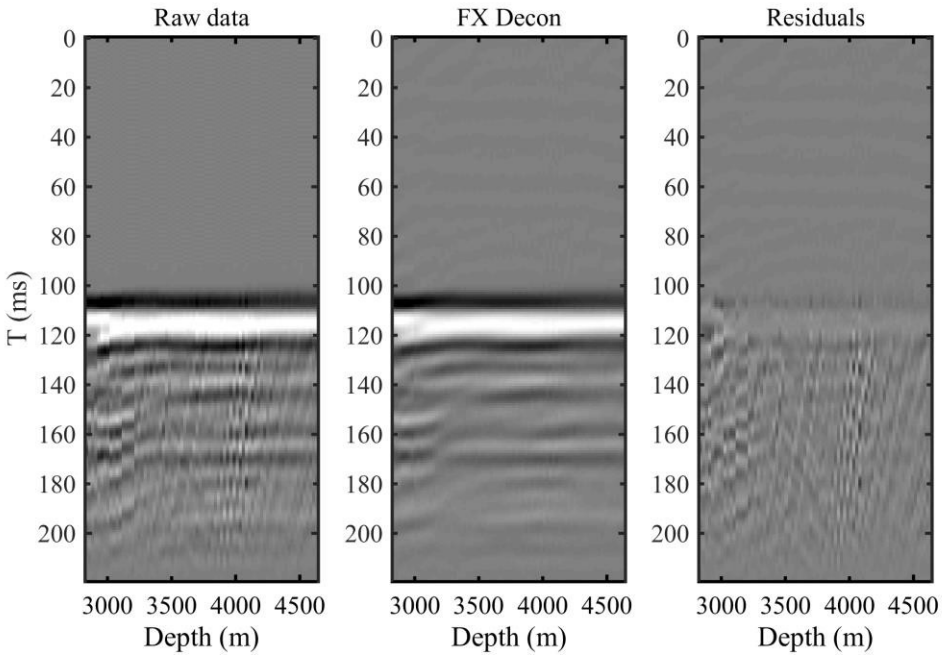

Figure A.30-3. Torosa 5. Results of attenuation of upgoing wavefield by using FX deconvolution. From left to right: original data, result of FX deconvolution and the difference.

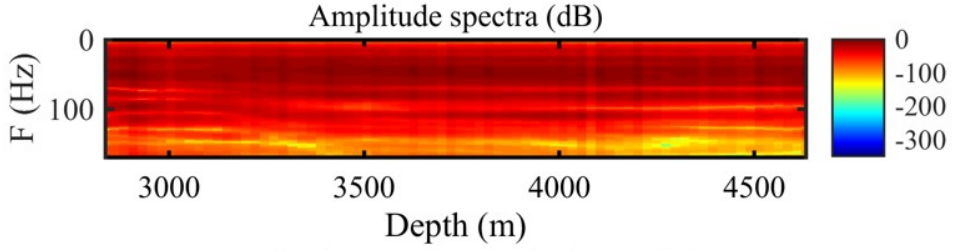

Figure A.30-4. Torosa 5. Amplitude spectra after FX deconvolution.

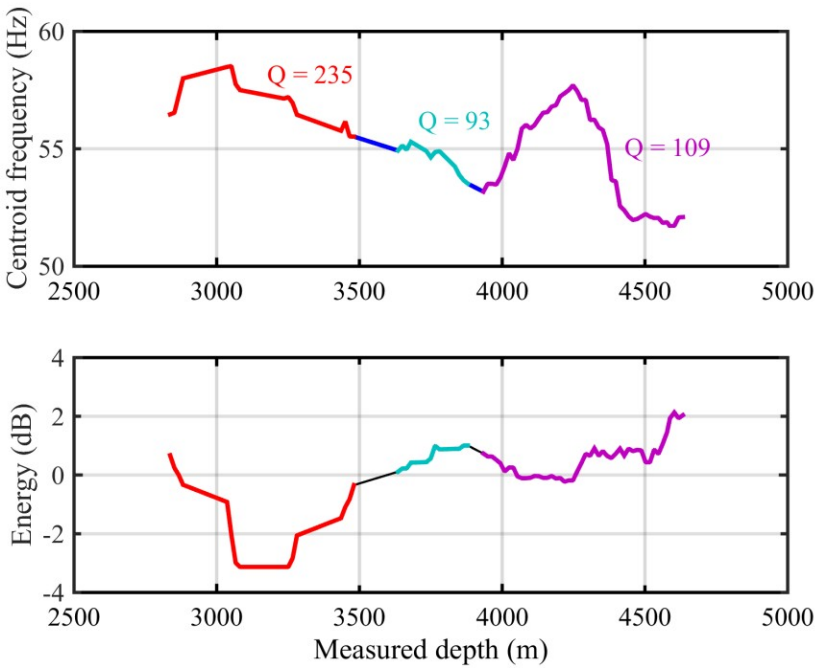

Figure A.30-5. Torosa 5. Results of centroid frequency (top panel) and energy (bottom panel) decay estimation. Estimated attenuation values are derived for 3 stratigraphic intervals.

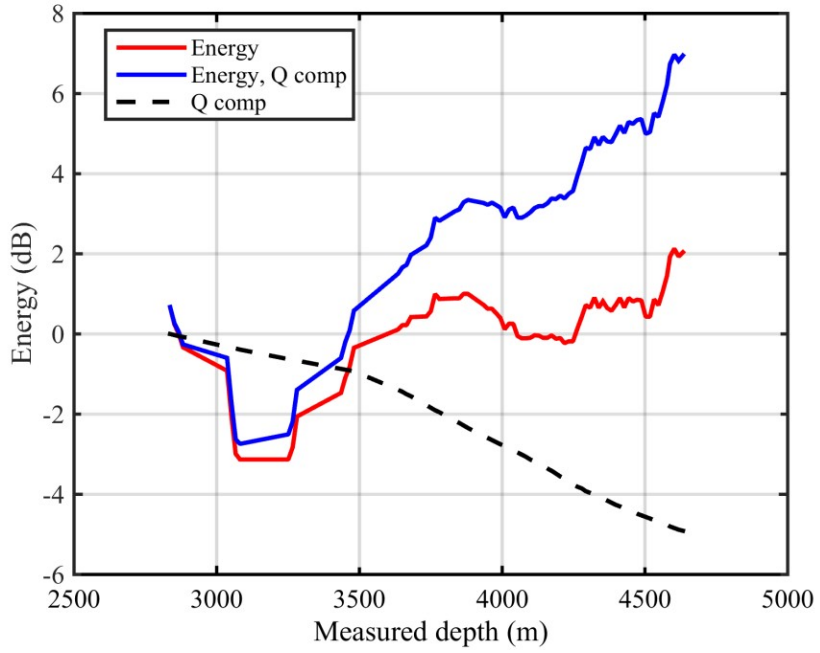

Figure A.30-6. Torosa 5. Results of energy decay curve from direct wave (divergence variation is applied) (red); attenuation component of the energy decay (black) and result of the energy decay compensation (blue).

A.31. Torosa 6 results

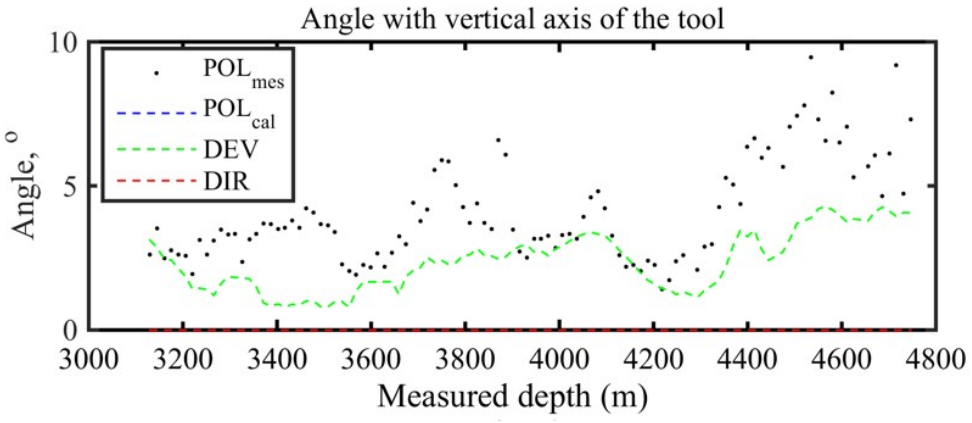

Figure A.31-1. Torosa 6. Results of the orientation: measured polarization of P-wave in respect to a vertical axis of the VSP tool (black dots); calculated polarization of P-wave in respect to a vertical axis of the VSP tool (blue dash line); well inclination (green dash line); angle between a vertical direction and the direction of P-wave propagation (red dash line).

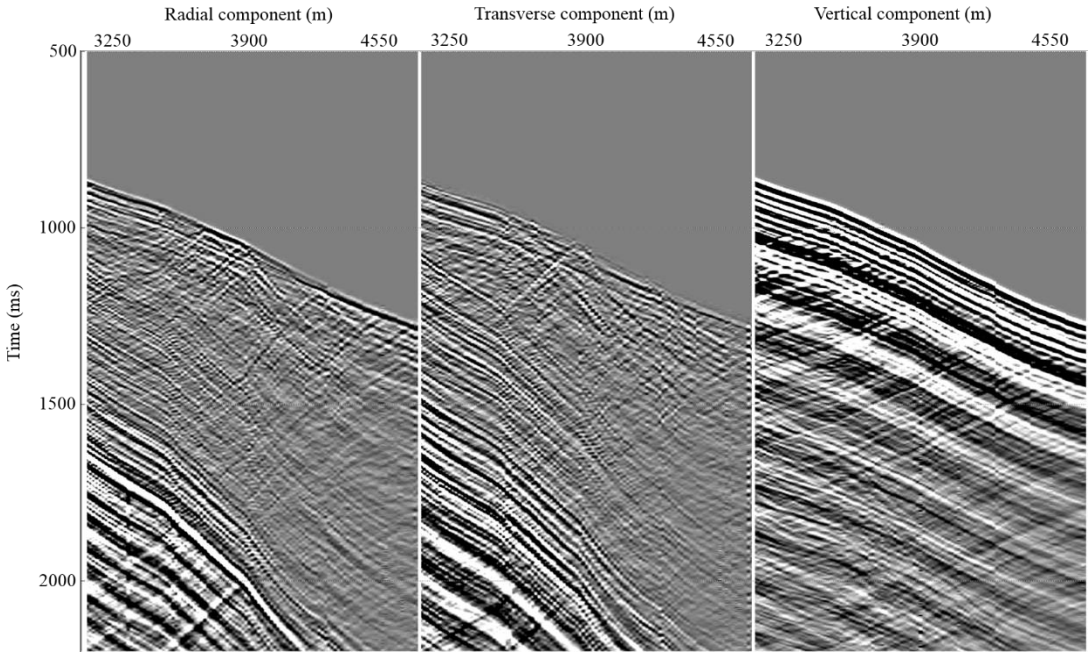

Figure A.31-2. Torosa 6. 3C VSP oriented data: radial (left panel), transverse (middle panel), and vertical (right panel) components.

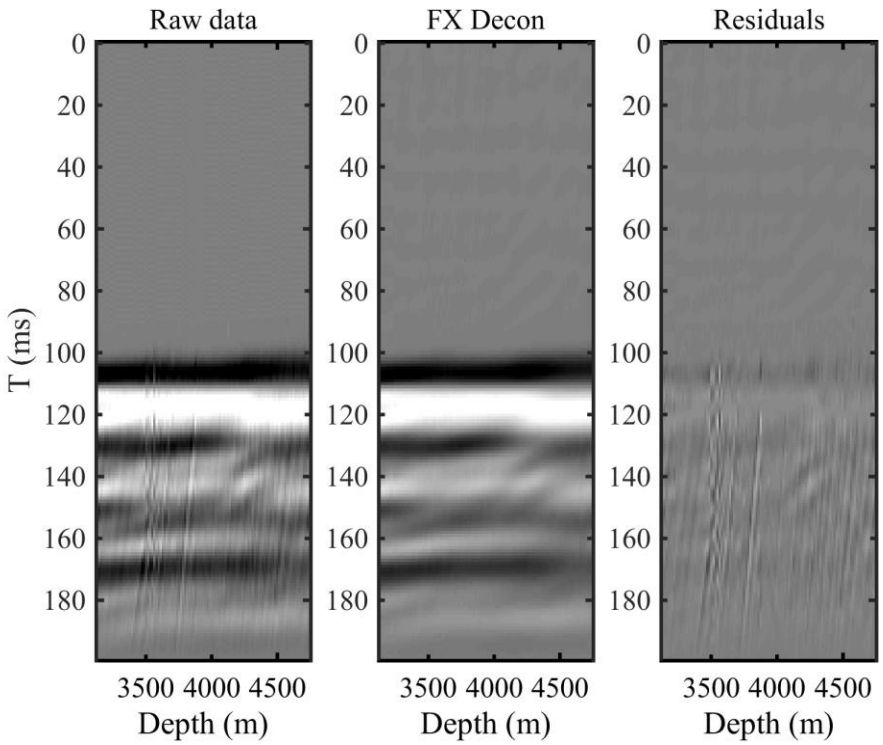

Figure A.31-3. Torosa 6. Results of attenuation of upgoing wavefield by using FX deconvolution. From left to right: original data, result of FX deconvolution and the difference.

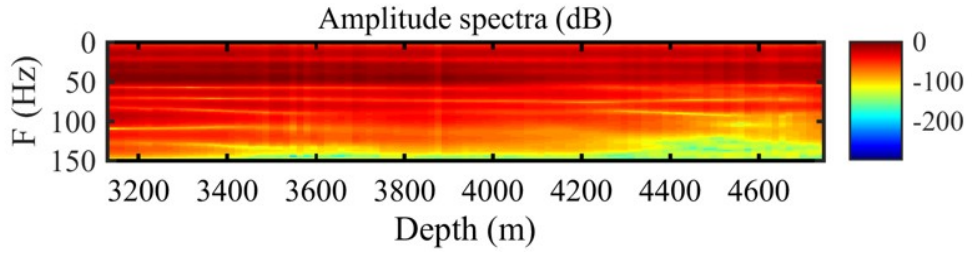

Figure A.31-4. Torosa 6. Amplitude spectra after FX deconvolution.

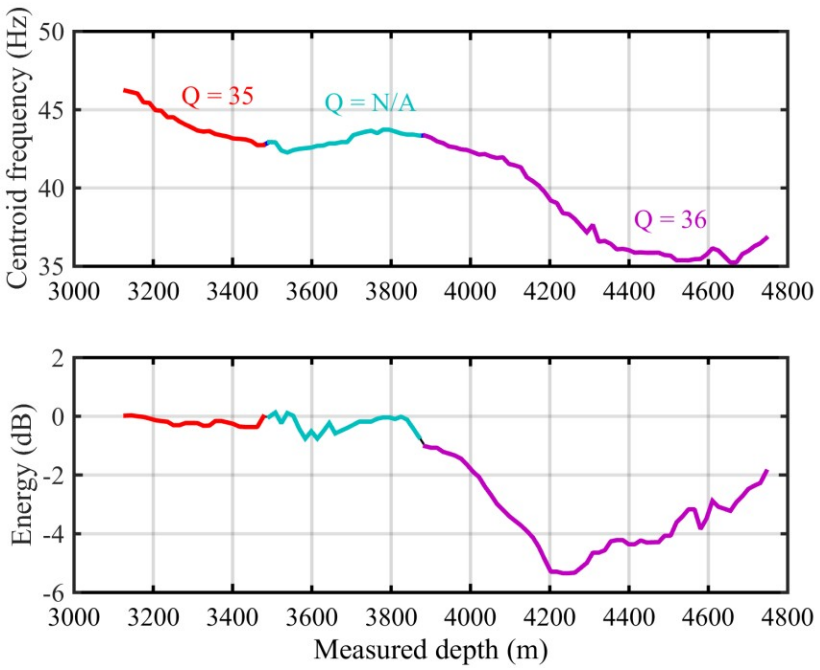

Figure A.31-5. Torosa 6. Results of centroid frequency (top panel) and energy (bottom panel) decay estimation. Estimated attenuation values are derived for 3 stratigraphic intervals.

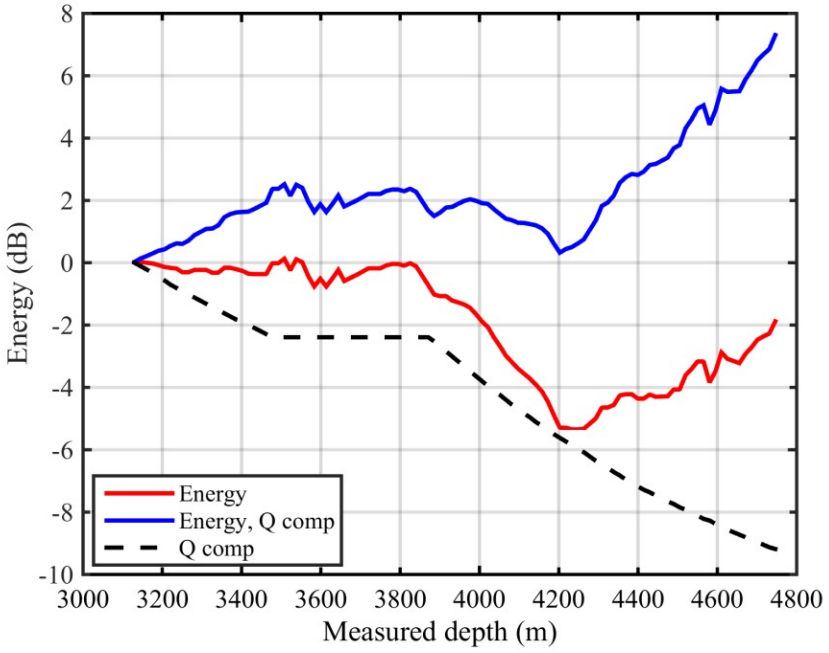

Figure A.31-6. Torosa 6. Results of energy decay curve from direct wave (divergence variation is applied) (red); attenuation component of the energy decay (black) and result of the energy decay compensation (blue).

A.32. Wheatstone 2 results

Apparent attenuation

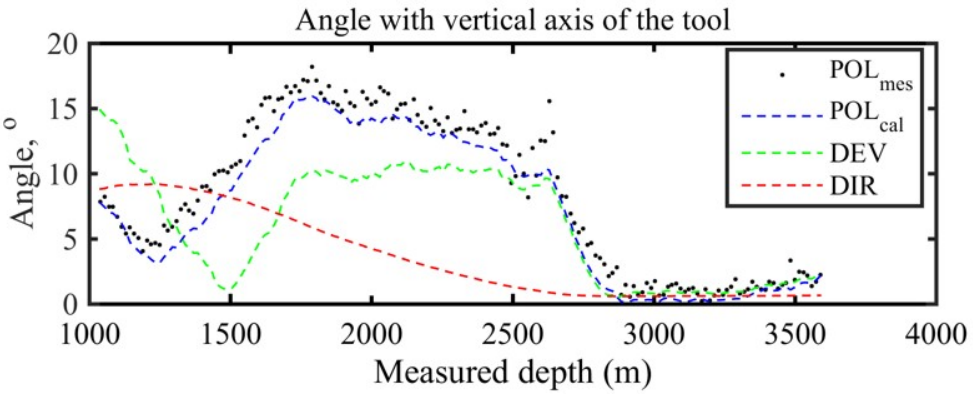

Figure A.32-1. Wheatstone 2. Results of the orientation: measured polarization of P-wave in respect to a vertical axis of the VSP tool (black dots); calculated polarization of P-wave in respect to a vertical axis of the VSP tool (blue dash line); well inclination (green dash line); angle between a vertical direction and the direction of P-wave propagation (red dash line).

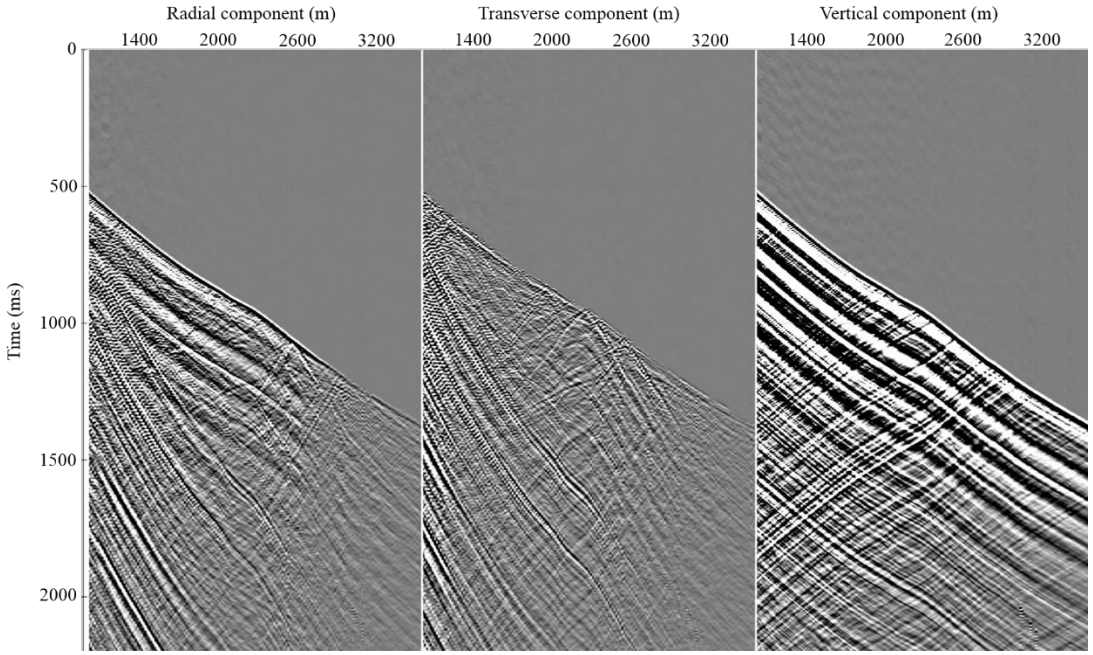

Figure A.32-2. Wheatstone 2. 3C VSP oriented data: radial (left panel), transverse (middle panel), and vertical (right panel) components.

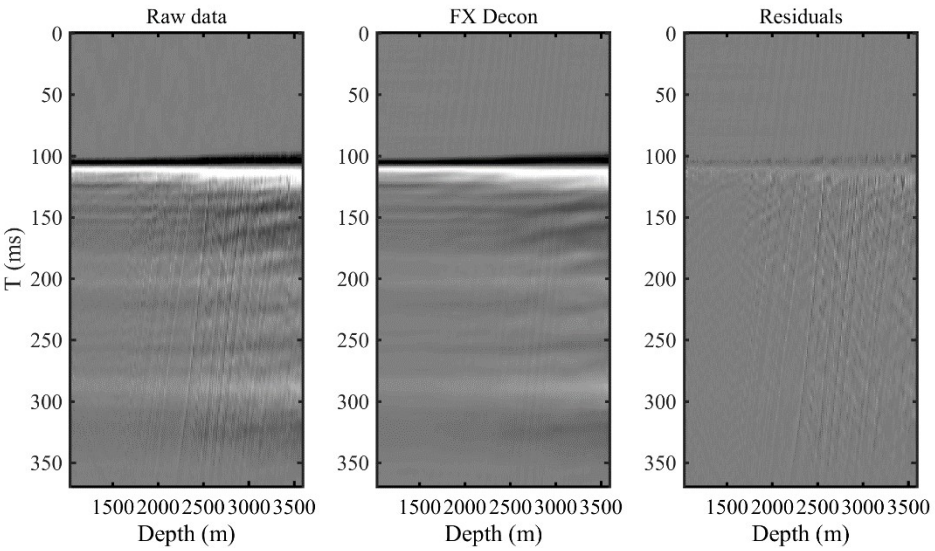

Figure A.32-3. Wheatstone 2. Results of attenuation of upgoing wavefield by using FX deconvolution. From left to right: original data, result of FX deconvolution and the difference.

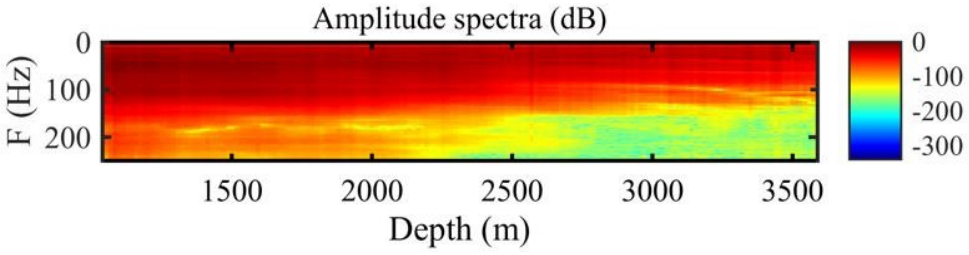

Figure A.32-4. Wheatstone 2. Amplitude spectra after FX deconvolution.

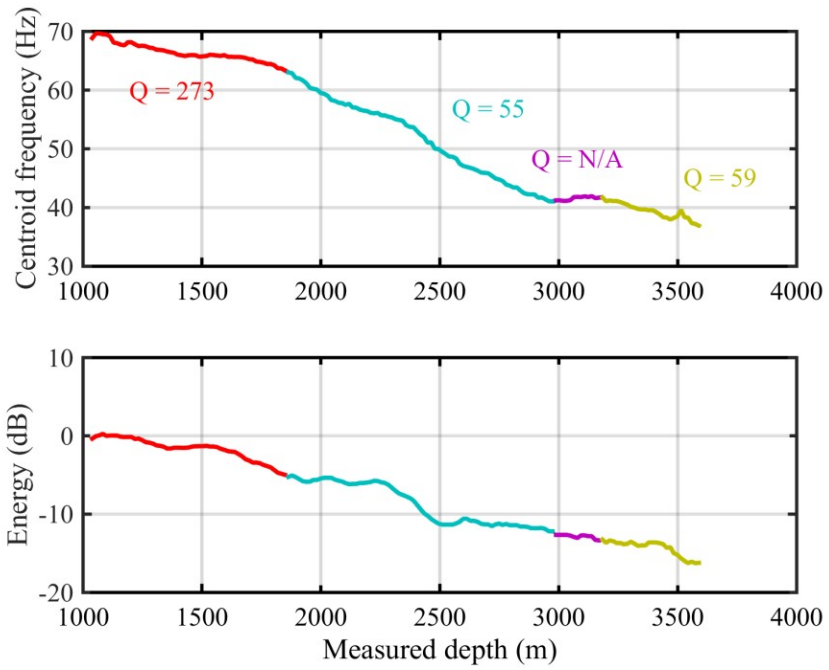

Figure A.32-5. Wheatstone 2. Results of centroid frequency (top panel) and energy (bottom panel) decay estimation. Estimated attenuation values are derived for 4 stratigraphic intervals.

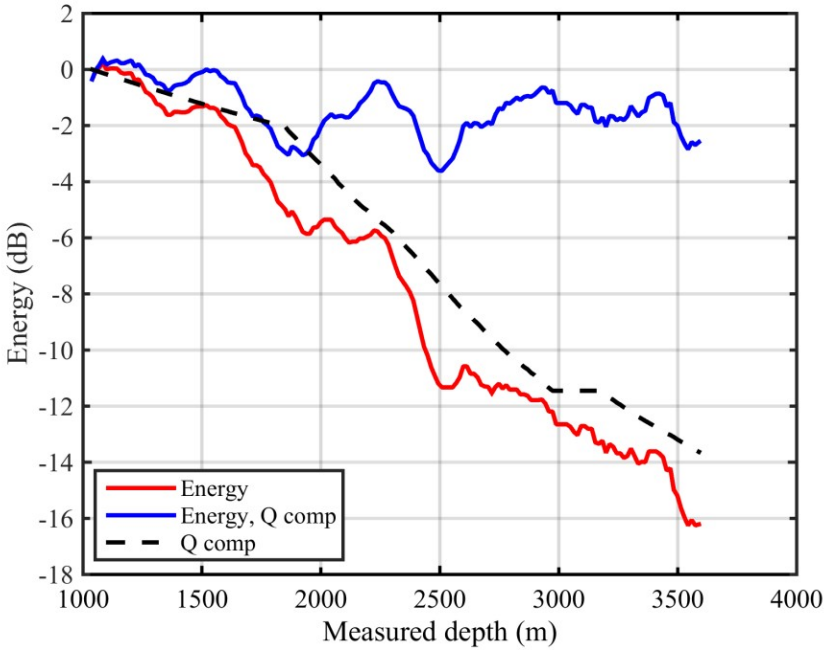

Figure A.32-6. Wheatstone 2. Results of energy decay curve from direct wave (divergence variation is applied) (red); attenuation component of the energy decay (black) and result of the energy decay compensation (blue).

Scattering attenuation

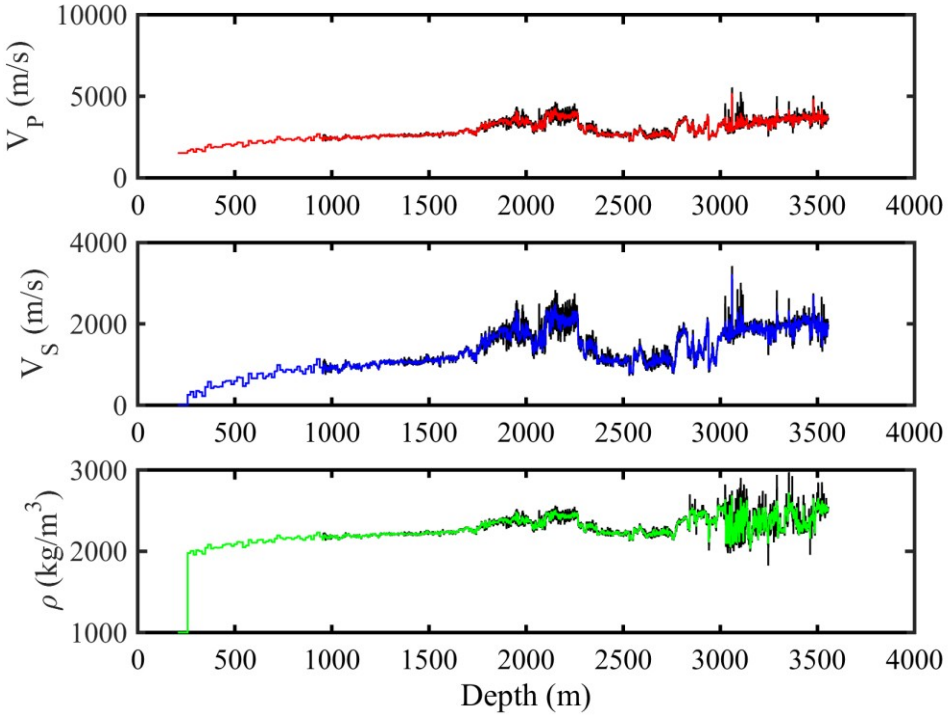

Figure A.32-7. Wheatstone 2. Elastic model. Black curve is log data, coloured curves are results of Backus averaging.

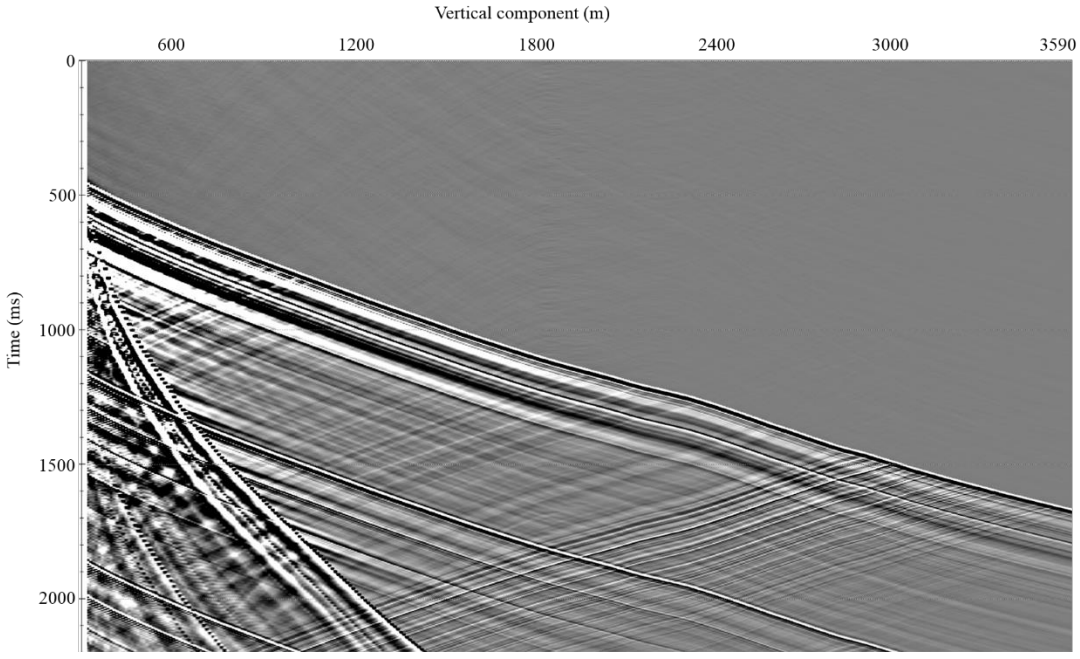

Figure A.32-8. Wheatstone 2. Synthetic zero-offset VSP seismogram.

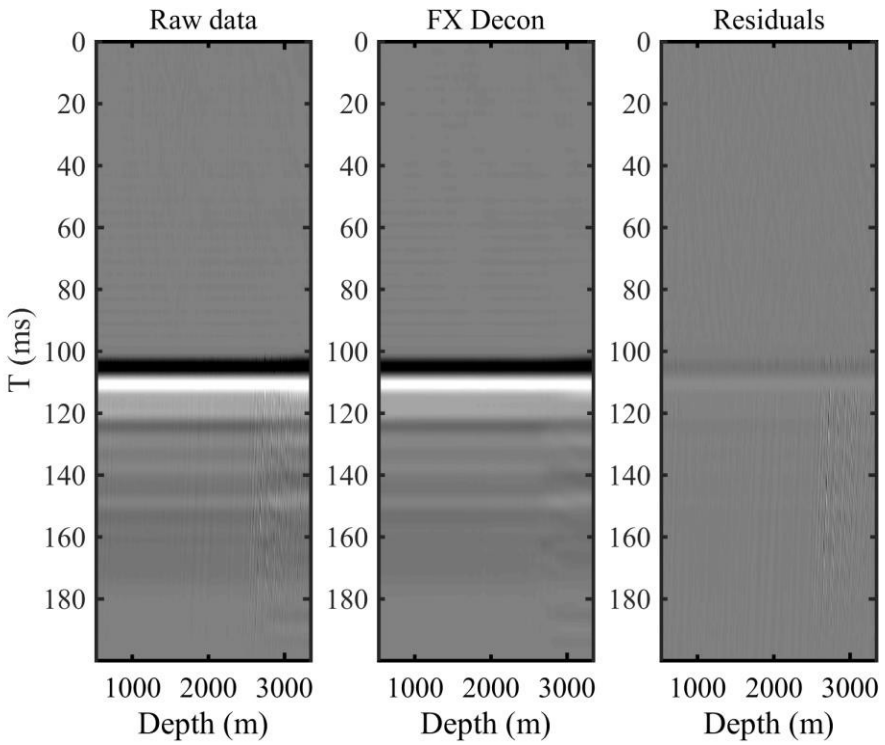

Figure A.32-9. Wheatstone 2. Synthetic data. Results of attenuation of upgoing wavefield by using FX deconvolution. From left to right: original data, result of FX deconvolution and the difference.

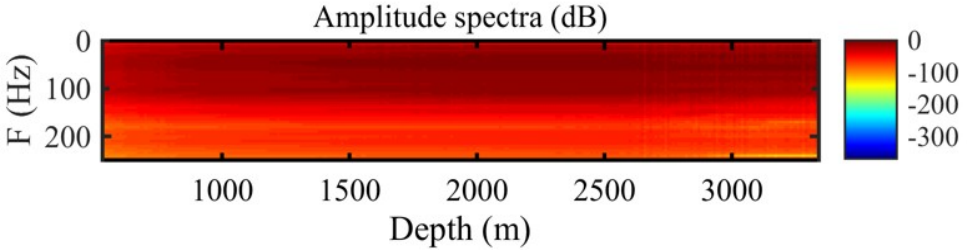

Figure A.32-10. Wheatstone 2. Synthetic data. Amplitude spectra after FX deconvolution.

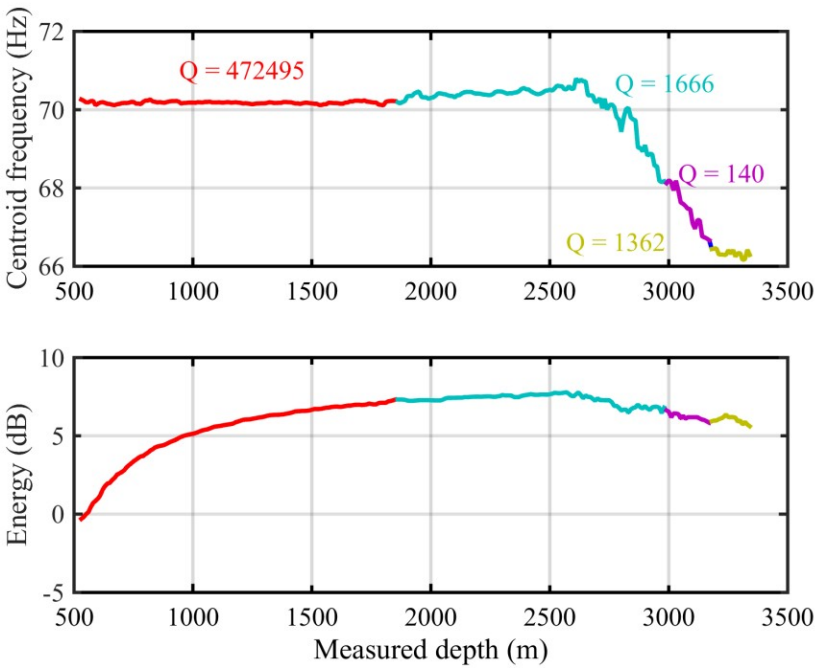

Figure A.32-11. Wheatstone 2. Synthetic data. Results of centroid frequency (top panel) and energy (bottom panel) decay estimation. Estimated values of scattering attenuation are derived for 4 stratigraphic intervals.

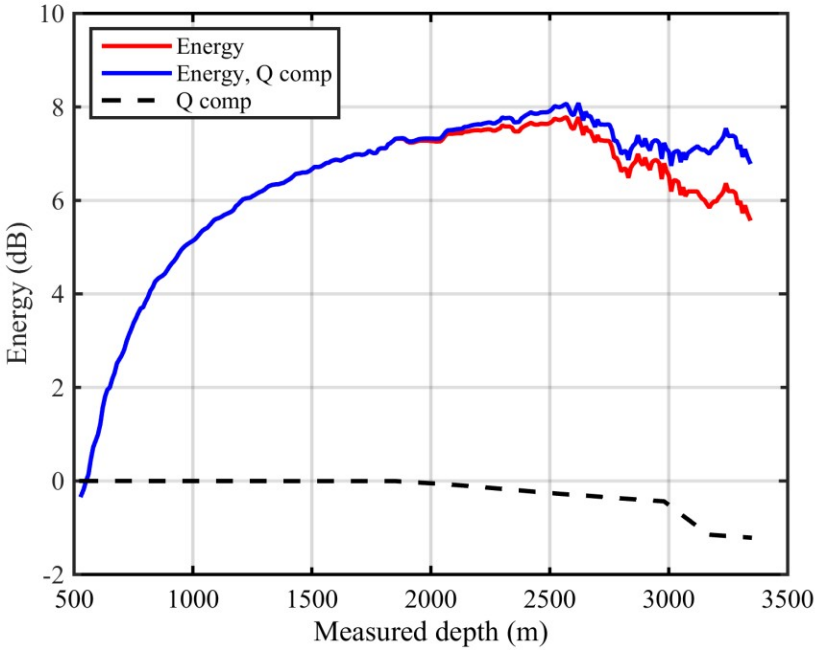

Figure A.32-12. Wheatstone 2. Synthetic data. Results of energy decay curve from direct wave (divergence variation is applied) (red); attenuation component of the energy decay (black) and result of the energy decay compensation (blue).

A.33. Wheatstone 3 results

Apparent attenuation

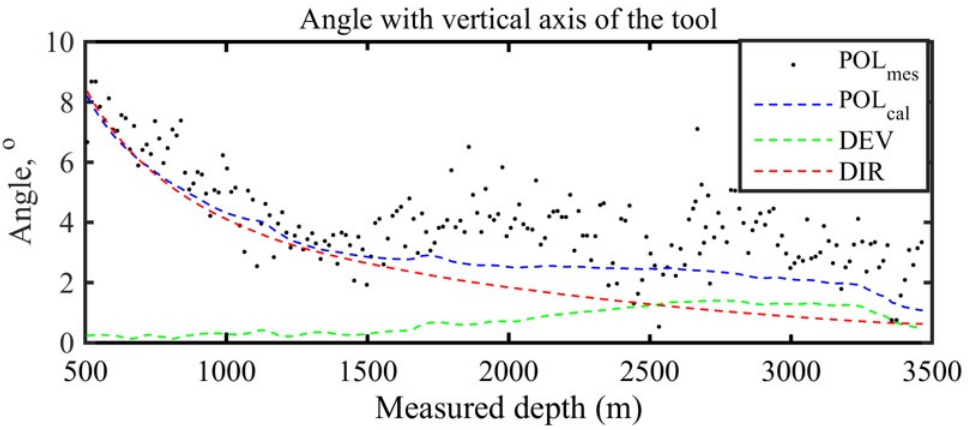

Figure A.33-1. Wheatstone 3. Results of the orientation: measured polarization of P-wave in respect to a vertical axis of the VSP tool (black dots); calculated polarization of P-wave in respect to a vertical axis of the VSP tool (blue dash line); well inclination (green dash line); angle between a vertical direction and the direction of P-wave propagation (red dash line).

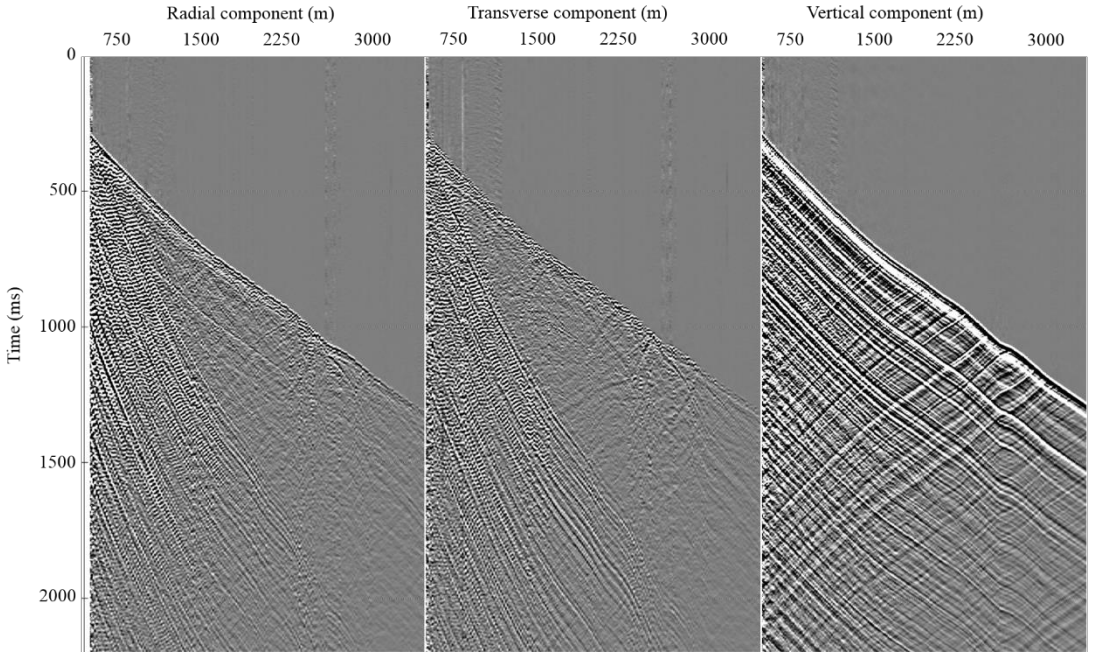

Figure A.33-2. Wheatstone 3. 3C VSP oriented data: radial (left panel), transverse (middle panel), and vertical (right panel) components.

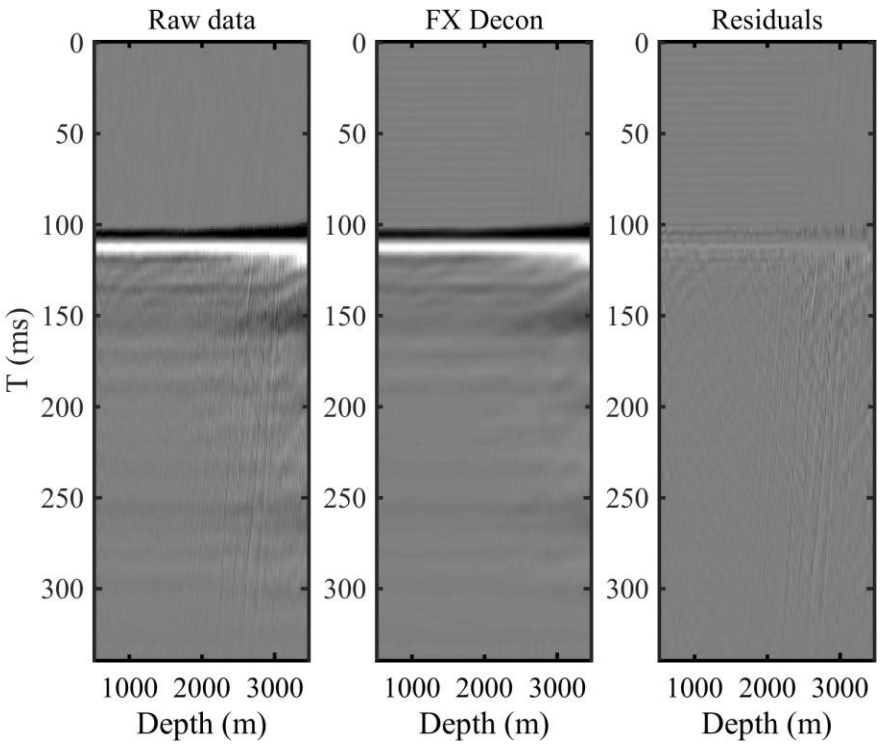

Figure A.33-3. Wheatstone 3. Results of attenuation of upgoing wavefield by using FX deconvolution. From left to right: original data, result of FX deconvolution and the difference.

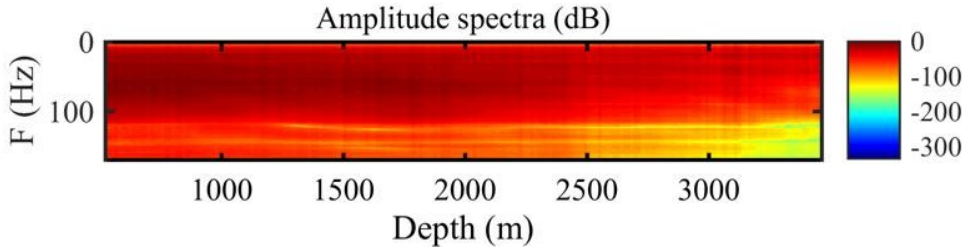

Figure A.33-4. Wheatstone 3. Amplitude spectra after FX deconvolution.

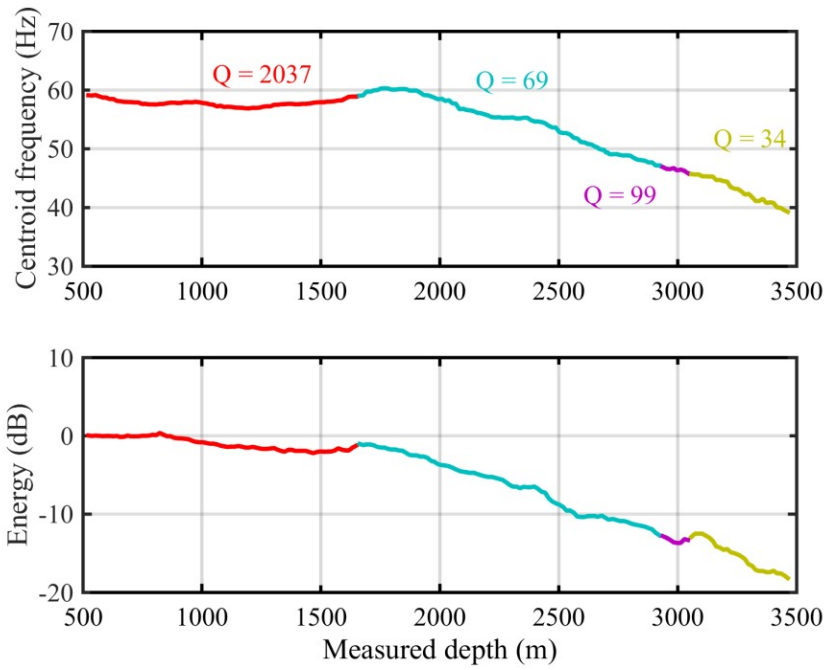

Figure A.33-5. Wheatstone 3. Results of centroid frequency (top panel) and energy (bottom panel) decay estimation. Estimated attenuation values are derived for 4 stratigraphic intervals.

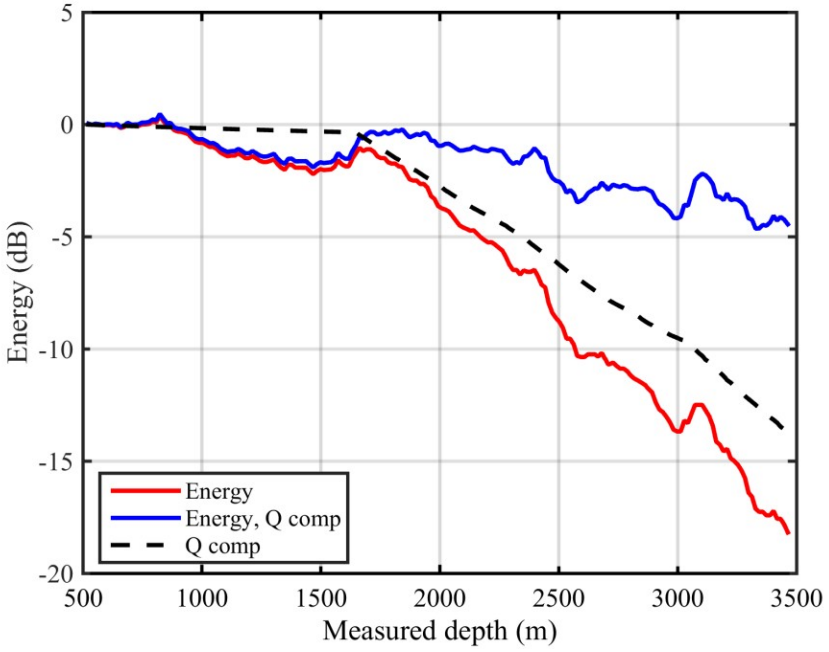

Figure A.33-6. Wheatstone 3. Results of energy decay curve from direct wave (divergence variation is applied) (red); attenuation component of the energy decay (black) and result of the energy decay compensation (blue).

Scattering attenuation

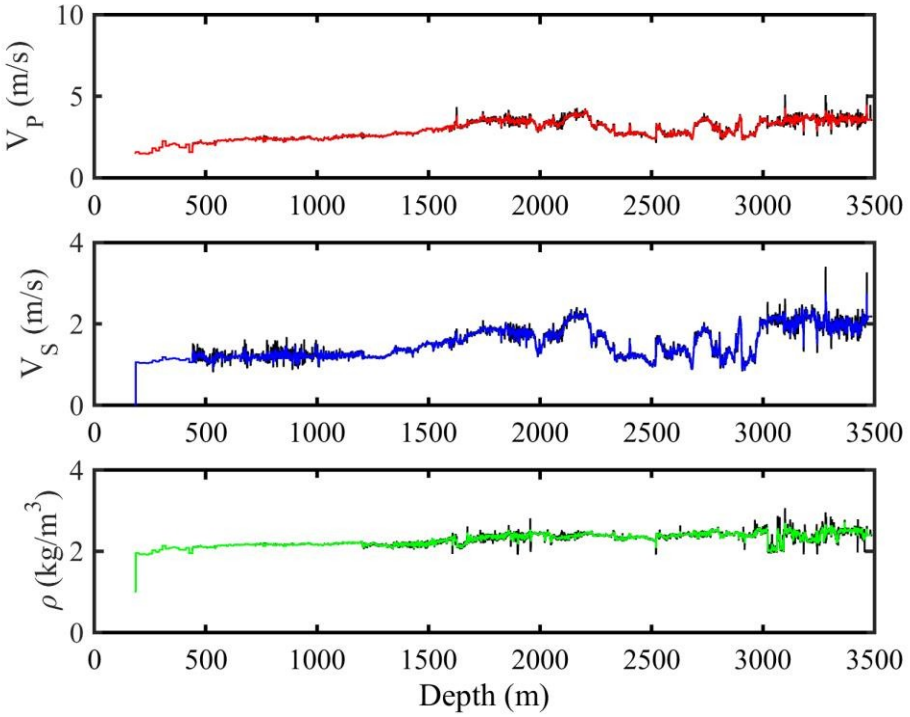

Figure A.33-7. Wheatstone 3. Elastic model. Black curve is log data, coloured curves are results of Backus averaging.

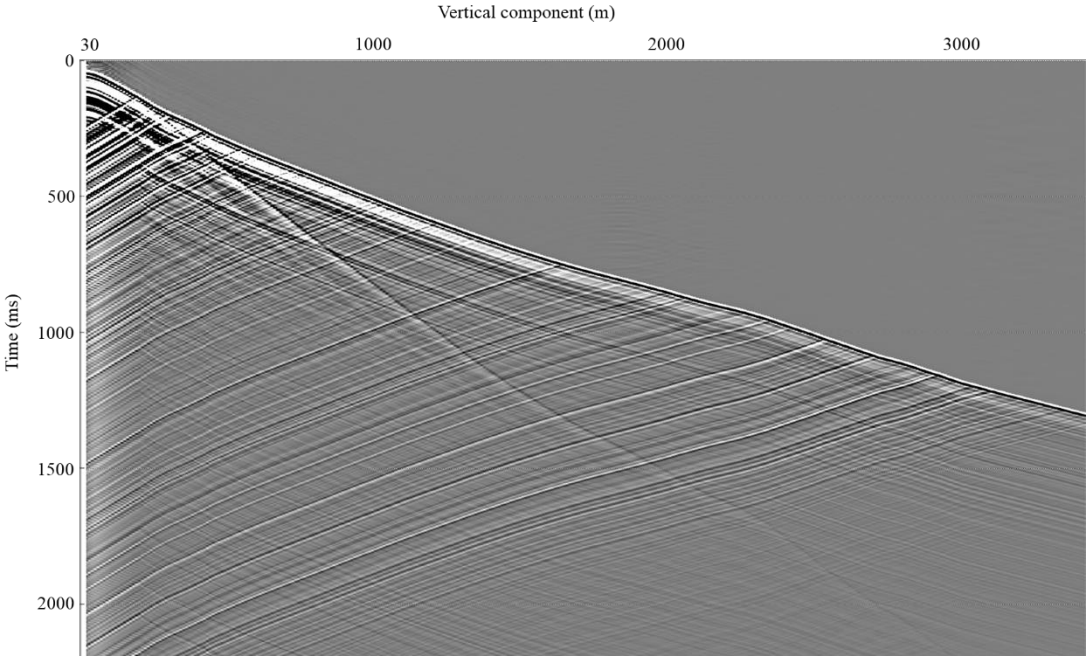

Figure A.33-8. Wheatstone 2. Synthetic zero-offset VSP seismogram.

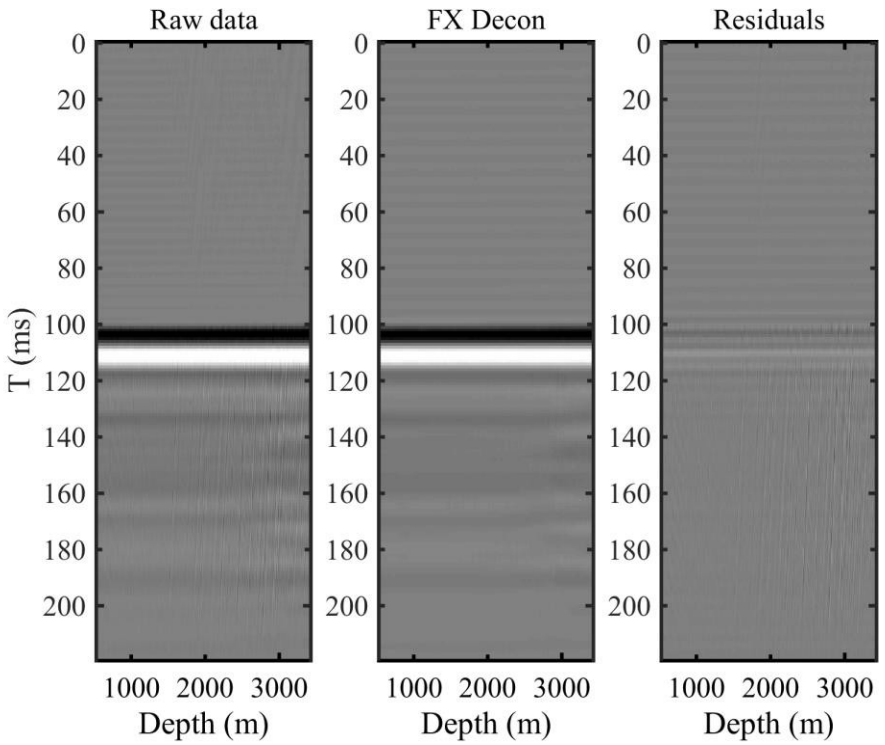

Figure A.33-9. Wheatstone 3. Synthetic data. Results of attenuation of upgoing wavefield by using FX deconvolution. From left to right: original data, result of FX deconvolution and the difference.

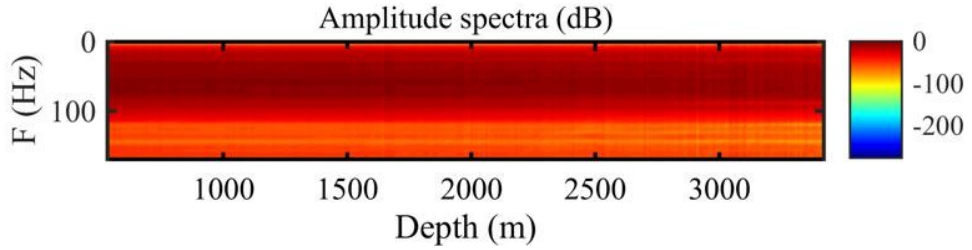

Figure A.33-10. Wheatstone 3. Synthetic data. Amplitude spectra after FX deconvolution.

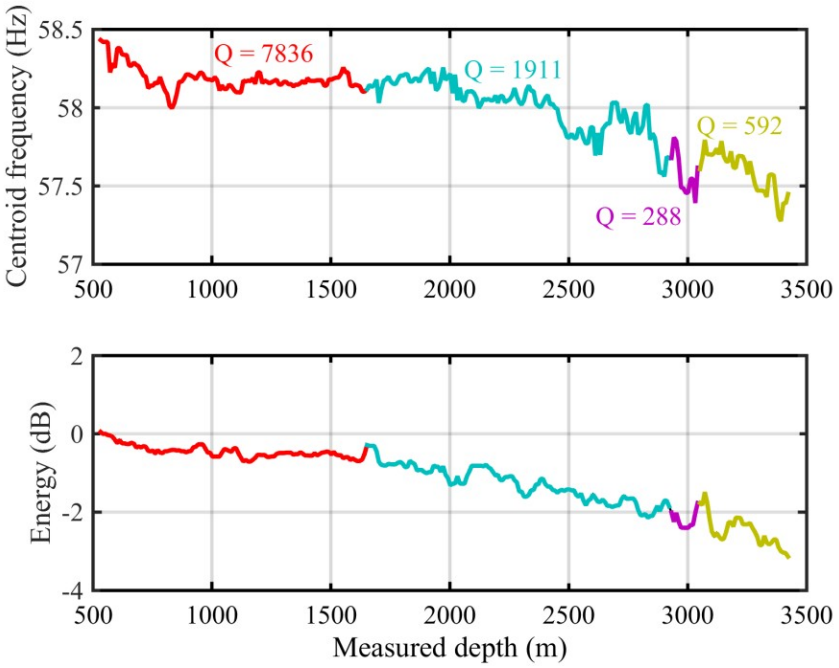

Figure A.33-11. Wheatstone 3. Synthetic data. Results of centroid frequency (top panel) and energy (bottom panel) decay estimation. Estimated values of scattering attenuation are derived for 4 stratigraphic intervals.

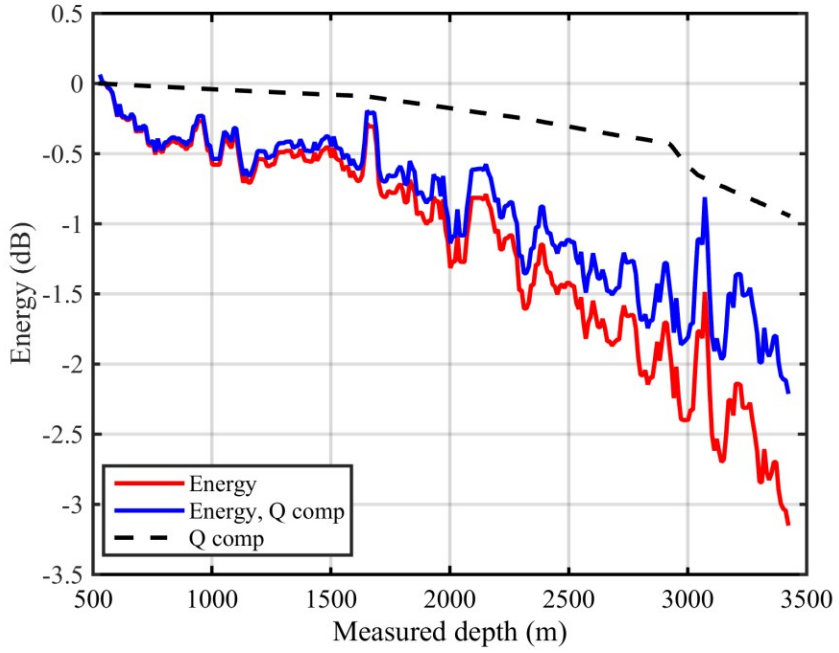

Figure A.33-12. Wheatstone 3. Synthetic data. Results of energy decay curve from direct wave (divergence variation is applied) (red); attenuation component of the energy decay (black) and result of the energy decay compensation (blue).

.

A.34. Xena 1 results

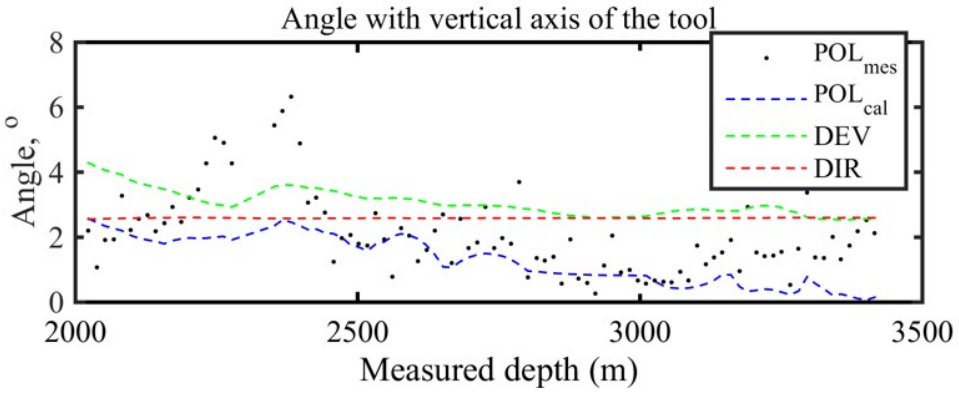

Figure A.34-1. Xena 1. Results of the orientation: measured polarization of P-wave in respect to a vertical axis of the VSP tool (black dots); calculated polarization of P-wave in respect to a vertical axis of the VSP tool (blue dash line); well inclination (green dash line); angle between a vertical direction and the direction of P-wave propagation (red dash line).

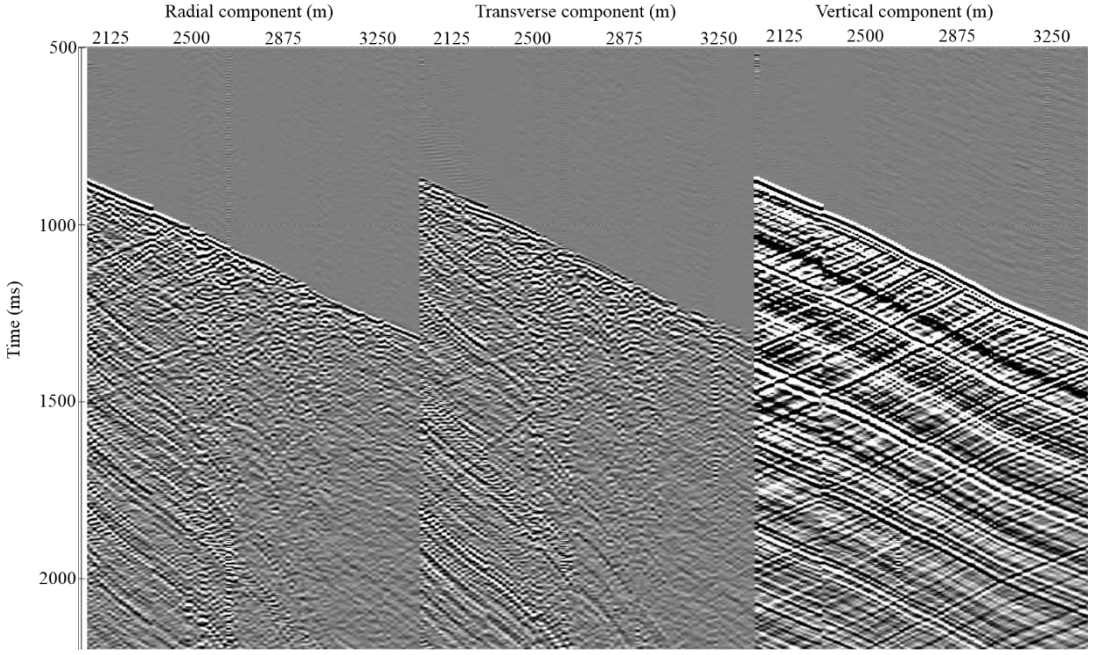

Figure A.34-2. Xena 1. 3C VSP oriented data: radial (left panel), transverse (middle panel), and vertical (right panel) components.

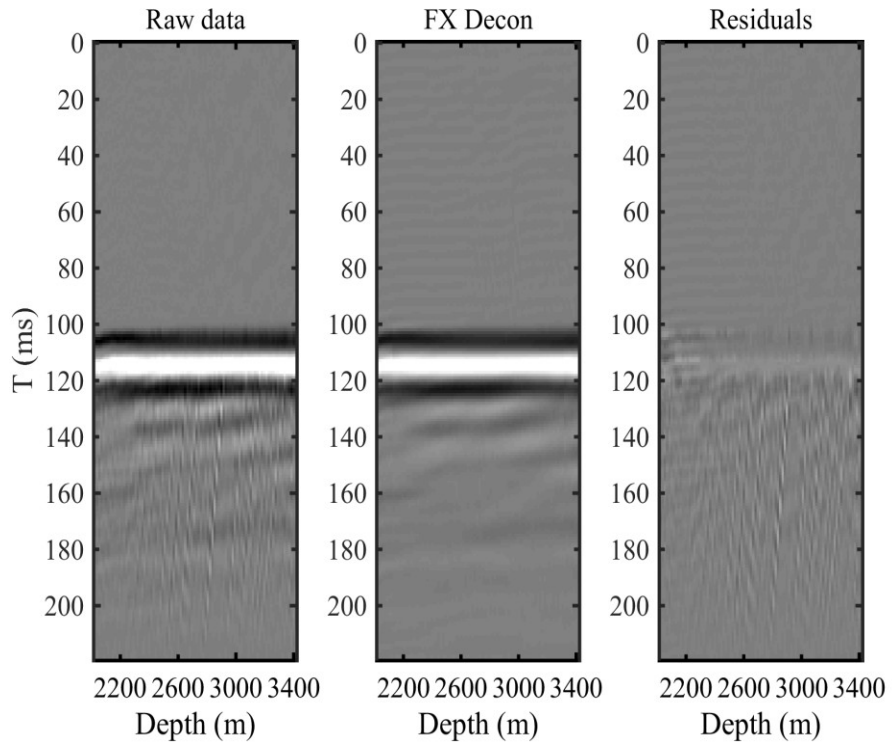

Figure A.34-3. Xena 1. Results of attenuation of upgoing wavefield by using FX deconvolution. From left to right: original data, result of FX deconvolution and the difference.

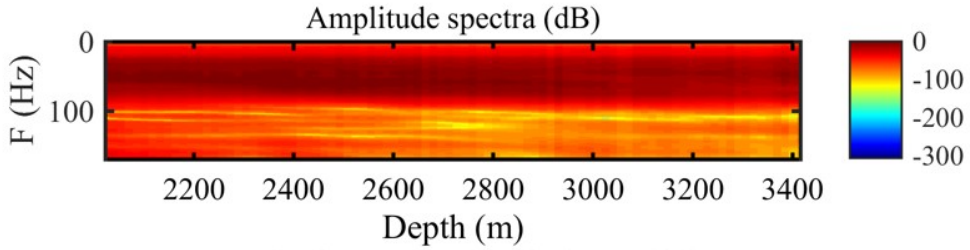

Figure A.34-4. Xena 1. Amplitude spectra after FX deconvolution.

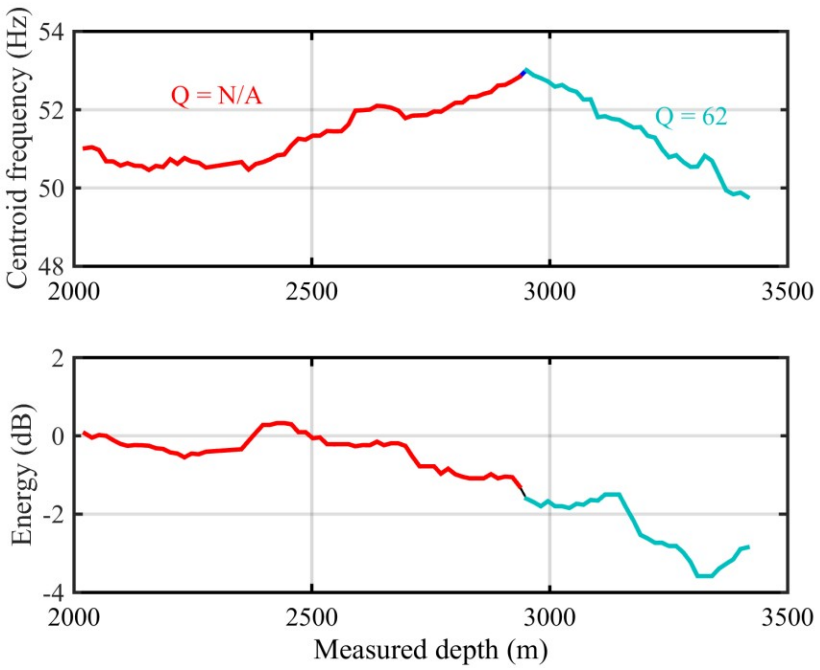

Figure A.34-5. Xena 1. Results of centroid frequency (top panel) and energy (bottom panel) decay estimation. Estimated attenuation values are derived for 2 stratigraphic intervals.

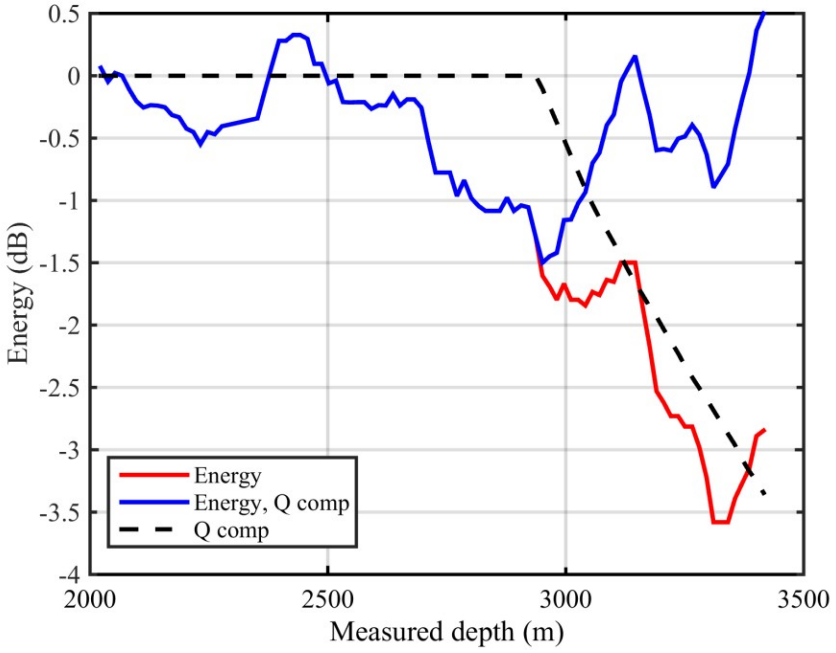

Figure A.34-6. Xena 1. Results of energy decay curve from direct wave (divergence variation is applied) (red); attenuation component of the energy decay (black) and result of the energy decay compensation (blue).

A.35. Xena 2 results

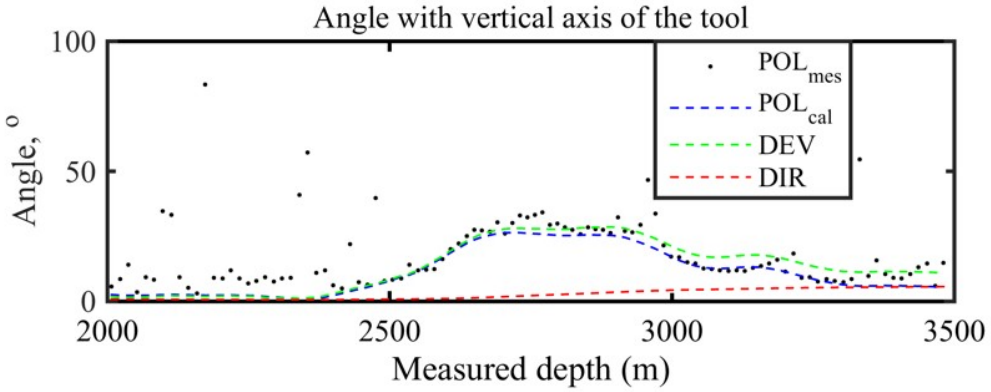

Figure A.35-1. Xena 2. Results of the orientation: measured polarization of P-wave in respect to a vertical axis of the VSP tool (black dots); calculated polarization of P-wave in respect to a vertical axis of the VSP tool (blue dash line); well inclination (green dash line); angle between a vertical direction and the direction of P-wave propagation (red dash line).

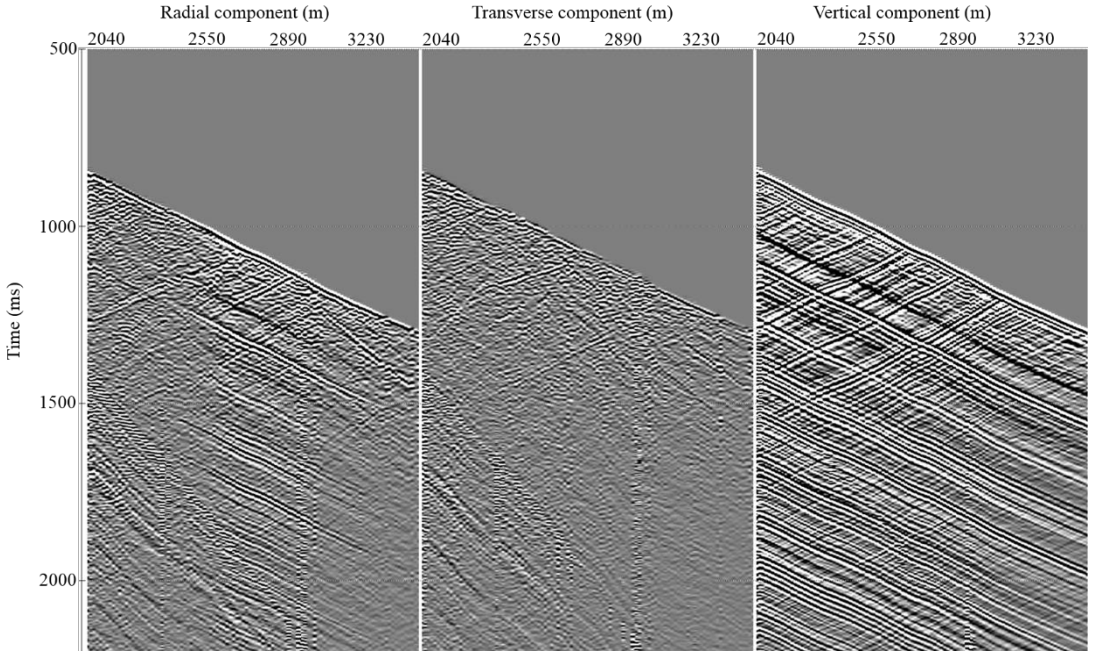

Figure A.35-2. Xena 2. 3C VSP oriented data: radial (left panel), transverse (middle panel), and vertical (right panel) components.

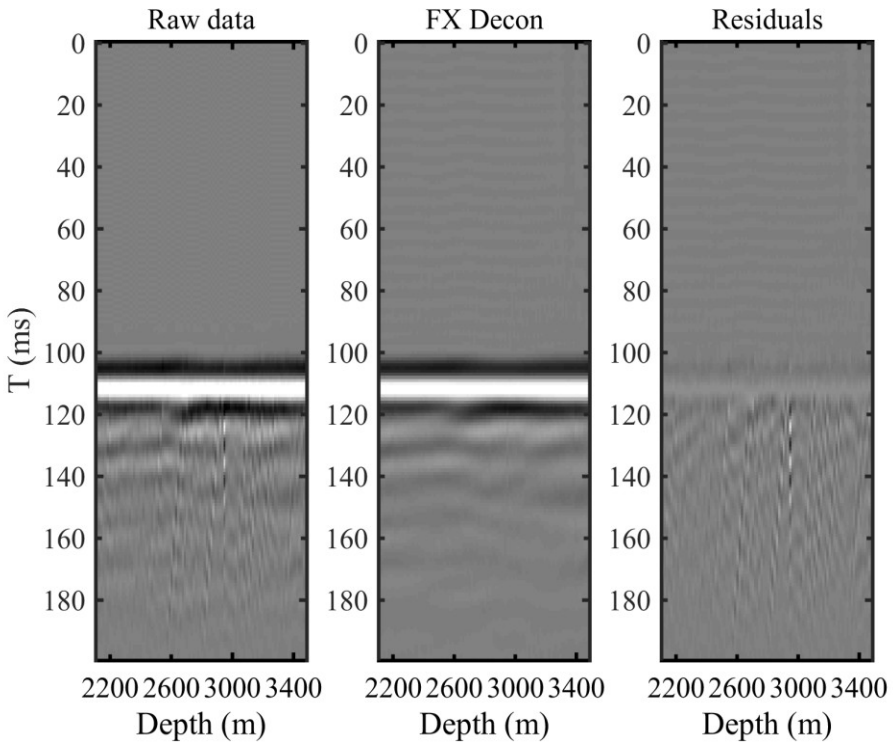

Figure A.35-3. Xena 2. Results of attenuation of upgoing wavefield by using FX deconvolution. From left to right: original data, result of FX deconvolution and the difference.

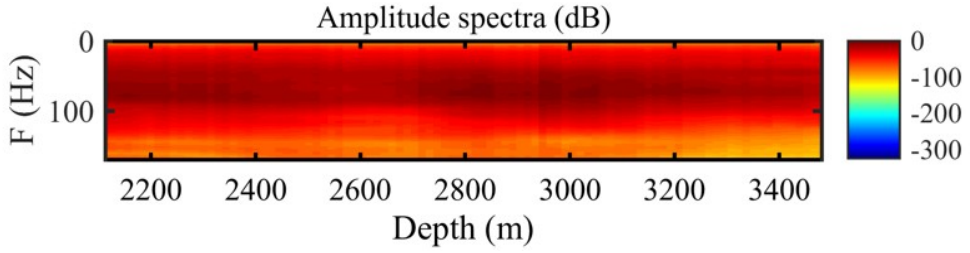

Figure A.35-4. Xena 2. Amplitude spectra after FX deconvolution.

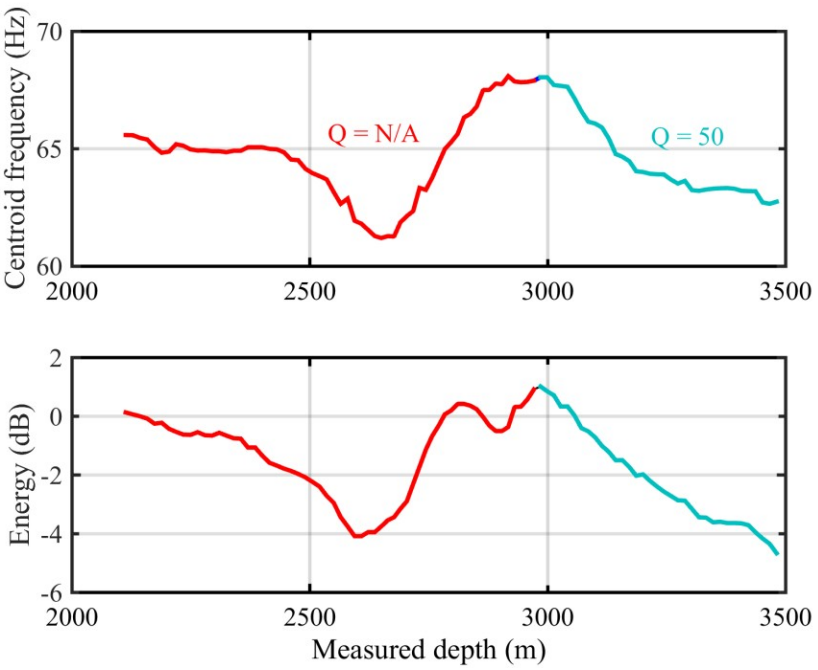

Figure A.35-5. Xena 2. Results of centroid frequency (top panel) and energy (bottom panel) decay estimation. Estimated attenuation values are derived for 2 stratigraphic intervals.

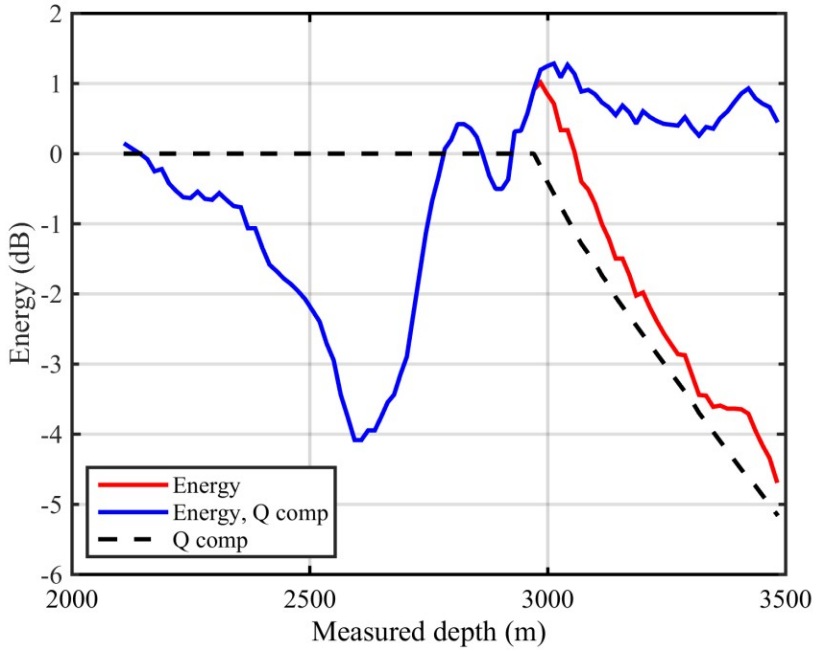

Figure A.35-6. Xena 2. Results of energy decay curve from direct wave (divergence variation is applied) (red); attenuation component of the energy decay (black) and result of the energy decay compensation (blue).

A.36. Kentish Knock-1

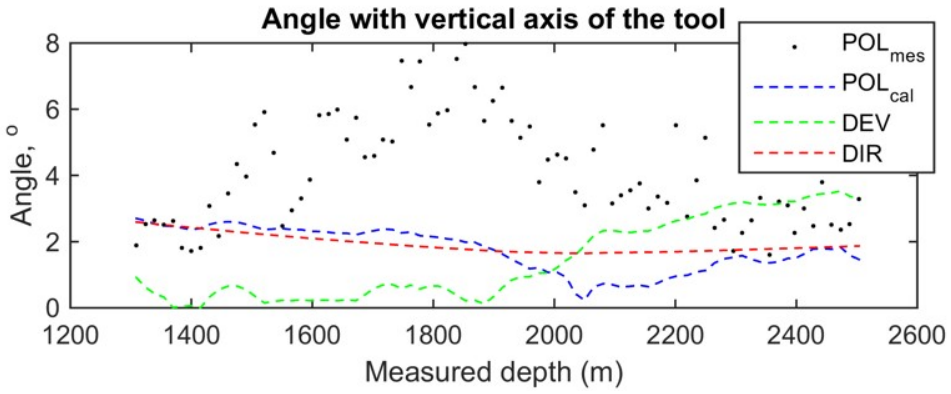

Figure A.36-1. Kentish Knock-1. Results of the orientation: measured polarization of P-wave in respect to a vertical axis of the VSP tool (black dots); calculated polarization of P-wave in respect to a vertical axis of the VSP tool (blue dash line); well inclination (green dash line); angle between a vertical direction and the direction of P-wave propagation (red dash line).

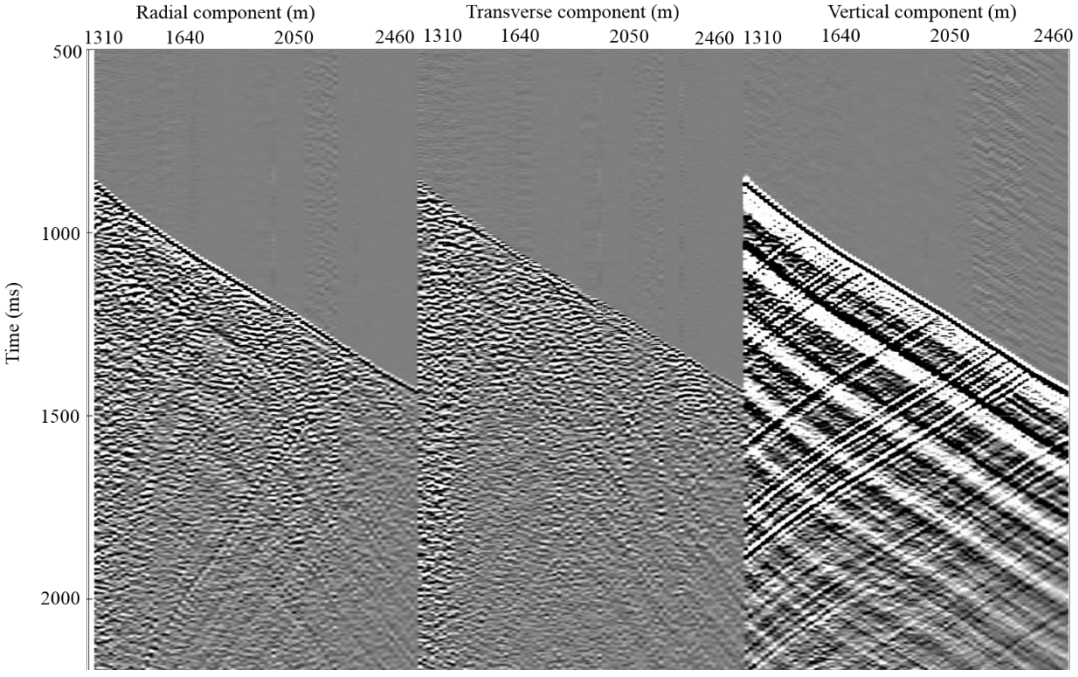

Figure A.36-2. Kentish Knock-1. 3C VSP oriented data: radial (left panel), transverse (middle panel), and vertical (right panel) components.

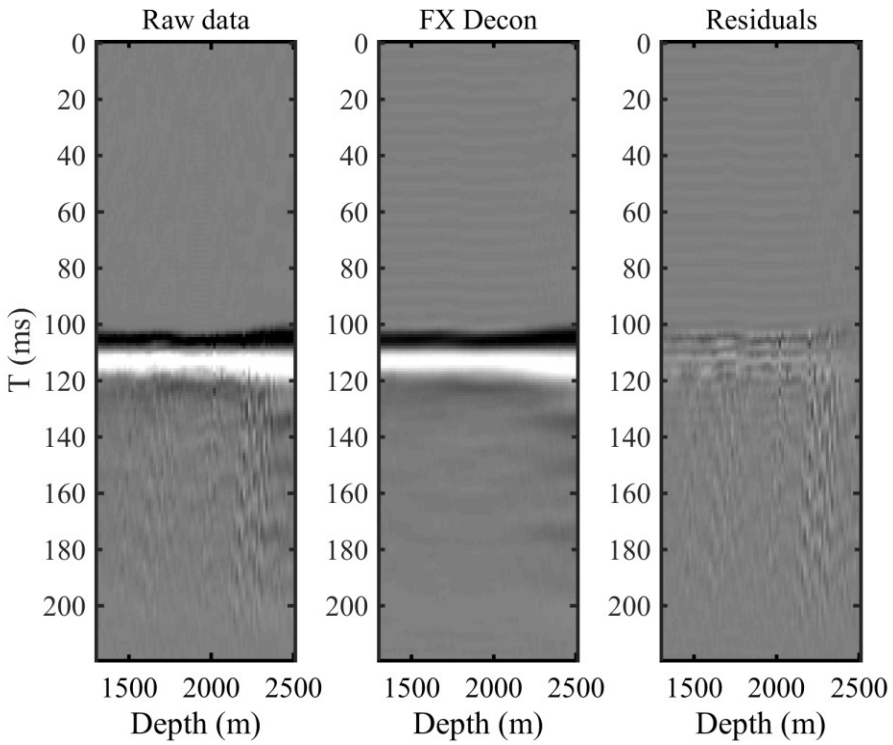

Figure A.36-3. Kentish Knock-1. Results of attenuation of upgoing wavefield by using FX deconvolution. From left to right: original data, result of FX deconvolution and the difference.

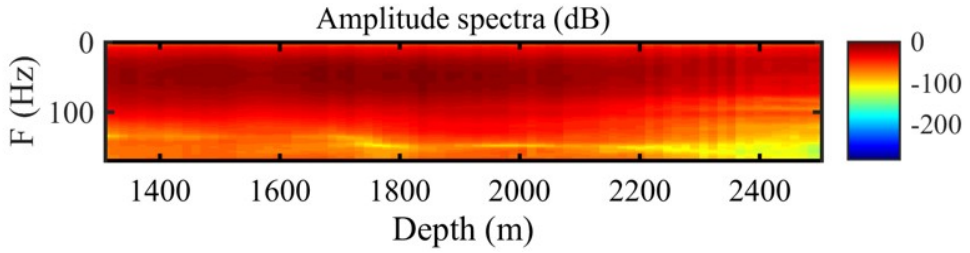

Figure A.36-4. Kentish Knock-1. Amplitude spectra after FX deconvolution.

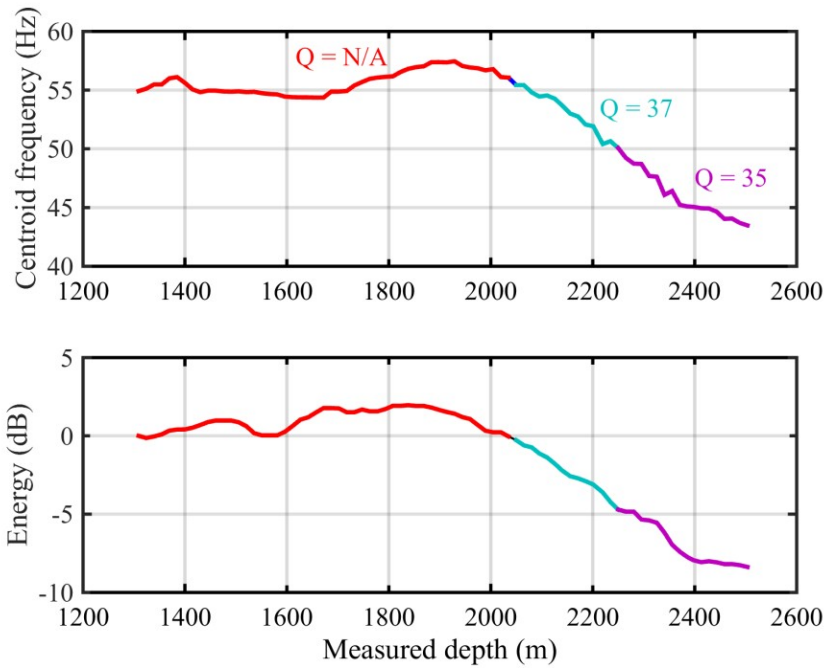

Figure A.36-5. Kentish Knock-1. Results of centroid frequency (top panel) and energy (bottom panel) decay estimation. Estimated attenuation values are derived for 3 stratigraphic intervals.

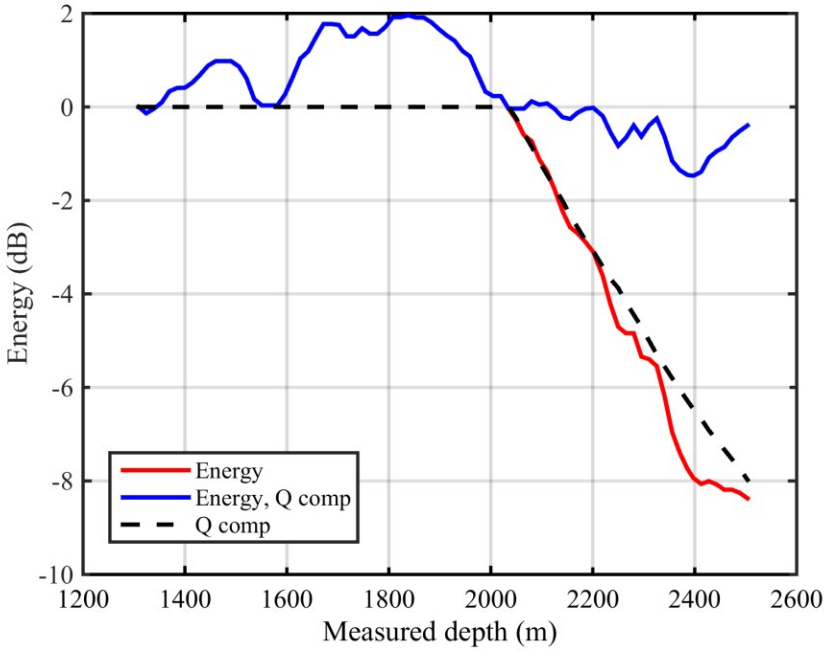

Figure A.36-6. Kentish Knock-1. Results of energy decay curve from direct wave (divergence variation is applied) (red); attenuation component of the energy decay (black) and result of the energy decay compensation (blue).

Appendix B

Copyright permissions

Abdulaziz Alasbali,
PhD Student in Exploration Geophysics,
Exploration Geophysics Department,
H Block,
Level 4, 26 Dick Perry Avenue,
Kensington,
WA, 6151

Wednesday 25 November 2015

CAMBRIDGE UNIVERSITY PRESS

Australia & New Zealand
477 Williamstown Road
Port Melbourne
Victoria 3207
Australia

Correspondence
Private Bag 31
Port Melbourne
Victoria 3207
Australia

www.cambridge.edu.au

Telephone +61 (03) 8671 1400
Fax +61 (03) 9676 9966
Email info@cambridge.edu.au
ABN 28 508 204 178

Dear Abdulaziz Alasbali,

Title:	***Exploration Seismology***
Author/s:	R.E.Sheriff & L.P. Geldart
ISBN:	9780521468268
Item/s:	**Figure 6.44**: Factors affecting amplitude, page 180
	Table 6.1: Absorption constants for rocks, page 180

Thank you for your notification dated 30 October and e-mail on 6 November 2015 in which you requested permission to include the above figures as part of your PhD dissertation for the Curtin University of Technology, Perth entitled '*Intrinsic and scattering attenuation from borehole seismic and well log data'*, which is to be submitted in January or February 2016.

Non-exclusive permission is granted free of charge for this specific use on the understanding:

1. That you have checked that we do not acknowledge another source for this material.

   Cambridge gives no warranty or indemnity in respect of any third party copyright material included in the article/chapter and the licensee must seek their own permission clearance.

2. Full acknowledgement of the source should be given (author, title, Cambridge University Press, year of publication) together with the appropriate copyright notice, to appear with the extract.

3. That you include the sources and references referred to in the original text each time the figure is reproduced.

Yours sincerely,

C.T. Jones

Catherine Tudor Jones
Administrative Coordinator / Executive Assistant
Cambridge University Press, Australia and New Zealand

Abdulaziz Farraj S Alasbali

From: Fredericks Elizabeth <Elizabeth.Fredericks@ga.gov.au> on behalf of Copyright <Copyright@ga.gov.au>
Sent: Thursday, 5 November 2015 7:22 AM
To: Abdulaziz Farraj S Alasbali
Subject: RE: ask for permeation [SEC=UNCLASSIFIED]

Hi Abdulaziz,

Thank you for your email in regards to using a Geoscience Australia image in your thesis. You are more than welcome to use the image of the Northern Carnarvon Basin under a Creative Commons Attribution 4.0 International Licence. Please attribute Geoscience Australia in the following manner;

Regards

Elizabeth

Elizabeth Fredericks
IP and Copyright Manager
Governance & Business Services
Corporate Services | **GEOSCIENCE AUSTRALIA**
Phone: +61 2 6249 9367 Fax: +61 2 6249 9989
Email: Elizabeth.Fredericks@ga.gov.au Web: www.ga.gov.au
Cnr Jerrabomberra Avenue and Hindmarsh Drive Symonston ACT
GPO Box 378 Canberra ACT 2601 Australia
Applying geoscience to Australia's most important challenges

From: Abdulaziz Farraj S Alasbali [mailto:a.alasbali@postgrad.curtin.edu.au]
Sent: Wednesday, 4 November 2015 10:46 PM
To: Copyright
Subject: ask for permeation

Dear Geoscience Australia

It is my understanding that your organisation holds copyrights in the following figure from http://www.ga.gov.au/scientific-topics/energy/province-sedimentary-basin-geology/petroleum/offshore-northwest-australia/canarvon

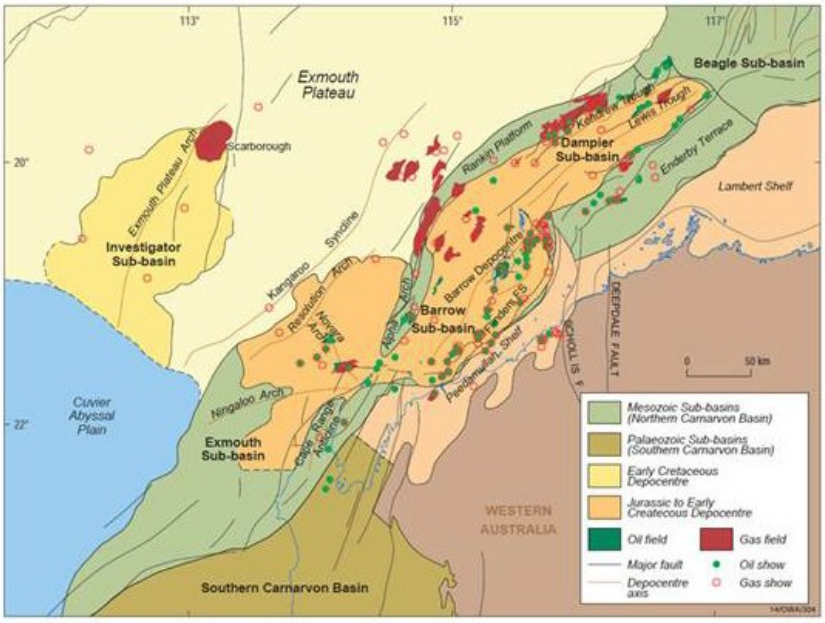

I would like to reproduce an extract of this work in a doctoral's thesis which I am currently undertaking at Curtin University of Technology in Perth, Western Australia.
I am carrying out this research in my own right and have no association with any commercial organisation or sponsor.

The figure that I would like to use for the purposes of the thesis is (*Northern Carnarvon Basin*).
Once completed, the thesis will be made available in hard-copy form in the Curtin Library and in digital form on the Internet via the Australasian Digital Thesis Program.

The material will be provided strictly for educational purposes and on a non-commercial basis.
Further information on the ADT program can be found at http://adt.caul.edu.au.

I would be most grateful for your consent to the copying and communication of the work as proposed.
If you are not the copyright owner of the material in question, I would be grateful for any information you can provide as to who is likely to hold the copyright.

I look forward to hearing from you and thank you in advance for your consideration of my request.

Yours sincerely

Abdulaziz Alasbali
PhD Student in Exploration Geophysics
Position | Department of Exploration Geophysics

Curtin University
Tel | +61 8 92663519
Fax | +61 8 9266 3407
Mobile | 0434 674 944
Address | Exploration Geophysics Department, H Block, Level 4, 26 Dick > Perry Avenue, Kensington, WA 6151, Australia

Email | a.alasbali@student.curtin.edu.au
Web | http://www.geophysics.curtin.edu.au